Engineering Materials

Sanjay Mavinkere Rangappa · Thottyeapalayam Palanisamy Satishkumar · Marta Maria Moure Cuadrado · Suchart Siengchin · Claudia Barile *Editors*

Fracture Failure Analysis of Fiber Reinforced Polymer Matrix Composites

Springer

Engineering Materials

This series provides topical information on innovative, structural and functional materials and composites with applications in optical, electrical, mechanical, civil, aeronautical, medical, bio- and nano-engineering. The individual volumes are complete, comprehensive monographs covering the structure, properties, manufacturing process and applications of these materials. This multidisciplinary series is devoted to professionals, students and all those interested in the latest developments in the Materials Science field, that look for a carefully selected collection of high quality review articles on their respective field of expertise.

More information about this series at http://www.springer.com/series/4288

Sanjay Mavinkere Rangappa ·
Thottyeapalayam Palanisamy Satishkumar ·
Marta Maria Moure Cuadrado · Suchart Siengchin ·
Claudia Barile
Editors

Fracture Failure Analysis of Fiber Reinforced Polymer Matrix Composites

Springer

Editors
Sanjay Mavinkere Rangappa
Natural Composite Research Group Lab
Department of Materials and Production Engineering
The Sirindhorn International Thai-German Graduate School of Engineering (TGGS)
King Mongkut's University of Technology North Bangkok
Bangkok, Thailand

Marta Maria Moure Cuadrado
Department of Bioengineering and Aerospace Engineering
University Carlos III of Madrid
Madrid, Spain

Claudia Barile
Department of Mechanics Mathematics and Management
Politecnico di Bari, Bari, Italy

Thottyeapalayam Palanisamy Satishkumar
Department of Mechanical Engineering
Kongu Engineering College
Perundurai, Tamil Nadu, India

Suchart Siengchin
Natural Composite Research Group Lab
Department of Materials and Production Engineering
The Sirindhorn International Thai-German Graduate School of Engineering (TGGS)
King Mongkut's University of Technology North Bangkok
Bangkok, Thailand

ISSN 1612-1317 ISSN 1868-1212 (electronic)
Engineering Materials
ISBN 978-981-16-0641-0 ISBN 978-981-16-0642-7 (eBook)
https://doi.org/10.1007/978-981-16-0642-7

This Springer imprint is published by the registered company Springer Nature Singapore Pte Ltd.
The registered company address is: 152 Beach Road, #21-01/04 Gateway East, Singapore 189721, Singapore

Editors are honored to dedicate this book to their parents

Preface

The fiber reinforced polymer (FRP) is an emerging area in polymer science and many structural applications. The rise in materials failure by fracture has forced scientists and researchers from all over the world to develop new higher strength materials for obtaining higher fracture toughness. Therefore, it is necessary to expand knowledge about the different mode of fracture behaviors of FRP composites to expanding the range of their application. So this book summarized the many of recent developments in the area of fracture behavior of FRP composites. The advances in fracture behaviors of FRP composites and replacement of conventional materials with FRP composites in the area of polymer science to achieve sustainable practice are described to the readers. Also, this book gives a sound knowledge of different fracture behaviors of FRP composites to the readers with numerous illustrations, methods, and results for graduate students, researchers, and industrialists. Academics, researchers, scientists, engineers, and students in the field of fracture analysis of FRP composites will benefit from this book.

Bangkok, Thailand — Sanjay Mavinkere Rangappa
Perundurai, India — Thottyeapalayam Palanisamy Satishkumar
Madrid, Spain — Marta Maria Moure Cuadrado
Bangkok, Thailand — Suchart Siengchin
Bari, Italy — Claudia Barile

Contents

Editors and Contributors

About the Editors

Dr. Sanjay Mavinkere Rangappa is currently working as Research Scientist and also 'Advisor within the office of the President for University Promotion and Development towards International goals' at King Mongkut's University of Technology North Bangkok, Bangkok, Thailand. He has received the B. E (Mechanical Engineering) in the year 2010, M. Tech (Computational Analysis in Mechanical Sciences) in the year 2013, Ph.D (Faculty of Mechanical Engineering Science) from Visvesvaraya Technological University, Belagavi, India in the year 2017 and Post Doctorate from King Mongkut's University of Technology North Bangkok, Thailand, in the year 2019. He is a Life Member of Indian Society for Technical Education (ISTE) and an Associate Member of Institute of Engineers (India). He acts as a Board Member for various international journals in the fields of materials science, and composites. He is a reviewer for more than 85 international Journals (for Nature, Elsevier, Springer, Sage, Taylor & Francis, Wiley, American Society for Testing and Materials, American Society of Agricultural and Biological Engineers, IOP, Hindawi, NC State Univesity USA, ASM International, Emerald Group, Bentham Science Publishers, Universiti Putra, Malaysia), also reviewer for book proposals, and international conferences. He has published more than 130 articles in high-quality international peer-reviewed journals, 5 editorial corners, 35 book chapters, one book, 15 books (Published in Elsevier, Springer, Taylor & Francis, Wiley), and also presented research papers at national/international conferences. Based on Google Scholar, the number of his citations amounts to 3700+ and his present H-index is 31 and i-10 index is 68. In addition, he has filed 1 Thailand Patent and 3 Indian patents. His current research areas include Natural fiber composites, Polymer Composites, and Advanced Material Technology. He is a recipient of the DAAD Academic exchange-PPP Programme (Project- related Personnel Exchange) between Thailand and Germany to Institute of Composite Materials, University of Kaiserslautern, Germany. He has received a Top Peer Reviewer 2019 award, Global Peer Review Awards, Powered by Publons, Web of Science Group. The KMUTNB selected him for the 'Outstanding Young

Researcher Award' 2020. He has recognized by Stanford University's list of the world's Top 2% of the Most-Cited Scientists in Single Year Citation Impact 2019.

Dr. Thottyeapalayam Palanisamy Satiskumar is currently working as Associate Professor at Department of Mechanical Engineering, Kongu Engineering College, Perundurai, Erode, Tamilnadu, India. He has received the B.E. (Mechanical Engineering) from M.P.N.M.J. Engineering College, Anna University, Chennai, India, in the year 2005, M.E. (Engineering Design) from Kongu Engineering College, Anna University, Chennai, in the year 2017, and Ph.D. (Faculty of Mechanical Engineering Science) from Anna University, Chennai, India, in the year 2014. He is a reviewer for many international Journals and international conferences (for Elsevier, Springer, Sage, Taylor & Francis). In addition, he has published more than 20 articles in high-quality international peer-reviewed journals, two book chapters and also presented research papers at national/international conferences. His current research areas includes natural and synthetic fiber composites, polymer composites and design of composites for bearing failures.

Dr. Marta Maria Moure Cuadrado received the B.Sc. in Mechanical Engineering at University Carlos III of Madrid (UC3M) in October 2010, the M.Sc. in Machines and Transports Engineering in October 2012, the M.Sc. in Advanced Structural Mechanics in June 2013 and the Ph.D. in Mechanical Engineering and Industrial Organization in April 2016 with mentions as International Ph.D. and the Extraordinary Doctoral Award. She is a reviewer for several international journals and international conferences (for Elsevier, Springer, Sage, Taylor & Francis, Wiley). In addition, her scientific results have been disseminated through the publication of 11 scientific-technical documents included in JCR (9 of them in the first quartile of his category), 2 book chapters, and by attending to 19 International Congresses and 5 National Congresses. All her research experience has been focused on the mechanical behavior of advanced materials, polymer composites, fiber composites, fracture mechanics, design of discrete damage mechanics models, experimental and numerical simulation of structures subjected to static and dynamic loads, ballistic impact and blast analysis.

Prof. Dr.-Ing. habil. Suchart Siengchin is President of King Mongkut's University of Technology North Bangkok. Prof. Dr.-Ing. habil. Suchart Siengchin, received his Dipl.-Ing. in Mechanical Engineering from University of Applied Sciences Giessen/Friedberg, Hessen, Germany in 1999, M.Sc. in Polymer Technology from University of Applied Sciences Aalen, Baden-Wuerttemberg, Germany in 2002, M.Sc. in Material Science at the Erlangen-Nürnberg University, Bayern, Germany in 2004, Doctor of Philosophy in Engineering (Dr.-Ing.) from Institute for Composite Materials, University of Kaiserslautern, Rheinland-Pfalz, Germany in 2008 and Postdoctoral Research from Kaiserslautern University and School of Materials Engineering, Purdue University, USA. In 2016 he received the habilitation at the Chemnitz University in Sachen, Germany. He worked as a Lecturer for Production and Material Engineering Department at The Sirindhorn International Thai-German Graduate

School of Engineering (TGGS), KMUTNB. He has been full Professor at KMUTNB and became the President of KMUTNB. He won the Outstanding Researcher Award in 2010, 2012 and 2013 at KMUTNB. His research interests in Polymer Processing and Composite Material. He is Editor-in-Chief: KMUTNB International Journal of Applied Science and Technology and the author of morethan 250 peer-reviewed Journal Articles. He has participated with presentations in more than 39 International and National Conferences with respect to Materials Science and Engineering topics. He has recognized and ranked among the world's top 2% scientists listed by prestigious Stanford University.

Prof. Eng. Claudia Barile achieved the master's degree in Mechanical Engineering magna cum laude in July 2008 at the Polytechnic University of Bari. She got the Ph.D. title on February 2012 in Advanced Production Systems. Currently she is senior Lecturer of Mechanical Design and Experimental Mechanics at the Department of Mechanics, Mathematics and Management (DMMM) of the Polytechnic University of Bari. Her research activities are mainly focused on the mechanical characterization of materials (composites, metals, polymers, etc.) with both traditional and innovative experimental techniques. Along her research activities, she keeps in touch and actively collaborates with numerous research centers and industrial partners. In 2017 she gained the National Scientific Qualification by the Italian Ministry of Education, Universities and Research as Associate Professor in the SSD 09/A3 (ING-IND/14). She took part in many international and national conferences as Relator and Invited Lecturer. She is member of the Editorial Board of the different international journals, and reviewer of lots of impacted international journals. She has published 110 scientific papers. Specifically she is author of 1 international book, editor of 2 international books, author of 3 book chapters, 47 papers published on international journals, and 45 on international conferences. She has recognized by Stanford University's list of the world's Top 2% of the Most-Cited Scientists in Single Year Citation Impact 2019.

Contributors

J. S. Alein Department of Civil Engineering, SRM Institute of Science and Technology, Kattankulathur, Chennai, India

V. Arul Mozhi Selvan Department of Mechanical Engineering, National Institute of Technology, Tiruchirappalli, India

H. Dineshkumar Department of Aerospace Engineering, Indian Institute of Science, Bengaluru, Karnataka, India

Divya Divakaran Research and Development Department, Pinnacle Bio-sciences, Kanyakumari, Tamil Nadu, India

Dineshkumar Harursampath Nonlinear Multifunctional Composites Analysis and Design Laboratory, Department of Aerospace Engineering, Indian Institute of Science, Bengaluru, Karnataka, India

Haris Ahmad Israr Department of Aeronautics, Automotive and Ocean Engineering, School of Mechanical Engineering, Faculty of Engineering, Universiti Teknologi Malaysia, Johor Bahru, Malaysia

Mahzan Johar Department of Mechanical Engineering, Faculty of Engineering and Science, Curtin University Malaysia, Miri, Sarawak, Malaysia

Mohit Hemanth Kumar Center for Nanoscience, Composite Research Center, Chennai, Tamil Nadu, India

Vinod Kushvaha Department of Civil Engineering, Indian Institute of Technology Jammu, Jammu, J&K, India

Alak Kumar Patra Department of Civil Engineering, Advanced Composite Research Centre, SRM Institute of Science and Technology, Kattankulathur, Chennai, India

Raja Soma Sundaram Pillai Department of Mechanical Engineering, Rohini College of Engineering and Technology, Palkulam, Kanyakumari, Tamil Nadu, India

Hemaraju Pollayi Advanced Composite Structures Laboratory, Department of Civil Engineering, GITAM University, Hyderabad, Telangana, India

Rajesh Rajamoni Department of Mechanical Engineering, Rohini College of Engineering and Technology, Palkulam, Kanyakumari, Tamil Nadu, India

P. Ramesh Department of Production Engineering, National Institute of Technology, Tiruchirappalli, India

V. R. Ranganath Structural Technologies Division, CSIR-National Aerospace Laboratories, Bengaluru, Karnataka, India

Indrajit Ray Department of Civil and Environmental Engineering, University of the West Indies, St. Augustine, Trinidad and Tobago

Aanchna Sharma Department of Civil Engineering, Indian Institute of Technology Jammu, Jammu, J&K, India

G. S. Sivagnanamani Department of Mechanical Engineering, Anna University, Chennai, India

H. Sreedhara Knowledge and Technology Management Division, CSIR-National Aerospace Laboratories, Bengaluru, Karnataka, India

Indran Suyambulingam Department of Mechanical Engineering, Rohini College of Engineering and Technology, Palkulam, Kanyakumari, Tamil Nadu, India

King Jye Wong Department of Applied Mechanics and Design, School of Mechanical Engineering, Faculty of Engineering, Universiti Teknologi Malaysia, Johor Bahru, Johor, Malaysia

Introduction to Fracture Failure Analysis of Fiber Reinforced Polymer Matrix Composites

Alak Kumar Patra, Indrajit Ray, and J. S. Alein

Abstract The fiber reinforced polymer composites (FRPC) are being widely used in several advanced engineering structures ranging from civil infrastructure to aircraft, spacecraft, ships, cars, sports goods and in many other outdoor and household applications. The major advantage is its high specific strength, stiffness, and durability leading to sustainable applications. However, the knowledge of the basic constituents, their roles, and failure mechanism are essential to properly understand the behaviour of the composites for design and manufacturing of FRPC components and structures. This chapter will provide an introduction of the FRPC, a brief history of FRPC and its constituents such as fibers and matrices. More detailed information on types, manufacturing, and classification of glass, carbon, and aramid fibers will also be provided. Similarly, descriptions on various polymer matrices such as epoxy resins, vinyl ester, phenolic resins, polyester resins, and polyurethane, and also emerging resins for special applications will be furnished. Different classes of FRPCs with their typical characteristics have been discussed. This chapter further describes the fracture failure mechanism of FRPCs from mechanics or fracture mechanics approach indicating the existing research gaps in different sections.

Keywords Classification of FRP · Fiber reinforced polymer composites · Fracture failure · Types of fibers and matrices

A. K. Patra (✉)
Department of Civil Engineering, Advanced Composite Research Centre, SRM Institute of Science and Technology, Kattankulathur, Chennai 603203, India
e-mail: AlakPatra19@gmail.com

I. Ray
Department of Civil and Environmental Engineering, University of the West Indies, St. Augustine, Trinidad and Tobago
e-mail: IndrajitRay29@gmail.com

J. S. Alein
Department of Civil Engineering, SRM Institute of Science and Technology, Kattankulathur, Chennai 603203, India
e-mail: jsalein1995@gmail.com

S. Mavinkere Rangappa et al. (eds.), *Fracture Failure Analysis of Fiber Reinforced Polymer Matrix Composites*, Engineering Materials,
https://doi.org/10.1007/978-981-16-0642-7_1

1 Introduction

Composites are systems or combinations of materials insoluble to one another. Composite materials and structures have become important potential field of research, development and applications to various advanced research centres, industries and key organizations like intelligence bureau, defence research, construction, transportation (including terrestrial, marine, aviation and space), science and technology of all most all the countries in the world for their advantages revealing national and international importance and billion dollars' market. As per American Composite Manufacturers Association [1], end products market of US composite industry is estimated to reach 113.2 billion dollars by 2022. Composite materials are going to replace more than 50% of conventional materials in near future for their high strength to weight ratio, durability, flexibility in design and production with several other advantages. Fiber reinforced polymer composites (FRPCs) are significant among the composites in the world. FRPCs are primarily fiber strengthened polymers. They are advantageous for their higher specific strength, stiffness, modulus, and lighter weight than conventional materials like metals or stones. Due to these multi-functional properties, FRPCs are largely used in aerospace, marine, mechanical (including automotive), construction, bio-medical, space and many other engineering and technological applications. Predominantly, high strength fibers have reinforced the demand and resulted in the highest share of production which is evident from the global annual estimated output of 20,000 tons of carbon fibers only for FRPC composites in the billion-dollar composite industry [57].

Fiber reinforced composites (FRPs) can be broadly classified into four classes, namely metal matrix composites (MMCs), polymer matrix composites (FRPCs), ceramic matrix composites and carbon matrix composites. Among the four broad classes of FRPs mentioned above, The book focuses on fiber reinforced polymer matrix composites (FRPCs) only.

2 History of FRPC

Nature provided human civilizations with many FRPCs through grasses (paddy, wheat, sugarcane, bamboo) and woods etc. to meet up the basic needs i.e., fooding, lodging, clothing and also for their survival. FRPCs can be assumed to be existed with or prior to the advent of life. Fiber reinforced polymeric composites were presumably produced in the form of peptidoglycans in Nature for the cell walls or cytoskeletons of prokaryotic bacteria about 3.7 billion years ago [37] or before 3.5 billion years [45, 47]. Common example of natural FRPCs are straws [21] and bamboos [22] used by mankind for residential, military or other purposes from ancient times. Cell walls of straws are composed of cellulose or hemicellulose fibers and lignin polymer matrix. Whereas bamboos are basically cellulose fiber reinforced cross linked lignin

polymers. Mud bricks with straws were used in ancient civilizations for making residences even in 9000 B.C. [27, 44, 51].

Manmade composite bows have been known from second millennium B.C.E. (2000 through 1001 B.C.E.) [35]. Modern versions are made with glass fiber bellies, backs and a natural or artificial core. Fibrous composite bows are mentioned in all the three epics of the world. FRPCs are used in engineering and technology from pre-historic era for their extra ordinary advantages. The FRPCs are everywhere from microscopic cells to very large barges. The current production of FRPC is focussed on emerging composite technologies and on the development of sustainable 3D-printed industrial composites, through the use of bio-polymers and bio-fiber, MADM (multi-attributes decision making) tools [43], Integrated Computational Materials Engineering (ICME) of composites or Composite Airframe Life Extension (CALE) program to withstand against fatigue load under extreme environmental conditions.

3 Composite Constituents

Primary constituents of FRPCs are polymer matrix and fiber reinforcements. There are accelerating or coupling agents and other types of fillers also. Forces are predominantly supported by fibers whereas matrix keeps them in their arrangements and positions. Fibers of different origin can be continuous (long) or discontinuous (short). In comparison to the unreinforced (neat) polymers, desired better properties are achieved through reinforcing with fibers. Thus, fibers are responsible for higher strength, stiffness or other improvements in composites. They are stiffer and better than bulk due to reduction of impurities in different forms and are used to achieve mechanical superiorities. Knowledge of fibers is very important in composite science and technology.

3.1 Fibers

Fibers are the ingredients responsible for superior strength, durability and serviceability of fiber reinforced polymer composite (FRPC) materials. These fibers not only reinforce the polymers but improves functionalities as integral constituents of FRPCs. Fibers may be used directly as in prepregs, as chopped strand mat (CSM) or as woven roving mat (WRM). There are natural as well as manmade fibers. Nature provides a wide range of plant, animal or mineral fibers like hemp, jute or asbestos. However, man-made fibers are derived from chemical processes controlled by people. As for example, Kevlar (aramid), glass or carbon are man-made fibers. Kevlar has superb toughness, modulus and thermal stability suited for advanced technological applications. Other types of fibers gaining importance faster today are hybrid fibers. Kevlar/Carbon or Kevlar/glass woven are the examples. Both manmade as well as natural fibers are being utilized in different engineering and technological fields

for their several functional applications. Manmade fibers are newer developments over natural counterparts meeting industrial and societal needs and have been briefly discussed in the following section.

3.1.1 Manmade Fibers

Manmade fibers are often termed as synthetic fibers. At present, several technical textiles are used in different medical, or bio-medical engineering applications. Textile fibers have become essential inclusions in composite industries today. Fibers may be broadly classified into manmade and natural fibers. The manmade fibers has gained popularity over the years because of their durability, consistency, and availability of standardized products with uninterrupted supply chain. In USA, the manmade fibers are divided into different groups per "Textile Fiber Products Identification Acts" (TFPIA). Table 1 shows the classification of manmade fibers based on the TFPIA. Synthetic fibers and artificial fibers are presented separately under the manmade class of technical textiles in the classification chart in the sense that the artificial fibers are chemically regenerated fibers from natural resources like cellulose-based viscose rayon whereas only chemicals not found in nature are used to manufacture synthetic fibers. Glass, carbon and aramid fibers are abundantly used among the synthetic fibers in composite industries. Glass fibers are most widely used in FRPCs for low cost, higher tensile strength and insulation with chemical resistance [5, 18, 32].

Table 1 Classification of man-made fibers

Manmade fiber					
Regenerated		Synthetic			
From cellulose	From other sources	Organic	Inorganic		
Viscose	Protein	Aramid	Metal	Special non-metal	Others
Modal	Alginate	Polyethylene	Stainless steel	Boron	Glass
Acetate	Rubber	Acrylic	Nickel		Carbon
Polynosic	Elastodiene	Polypropylene	Titanium		Silicon-carbide
Tencel		Polyester	Copper		Zirconia
		Polyurethane	Aluminium		Others
		Elastane	Gold		
		Fluorofiber	Silver		
		Trivinyl			
		Chlorofiber			

Glass Fibers

Glass fibers in the form of hair like strands are drawn from molten silica (SiO_2) reach materials (called glassy materials) above their glass transition temperatures, Tg [2]. Polymers, ceramics or even metallic materials can be used to produce glassy materials [2]. Optical glass fibers have revolutionized the sensing as well as communication system with a Noble Prize to Charles Kao in 2009 [2]. Viscoelastic glassy substances show viscosity dependant linearly proportional relationship between stress and strain above their transition temperature (Tg). That is stress varies as strain above Tg at constant volume. As a result, increase in length is accompanied with decrease in diameter.

The property discussed in previous section can be presented mathematically as

$$\sigma = \eta\varepsilon \tag{1}$$

where σ is the stress, η is the viscosity, and ε is the longitudinal axial strain in the viscelastic cylindrical fiber. Similarly, if the increase in length, dx is accompanied with the decrease in cross sectional area −da, then for constant volume under Newtonian viscosity,

$$dx/x = (-)da/a \tag{2}$$

where 'x' is the original length and 'a' is the initial cross-sectional area of the spun semi crystalized glassy material. Depending on this basic principle, melted source material kept on electrically heated and perforated (200–400 nos) platinum-based bushings to drop under gravity and finally processed as glass fibers at revolving collectors at a speed of 1–2 km/min [2]. Basically, glass consists of SiO_2 in a mixture of silicate type, though it may contain different amorphous metal oxides. Different types of glass fibers have been developed to meet several purposes in the society. Glass fibers compositions depend primarily on the types of glasses (i.e., A-glass, E-glass or S-glass etc.) used for their manufacturing [3, 56]. More than 90% of glass fibers are processed from E-glass. The name E-glass came from good electrical resistance. Others are of special types for specific uses. The classification of glass fibers is presented on the next page. Industrially used glass fibers can be categorized into the following classes:

E-glass fibers are relatively inexpensive and contain silica (52–56% by weight), alumina (12–16%) and the oxide of Boron (5–10% by weight) with a very low alkali content (1% by weight). They are generally used for circuit boards which are printed and for applications in aerospace industries.

In S-glass fibers, S stands for strength. S-1 HM glass fibers are produced with highest tensile modulus of 90 GPa among the glass fibers. S-3 HDI® fibers are used in electronic products for better performance while S-1 HM® and S-3 UHM™ fibers are employed for higher stiffness.

Typically, S2-glass fiber, a brand name developed by Owens-Corning is currently under AGY Holding Corporation's trademark is one of the topmost GF. S2-GF is

10 times more costly and 40% more strong in tensile strength and 21% more tensile modulus than E-glass fibers ("Glass fiber," n.d.). Though S-glass is costlier, they are used for the aerospace industries.

Glass fibers with higher silica (64–75% SiO_2 by weight), deferred alumina (16–24% Al_2O_3 by weight) and MgO (0.25–3% by weight) have been invented [13]. There are variety of glass fibers. Selection of a particular type depends on the price, service they provide and the applications.

Other GFs developed for special purposes are tabulated in the previous page. They are briefly mentioned below:

A-GF: manufactured with sodium carbonate, SiO_2, lime, Al_2O_3, dolomite and fining agents. The A-glass is typically used (for flat glasses for windows etc.) or glass containers (like jars).

AR type GF: Alkali-resistant glass fibers made of alkaline zirconium silicates [53] these are specially processed for concreting.

C-glass fibers: Essential ingredients are Calcium, Boron and silica and they are resistant against acidic corrosion. They are employed in environment subjected to corrosive acids. The glass is known as chemical glass.

D-GFs-A glass fiber with lower dielectric constants is manufactured from boron trioxide and silica It is suitable for optical, electrical and cookware.

ECR-glass fibers—It has both electrical as well as chemical (both acid and alkali) resistivity; hence the name is ECR. Maximum alkali content is 2% by weight and is used in cases where high electrical and chemical resistivities are desired in strong fibers.

R-glass—Basically this is calcium alumino-silicate glass. These are used as reinforcement for higher strength and acid corrosion resistance.

In addition to the above, there are several other types of glass fibers used for several special purposes. As for example, ultra-pure silica fibers [56], hollow [30] and trilobal [24] GFs. Ultra-pure glass fibers have high silica contents and are fit for fiber optic communication. Hollow glass fibers are used in aerospace and automotive industries for their self-healing capability. Their specific strength and elasticity are higher than other GFs. Trilobal glass fibers have higher surface area and are used for higher thermal and acoustic insulation.

Adventex glass fibers are another special type of GFs, which is manufactured to combine the electrical resistance of E-glass with the acid corrosion resistance of ECR glasses with high melting point. They are used in industrial sectors with higher temperature fluctuations; such as power plants, oil and gas industries, waste water disposal system etc.

Glass fibers are mostly used in the form of chopped strand mats (CSM), or woven roving mats (WRM). There are other forms like tow, or veil mats and some other forms. Interested readers are suggested to go through references [2, 3, 6, 13, 53, 56] for further concepts and knowledges. It is already mentioned earlier that another most abundantly used fibrous reinforcements are carbon fibers. Carbon fibers will be briefly discussed in the following section.

Carbon Fibers

The fibers with greater than 92% carbon by weight is termed as carbon fibers. The carbon content may vary from 92 to 100 wt%. These fibers are thermally treated over a temperature range of 1000–1500 °C [38]. Historically, carbon fibers were first developed and used by Edison for his carbon filament lamps. Carbon fibers are primarily used in aerospace and automotive industries for their higher tensile modulus, fatigue resistance, thermal conductance [32] and good electrical conductivity. In addition to the stated advantages, the other reasons for the application of carbon fibers in aerospace, civil, military, marine, mechanical engineering and other industries are that carbon fiber reinforced composites have greater specific strength and resistance to impact [49] with low thermal expansions. As on 2012, the global market of carbon fibers was estimated as 1.7 billion dollars with an average projected annual growth of 10–12% per annum for a period from 2012 to 2018 ("Carbon fibers," n.d.). Though in composite technology, sometimes both carbon and graphitic fibers are called carbon fibers, graphitic fibers contains more than 99% graphite and are treated over 2000 °C. Low-cost production of carbon fibers and alternative precursors are still a good challenge to the manufacturing industries. Typically, they have diameter ranging from 5 to 10 μm. Carbon fibers being two times stiffer and five times stronger are lighter than steel (Innovative composite Engineering. n.d Retrieved from https://www.innovativecomposite.com/what-is-carbon-fiber/) are preferred by designers for components of important structures.

Manufacturing of carbon fibers

Generally, carbon fibers (CF) are manufactured from synthetic fibers made from either polyacrylonitrile, rayon or pitch. Polyacrylonitrile is commonly known as PAN and pitch used is derived from petroleum containing higher proportion of organic polymers. Almost 90% of the CFs are manufactured from PAN precursor and 10% CFs are produced from pitch of petroleum or rayon. More linear polymers as well as cyclic polymers can be used for inexpensive production of CFs [39].

PAN precursors are produced through different polymerization methods. In almost all cases, monomers and catalysts or initiators are indispensable. The easiest way of polymerization is to mix the initiator directly into the liquid monomers. In another method, acrylonitrile (AN), comonomer, are dissolved into a solvent for polymerization in presence of catalysts. The end products of such polymerizations are the precursors which are treated chemically and mechanically to manufacture carbon fibers.

The first step of the production of carbon fibers from the PAN precursors is to stabilize them at about 200–300 °C temperature in presence of air (depending on the chemical character of the precursor) for half an hour to two hours to arrive at ladder bonding from the linear bonding. The second step is to carbonize [11] the fibers by stretching and heating the fibers through 1000–1600 °C in absence of oxygen in an inert gaseous environment for severe vibration of carbon atoms to expel almost all other non-carbon atoms without burning the fibers. Through this process, fibers are transformed into a chain of tightly packed long carbon atom with a little or no more

non carbon atoms. Different compositions of process materials for the processing of carbon fibers are trade secrets. Finally, sometimes these fibers are treated and sized before marketing. Regarding the CF mats, apart from 2-D crimped weaves, there are advancements in 3-D, multi-dimensional as well as weaves without crimps.

Classification of Carbon fibers

Carbon fibers are widely used in composites, as stated earlier, for their high strength, stiffness and light weight. Depending on these engineering advantages, CFs can be broadly classified into low modulus low-strength, high tensile strength, high tensile modulus fibers. Isotropic CFs are of low modulus (~100 GPa) category but inexpensive, in which crystals are randomly oriented, the second one, which belongs to high strength category, has higher modulus than isotropic (~300 GPa) and finally the high modulus type with excellent properties, can be further sub divided into ultra high modulus (>500 GPa, heat treated beyond 2000 °C), high modulus (>300 GPa) and moderate modulus (<300 GPa) categories. Some developed (like USA, Germany, UK etc.) and developing countries are patent holders of CFs. CFs can be classified based some other factors which is avoided in this introductory chapter. Finally yet importantly, aramid fibers are discussed in the following section for their extra ordinary characteristics.

Aramid Fibers

Aramid fibers are man-made synthetic fibers. They are placed under synthetic organic fiber group. The name came from aroma (aromatic) and amide (Polyamide). These are organic polymers which fall under newly developed polymeric fibers. Aramid fiber was first developed in the laboratory of Du Pont as Kevlar by scientist Kwolek. From its first appearance, Kevlar (a brand name from Du Pont) got importance both in research and commercial fields through a numerous research and developmental projects. This fiber has high strength with surprisingly high stiffness [(five times stronger than steel [54]), better damage-resistance and damping properties, higher impact resistance, lesser flammability, high melting point and integrity at higher temperature. Aramid fiber composites have highest specific tensile strength. Strength is provided by strong bonds of CO–NH (amide) groups. Aramid fibers are famous for applications for ballistic, armour and military usage among numerous engineering and technological applications. The major demerits of aramid fibers is the problem in cutting or machining and lower resistance to compression and bending [11]. There are different varieties of Kevlar like Kevlar 49, Kevlar 29, and Kevlar 149. The last one possesses maximum modulus value under tension among the aramid fibers. USA, Japan, Korea and China are major producers of aramid fibers. Several new fibers of polymeric origins are continuously being developed now.

The other fibers under artificial and synthetic groups are developed for specific purposes. Some of them are very much expensive like boron fibers (high tensile modulus and compressive stress). While ceramic fibers like silicon carbide SiC or

alumina (Al_2O_3) are suitable at high temperature applications are expected to be discussed in following chapters as and when will be necessary.

Natural fibers are being proposed as replacements for the synthetic fibers primarily from environmental point of view. Primarily they are plant or animal fibers. Some natural resources are used for processing artificial fibers. Synthetic fibers are still widely used in manufacturing of composites to serve the world. Natural fibers have both advantages and disadvantages. The advantage of natural fibers is that they are bio degradable. On the other hand, natural fibers are normally lesser strong and durable than high grade synthetic fibers. Another problem is the matrix, most of the matrix used for composite constructions today are non-bio-degradable. Although a good deal of research works have been performed to develop bio degradable resins or bio-degradable other matrices, it still remains an open and vast field of research. Natural fibers are to be discussed in more details in third chapter. Both bio-fibers and bio-degradable matrices are growing fields of research.

Matrices are other primary constituents of FRPCs. Generally, they occupy 30–40 vol% within the fiber reinforced composites and serve several important purposes. The processing of matrices also plays roles on the performance of composites. In this context, it is relevant to discuss on the matrices now.

3.2 Matrices

Matrices hold the fibers in their positions in desired directions, distribute the stress among the reinforcements and share some part of the loads supported by FRPC components or structures. This is a continuous phase where fibers are dispersed protects the fibers from the environment. There is an interphase between matrix and fiber which is important from stress distribution point of view.

3.2.1 Types of Matrices

Matrices may be broadly classified into polymeric, metallic, ceramic and carbon matrices. But there are advancements in matrix research and some new developments have been included in to composite science and technology like Bismaleimide (BMI) resins.

Polymer Matrix

Most of the polymer matrices are resins. They can be divided into two major classes, namely thermoset resins and thermoplastic resins. Thermosets are those which set permanently and cannot be remoulded after curing. Unlike thermosets, thermoplastics can be moulded again with some treatments due to absence of cross links. One of the examples of thermoplastic resin is poly ether ketone (PEEK). Thermoplastics

reduces the cost of production by faster processing. The polymer resins are available in several varieties with different properties as follows:

Epoxy resins

Epoxy resins are intermediate produced from basic monomer bisphenol A diglycidyl ether (BADGE) or DGEBA [10]. This basic monomer is derived from the reaction between epychlorohydrine and bisphenol A (BPA). Though there are debatable issues with the BPA about the merits and hazards caused by it with a list of moderate hazard warning on the considerable exposure of infant lab animals to BPA [4], BPA based epoxy resins are largely used in manufacturing of numerous products ranging from aerospace structures to baby feeding bottles sharing about 80–90% of the market. Not only monomeric, but epoxy resins may be oligomeric chemicals. These resins are some intermediate products of reactions [33] and need another process of cross linking called curing (with curing agents) for complete polymerization and formation of more stable 3-D network of atoms. Typically, epoxy resins are characterized by epoxide group, a ring of one carbon and two oxygen atoms [40].

The other types of resins are:

- Vinyl ester resins
- Phenolic resins
- Polyester and
- Polyurethane.

Vinyl ester resins

Principles of epoxy and polyester resin productions are combined to produce vinyl ester resins to have some advantages of both with intermediate cost between polyester and epoxy resins. They provide superior chemical and water resistance, higher strength and stiffness at high temperature than polyester resins. These resins are widely used in marine and construction industries. Vinyl ester resins are also used in construction of small hull vessels (speed boats, canoes etc.).

Phenolic resins

These resins are highly fire resistant but lower mechanical strengths. They are used in structural applications for their better flame resistance, lower smoke and toxic gas emission and high operating temperature they are used in airplane interiors, ship decks, internal bulkheads as well as ship furnishings.

Polyester resins

Polyester resins are synthetic in nature and is unsaturated. These are derived from the reaction between organic acids and alcohols. These are mostly used in toner of printer, bulk and sheet moulding. Polyester resin is the most frequently used matrix in polymeric composites for their lower cost. Epoxy resins with better adhesive and lesser shrinkage properties hold the second place in market demand for higher costs.

Polyurethane

These are copolymers developed from polyols (containing more than two hydroxyl groups) and polymeric or dual isocyanates. They are good elastic-adherents with balance in hardness. These are used in production of rubbers, medicines and several other products ranging from plastics to inks. The material can be used for very soft to very hard end products.

Newly developed resins for better performance

These resins can be used in aerospace industries with notable advantages over epoxy resins. Polyimide (PI) resins and bismaleimide (BMI) are two examples of such resins. Apart from the aerospace industries, they can be employed in several other composite constructions for these advantages.

The important disadvantage of these polymeric resins is resistance to bio-degradation. Development of bio-degradable resins or some chemicals to increase feasibility of degradation of these compounds cover a wide range of current trends in research and developments.

Metal Matrix

Though metal matrices are not used frequently, Metal matrix composites are still preferred in defence to perform at elevated temperatures. Generally, aluminium, magnesium and titanium alloys are used as metal matrix for boron, carbon, alumina and silicon carbide fibers. In addition, copper, lead, silver and nickel sometimes are used as metallic matrices.

Ceramic Matrix

Molybdenum disilicide ($MoSi_2$), SiC, silicon nitride (Si_3N_4), Al_2O_3, lithium-aluminium silicate (Li-Al-silicate or glass ceramic) are used as ceramic matrices for niobium (Nb), carbon and SiC fibers in processing ceramic composites.

The important compound used with polymeric resins for faster and complete polymerizations of resins are hardeners. Moreover, several modifiers are used for production of FRPCs.

3.3 Fillers and Other Modifiers

The main purposed served by the fillers or modifiers (additives) in polymeric matrix is to reduce the cost by saving expensive resins. Additionally, gain in modulus, smoothness and viscosity can be achieved through addition of additives. Moreover, processability, lubricating efficiency and many permeability reductions can

be achieved using fillers. Fillers commonly used for ester resins are carbonate of calcium reducing shrinkage in moulds. Among the other fillers, some microspheres of glasses, or even mica or clay can be used as additives also.

Apart from the advantages mentioned above, they can reduce the resistance to impact, make composites weaker sometimes. Therefore, choice of fillers or modifiers is a judicious problem. On the other hand, additives like some elastomers can be effectively used for increasing resistance against crash and impact of thermoset resins which are otherwise brittle in nature. Rubbers, silicon and titanium dioxide can be used for improving different characteristics of FRPCs; like some can reduce flammability (trioxide of antimony etc.), other can add some colours, or resist fading out of colours and hazards caused by exposure to ultra violate (UV) rays (benzotriazoles etc.).

4 Typical FRPCs

Fiber reinforced polymer matrix composites (FRPCs) are processed from the constituents discussed in the preceding sections. Generally, in the first stage, laminae are developed as their basic units.

4.1 Laminae

A typical lamina is a thin layer of FRPC (0.1–1 mm thick). Numerous fibers are embedded within matrices. Lamina can be made of unidirectional fiber layout (UD lamina or ply), bidirectional or even multidirectional fibrous laminae are produced to achieve better mechanical performance in two or more directions. UD ply has a Typical thickness of UD lamina is about 0.12 mm and that of woven one is about 0.25 mm.

It is evident from the above discussion that depending on the fiber orientation, laminae can be divided into unidirectional, bidirectional or multidirectional laminae. In bi-directional laminae, normally fibers are arranged in 0° and 90° directions. But the orientation angle may vary and the fibers can be arranged in different directions to develop multi directional laminae. Currently, 3-D woven fibers are used for superior performances. In UD lamina, fiber direction is generally designated as principal direction or direction 1, the inplane direction perpendicular to the fibers is designated as matrix direction 2 (transverse direction) while the direction perpendicular to the plane of the lamina is denoted as matrix direction 3. Stress and strains are to be expressed with reference to these principal material directions.

Several laminae can be arranged one over the other, bonded together and sometimes heat pressed to produce laminates.

4.2 Laminates

Laminate is the most common form of FRPCs. Thicker single layer (thicker than typical lamina) fiber reinforced composite of thickness 2–3 mm can be used as skins of sandwich composites. Primary advantage of sandwich composites is their higher strength to weight ratios. Laminates are designed for thicknesses required to support the loads with limited deformations. Direction of fibers sequence of stacking for different layers of laminates can be adopted to achieve desired advantages.

Several types FRPCs are processed to meet numerous purposes. The FRPCs can be classified into different classes based on different criteria.

4.3 Classification of FRPCs

Classification based on fibrous reinforcement used:

Based on fibrous reinforcement used, FRPCs can be classified into following categories:

4.3.1 Carbon Fiber Reinforced Composites (CFRPs)

These are the FRPCs which are processed from polymer matrix reinforced with carbon or graphitic fibers. These are of high demands in aerospace industries. But their applications are realized in many engineering and technological fields for the many fold developments of the fibers and matrices especially for their high strength and light weight. But these are costlier than glass fiber reinforced polymer composites which is accepted in the composite industries for their several advantages.

4.3.2 Glass Fiber Reinforced Polymer Composites (GFRPs)

Essentially, the reinforcing fibers which strengthen the polymer matrices are glass fibers. These FRPCs are abundantly used in the industries for optimum performances with respect to their prices. Glass fibers are treated to render added advantages. They are suitable for almost all types of polymeric resins. Wide range of applications of GFRPs ranges from helmets to aerospace structural components. Vast field of their application includes but not limited to automotive, marine engineering and naval architecture.

4.3.3 Polymer Fiber Reinforced Polymer Composites

Aramid fiber, especially Kevlar is the most famous polymer fiber for the advantages mentioned in earlier sections. They are preferred in both defence as well as front sectors of military organizations.

Polymer fibers as well as their polymeric composites are still a growing field of research and development in many countries of the world.

4.3.4 Ceramic Fiber Reinforced Polymer Composite

Polymer resin strengthened with ceramic fibers are included in this group. Epoxy resin reinforced with ceramic fibers and microsilica additive have been reported for aerospace applications [48]. Throughout the world high temperature application of ceramic fiber reinforced composites are well practised. But still degradation in mechanical properties is an open field of research within this area of study.

Classification based on polymer matrices used:

It is already mentioned that FRPCs can be broadly classified into the following classes:

1. Fiber reinforced thermoset polymer composites.
2. Fiber reinforced thermoplastic polymer composites.

These two classes have been briefly discussed earlier and further discussion on this topic is avoided here to avoid repetition.

4.4 Speciality of FRPCs

Fiber reinforced polymer composites have strong direction dependence in their characteristics. The measurable parameters indicating their properties depend both on the orientation of fibers as well as direction of applied loads. Conventional metals are normally regarded as isotropic, however, fiber reinforced polymer matrix composites are anisotropic or orthotropic in nature. They exhibit higher modulus values in fiber direction. That is the stiffness in longitudinal fiber direction, in UD FRPC is significantly higher than that in transverse direction. In case of multidirectional arrangement of fibers, this difference in stiffness different directions are tried to reduce. Not only the longitudinal tensile modulus but the other properties like the thermal extensions, conductance or tensile strengths are considerably different in fiber and transverse direction in UD FRPCs. The stress distribution along the longitudinal direction are observed to be different in different cross sections at different distances from the end tabs of the specimen also in some cases. The design of FRPC components or structures is not so much straight forward as the metallic counterparts for the failure mechanism in this case is much more complex than metals due to fiber directions and the complex stress distribution within the interface between the fiber and the matrix.

The failure due to fracture in FRPCs is a complicated problem and depends on so many factors like the constituent fibers (different natural and man-made fibers), the matrices, their interactions especially at the interface, the loading types and directions, sensitivities of the constituents to the loads (static, dynamic, thermal etc.) and the environmental factors like including electrical and magnetic influences etc. These fracture failures of FRPCs are briefly introduced in the following section.

5 Fracture Failures of FRPCs

It is already mentioned that failures caused by fractures is complicated phenomenon and depends on several factors. Fibers are key role players in FRPCs. It is therefore may be an acceptable approach to start with the interaction of fibers with the matrices during fractures. There are several studies considering fibers and matrices as separate entities. The problem may be addressed from different points of views. One of such views of addressing this problem can be studying the fiber-stresses, stresses in matrices holding the fibers in positions, the interface stresses, fiber breakage, matrix cracks, fiber interactions, varying distances between the fibers, influence of other fibers on the broken one, or localized yields of matrix or fibers. This view of addressing localized effects of interaction between matrices and fibers is micromechanics [20, 35]. On the other hand, composite components and structures made of FRPCS are of interests for different sections of think tanks throughout the world. The deformation, buckling and fatigue loads, thermal behaviours, damping, energy absorbing capacity, effect of holes or similar discontinuities etc., the global responses are of interests. Response of a layer or a number of layers are intermediate in nature between these two approaches. In this approach, the deflection or load carrying capacity of individual layer, or that of the laminates of a groups of layers along with the interactions between the different layers of laminates are studied to predict their failures. Role of fiber orientation or constituent materials in a single layer or the layers of a laminate is an ever-growing field of study due to invention and development of new constituent materials for both fibers and matrices. In this, the investigation can be started with the deformation or other responses of some element of a layer with many fibers can be addressed first without going to the responses of individual fiber, matrix and the interaction between the matrix and fibers (as done in micromechanics).

The defect or flaws plays the key role in the strength exhibited by any material. These flaws are very much important in fracture failure of FRPCs [23]. The micro or macro-cracks governs the strength of the FRPCs. Thus fracture mechanics is an essential field of study in the fracture failures of the FRPCs, be it at micro or macro levels for strength of materials approach is essential but not sufficient to explain the behaviours of FRPCs. Three major stages are to be considered in fractures due to cracks: nucleation or initiation of microcracks, growth and coalescence and crack propagation. In the growth phase, microcracks grow stably to join with other micro cracks to form a macro crack. In the final stage, these macro cracks propagate fast leading to fracture. This happens at a stress level which is critical for unstable crack

growth. In brittle CFRPs, stage two is not prominent to be realized. Another point is to be noted here is that FRPCs have high level crack resistance due to matrix ductility and crack-arresting capability of fibers at the interface between fiber and matrix.

5.1 Modes of Macroscopic Fractures in FRPCs

Depending on the application of loads, fracture failures may occur due to following modes:

1. Fracture failure due to mode I.
2. Fracture failure due to mode II.
3. Mode III fracture failures.
4. Mixed mode fractures.

In mode I, tensile load is applied perpendicular to the facture plane leading to opening mode of fracture. It is termed as opening mode for the joints between the fracture surfaces at the crack tips open like opening some page in writing pad.

In mode two fracture, the load applied is parallel to the fracture plane and results in sliding the two newly developed fracture surfaces parallel to the crack surface and in the same direction to the crack front due to shear stress perpendicular to the crack front.

Mode III fracture occurs when load is applied in such a way that the shear stress is parallel to the crack front crack plane both. The load is applied out of plane to the shearing plane like tearing a paper by applying forces by two hands at one edge in reverse directions.

Mixed mode of fractures:

This mode of fracture can be characterized by the presence of two or more modes (Mode I and mode II, Mode I and Mode III or all modes) mixed at the crack front. This mixed mode fracture is common in case of sandwich composites due to asymmetry in both material and geometry of layers.

The pure modes of fractures (mode I, Mode II and Mode III) are shown in Fig. 1.

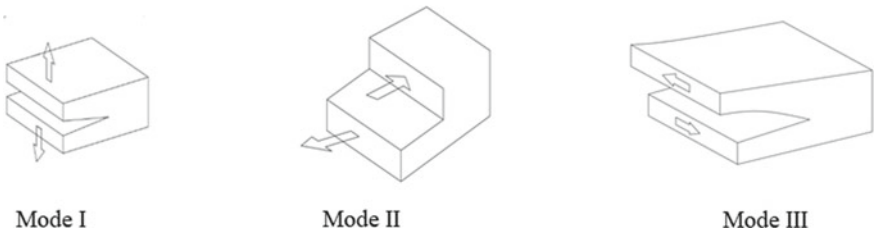

Fig. 1 Pure modes of fractures

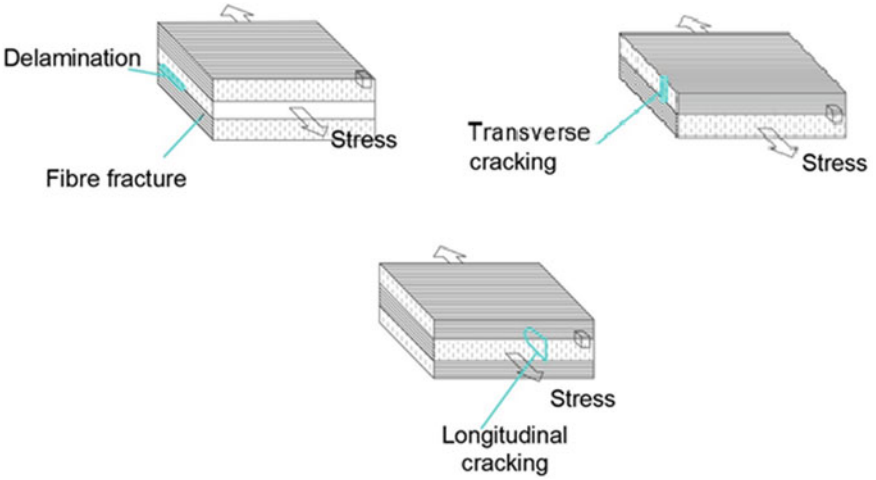

Fig. 2 Typical macro-scale failures in FRPCs

5.2 Fracture Failure Procedures

In fracture mechanics, two well accepted hypotheses are:

1. Every real material has inherent flaws, and
2. fracture occurs due to higher stress at the location of flaws than the adjacent materials [23].

In FRPCs, there are several anomalies or flaws present in the composites in microscales [46] and these are the breeding points of crack-initiations, growth and propagation due to the higher stress concentration at flaws than the surrounding materials. In macroscopic scales, failures mechanisms in FRPCs can be divided in to major four classes as follows:

1. Delamination,
2. Transverse cracking,
3. Fiber breakage and
4. Longitudinal cracking.

The failure mechanisms in macroscopic scales are presented in Fig. 2.

5.3 Fracture Mechanics Approach in FRPC Problems

Some concepts of isotropic material approach in linear elastic fracture mechanics is difficult to implement for FRPCs for anisotropy and inhomogeneity. Anisotropy and

inhomogeneity are there both in materials, and stacking sequence of laminae (i.e. several laminas in different directions) within the laminates invite complex problems.

The anisotropic materials with homogeneity can be used with fracture mechanics approach to deal with the FRPCs. Here, composite materials are assumed to be homogeneous but anisotropic. But in most of the cases FRPCs are not homogeneous revealing that this assumption is also insufficient to explain the behaviours of the FRPcs in true sense. Stress distribution around the crack tip is reported by Wu [58]. He finds that the stress intensities around the crack in affected by the properties of anisotropic materials, crack orientation with respect to the principal material axis and crack parameters. The researchers worked on the advancements in application of fracture mechanics to the problems of composite materials [7, 50, 55]. The problem is more critical in the case of fatigue. It is a complex phenomenon. Crack tends to grow parallel to the fibers in a self-similar pattern if the crack is cut in parallel to the fiber direction, whereas the crack growth is parallel to the fibers if cut at an angle to the fibers not parallel to the crack itself. In a laminate of various layers, the crack growth is much more complicated. Therefore, the growth prediction of different cracks in FRPCs is a complicated problem in reality.

5.4 Effect of Transverse Shear

Transverse shear plays an important role in predicting failures of FRPCs for the modulus of matrix materials is much lower than the fiber-materials and even lower than the FRPC laminates as a whole. The shear characteristics of entire laminate can be considered as the sum of all the transverse shear effects in different interlaminar regions. Thus, transverse shear stresses have much more effects on FRPCs than isotropic plates.

5.5 Failure of FRPCs Under Compression

The failures of FRPCs under compression is studied for CFRP laminates with vascules embedded within the composites [19]. It is observed that among the several parameters like diameter of vascule, length and areas of resin pockets, disturbance parameters of the fibers and layup systems, length of the resin pocket has important influence on the integrity of the FRPC components. Finally failure occurs due to micro buckling of the fibers.

5.6 Fracture Failures of FRPCs in Different Scales

It is clear from the foregoing discussions that the fracture failure analysis of FRPCs is a complicated problem. Different approaches have been proposed to explain the behaviours of FRPCs subjected to fractures. Some of them are competent to explain certain behaviour of particular or a group of FRPCs, but insufficient for others. This is still an open field of research. To handle this complex problem of fracture failure, one such approach may be acceptable. The problem can be examined in different length scales to make it convenient for study. In this context, it is logical to discuss on the failure mechanisms those occur in different scales, i.e. micro, meso and macro scales [29].

5.6.1 Fracture Study in Micro-scale

It is evident that there are inherent flaws within FRPCs due to manufacturing defects or some other reasons. These are the hotspots for the fracture initiation and further growths. Fracture starts at molecular or atomic levels. The bonds are damaged due to force exceeding some limits to initiate crack growth. Monte-Carlo simulation was used by the investigators for prediction of failure [15, 28]. But there are limitations in capturing the complicacy as a whole. The diameter of the fiber (in microns) and their lengths are taken as input parameters which are much and much larger than atomistic scales which shows the incapability of this simulation in constituting microstructure explicitly. This is so much important for it permits to realize different failure mechanisms besides failure of individual ingredients. It is started with the flaws in micro scale around each fiber.

5.6.2 Fracture Study in Meso-scale

Meso scale is characterized by several hundred microns. Therefore, it addresses flaws extending through several fibers. Meso scale fracture study is useful for FRPCs made with textile fibers. Meso-scale fracture study can well address the inter-ply delamination as well as splitting. The important input parameter for the inter-ply delamination is the adhesion between the fiber and the matrix. The surfaces of fracture exhibit noticeable mutilated or hackle structures through branching and deflection of cracks [12] for increased bond strength consuming more energy for the same propagation length of relevant macroscopic crack.

5.6.3 Fracture Study in Macro-scale

The scale ranges from some millimetres to metres. In this study, the laminate thickness or a whole structure can be covered. This macro-scale fracture is defined by

the types of applied loads for a large range of mechanisms are covered within micro and meso scales. Fracture type inter-fiber may not result into fracture in macroscopic scales. But it may impair the stiffness. Macro level fracture may be due to an integral effect of several microscopic and mesocopic failures. One of such failures may be damage due to impact. In the case of impact of low velocity, the damage may not be directly visible on the exposed surfaces but may cause serious damages in micro and meso scales causing delamination within the laminates leading to fracture.

5.7 FRPC Failure Theories

Many theories have been proposed to predict the failures of FRPCs over the decades to interlink the different microscopic and mesoscopic failure mechanisms leading to failures at macro-scales. Additionally, these vary for different type of loading and materials. The theories can be grouped under different categories based on their field of applications as follows:

1. Failure theories for static or quasi-static loads
2. Failure theories for damage mechanism, growth and degradation
3. Theories of failures under creep, fatigue and rupture due to stress
4. Theories for high strain rate failures.

5.7.1 Failure Theories for Static or Quasi-static Loads

Tsai-Wu-Criteria is one of the famous such failure theories [52, 59]. Hashin showed that this criterion is not consistent with all the stress states of FRPCs [14] inviting new development in the theories. Hashin adopted Mohr's criterion [34] for fracture failure of brittle materials. Hinton with the team performed a notable task to work out predictive capabilities of the failure theories [16, 17, 25]. In this series of attempts, the theories provided by Pinho et al. [41], Cuntze [8] and other two researcher groups were capable of holding best position for predicting the behaviours under 3-D state of stresses.

5.7.2 Failure Theories for Damage Mechanism, Growth and Degradation

Failure at macroscopic level through the summation of microscopic failure mechanism is experimentally challenging. In addition to it, the computational exercise in microscopic level in fact is very much intensive from computational point of view. Stress–strain relations in macro-scales, homogeneity, orthotropic symmetry with layers free from defects are considered to be acceptable for analytical analyses. In this approach, classical laminate theory (CLT) is valid. Layer-wise theory is used to predict the failures. Progress of damage within laminates with fracture mechanics

concepts using strain energy of laminates subjected to triaxial loading is studied [9]. In another notable study, the capability of different criteria to predict delamination and initiation of cracks within the matrix has been compared [26] to conclude that experimental verification will be necessary to select which theory will be best in this approach to predict the behaviour.

5.7.3 Theories of Failures Under Creep, Fatigue and Rupture Due to Stress

The investigations on prediction of failures due to creep, fatigue and ruptures caused by stresses are limited. As per definition [42] a strain rate less than 10^{-6} s^{-1} is considered as creep. In case of polymers reinforced with fibers creep generally cause unacceptable degradation but not always. Besides some studies, there are no much theories proposed for this type of failures of the FRPCs. In case of stress rupture, different theories produced similar results in prediction of life time. Some accelerated tests discussed [36] in literature needs further validation regarding stress-rupture. The investigation on viscoelastic materials in this field is extremely limited. Study of FRPCs under fatigue load is being continued for a long time. Behaviour of FRPCs under fatigue load is extremely complicated and challenging field both from experimental as well as computational point of view. Studies are still being continued in several composite research centres. Prediction of actual point of time for initiation of cracks is really challenging. Statistical approach is essential for large number of scattered data. Nevertheless, the study and prediction of fatigue lives are essential for important structural designs. Different criteria have been proposed with their competencies and limitations.

5.7.4 Theories for High Strain Rate Failures

Currently, use of FRPCs in crash-worthy structures has been increased. This ensures the importance of studies under high strain rates. Unlike the other failures discussed in foregoing sections, the failure is sudden. A The rate of strain beyond 10^2 per second is considered as high strain rate. A strain rate of 10^6 per second can also be realized from special cases. The failure is of different nature for there is no scope of stress redistribution or relaxation etc. Instead of failure theories, several investigations have been carried out in this field with continuous refinements and developments along with the use of digital image correlation (DIC) techniques [31]. The location and the impact energy are being monitored by using sensors.

6 Experimental Investigations on FRPCs

Experimental mechanics, especially experimental fracture mechanics are frequently used to measure the parameters and to realize the behaviours of FRPCs for the different limitations of the mathematical prediction theories and criteria. Experimental investigation itself may suffer from errors due to error in experimental setup and different other factors. Experimental setup for advanced fiber reinforced composites is generally expensive but experimental approach is the only way where reliable input data are not available for numerical simulations or analytical studies. Recently, both the industrial and political sectors of some countries have realized the importance of research on FRPCs. Experimental investigations play a great role towards fulfilment of this demand goals of research in this field.

The topics discussed so far are on the materials and their characters with emphasis on their fracture failures. As mentioned, different materials are used for both fibers and the matrices. The fracture failures of FRPCs with different fibers and matrices along with environmental effects on these materials will be discussed in following chapters.

7 Conclusions and Future Prospective

The chapter started with the definition of composite and fiber reinforced composite materials (FRPCs) followed by historical background of the development of FRPCs. In subsequent sections, different constituents of FRPCs including readymade constituents with their ingredients and productions along with their different classes are addressed from material science point of views. Different classes of FRPCs with their typical characteristics have been discussed. Finally, different types of fractures and failure mechanisms have been presented from mechanics or fracture mechanics approach indicating the existing research gaps in the studies. Advanced learners are requested to go through the references of this and the following chapters.

References

1. American Composites Manufacturers Association: Composites Industry Overview (2019). https://acmanet.org/composites-industry-overview/. Accessed 2 July 2019
2. Bilisik, K., Kaya, G., Ozdemir, H., Korkmaz, M., Erdogan, G.: Applications of glass fibers in 3D preform composites. Adv. Glass Sci. Technol. **207** (2018)
3. Bingham, P.A., Wallenberger, F.T.: Fiberglass and Glass Technology: Energy-Friendly Compositions and Applications. Springer, Berlin (2010)
4. Borrell, B.: The big test for bisphenol A: after years of wrangling over the chemical's toxicity, researchers are charting a new way forwards. Brendan Borrell investigates how the debate has reshaped environmental-health studies. Nature **464**(7292), 1122–1125 (2010)

5. Campbell Jr, F.C. (ed.): Manufacturing Processes for Advanced Composites. Elsevier, Amsterdam (2003)
6. Chawla, K.: Fibrous Materials. Cambridge University Press, Cambridge (2016)
7. Corton, H.T.: Micromechanics and fracture behavior of composites. Mod. Compos. Mater. 27–105 (1967)
8. Cuntze, R.G.: Comparison between experimental and theoretical results using Cuntze's "failure mode concept" model for composites under triaxial loadings—part B of the second world-wide failure exercise. J. Compos. Mater. **47**(6–7), 893–924 (2013)
9. Doudican, B.M., Zand, B., Amaya, P., Butalia, T.S., Wolfe, W.E., Schoeppner, G.A.: Strain energy based failure criterion: comparison of numerical predictions and experimental observations for symmetric composite laminates subjected to triaxial loading. J. Compos. Mater. **47**(6–7), 847–866 (2013)
10. Epoxy Resin Committee: Epoxy Resins-Assessment of Potential BPA Emissions-Summary Paper (2015)
11. Frank, E., Hermanutz, F., Buchmeiser, M.R.: Carbon fibers: precursors, manufacturing, and properties. Macromol. Mater. Eng. **297**(6), 493–501 (2012)
12. Greenhalgh, E.: Failure Analysis and Fractography of Polymer Composites. Elsevier, Amsterdam (2009)
13. Hartman, D.R., Greenwood, M.E., Miller, D.M.: High strength glass fibers. In: Moving Forward With 50 Years of Leadership in Advanced Materials, vol. 39, pp. 521–533 (1994)
14. Hashin, Z.: Failure criteria for unidirectional fiber composites (1980)
15. He, F., Tan, C.M., Zhang, S., Cheng, S.: Monte Carlo simulation of fatigue crack initiation at elevated temperature. In: 13th Conference on Fracture, pp. 1–10 (2013)
16. Hinton, M.J., Kaddour, A.S.: The background to part b of the second world-wide failure exercise: evaluation of theories for predicting failure in polymer composite laminates under three-dimensional states of stress. J. Compos. Mater. **47**(6–7), 643–652 (2013)
17. Hinton, M.J., Kaddour, A.S.: Triaxial test results for fiber-reinforced composites: the second world-wide failure exercise benchmark data. J. Compos. Mater. **47**(6–7), 653–678 (2013)
18. Hoa, S.V.: Principles of the Manufacturing of Composite Materials. DES tech Publications, Inc., USA (2009)
19. Huang, C.Y., Trask, R.S., Bond, I.P.: Characterization and analysis of carbon fiber-reinforced polymer composite laminates with embedded circular vasculature. J. R. Soc. Interface **7**(49), 1229–1241 (2010)
20. Hyer, M.W., White, S.R.: Stress Analysis of Fiber-Reinforced Composite Materials. DEStech Publications, Inc., USA (2009)
21. Jahn, C.E., Mckay, J.K., Mauleon, R., Stephens, J., McNally, K.L., Bush, D.R., et al.: Genetic variation in biomass traits among 20 diverse rice varieties. Plant Physiol. **155**(1), 157–168 (2011)
22. Javadian, A., Smith, I.F., Saeidi, N., Hebel, D.E.: Mechanical properties of bamboo through measurement of culm physical properties for composite fabrication of structural concrete reinforcement. Front. Mater. **6**, 15 (2019)
23. Jones, R.M.: Mechanics of Composite Materials. CRC Press, Boca Raton (2018)
24. Jung, I., Kim, S.Y., Oh, T.H.: Effects of spinning conditions on shape changes of trilobal-shaped fibers. Text. Res. J. **80**(1), 12–18 (2010)
25. Kaddour, A.S., Hinton, M.: Maturity of 3D failure criteria for fiber-reinforced composites: comparison between theories and experiments: Part B of WWFE-II. J. Compos. Mater. **47**(6–7), 925–966 (2013)
26. Kaddour, A.S., Hinton, M.J., Smith, P.A., Li, S.: A comparison between the predictive capability of matrix cracking, damage and failure criteria for fiber reinforced composite laminates: part A of the third world-wide failure exercise. J. Compos. Mater. **47**(20–21), 2749–2779 (2013)
27. Kenyon, K.M.: Excavations at Jericho, 1956. Palestine Explor. Q. **88**(2), 67–82 (1956)
28. Kermode, J.R., Albaret, T., Sherman, D., Bernstein, N., Gumbsch, P., Payne, M.C., et al.: Low-speed fracture instabilities in a brittle crystal. Nature **455**(7217), 1224–1227 (2008)

29. Kimura, M., Watanabe, T., Takeichi, Y., Niwa, Y.: Nanoscopic origin of cracks in carbon fiber-reinforced plastic composites. Sci. Rep. **9**(1), 1–9 (2019)
30. Kling, S., Czigány, T.: Damage detection and self-repair in hollow glass fiber fabric-reinforced epoxy composites via fiber filling. Compos. Sci. Technol. **99**, 82–88 (2014)
31. Koerber, H., Xavier, J., Camanho, P.P.: High strain rate characterisation of unidirectional carbon-epoxy IM7-8552 in transverse compression and in-plane shear using digital image correlation. Mech. Mater. **42**(11), 1004–1019 (2010)
32. Mallick, P.K.: Fiber-Reinforced Composites: Materials, Manufacturing, and Design. CRC Press, Boca Raton (2007)
33. Massingill Jr, J.L., Bauer, R.S.: Epoxy resins. In: Applied Polymer Science: 21st Century, pp. 393–424. Pergamon, UK (2000)
34. Mohr, O.: Welche Umstände bedingen die Elastizitätsgrenze und den Bruch eines Materials. Z. Ver. Dtsch. Ing. **46**(1524–1530), 1572–1577 (1900)
35. Mukhopadhyay, M.: Mechanics of Composite Materials and Structures. Universities Press (2005)
36. Nakada, M., Okuya, T., Miyano, Y.: Statistical prediction of tensile creep failure time for unidirectional CFRP. Adv. Compos. Mater. **23**(5–6), 451–460 (2014)
37. Ohtomo, Y., Kakegawa, T., Ishida, A., Nagase, T., Rosing, M.T.: Evidence for biogenic graphite in early Archaean Isua metasedimentary rocks. Nat. Geosci. **7**(1), 25–28 (2014)
38. Park, S.J.: Carbon Fibers. Springer, Berlin (2015)
39. Park, S.J.: Precursors and manufacturing of carbon fibers. In: Carbon Fibers, pp. 31–67. Springer, Singapore (2018)
40. Pham, H.Q., Marks, M.J.: Epoxy resins. Ullmann's Encyclopedia of Industrial Chemistry (2000)
41. Pinho, S.T., Vyas, G.M., Robinson, P.: Material and structural response of polymer-matrix fiber-reinforced composites: part B. J. Compos. Mater. **47**(6–7), 679–696 (2013)
42. Ramesh, K.T.: High strain rate and impact testing. In: Springer Handbook of Experimental Solid Mechanics, pp. 929–960. Springer, New York (2008)
43. Rao, R.V.: Introduction to multiple attribute decision-making (MADM) methods. Decision Making in the Manufacturing Environment: Using Graph Theory and Fuzzy Multiple Attribute Decision Making Methods, pp. 27–41 (2007)
44. Rosenberg, D., Love, S., Hubbard, E., Klimscha, F.: 7,200 years old constructions and mudbrick technology: the evidence from Tel Tsaf, Jordan Valley, Israel. PLoS ONE **15**(1), e0227288 (2020)
45. Rosing, M.T.: 13C-depleted carbon microparticles in >3700-Ma sea-floor sedimentary rocks from West Greenland. Science **283**(5402), 674–676 (1999)
46. Sause, M.G.: In Situ Monitoring of Fiber-Reinforced Composites: Theory, Basic Concepts, Methods, and Applications, vol. 242. Springer, Berlin (2016)
47. Schopf, J.W.: Disparate rates, differing fates: tempo and mode of evolution changed from the Precambrian to the Phanerozoic. Proc. Natl. Acad. Sci. **91**(15), 6735–6742 (1994)
48. Sekhar, K.M.: Manufacturing of Composite Material using Ceramic Fiber, Epoxy Resin and Microsilica for Aircraft Applications. Int. J. of Engg. Res. Techol. **6**(4), 1140–1144 (2017)
49. Seydibeyoglu, M.O., Mohanty, A.K., Misra, M. (eds.): Fiber Technology for Fiber-Reinforced Composites. Woodhead Publishing, UK (2017)
50. Sih, G.C., Chen, E.P.: Fracture analysis of unidirectional composites. J. Compos. Mater. **7**(2), 230–244 (1973)
51. Tellier, L.N.: Urban World History: An Economic and Geographical Perspective. Springer Nature, Berlin (2019)
52. Tsai, S.W., Wu, E.M.: A general theory of strength for anisotropic materials. J. Compos. Mater. **5**(1), 58–80 (1971)
53. Utility, F.C.: High strength glass fibers. Moving Forward With 50 Years of Leadership in Advanced Materials **39**, 521–533 (1994)
54. Volovikov, A.Y., Ali, A., Salit, S., Briscoe, B.J.: Fiber takes the prize. Phys. Bull. **38**(10), 371(1987)

55. Waddoups, M.E., Eisenmann, J.R., Kaminski, B.E.: Macroscopic fracture mechanics of advanced composite materials. J. Compos. Mater. **5**(4), 446–454 (1971)
56. Wallenberger, F.T., Watson, J.C., Li, H.: Glass fibers. In: ASM Handbook, vol. 21(06781G), pp. 27–34 (2001)
57. Wang, R.M., Zheng, S.R., Zheng, Y.G.: Polymer Matrix Composites and Technology. Elsevier, Amsterdam (2011)
58. Wu, E.M.: Application of fracture mechanics to anisotropic plates (1967)
59. Wu, E.M.: Phenomenological anisotropic failure criterion. Mech. Compos. Mater. **2**, 353–354 (1974)

Effect of Fiber Loading Rate on Various Properties of the Fiber Reinforced Polymer Composites

Raja Soma Sundaram Pillai, Rajesh Rajamoni, Indran Suyambulingam, and Divya Divakaran

Abstract Today's industrial scenarios had imposed many academicians and researchers to develop an eco-friendly, sustainable and cost-effective polymer composite material instead of synthetic fibers. The implementation of natural fiber reinforced polymer composites provided a most significant contribution in the development of more biodegradable polymer-based composites. The mechanical characteristics of natural fiber-reinforced composite depends not only on the properties of the fiber, but also on the concentration of fibers loaded on the matrix phase. The loading rate of reinforcement are usually influenced by the features of fiber and matrix employed for the composite preparation. Determination of appropriate fiber loading rate is an important parameter necessary for significant strengthening and improvement of interfacial bond between fiber and matrix of the composite material. This chapter discusses the consequence of the percentage of different fiber content on the mechanical and water absorption behavior of the polymer composites.

Keywords Natural fiber · Polymer composites · Fiber loading · Mechanical properties · Water absorption

R. S. S. Pillai · R. Rajamoni · I. Suyambulingam (✉)
Department of Mechanical Engineering, Rohini College of Engineering and Technology, Palkulam, Kanyakumari, Tamil Nadu 629401, India
e-mail: indransdesign@gmail.com

R. S. S. Pillai
e-mail: rajasomantech@gmail.com

R. Rajamoni
e-mail: rajesh1576@yahoo.co.in

D. Divakaran
Research and Development Department, Pinnacle Bio-sciences, Kanyakumari, Tamil Nadu 629701, India
e-mail: divyad3121@gmail.com

S. Mavinkere Rangappa et al. (eds.), *Fracture Failure Analysis of Fiber Reinforced Polymer Matrix Composites*, Engineering Materials,
https://doi.org/10.1007/978-981-16-0642-7_2

1 Introduction

Many manufacturing sectors like aerospace, biomedical, electrical, structural, packing and automotive area are started to manufacture their products using natural fiber reinforced polymer composites due to their lower production cost, light-weight nature, environmental policy and increasing energy crisis [1]. On the other hand, polymers reinforced with natural fiber has some limitations which have notable shortfalls in their properties in contrast to artificial materials. Generally, the chemical contents such as lignin, hemicelluloses and waxy substances present in the fiber will permit absorption of moisture from the surroundings, which creates a weak bonding between the fiber and polymer [2]. Furthermore, fiber-matrix bonding also influences by the chemical nature of both matrix and the fiber. This problem can be reduced by selecting a suitable matrix, proper chemical treatments and manufacturing process.

Apart from these factors, fiber loading is considered to be one of the most persuading parameters which determine composites mechanical properties and moisture absorption rate. When a load is subjected to a fiber-reinforced composite, fibers acts as a load carrier and as a result uniform distribution occurs by the transfer of stress from the matrix along with the fibers. Such uniform stress distribution of fiber and matrix mainly depends upon the fiber loading percentage. Lower fiber loading causes failure of the matrix since it does not have enough fiber to carry the load, where stress gets accumulated at a certain point [3]. This phenomina causes cracks generation that further leads to fiber-matrix de-bonding. Similarly, if the fiber loading rate was higher than that of critical level, it also affects the interfacial bonding and reduces mechanical strength of the composites.

During composite fabrication, the flow of resin around the space of the fiber is complicated due to the limited time and passage. Moreover, the dispersion of the fibers within the polymer matrix is difficult which needs more care since where fiber to fiber interaction becomes maximum. Hence intermediate level of fiber loading rate is recommended to assure efficient stress transfer from the matrix to the fiber [4]. The amount of fiber loading percentage depends on the criteria such as resin, fiber orientation and architecture of the fiber. Some of the research carried out on natural fibers to examine the effect of fiber content on the mechanical properties of composites are illustrated in Table 1 and a critical review on this aspect is presented below in detail.

2 Effect of Fiber Loading on Tensile Properties of the Composites

The tensile strength of the material is largely influenced by the reinforcement parameters such as fiber length and fiber content. The appropriate volume content of the fibers reinforced into matrix combination provides absolute tensile strength to the respective composite. For instance, a maximum tensile strength of 90.20 MPa and

Table 1 Mechanical properties of the various natural fiber reinforced in polymer composites and its optimum fiber loading

S. No.	Fiber	Matrix	Method	Optimum fiber		Tensile strength MPa	Tensile modulus GPa	Flexural strength MPa	Flexural modulus GPa	Impact strength kJ/m^2	Hardness	References
				Length in mm	Loading in %							
1.	Cissus Quadrangularis Stem Fiber	Polyester	Hand layup	40	30	90.200	1.400	103.040	2.250	107	92	[1]
2.	Tamarind Fruit Fiber	Polyester	Compression Molding	50–100	40	77.4	1.4	88.5	1.5	73	90	[5]
3.	Areca Fruit Husk Fiber	Polyester	Compression molding	–	40	68.20	1.32	73.91	1.62	68.26	76	[6]
4.	Treated Tamarind Fibers	Polyester	Hand layup	10–15	25	30.6	3.085	41.1	3.865	–	–	[7]
5.	Coconut Coir Fiber	Polyester	Hand layup	–	30	12.4	0.9	22.1	2.1	80	–	[8]
6.	Treated Sisal Fiber	Polyester	Compression molding	30	30	105	–	6380	–	–	–	[9]
7.	Treated Bent Grass Fiber	Polyester	Hand layup	7	40	23.46		128.6		70.86	–	[10]
8.	Sugarcane Leaf Sheath Fibers	Polyester	Hand layup		30	9.25	0.83	14.24	1.01	21	–	[8]
9.	Shorea Robusta Fiber	Polyester	Hand layup	0.005–0.01	20	14.02	0.960	26.16	1.81	2.6	–	[11]
10.	Sansevieriacylindrica Fiber	Polyester	Compression molding	30	40	75.75	1.102	84	3	95	–	[4]
11.	Snake Grass Fiber	Polyester	Hand layup	30	25	35.89 MPa	0.481	75.29	15.99			[12]
12.	Sisal Fiber	Epoxy	Hand layup	10	30	40.25	0.187	104.78	11.896	13.66	–	[13]
13.	Treated Luffa Fiber	Epoxy	Compression molding	30	6	18.3	0.0101	220		3.4		[14]

(continued)

Table 1 (continued)

S. No.	Fiber	Matrix	Method	Optimum fiber		Tensile strength MPa	Tensile modulus GPa	Flexural strength MPa	Flexural modulus GPa	Impact strength kJ/m^2	Hardness	References
				Length in mm	Loading in %							
14.	Kenaf Fiber	Epoxy	Hand layup		40	105		165		3.85	78	[15]
15.	Harakeke Fiber	Epoxy	Compression molding	220	55	223	16.8	190	9.5			[16]
16.	Banana Fiber	Epoxy	Hand layup	15	16	16.39	0.652	57.53	8.92	2.25		[17]
17.	Dichrostachyscinerea Bark Fiber	Epoxy	Hand layup		30	46.69	0.484	68.89	4.456	7.57		[18]
18.	Treated Kenaf Fiber	Epoxy	Hand layup		40	118		178		4.23	78	[15]
19.	Jute Fiber	Epoxy	Hand layup	30	20	75.15	0.638	124.01	2.61	3.2		[19]
20.	Coconut Coir Fiber	Epoxy	Hand layup	30	30	13.05	2.064	35.42	–	17.5	16.9	[20]
21.	Pineapple/Flax	Epoxy	Compression molding	10	17.5 (Both)	23.04		49.3		64.3	19.8	[21]
22.	Prosopis Juliflora (PJ)/Rice husk (RH)	Epoxy	Press molding	PJ 13-15 RH-0.5-2	PJ-50 RH- 20	106.2		56.34			51.08	[22]
23.	Treated Betel Nut Fibers	Epoxy	Compression molding	5	5	15.6 ± 0.045					55	[23]
24.	Castor Oil Cortex Fiber	Epoxy	Hand layup		40					6.9951		[24]
25.	Coconut Shell Particles	Epoxy	Hand layup	0.1	20	37.31	0.688			7	9.5	[25]

(continued)

Table 1 (continued)

S. No.	Fiber	Matrix	Method	Optimum fiber		Tensile strength MPa	Tensile modulus GPa	Flexural strength MPa	Flexural modulus GPa	Impact strength kJ/m^2	Hardness	References
				Length in mm	Loading in %							
26.	Treated Hazelnut Shell waste	Epoxy	Hand layup	0.106	20	63 ± 4.6	4.68 ± 0.40				87 ± 6.3	[26]
27.	Date Palm Seeds (Phoenix *dactylifera L.)*	Vinyl Ester	Compression molding			40.3	1.03	149	–	17.03	51	[27]
28.	Treated Jute Fiber	Vinyl Ester	Hand layup		35	14.690		238.90		21.92		[28]
29.	Pine Needles Fiber	Resorcinol-Formaldehyde (RF)	Compression molding	3	30	15.11	0.435	89.24	5.591			[29]
30.	Bamboo Fiber	High Density Polyethylene (HDPE)	Injection molding	0.006	30	25.47	2.674	27.86	2.911	57.36		[28]
31.	Treated Bamboo Fiber	High Density Polyethylene (HDPE)	Injection molding	0.006	30	25.47	0.758	26.78	1.666	69.62		[28]
32.	Musa Paradisiac Banana Fiber	Polypropylene (PP)	Compression molding	70	20	47	2.642	73.24	–	26.56	75	[30]
33.	Eucaliptus Bleached Fiber	Polyoxymethylene	Injection molding		30	49.69	5.75					[31]

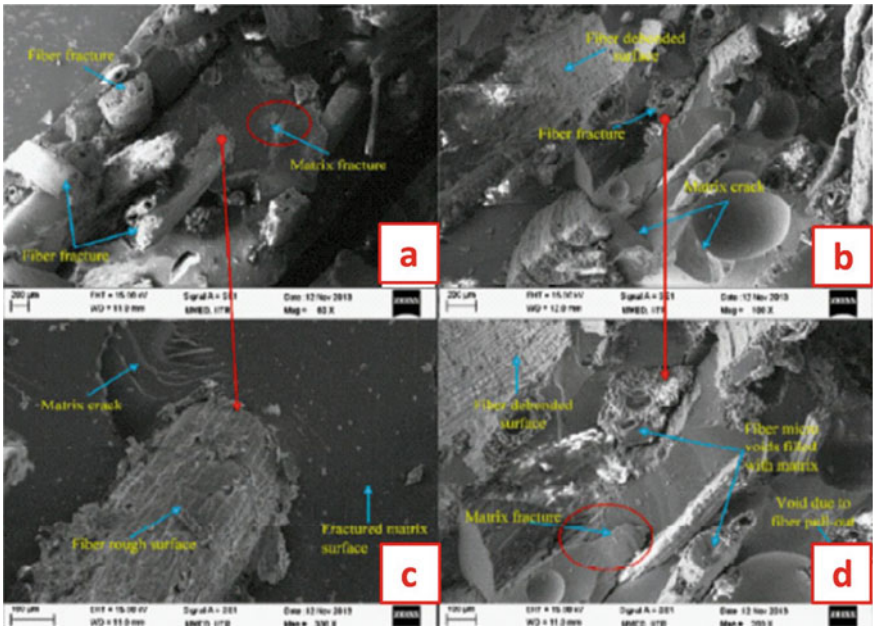

Fig. 1 SEM images of composite reinforced with 40 mm fiber length with different fiber contents (**a**, **b** 30 weight percentage and **c**, **d** 40 weight percentage) [1]

Young's modulus of 1.40 GPa was observed for the *Cissus quadrangularis* (CQ) stem fiber reinforced polyester composite that loaded with 30 wt% fiber content and 40 mm fiber length [1]. The scanning electron microscopic images of the fractured specimens of CQSF shown that the bonding of CQ fiber with the matrix was not good beyond 30 wt% due to the improper filling of the matrix in the fiber voids and higher fiber to fiber interface was noted (Fig. 1). Hence the study revealed that inappropriate fiber content decreases the total strength of the composite.

Hence it is concluded from the study that fiber concentration is an important factor that affects composite quality in greater extent. Likewise, Tamarind fruit fiber was employed as reinforcements in polyester composites showed good specific properties [5]. It was also found from the study that 40% fiber addition enhanced the tensile properties (77.44 MPa) of the fiber, which was 2.08 times higher than that of pure cured resin. Whilst beyond that specific point, the composite strength gets distracted. The Areca fruit husk fiber (AFHF) reinforced in polyester composite was investigated to determine the optimum filler content [6]. Tensile and modulus strength was found to be a peak at 40 wt% of the fiber reinforced composite with a value of 68.2 MPa for tensile and 1.124–3.155 GPa for modulus.

The mechanical behavior of chemically treated tamarind fruit fiber reinforced in polyester composite was studied in another study [7]. The three chemical treatments such as silane, alkali, alkali with silane were applied to accomplish surface modification of natural fiber to improve its various characteristics. Results concluded that

higher tensile strength was attained at 25% reinforcement of fiber by its weight in all the treatment. Alkali with silane treated fiber reinforced composite containing 25 wt% of fiber content exhibited higher tensile modulus and strength as 308.5 MPa and 30.6 GPa. However, the chemically treated fiber reinforced composites provided better strength than raw fiber reinforced composites. Since chemical treatments increases the roughness of the fiber surface that ensure better interlock between fiber and matrix during reinforcement and this implied as raise in tensile properties.

The various weight percentage of coconut coir fiber and sugarcane leaf sheath (SLS) fiber were reinforced as a hybrid fiber with polyester matrix [8]. In the 30 wt% of hybrid fiber used, 15 wt% consists of SLS and 15 wt% consists of coir fiber. Such 30 wt% reinforced polyester matrix exhibits a better tensile strength of 16.88 MPa and tensile modulus of 1.20 GPa when compared to other weight percentage reinforcement. Bent Grass fiber-reinforced with polyester matrix was investigated to determine its tensile behavior [10]. The weight percentage of reinforcement used varied from 20 to 40% with varying fiber length of 3 mm, 5 mm and 7 mm. The tensile strength of the composite was higher (23.46 MPa) with 40 wt% volume and 7 mm fiber length, as shown in Fig. 2.

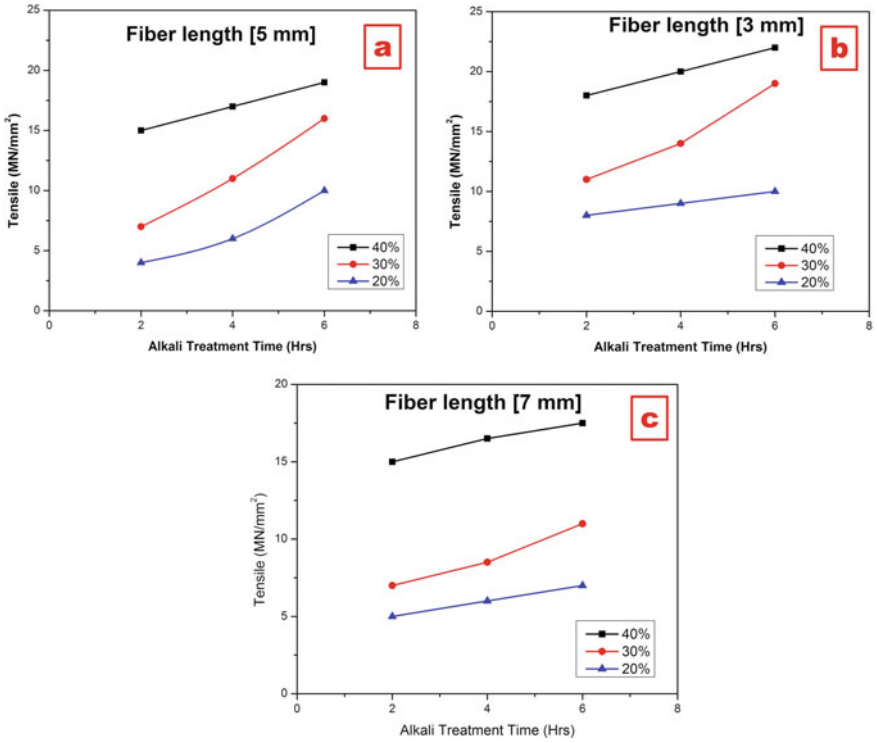

Fig. 2 Effect of varying fiber length and content (**a** fiber length 5 mm, **b** fiber length 3 mm, **c** fiber length 7 mm) on the tensile strength of Bent Grass fiber reinforced polymer composites [10]

Another study used fine sized Shorearobusta as a filler for reinforcement in unsaturated isophthalic polyester resin [11]. The corresponding tensile properties were determined for 5, 10, 15, 20 and 25 volume percentage of filler reinforced in the polymer composite. A maximum tensile strength value of 960.62 MPa was observed through filler addition at 20% volume while further addition resulted deterioration of the properties. An experimental investigation performed using *Sansevieria cylindrical* fiber reinforced composites with varying fiber lengths of 10–50 mm and weight percentage of 10–50 wt% [4]. The composite was manufactured with the fibre weight percentage of 10%, 20%, 30%, 40%, and 50%, and different fiber length of 10 mm, 20 mm, 30 mm, 40 mm and 50 mm. A critical fiber length of 30 mm determined was used to test the effect of fiber weight percentage on composite performance. *Sansevieria cylindrical* fibre exhibits an increase in tensile strength and Young's modulus up to 40% fiber content while decreased to 50 wt%. The addition of fiber weight percent had increased elongation value due to the reduction in the brittleness property of polyester resin. Furthermore, the tensile property of snake grass fiber reinforced polyester composite with varying fiber length and weight percentage was investigated [12]. A critical fiber length of 30 mm with 25% volume fraction of fiber content resulted higher tensile strength (35.89 MPa) than other combinations.

The tensile property of the Luffa fiber was also investigated by varying weight percentage of fiber- epoxy composites [14]. The optimum fiber reinforcement was identified as 60 wt%, which exhibits a tensile strength of 18.3 MPa. While beyond that fiber content, lower tensile strength was observed. The enhancement in composite strength was due to the H-bond formation between oxy-group of epoxy composite and OH group of cellulose present in the fiber. The addition of harakeke fiber enhanced tensile strength and Young's modulus of composites manyfold and which was 4.3 fold higher than that of neat epoxy composite that possess 55 wt% fiber content [16]. An average tensile value of 223 MPa and 16.8 GPa was determined at a fiber content of 55 wt%. Beyond 55 wt%, decrease in tensile strength was obtained whereas a moderate increase in Young's modulus was observed. Hence it is established that the harakeke fiber bonding parameter is not related to Young's modulus of the fiber.

Changes in the tensile property for banana fiber in epoxy polymer composite was investigated was determined by varying fiber loading rate [17]. Increase in weight ratio up to 12% provided increased tensile strength and modulus of 16.39 MPa and 0.652 GPa. While further increase in weight ratio caused decreased tensile properties. The *Dichrostachys cinerea* bark fibers (DCFs) reinforced epoxy composite was studied with varying its fiber weight fractions [18]. The increasing trend in the tensile property was noted up to 30 wt% loading rate and subsequent loading rate leads a drop in tensile value. The use of Date seed as a filler material in the fabrication of vinyl ester composite was studied for finding optimum filler loading percentage [27]. The filler loading rate from 5 to 50 wt% at an interval of 5% where an optimum tensile strength of 40.3 MPa was observed at 30 wt% of fiber content.

The tensile properties of Jute fiber/vinyl ester composite was investigated by changing its fiber volume percentage from 0 to 35% [28]. The tensile test was performed on the untreated and treated fiber reinforced composites to find out the

effects of varied fiber loading rate. The treated fibers were classified based on the treatment hours, and the results are shown in the Table 2. Which confirmed that composites made with 35% fiber volume treated for 4 h showed maximum improvements in the tensile property.

A green polymer composite was manufactured using pine needles fiber with different fiber content of 10%, 20%, 30% and 40%, and a Resorcinol-Formaldehyde (RF) matrix by compression molding technique [29]. The 30 wt% fiber loading exhibits maximum tensile strength followed by 40 wt%, 20 wt%, and 10 wt% showed considerable tensile strength. Conversely, bamboo fiber reinforced composites prepared with HDPE matrix using 10% to 30% fiber content by injection molding technique [28]. The bamboo fiber based composites at 30% fiber content provided

Table 2 Tensile properties of raw and treated jute/vinyl ester composites [28]

Jute fiber content	Fiber type	Modulus (GPa)	
		Mean value	Standard Deviation
8	Untreated	4.220	0.33
	2 h treated	3.446	0.53
	4 h treated	4.205	0.71
	6 h treated	3.967	0.66
	8 h treated	3.130	0.43
15	Untreated	5.544	0.55
	2 h treated	6.024	0.04
	4 h treated	6.539	0.42
	6 h treated	5.546	0.21
	8 h treated	5.337	0.26
23	Untreated	7.355	0.51
	2 h treated	8.065	0.79
	4 h treated	9.384	0.44
	6 h treated	8.542	0.41
	8 h treated	7.132	0.45
30	Untreated	10.030	0.62
	2 h treated	10.990	0.27
	4 h treated	12.850	0.27
	6 h treated	12.490	0.94
	8 h treated	11.170	0.42
35	Untreated	11.890	0.62
	2 h treated	12.700	0.37
	4 h treated	14.690	0.85
	6 h treated	14.890	1.17
	8 h treated	12.320	0.35

maximum tensile strength and modulus of 25.27 MPa and 2674.67 GPa, whereas a decline in the tensile properties was achieved in the remaining fiber contents used. *Eucaliptus* bleached fiber reinforced polyoxy methylene composites formulated with 20% to 40% fiber contents were investigated to determine its altered tensile strength [31]. It seems that 40% EBF reinforced composites exhibited high tensile value compared to other fiber contents tested.

3 Effect of Flexural Properties on Varying Fiber Loading

The flexural property is considered as an essential constraint to define the structural applications of plant fibers. Varied fiber contents in the composite showed noticeable effect on its flexural property. A maximum flexural strength of 103.04 MPa and flexural modulus of 2.25 GPa was obtained for *Cissus quadrangularis* stem fiber reinforced polymer composite with 40 mm fiber length and 30 wt% fiber content [1]. The flexural property analysis of tamarind fruit fiber reinforced polyester composite showed that the composite possesses a maximum flexural strength of 88.53 MPa at 40% reinforcement rate [5].

Flexural strength and modulus of randomly oriented Areca fruit husk fiber reinforced polyester matrix exhibited maximum flexural strength value of 73.9 MPa at 40 wt% of the fiber [6]. On the other hand, such composite possess 70% higher value than the flexural property reported for cured resin. The flexural behavior of treated tamarind fruit fiber reinforced polyester composite was investigated using three-point bending mode in a UTM machine, in another study [7]. Where, a fiber loading rate up to 25% enhanced the flexural strength and modulus, while above that point the properties reported in decreased range. The highest flexural modulus and strength of 3865 GPa and 41.1 MPa were identified for the fiber treated with alkali with silane. This increment was achieved due to the removal of the impurities and hemicellulose present on the surface of the fiber.

Fine sized Shorearobusta with 5%, 10%, 15%, 20% and 25% concentrations were used as filler reinforcement in unsaturated isophthalic polyester resin to study its flexural properties, as reported in another study [11]. Maximum flexural strength of 26.16 MPa and modulus of 1810 GPa were observed for filler addition up to 20% of fiber volume. Further addition of increased filler volume resulted deterioration of the flexural properties. It is also observed that this decrease in the properties was due to the weak interface and filler agglomeration as observed through the SEM image. Flexural strength and modulus of Sansevieria cylindrical fibre reinforced composite was investigated in later through another attempt [4]. The increase in flexural strength and modulus up to 40% fiber weight percentage but a decrease in the property as noted with factors of increasing fiber loading over 40%. A maximum flexural strength and modulus of 84 MPa and 3 GPa were accomplished in the study with 30 mm fiber length and 40% fiber weight. The effect of different fiber weight percentage on the flexural property of snake grass fiber reinforced polyester composite was established [12]. Results showed that there were a gradual increase in the flexural property of the

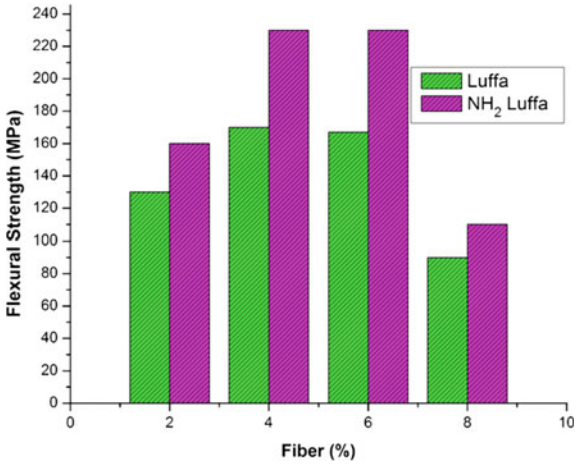

Fig. 3 Flexural strength versus fiber volume for treated and non-treated Luffa fiber [14]

composite with 20% weight percentage. This increasing trend continued up to 25% fiber content, where a maximum flexural strength and modulus of 75.29 MPa and 15.99 GPa were obtained. Beyond 25% weight percentage, the flexural strength gets drastically reduced. Conversely, Luffa fiber in epoxy composites showed increase in flexural strength up to 6% volume, while a decrease has found beyond that level. [14]. The Non-Treated Luffa fiber and amine treated Luffa fiber exhibited specific flexural strength of 33 and 43%, which was higher than that of plain epoxy resin, as shown in Fig. 3.

The addition of harakeke fiber up to 49 wt% had increased flexural strength and flexural modulus of epoxy composites [16]. However, no improvements in the flexural properties were observed on the further addition of harakeke fiber. The 49 wt% harakeke fiber reinforced epoxy composite exhibits maximum flexural strength and modulus of about 223 MPa, 13.7 GPa, respectively. Changes in flexural properties of banana fiber reinforced epoxy composite was investigated through a similar work [17]. The maximum flexural strength and modulus of banana fiber reinforced epoxy composite was determined as 57.53 MPa and 8.92 GPa with a fiber length of 15 mm and fiber weight of 16%. Beyond the 16% fiber content, a reduction in the flexural property was observed. Flexural properties of *Dichrostachys cinerea* bark fibers (DCFs) reinforced epoxy composite was analyzed by varying weight fraction of the fiber [32]. The 30 wt% of DCF in composite showed maximum flexural strength of 68.89 MPa and modulus of 4.456 GPa. Higher flexural strength was observed due to better bonding as reflected in the SEM images of the broken specimen used in the flexural test (Fig. 4).

Date seed was utilized as a reinforcement filler in the fabrication of vinyl ester based composite to identify the optimum filler loading percentage for higher flexural strength [27]. It was observed that 30 wt% date seed showed higher flexural strength

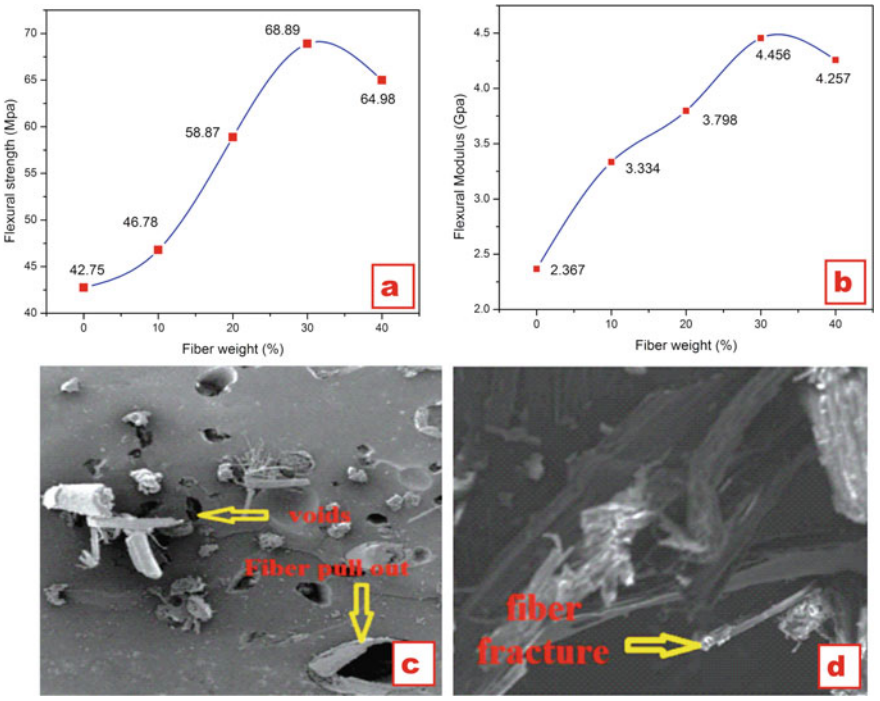

Fig. 4 Flexural strength versus Fiber volume for treated (**a**) and non-treated (**b**) *Dichrostachys cinerea* bark fibers and the broken SEM (**c**, **d**) image [32]

and modulus. Jute fibers/vinyl ester composites investigated in another study to determine the flexural property by changing fiber volume percentage from 0 to 35% [28]. The 35% fiber loading provided an improvement in the flexural property up to 20% when compared with pure resin. Moreover, green polymer composite was manufactured and investigated to study the flexural behavior of pine needle fiber [29]. The pine needle fiber with 10%, 20%, 30%, and 40% weight content in resorcinol-formaldehyde (RF) matrix was used to fabricate composite by compression molding technique. The flexural strength was maximum (297.32 MPa) at 30 wt% fiber loading, followed by 40 wt%, 20 wt% and 10 wt% showed respective flexural strength.

4 Effect of Fiber Loading on Impact Properties

Impact resistance and fracture toughness of the composite can be enhanced by assuring the approximate fiber content. Furthermore, the impact strength can be improved by the addition of right compatibilizer, which will increase the flexibility of the molecular interface chain that results better energy absorption. Hence

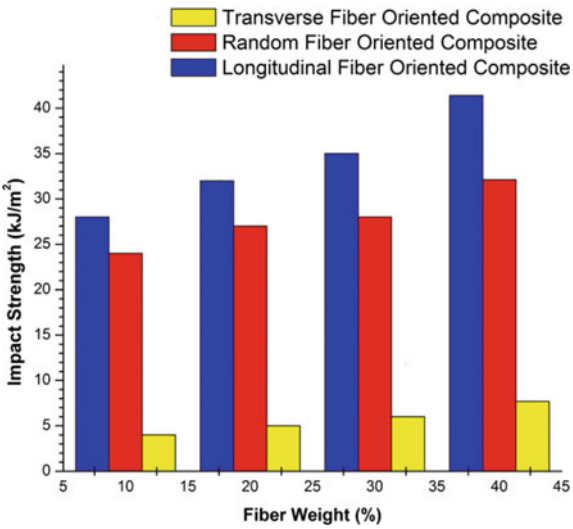

Fig. 5 Effect of impact strength on changing fiber content and orientation [33]

impact properties depend on the factors such as fiber content, fiber strength, interfacial bonding, percentage of elongation, etc. More impact energy is observed when composite possess higher fibers content [33]. Energy absorption is less for lower fiber content due to the more considerable distance between fibers. Moreover, impact strength decreased significantly if the fibers laid parallel to the impact loading direction. The *Ricinus communis* plant fiber reinforced polyester composite by varying fiber content provided utmost impact strength at 40 wt%, as shown in Fig. 5.

The effect of fiber loading on impact strength was analyzed by varying weight fraction of raw and treated *Dichrostachys cinerea* bark fibers (DCFs) that reinforced with epoxy composite [32]. The impact test was carried out with different fiber loading rate from 10 to 40 wt%. As a result, the maximum impact strength was achieved at 30% reinforcement with a value of 75.773 and 84.633 kJ/m^2 for raw and treated fiber composites, as shown in Fig. 6. There were a decrease in the fiber content was observed at 40 wt% as 68.996 kJ/m^2 and 76.553 kJ/m^2 for raw and treated composite.

The impact properties were decreased beyond 40% reinforcement in the case of tamarind fruit fiber reinforced polyester composite, due to restricted space in the filling of the resin [5]. Hence maximum impact strength of 7.3 J/cm^2 was found at 40% fiber reinforcement used. Although, Areca fruit husk fiber was reinforced in the polyester matrix by varying fiber weight percentage in the composite and found that 40 wt% of fiber content yielded better impact strength of 6.826 J/cm^2 [6]. Impact strength of polyester composite fabricated with different weight percentage reinforcement of hybrid fiber that consists of sugarcane leaf sheath and coconut coir fibers were investigated to explore absolute reinforcement concentration [8]. The 30 wt% of hybrid fiber that contains 15 wt% of sugarcane leaf sheath and 15 wt% of coir

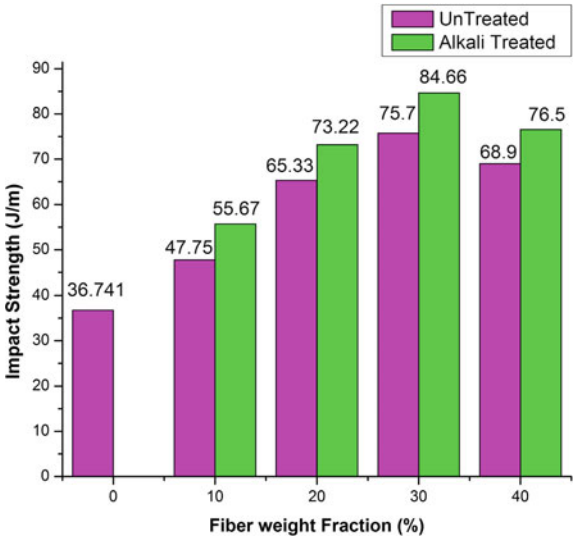

Fig. 6 Impact strength versus fiber volume of treated and non-treated *Dichrostachys cinerea* bark fibers [32]

reinforced with polyester matrix exhibits better impact strength of 0.95 J/m when compared to other weight percentage reinforcement.

Impact properties of treated Bent Grass fiber reinforced with polyester matrix was studied in a concurrent study [10]. The impact strength (70.86 J/m) of the composite was found higher at 40wt% fiber content with 7 mm fiber length. The influence of fine-sized *Shorearobusta* fiber as a filler in polyester composite was determined to establish its impact properties [11]. The results revealed that the incorporation of *Shorearobusta* filler up to 10 wt% volume were not improved the material's impact property. But an addition up to 20 wt% volume of filler increased the impact strength moderately while decreased in further addition.

Sansevieria cylindrical fibre with varying reinforcement percentage in polyester composite was studied for its impact property [4]. The composite reinforced with 30 mm length and 40% weight exhibits 23.6 times greater impact strength than pure polyester resin, which shows the potential of *Sansevieria cylindrical* fibre. A minor decrease in the impact strength by a factor of 0.12 was observed when fiber weight percentage is augmented from 40% to 50%. The presence of Luffa fiber had improved the composite's impact strength. The maximum impact strength was observed as 3.15 J/m and 3.3 J/m at 8% for un-functionalized and functionalized fiber composites, respectively. From the results, it was clear that the impact strength of the composites improved with increase in Luffa fiber content, owing to the fact that the cellulosic fibers enhance the energy absorption capacity and stiffness of the composites [14]. Change in impact strength by varying banana fiber loading in epoxy composite was also investigated [17]. Impact strength increases up to 16% fiber loading rate and the impact value is found to be 2.25 J/m. However, it was observed

that the functionalized composites always possessed superior impact strength when compared to the un-functionalized composites.

The effect of date seed as a filler material in the fabrication of vinyl ester composite was investigated through impact analysis [27]. Significantly, the proposed composite exhibited higher impact strength of 17.03 kJ/m^2 resin at 30% filler loading. This was 43.96% superior than the pure vinyl ester. Bamboo fibers at 10–30 wt% were reinforced in HDPE composites was examined to study about the Impact behavior of the composites [34]. It was noted that the impact toughness decreases with fiber content increases. This decreases in impact property was due to the fiber agglomeration at higher fiber content, which creates regions of stress concentration that make a path in lesser energy to propagate a crack. Waste pseudo stem fiber of the banana plant is reinforced in polypropylene (PP) was used to study its impact strength [35]. Results revealed that 20% weight volume of xylanase treated fiber showed 120% increase in impact value compared to pure matrix.

5 Effect of Varying Fiber Loading on Hardness Properties

The toughness of the composite is mainly depend upon the fiber content and the distribution of fibers throughout the composite [36]. The hardness behavior of Areca fruit husk fiber reinforced polyester composite was investigated, where the optimum hardness value is found at 40 wt% of the fiber [6]. A significant reduction in hardness property was observed as fiber content increases beyond 40 wt%, which might be due to the poor fiber-matrix bonding. Similarly, the optimum hardness property of 92 HRRW was resulted at 40 wt% fiber content for *Cissus quadrangularis* stem fiber reinforced polyester composite [1]. The addition of tamarind fruit fiber in polyester matrix had increased the hardness of polyester based composite from 62 HRRW to 90 HRRW with 40 wt% fiber and beyond that rate further raise in the feature was observed [5]. The hardness behavior of the date seed reinforced vinyl ester composite was studied and found that addition of filler up to 30% weight concentration had increased the hardness 1.94 times higher than that of pure resin [27].

6 Effect of Fiber Loading Rate on Water Absorption Characteristics

For the composites used in the aquatic environment, the determination of water absorption characteristics is vital. An increase in the fiber content will enhance the percentage intake of water absorbed in the composite. But this can be reduced if the fibers are treated chemically prior to composite formation. The absorption percentage for tamarind fruit fiber (40 wt%) reinforced polyester composite in fresh and seawater were investigated [5]. The rate of absorption was found to be at 6%, which suites

the usage of that material in the aquatic environment. Silane treated tamarind fruit fiber in polyester composite was studied to understand its moisture absorption rate with the concept that chemical treatment reduces composite's moisture absorption rate [7]. This work reported that the addition of silane agent had reduced the number of cellulose hydroxyl group present in the interface of the fiber and matrix. When the composite is silane treated, the hydrolysable alkoxy group leads to the formation of silanol. Afterwards, the silanol reacts with the hydroxyl group of the fiber which results in the development of covalent bonding between the fiber and the matrix. This strong bonds will acts as a barrier against fiber swelling by developing a cross-linked network along with the interface. Hence, most of the treated fibers showed decreased water absorption rate when compared to its raw fibers that resulted high moisture absorption rate.

Date seed vinyl ester composite was employed to study its water absorption capacity in four watery environmental conditions such as normal water, cold water, salt water and hot water [27]. This experiment was conducted by using different fiber content in the reinforced composites to establish better fiber-matrix combination. It is concluded from the study that an increase in the filler loading had increased water absorption percentage since raw fibers possess more hydrophilic groups in contrast to the polymer matrix. A consequence of fiber content along with the fiber length on the water absorption property of the banana/epoxy composite were investigated, and the results were shown in Fig. 7. The corresponding study driven out that when fiber content increases, the moisture uptake of the composite also gets increased. Moreover, variation in the fiber length could not resulted any effect on water absorption property of banana/epoxy composite [17].

7 Conclusion and Future Perspective

The demand of natural plant fiber reinforced polymer composites increasing day by day with the aspect of obeying current environmental policies that confines the replacement of detrimental synthetic polymer material with biodegradable, renewable, eco-friendly natural fiber based polymer materials. The reinforcement of natural fibers had resulted positive effects on the polymer composite, which enhances the overall mechanical properties of the composite in greater extent. It was established that the fiber loading rate largely influence the mechanical properties of the composites. The maximum properties of fiber reinforced polymer composites can be accomplished by assuring appropriate fiber weight percentage and matrix combination, while beyond that fiber content the total performance of the composite reduces. This chapter discussed about the effect of varied fiber content on diverse properties of the fiber reinforced polymer composites. The effect of different concentrations of reinforcements on tensile, flexural, impact, hardness and moisture absorption characteristics of various composites are clearly conferred in this chapter. In the view of water absorption, an increase in the fiber content leads a decrease in the moisture

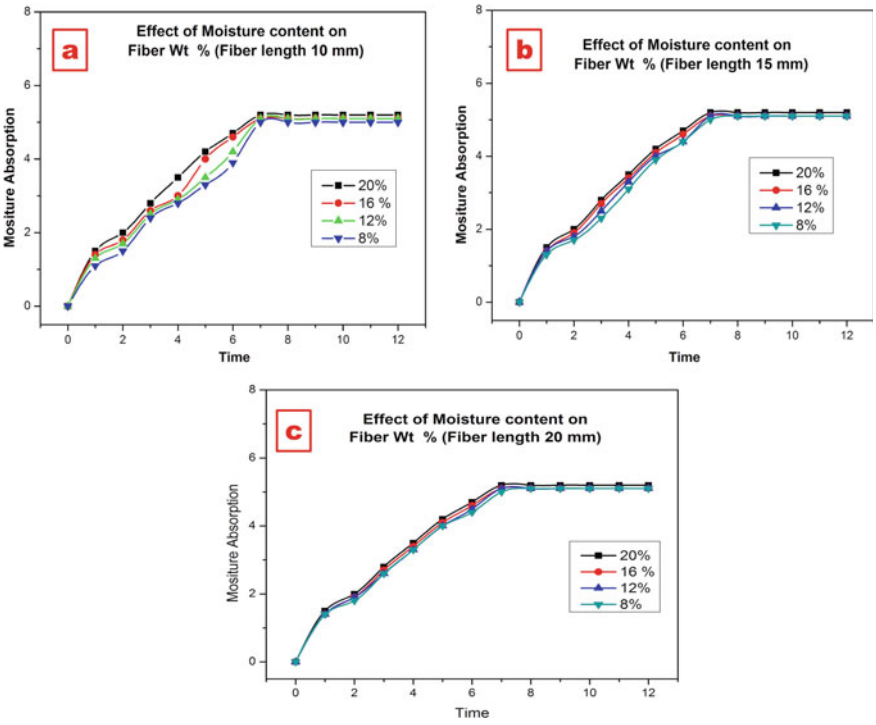

Fig. 7 Effect of fiber length and fiber content towards water absorption characteristics (**a** Fiber length 10 mm, **b** fiber length 15 mm, **c** fiber length 20 mm) [17]

absorption rate and also chemical treatment or hybridization of various fibers recommended to enhance the surface properties of the composites that obviously reduce the moisture absorption rate. Hence, it is concluded from this review that proper optimization of fiber loading parameters is necessary to attain maximum mechanical properties of the composite.

References

1. Indran, S., Dhas, R., Raj, E., Samuel, B., Daniel, S., Binoj, J.S.: Comprehensive characterization of natural *Cissus quadrangularis* stem fiber composites as an alternate for conventional FRP composites. Bionic Eng. **15**, 914–923 (2018)
2. Binoj, J.S., Raj, R.E., Indran, S.: Characterization of industrial discarded fruit wastes (*Tamarindus indica* L.) as potential alternate for man-made vitreous fiber in polymer composites. Process Saf. Environ. Prot. **116**, 527–534 (2018). https://doi.org/10.1016/j.psep.2018.02.019
3. Sathishkumar, T.P., Navaneethakrishnan, P., Shankar, S.: Characterization of new cellulose sansevieria ehrenbergii fibers for polymer composites. Compos. Interfaces **20**, 575–593 (2013). https://doi.org/10.1080/15685543.2013.816652

4. Sreenivasan, V.S., Ravindran, D., Manikandan, V., Narayanasamy, R.: Mechanical properties of randomly oriented short Sansevieria cylindrica fiber/polyester composites. Mater. Des. **32**, 2444–2455 (2011). https://doi.org/10.1016/j.matdes.2010.11.042
5. Binoj, J.S., Edwin Raj, R., Daniel, B.S.S.: Comprehensive characterization of industrially discarded fruit fiber, *Tamarindus indica* L. as a potential eco-friendly bio-reinforcement for polymer composite. J. Clean. Prod. **116**, 527–534 (2018). https://doi.org/10.1016/j.jclepro.2016.09.179
6. Binoj, J.S., Raj, R.E., Daniel, B.S.S., Saravanakumar, S.S.: Optimization of short Indian *Areca* fruit husk fiber (*Areca catechu* L.) reinforced polymer composites for maximizing the mechanical property. Polym. Anal. Charact. **21**, 112–122 (2016). https://doi.org/10.1080/1023666x.2016.1110765
7. Maheswari, C.U., Reddy, K.O., Muzenda, E., Shukla, M., Varada, A.: Mechanical properties and chemical resistance of short tamarind fiber/unsaturated polyester composites: influence of fiber modification and fiber content. Polym. Anal. Charact. **18**, 520–533 (2013). https://doi.org/10.1080/1023666x.2013.816073
8. Arul, M., Sasikumar, K.S.K., Sambathkumar, M., Gukendran, R., Saravanan, N.: Mechanical and fracture study of hybrid natural fiber reinforced composite—coir and sugarcane leaf sheath. Mater. Today Proc. 1–3 (2020). https://doi.org/10.1016/j.matpr.2020.02.677
9. Venkatram, B., Kailasanathan, C., Seenikannan, P., Paramasamy, S.: Study on the evaluation of mechanical and thermal properties of natural sisal fiber/GP composites reinforced with nano clay. Polym. Anal. Charact. **21**, 647–656 (2016). https://doi.org/10.1080/1023666x.2016.1194616
10. Balakrishna, A., Reddy, M.I., Seshank, A.S.P., Raghuveer, C., Kumar, M.A.: Characterization of process parameters on mechanical properties of short and randomly oriented Agrostis (Bentgrass) fiber reinforced composite. Mater. Today Proc. **5**, 25766–25772 (2018). https://doi.org/10.1016/j.matpr.2018.06.568
11. Vimalanathan, P., Venkateshwaran, N., Santhanam, V.: Mechanical, dynamic mechanical and thermal analysis of *Shorea robusta* dispersed polyester composite. Polym. Anal. Charact. **21**, 314–326 (2016). https://doi.org/10.1080/1023666x.2016.1155818
12. Sathishkumar, T.P., Navaneethakrishnan, P., Shankar, S.: Tensile and flexural properties of snake grass natural fiber reinforced isophthallic polyester composites. Compos. Sci. Technol. **72**, 1183–1190 (2012). https://doi.org/10.1016/j.compscitech.2012.04.001
13. Om, H., Gupta, M.K., Srivastava, R.K., Singh, H.: Study on the mechanical properties of epoxy composite using short sisal fiber. Mater. Today Proc. **2**, 1347–1355 (2015). https://doi.org/10.1016/j.matpr.2015.07.053
14. Dharmalingam, S., Meenakshisundaram, O., Boopathy, R.S.: An investigation on the interfacial adhesion between amine functionalized luffa fiber and epoxy resin and its effect on thermal and mechanical properties of their composites. J. Nat. Fibers 1–16 (2020). https://doi.org/10.1080/15440478.2020.1726238
15. Prakash, V.R.A., Viswanthan, R.: Fabrication and characterization of echinoidea spike particles and kenaf natural fibre-reinforced Azadirachta-Indica blended epoxy multi-hybrid bio composite. Compos. Part A **118**, 317–326 (2019). https://doi.org/10.1016/j.compositesa.2019.01.008
16. Minh, T., Louise, K.: Composites: Part A The potential of harakeke fiber as reinforcement in polymer matrix composites including modelling of long harakeke fiber composite strength. Compos. PART A **76**, 44–53 (2015). https://doi.org/10.1016/j.compositesa.2015.05.005
17. Venkateshwaran, N., Elayaperumal, A., Jagatheeshwaran, M.S.: Effect of fiber length and fiber content on mechanical properties of banana fiber/epoxy composite. Reinf. Plast. Compos. **30**, 1621–1627 (2011). https://doi.org/10.1177/0731684411426810
18. Baskaran, P.G., Kathiresan, M., Senthamaraikannan, P., Saravanakumar, S.S.: Characterization of new natural cellulosic fiber from the bark of *Dichrostachys cinerea*. J. Nat. Fibers **15**, 62–68 (2018). https://doi.org/10.1080/15440478.2017.1304314
19. Ramakrishnan, S., Krishnamurthy, K., Rajasekar, R., Rajeshkumar, G.: An experimental study on the effect of nano-clay addition on mechanical and water absorption behaviour of jute fiber

reinforced epoxy composites. Ind. Text. **49**, 597–620 (2019). https://doi.org/10.1177/1528083718792915
20. Biswas, S., Kindo, S., Patnaik, A.: Effect of fiber length on mechanical behavior of coir fiber reinforced epoxy composites. Fibers Polym. **12**, 73–78 (2011). https://doi.org/10.1007/s12221-011-0073-9
21. Sumesh, K.R., Kanthavel, K., Kavimani, V.: Peanut oil cake – derived cellulose fiber: Extraction, application of mechanical and thermal properties in pineapple/flax natural fiber composites sumesh. J. Int. J. Biol. Macromol. **150**, 775–785 (2020). https://doi.org/10.1016/j.ijbiomac.2020.02.118
22. Santhosh, M.S., Karthikeyan, G., Sasikumar, R., Hariharan, R., Mohanraj, R.: Mechanical and morphological behaviour of rice husk/prosopis juliflora reinforced bio composites. Mater. Today Proc. **27**, 556–560 (2019). https://doi.org/10.1016/j.matpr.2019.12.021
23. Borah, J., Dutta, N.: Development and properties evaluation of betel nut fibers composite material. Mater. Today Proc. **5**, 2229–2233 (2018). https://doi.org/10.1016/j.matpr.2017.09.223
24. Egala, R., Setti, S.G.: Impact characterization of epoxy LY556/ricinus communis L plant natural fiber composite materials. Mater. Today Proc. **5**, 26799–26803 (2018). https://doi.org/10.1016/j.matpr.2018.08.159
25. Sarki, J., Hassan, S.B., Aigbodion, V.S., Oghenevweta, J.E.: Potential of using coconut shell particle fillers in eco-composite materials. J. Alloys Compd. **509**, 2381–2385 (2011). https://doi.org/10.1016/j.jallcom.2010.11.025
26. Kocaman, S., Ahmetli, G.: Effects of various methods of chemical modification of lignocellulose hazelnut shell waste on a newly synthesized bio-based epoxy composite. J. Polym. Environ. **28**, 1190–1203 (2020). https://doi.org/10.1007/s10924-020-01675-1
27. Nagaprasad, N., Stalin, B., Vignesh, V., Ravichandran, M., Rajini, N., Ismail, S.O.: Ismail, Effect of cellulosic filler loading on mechanical and thermal properties of date palm seed/vinyl ester composites. Biol. Macromol. **147**, 53–66 (2019). https://doi.org/10.1016/j.ijbiomac.2019.11.247
28. Ray, D., Sarkar, B.K., Rana, A.K., Bose, N.R.: The mechanical properties of vinylester resin matrix composites reinforced with alkali-treated jute fibers. Compos. Part A. **32**, 119–127 (2001)
29. Thakur, V.K., Singh, S.A., Kaur, M.I.: Renewable resource-based green polymer composites: analysis and characterization. Polym. Mater. Polym. Biomater. **58**, 217–228 (2010). https://doi.org/10.1080/10236660903582233
30. Vardhini, K.V., Murugan, R., Surjit, R.: Effect of alkali and enzymatic treatments of banana fiber on properties of banana/polypropylene composites. Ind. Text. **47**, 1849–1864 (2017). https://doi.org/10.1177/1528083717714479
31. Espinach, F.X., Granda, L.A., Tarres, Q., Duran, J., Fullana-i-palmer, P., Mutjé, P.: Mechanical and micromechanical tensile strength of eucalyptus bleached fibers reinforced polyoxymethylene composites. Compos. Part B. **116**, 333–339 (2016). https://doi.org/10.1016/j.compositesb.2016.10.073
32. Baskaran, P.G., Kathiresan, M., Pandiarajan, P.: Effect of alkali-treatment on structural, thermal, tensile properties of *Dichrostachys cinerea* bark fiber and its composites. Nat. Fibers. **0478** (2020). https://doi.org/10.1080/15440478.2020.1745123
33. Nijandhan, K., Muralikannan, R., Venkatachalam, S.: Ricinus communis fiber as potential reinforcement for lightweight polymer composites. Mater. Res. Express. **5**, 1–10 (2018)
34. Mohanty, S., Nayak, S.K.: Short bamboo fiber reinforced HDPE composites: Influence of fiber content and modification on strength of the composite. Reinf. Plast. Compos.**29** (2010). https://doi.org/10.1177/0731684409345618
35. Preethi, P., B.M.G, Physical and chemical properties of banana fiber extracted from commercial agrotechnology physical and chemical properties of banana fiber extracted from commercial banana cultivars grown in Tamil Nadu State, Agrotechnology. 11. 8–11 (2013). https://doi.org/10.4172/2168-9881.s11-008
36. Nath, S., Jena, H., Deepak, P.: Analysis of mechanical properties of jute epoxy composite with Cenosphere filler, Silicon. 11. 659–671 (2019). https://doi.org/10.1007/s12633-018-9941-x

Characterisation of Mixed-Mode I-II-III Delamination in Composite Laminates

King Jye Wong, Mahzan Johar, and Haris Ahmad Israr

Abstract Owing to low interlaminar strength, delamination is a commonly observed in composite structures. Due to complex loadings in real life applications, delamination is usually occurred in mixed-mode. This chapter begins with the review of the mixed-mode I-II-III delamination characterisation methods. The shear-torsion-bending, pre-stressed beam and bending plate tests are extensively discussed, which include the test setup configuration, advantages and drawbacks of each method. The interactions between different modes on the fracture toughness distribution are also plotted and compared. Subsequently, a new method is proposed to characterise mixed-mode I-II-III delamination. This ten-point bending plate test (10PBP) test induces mode I, II and III concurrently through the bending of the specimen about different axes. This test is successfully implemented on a carbon/epoxy composite. Crack growth is observed along the mid-plane of the specimen where a Teflon is placed. Finite element modelling is required in the future work to quantify the participation of each mode and analyse the delamination behaviour.

Keywords Composite materials · Delamination · Mixed-mode · Fracture toughness · Ten-point bending plate test

K. J. Wong (✉)
Department of Applied Mechanics and Design, School of Mechanical Engineering, Faculty of Engineering, Universiti Teknologi Malaysia, Johor Bahru, Johor, Malaysia
e-mail: kjwong@mail.fkm.utm.my

M. Johar
Department of Mechanical Engineering, Faculty of Engineering and Science, Curtin University Malaysia, Miri, Sarawak, Malaysia
e-mail: mahzan.johar@curtin.edu.my

H. A. Israr
Department of Aeronautics, Automotive and Ocean Engineering, School of Mechanical Engineering, Faculty of Engineering, Universiti Teknologi Malaysia, Johor Bahru, Malaysia
e-mail: haris@mail.fkm.utm.my

S. Mavinkere Rangappa et al. (eds.), *Fracture Failure Analysis of Fiber Reinforced Polymer Matrix Composites*, Engineering Materials,
https://doi.org/10.1007/978-981-16-0642-7_3

1 Introduction

Composite materials are getting their importance to be used in aeronautics, automotive, marine and civil applications. It is mainly due to their advantages of high specific strength and stiffness due to their lower density as compared to metals. Soutis [1, 2] reported that one kilogram of weight reduction in an aircraft structure can save over 2900 litres of fuel per year. Nevertheless, laminated composites are susceptible to delamination, which is the separation of the neighbouring laminas [3–5, 6]. This is due to low interlaminar strength, which is one of the major weaknesses of laminated composites. Delamination would deteriorate the overall performance of the composite structures and lead to premature failure. Therefore, it is of paramount importance to understand the delamination characteristics of composite laminates for a better design of the structures.

In real life applications, the loadings on the structures are generally complex. Hence, delamination is usually occurred under mixed-mode loadings. In view of this, it is essential to characterise the delamination behaviour that involves mixed-mode I-II-III. Currently, only mode I, II and mixed-mode I-II testing methods have been standardised through ASTM D5528 ("ASTM D5528. Standard test method for mode I interlaminar fracture toughness of unidirectional fiber-reinforced polymer matrix composites" [7], ASTM D7905 ("ASTM D7905. Standard test method for determination of the mode II interlaminar fracture toughness of unidirectional fiber-reinforced polymer matrix composites" [8] and ASTM D6671 ("ASTM D6671. Standard test method for mixed mode I-mode II interlaminar fracture toughness of unidirectional fiber reinforced polymer matrix composites" [9], respectively. Obviously, there are more works needed to establish reliable testing procedures for other modes of delamination, which include pure mode III, mixed-mode I-III, II-III and I-II-III. Therefore, this chapter will firstly review the shear-torsion-bending (STB) and pre-stressed beam tests, which are the two delamination tests that involve mixed-mode I-II-III characterisation available in the open literature. It is followed by the review of bending plate tests, which involve characterisation of pure mode III, mixed-mode I-III and II-III delamination. After that, a new testing method for mixed-mode I-II-III delamination, which is called as ten-point bending plate (10PBP) test, is proposed. The jig design is described and the experimental results are also discussed.

2 Mixed-Mode I-II-III Delamination Tests

This section provides the review of the shear-torsion-bending (STB) and pre-stressed beam tests, which are the mixed-mode I-II-III delamination tests available in the open literature. After that, it is followed by the review of bending plate tests, which involve characterisation of pure mode III, mixed-mode I-III and II-III delamination.

2.1 Shear-Torsion-Bending Test

Davidson and Sediles [10] developed a shear–torsion–bending (STB) test (Fig. 1) to characterise mixed-mode I–II–III delamination toughness determination. STB test has the advantage of utilising traditional beam-like specimens. This eases the preparation of the specimens and reduces the cost of materials. In addition, through three-dimensional finite element analysis, it was shown that STB test could be used at any mode I, II and III ratio. Not only that, it has the advantage of uniform strain energy release rate distribution along the crack front. Furthermore, there is a data reduction method for the calculation of the mixed-mode fracture toughness. Nevertheless, the major disadvantage is complicated test setup.

The authors performed experimental tests on two types of toughened unidirectional carbon/epoxy composites, which were T800S/3900-2B and IM7/977-3. A 12.7 μm thick Teflon was placed at the mid-thickness location to induce pre-crack and edge delamination. Through pure mode III characterisation using STB test, the authors reported average mode III fracture toughness G_{IIIC} for 18-ply T800S/3900-2B and 26-ply IM7/977-3 composites were 1697 N/m and 1463 N/m, respectively. In addition, the average mode II fracture toughness G_{IIC} for those two composites were 2176 N/m and 1020 N/m, respectively. It is apparent that T800S/3900-2B carbon/epoxy composite has a larger G_{IIC} compared to G_{IIIC}, while IM7/977-3 carbon/epoxy composite has a larger G_{IIIC} than G_{IIC}. This highlights that it is not suitable to be generally assume G_{IIC} to be equal to G_{IIIC}. One of the immediate future works would be the comparison of G_{IIIC} with other mode III testing methods.

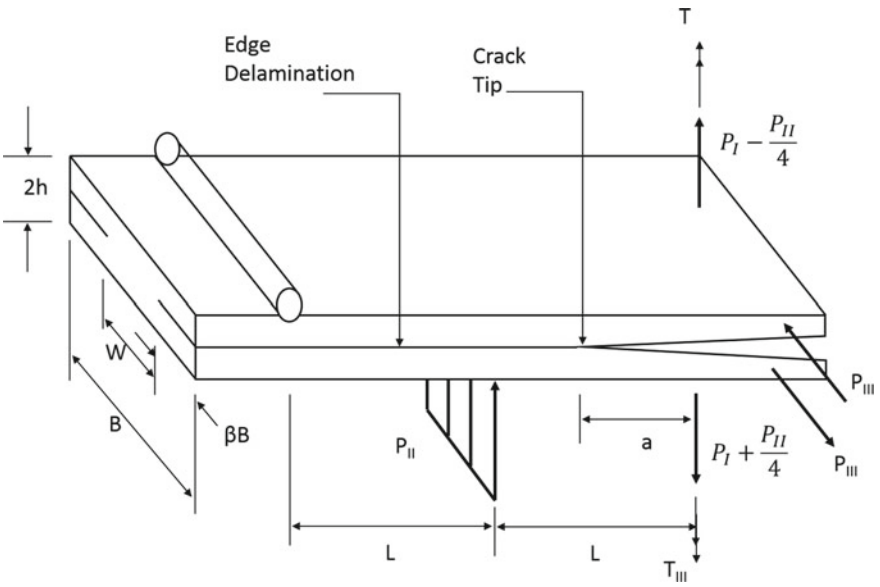

Fig. 1 Schematic diagram for the test setup of shear–torsion–bending (STB) test

2.2 Pre-stressed Beam Tests

Szekrényes [11] used pre-stressed end-notched flexure ($PENF_{I\text{-}II}$) test to evaluate mixed-mode I-II delamination of an unidirectional E-glass/polyester composite. The composite was fabricated at the stacking sequence of $[0_7//0_7]$, where//indicated the location of the 0.03 mm polyamide (PA) pre-crack. The composite has an average fibre volume fraction $V_f = 0.43$. Table 1 lists the lamina properties of the E-glass/polyester composite [11].

Figure 2 illustrates the test setup of $PENF_{I\text{-}II}$ test. Mode I is induced by the steel roller, whereas the mode II is induced by the downward lateral load at the mid-span. The test is performed using three-point bending test setup, which is simple and low cost.

Figure 3 plots the mixed-mode I-II fracture toughness of the E-glass/polyester composite, including pure mode I (mode ratio $G_{II}/G_T = 0$) and pure mode II (mode ratio $G_{II}/G_T = 1$). Pure mode I test was conducted using double cantilever beam (DCB), while end notched flexure (ENF) test was performed to characterise pure mode II delamination. The author reported mode I fracture toughness G_{IC} to be 260.9 N/m using improved beam theory (IBT). As for mode II fracture toughness G_{IIC}, an average value of 724.1 N/m was obtained using direct beam theory (DBT). All specimens were tested at initial crack length $a = 55$ mm and half span length $L = 150$ mm. It is worth to note that in the original plot by Szekrényes, the author presented the fracture envelope by plotting the values as mode I versus mode II. However, O'Brien et al. Kevin O'Brien et al. [12] mentioned that it is more reasonable to plot the fracture envelope as total fracture toughness versus mode ratio. Reeder

Table 1 Lamina properties of the E-glass/polyester composite [11]

Longitudinal modulus	E_{11}	33 GPa
Transverse modulus	E_{22}	7.2 GPa
In-plane shear modulus	G_{12}	3 GPa
In-plane poisson's ratio	ν_{12}	0.27

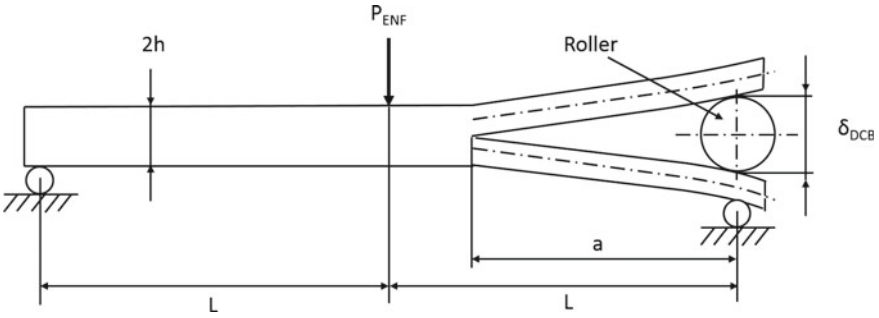

Fig. 2 Schematic diagram of the test setup for pre-stressed end-notched flexure ($PENF_{I\text{-}II}$) test

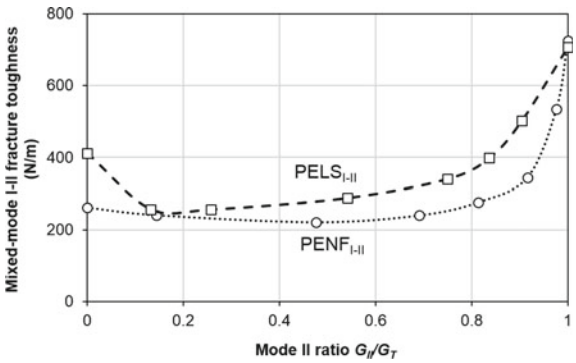

Fig. 3 Variation of mixed-mode I-II fracture toughness with respect to mode ratio for E-glass/polyester composite. Replotted using the data from References [11, 14]

[13] also described that the fracture envelope shows a more regular pattern using the same type of plot.

In addition, Szekrényes [14] also characterised mixed-mode I-II delamination of the E glass/polyester composite by combining double cantilever beam (DCB) and end loaded split (ELS) tests to develop pre-stressed end loaded split (PELS$_{I-II}$) test (Fig. 4). The G_{IC} and G_{IIC} values determined using IBT were 412 N/m and 707 N/m, respectively. By using PENF$_{I-II}$ as reference (G_{IC}= 260.9 N/m and G_{IIC} = 724.1 N/m), the G_{IC} value determined by PELS$_{I-II}$ test was found to have a significant difference of 58%. Nevertheless, negligible difference was found between the G_{IIC} values. The mixed-mode fracture toughness obtained through PELS$_{I-II}$ test at initial crack length a = 105 mm are also plotted in Fig. 3. It could be seen that the mixed-mode fracture toughness determined using PENF$_{I-II}$ and PELS$_{I-II}$ tests are in general differing from each other except at mode ratio $G_{II}/G_T \approx 0.14$. This illustrates the testing configuration dependence of mixed-mode fracture toughness using both tests. Nevertheless, both tests exhibit a similar trend, where the mixed-mode fracture toughness values are smaller than G_{IC} value at mode ratio $G_{II}/G_T < 0.9$.

To characterise the mode III delamination of E-glass/polyester composite, Szekrényes [15, 16] adopted modified split cantilever beam (MSCB) test (Fig. 5). The advantage of MSCB test is the beam-like specimen geometry which is similar to mode I and mode II delamination tests. In addition, it allows determination of the mode III energy release rate G_{III} at a wide range of initial crack length a. Figure 6 depicts the crack length dependence of G_{III} with a. Surprisingly, the trends obtained from References [15, 16] are contradicting with one another. In Reference [15], G_{III} increases with a; however, G_{III} is found to decrease with a in Reference [16]. The difference is possibly attributed to the difference in the test setup. In Reference [15], a small rig was used to conduct the experiments for a = 80–150 mm. All specimens' width b was fixed at 9 mm. However, in Reference [16], the same small rig was employed for b = 9, 12.5 and 14.5 mm at a = 42–90 mm. In addition, another bigger rig was for b = 9, 12.5, 14.5 and 20 mm at a = 95 – 155 mm. The author found that

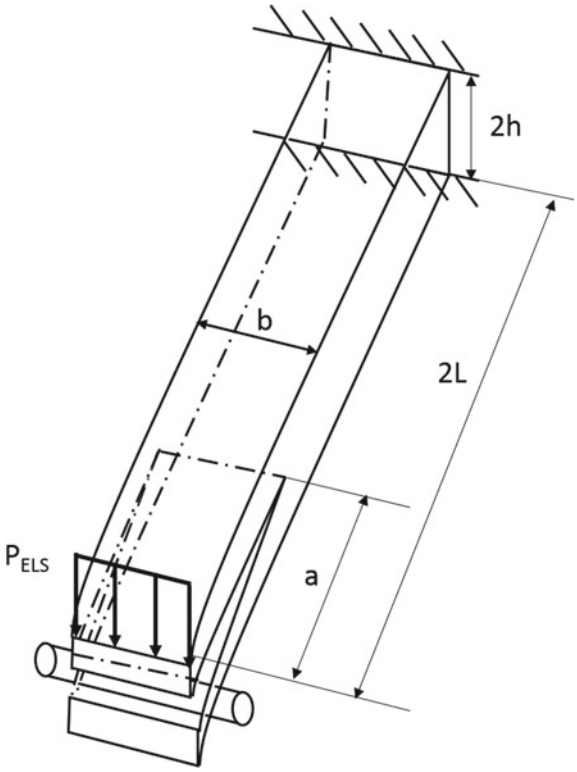

Fig. 4 Schematic diagram of the test setup for pre-stressed end-notched flexure ($PELS_{I\text{-}II}$) test

G_{III} was independent of b. Since there was no steady-state value obtained within the range of the a considered by the author, none of the G_{III} values could not be regarded as the mode III fracture toughness G_{IIIC} of the E-glass/polyester composite. Therefore, the author concluded that it is either MSCB test or the data reduction scheme is inappropriate. It is apparent that more works are needed to further improve MSCB test.

Subsequently, Szekrényes [17] combined DCB and MSCB to propose pre-stressed split cantilever beam ($PSCB_{I\text{-}III}$) test (Fig. 7) to evaluate mixed-mode I-III delamination of the E-glass/polyester composite. Figure 8 plots the variation of the mixed-mode fracture toughness with respect to the mode III ratio G_{III}/G_T. It is to note that all values are plotted using improved beam theory (IBT) for specimens tested at initial crack length $a = 105$ mm. It is apparent that the mixed-mode fracture toughness decreases with the mode III ratio G_{III}/G_T.

To evaluate mixed-mode II-III delamination of the E-glass/polyester composite, Szekrényes [18] combined ENF and MSCB tests to develop pre-stressed end notched flexure ($PENF_{II\text{-}III}$) test (Fig. 9). Figure 10 plots the variation of the mixed-mode fracture toughness with respect to the mode III ratio G_{III}/G_T. The values are plotted

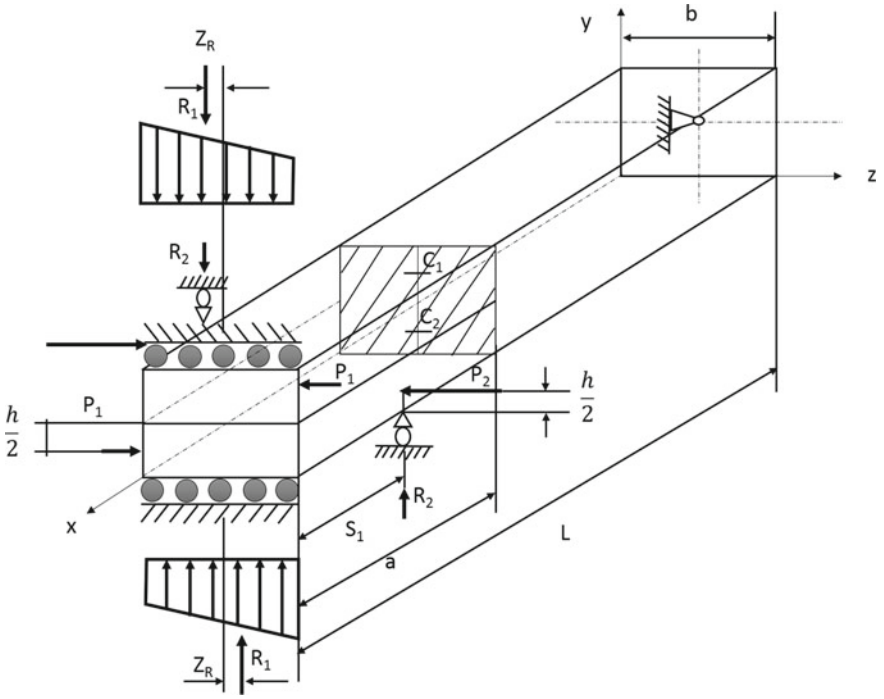

Fig. 5 Schematic diagram of the test setup for modified split-cantilever beam (MSCB) test

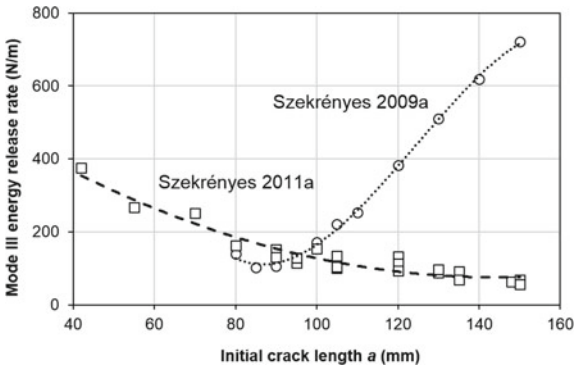

Fig. 6 Mode III energy release rate of the E-glass/epoxy composite measured by modified split cantilever beam (MSCB) test. Replotted using the data from References [15, 16]

using improved beam theory (IBT) for specimens tested at initial crack length $a =$ 55 mm and half span length $L = 75$ mm. It is noticed that mixed-mode fracture toughness decreases with G_{III}/G_T.

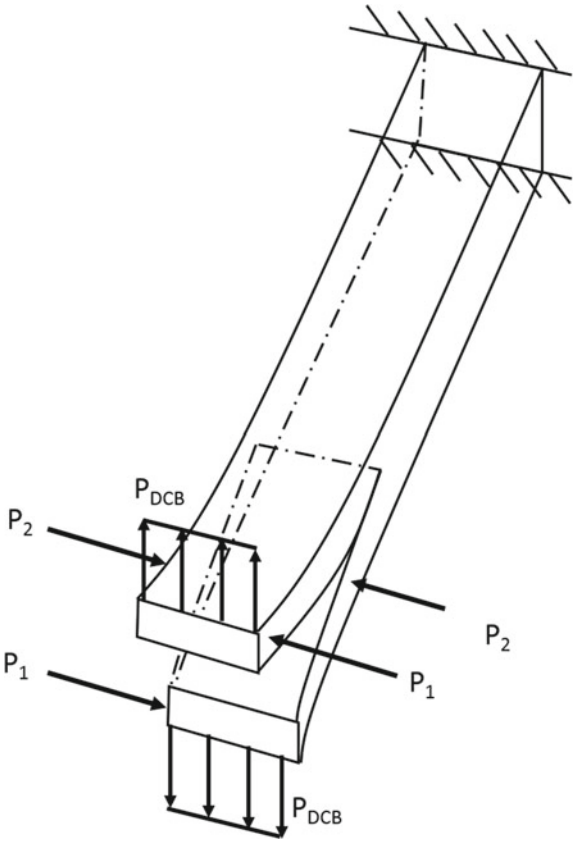

Fig. 7 Schematic diagram of the test setup for mixed-mode I-III pre-stressed modified split cantilever beam ($PSCB_{I\text{-}III}$) test

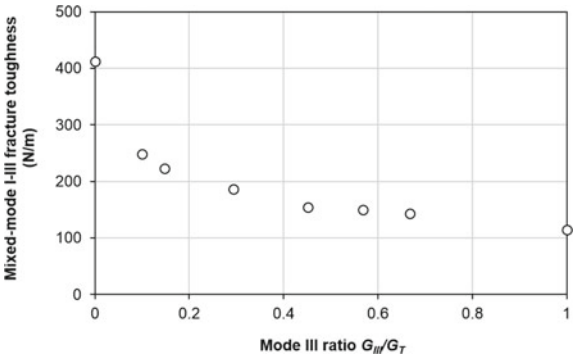

Fig. 8 Variation of mixed-mode I-III fracture toughness with respect to mode ratio for E-glass/polyester composite. Replotted using the data from Reference [17]

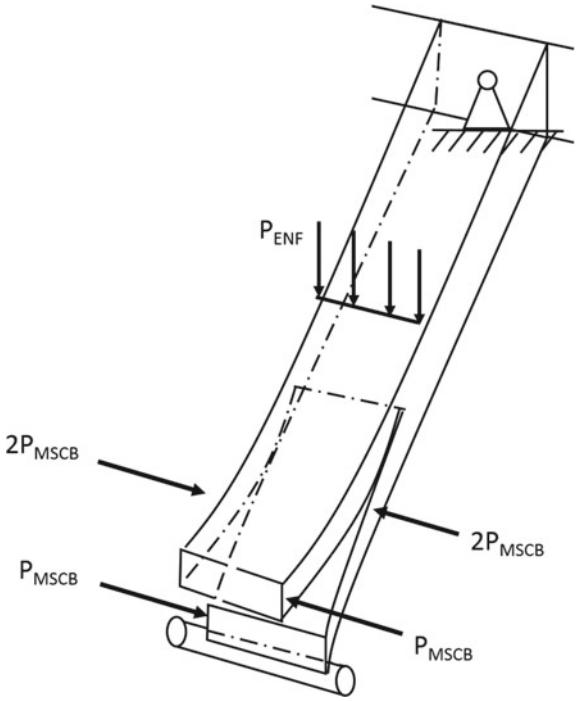

Fig. 9 Schematic diagram of the test setup for pre-stressed end-notched flexure ($PENF_{II\text{-}III}$) test

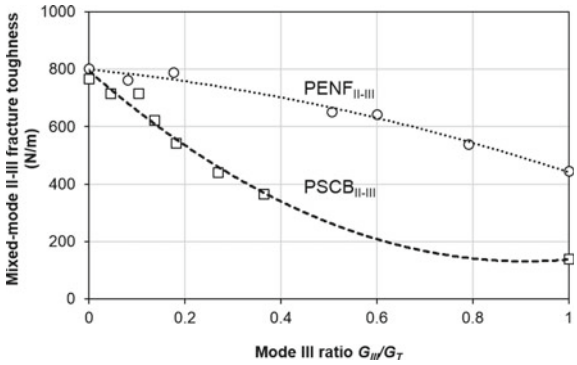

Fig. 10 Variation of mixed-mode II-III fracture toughness with respect to mode ratio for E-glass/polyester composite. Replotted using the data from References [18, 19]

After that, Szekrényes and Vicente [19] proposed mixed-mode II-III pre-stressed split cantilever beam ($PSCB_{II\text{-}III}$) test. This test combines end loaded split (ELS) and modified split cantilever beam (MSCB) tests (Fig. 11). Compared to $PENF_{II\text{-}III}$ test, it allows a larger range of initial crack lengths. In addition, mode III component

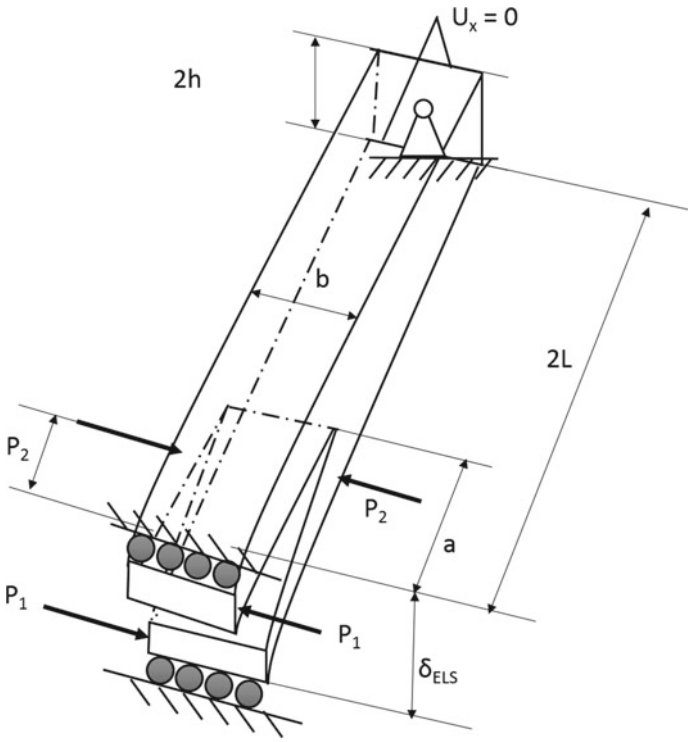

Fig. 11 Schematic diagram of the test setup for mixed-mode II-III pre-stressed modified split cantilever beam ($PSCB_{II\text{-}III}$) test

is pre-stressed in $PENF_{II\text{-}III}$ test, whereas in $PSCB_{II\text{-}III}$ test, mode II component is pre-stressed. Pre-stressing mode II component is more appropriate due to a higher compliance in mode II loading direction compared to mode III loading direction.

The variation of the mixed-mode fracture toughness with the mode III ratio G_{III}/G_T is plotted in Fig. 10. The values are plotted using virtual crack closure technique (VCCT) for specimens tested at initial crack length $a = 105$ mm. Similar to $PENF_{II\text{-}III}$ test, the mixed-mode fracture toughness values from $PSCB_{II\text{-}III}$ test are also decreasing with G_{III}/G_T. Nevertheless, there is a significant difference between the mixed-mode II-III values determined using $PENF_{II\text{-}III}$ and $PSCB_{II\text{-}III}$ tests. The values obtained from $PENF_{II\text{-}III}$ test are always larger than the one determined from $PSCB_{II\text{-}III}$ test. This illustrates the testing configuration dependence of mixed-mode fracture toughness using both tests.

To evaluate mixed-mode I-II-III delamination, Szekrényes [20] developed pre-stressed end notched flexure ($PENF_{I\text{-}II\text{-}III}$) test (Fig. 12). $PENF_{I\text{-}II\text{-}III}$ test combines double cantilever beam (DCB), end notched flexure (ENF) and modified split cantilever beam (MSCB) tests. Mode I and mode III are being pre-stressed, while mode II component is induced by the machine using three-point bending setup. The

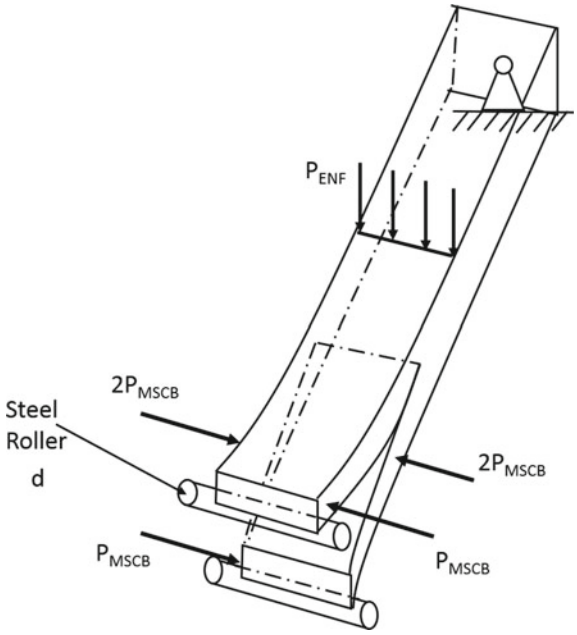

Fig. 12 Schematic diagram of the test setup for mixed-mode I-II-III pre-stressed end notched flexure ($PENF_{I\text{-}II\text{-}III}$) test

author used improved beam theory (IBT) to quantify the fracture energy at each mode. Pure mode I, II and III fracture toughness were determined using DCB, ENF and MSCB tests, respectively. In addition, $PENF_{I\text{-}II}$, $PSCB_{I\text{-}III}$ and $PENF_{II\text{-}III}$ tests were performed to obtain the mixed-mode I-II, I-III and II-III fracture toughness. All tests were conducted at initial crack length $a = 55$ mm and half span length $L = 75$ mm. However, in Reference [20], the energy release rate values of mixed-mode I-II-III were not reported by the author. The three-dimensional (3D) plot is therefore not able to be reproduced here. Readers could refer to Reference [20] for the 3D plot of the energy release rates.

After that, Szekrényes [21] combined double cantilever beam (DCB), end loaded split (ELS) and modified split cantilever beam (MSCB) tests to propose pre-stressed split cantilever beam test ($PSCB_{I\text{-}II\text{-}III}$) test (Fig. 13) to quantify the fracture energy at any combination of mode ratio. In $PSCB_{I\text{-}II\text{-}III}$ test, mode I and mode II are being pre-stressed, while mode III component is induced by the machine. The author used virtual crack-closure technique (VCCT) to quantify the fracture energy at each mode. Pure mode I, II and III fracture toughness were determined using DCB, ELS and MSCB tests, respectively. In addition, $PELS_{I\text{-}II}$, $PSCB_{I\text{-}III}$ and $PSCB_{II\text{-}III}$ tests were performed to obtain the mixed-mode I-II, I-III and II-III fracture toughness. This has ensured the consistency in the loading configurations to induce mixed-mode I-II-III.

Figure 14 plots the mixed-mode I-II-III fracture toughness in three-dimensional plane. All tests were conducted at initial crack length $a = 105$ mm. It is apparent

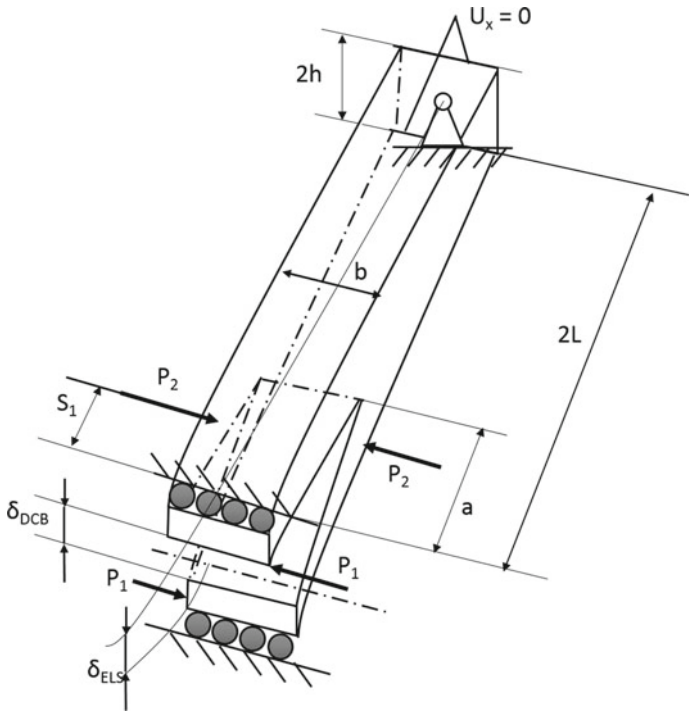

Fig. 13 Schematic diagram of the test setup for mixed-mode I-II-III pre-stressed split cantilever beam ($PSCB_{I\text{-}II\text{-}III}$) test

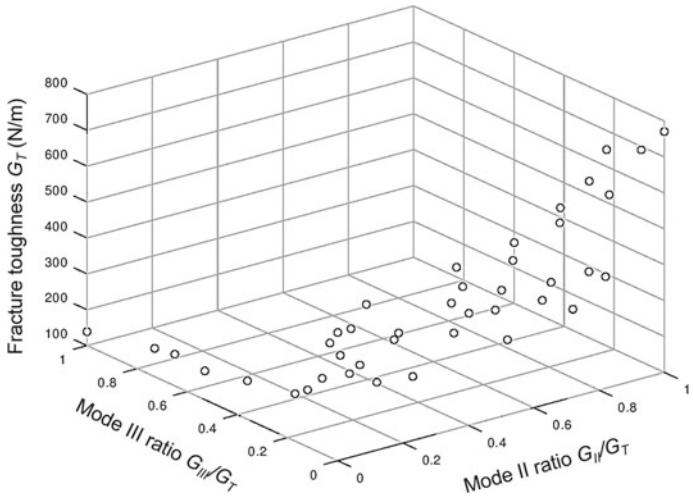

Fig. 14 Three-dimensional plot of the variation of mixed-mode I-II-III fracture toughness for E-glass/polyester composite using $PSCB_{I\text{-}II\text{-}III}$ test. Replotted using the data from Reference [21]

that the E-glass/polyester composite used by the author has the largest resistance to crack initiation in shearing mode (mode II). It is relatively weak in opening mode (mode I) and tearing mode (mode III). Since the loadings in real life applications are usually complex, that delamination is usually occurred in mixed-mode, further research could be conducted to enhance the resistance to fracture of the material under mode I and mode III loadings.

Based on the previous discussion, it could be summarised that pre-stressed beam tests have the advantage of utilising the conventional beam-like specimens like those used for DCB (mode I) and ENF (mode II) tests. This provides convenience in the preparation of the specimens. In addition, it saves some of the experimental cost, because the size of the specimens is relatively small. Not only that, the pre-stressed beam tests allow the determination of the energy release rate at a wide range of mixed-mode ratio. In addition, the closed-form solution is available, that the energy release rate could be calculated analytically. Furthermore, the imposed displacement is not large in order to initiate the delamination, that the geometrical nonlinearities are not significant. This allows an easier and more accurate determination of the critical load to calculate the energy release rate.

Nevertheless, pre-stressed beam tests have several drawbacks. Firstly, the specimens have the tendency to rotate during testing. Secondly, the mixed-mode ratio is not uniform along the crack front. Thirdly, the mode ratio varies with the crack length and applied load. Therefore, the specimens need to be transparent. Fourthly, the mode ratio cannot be predetermined before carrying out the experiment. Fifthly, the tests can only quantify the energy release rate at crack initiation. If there is fibre bridging behaviour during delamination, this phenomenon cannot be quantified.

2.3 Bending Plate Tests

De Morais and Pereira characterised the mode I, mode II and mixed-mode I-II delamination of HS 160 REM composite using double cantilever beam (DCB), end notched flexure (ENF) and mixed-mode bending (MMB) tests (Fig. 15), respectively [22]. HS 160 REM composite consists of T300 high strength carbon fibres and toughened epoxy. The single ply thickness is 0.15 mm with fibre volume fraction $V_f = 0.65$ [22]. The lamina properties are shown in Table 2 [23, 24]. The stacking sequence of the unidirectional laminate is $[0_{14}//0_{14}]$, where //refers to the location of the pre-crack (a 13 μm polytetrafluoroethylene (PTFE) film). They reported the mode I fracture toughness G_{IC} and mode II fracture toughness G_{IIC} to be approximately 250 N/m and 815 N/m, respectively. Figure 16 describes the variation of the mixed-mode fracture toughness with respect to the mode II ratio G_{II}/G_T. It is obvious that the fracture toughness increases with the mode ratio. In addition, the mode II to mode I fracture toughness ratio, G_{IIC}/G_{IC} for this material is approximately 3.2. A higher G_{IIC} compared to G_{IC} is commonly noticed in brittle matrix materials [25], which has been summarised by Johar et al [4] as well.

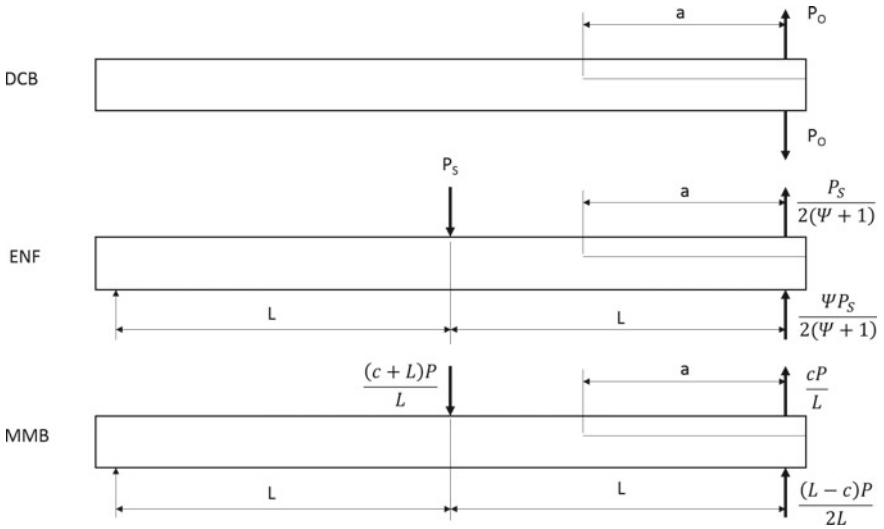

Fig. 15 Schematic diagram of the test setup for double cantilever beam (DCB), end notched flexure (ENF) and mixed-mode bending (MMB) tests

Table 2 Lamina properties of HS 160 REM carbon/epoxy composite [23, 24]

Longitudinal modulus	E_{11}	130 GPa
Transverse modulus	E_{22}	8.2 GPa
In-plane shear modulus	G_{12}	4.1 GPa
In-plane poisson's ratio	v_{12}	0.34
Out-of-plane poisson's ratio	v_{23}	0.41

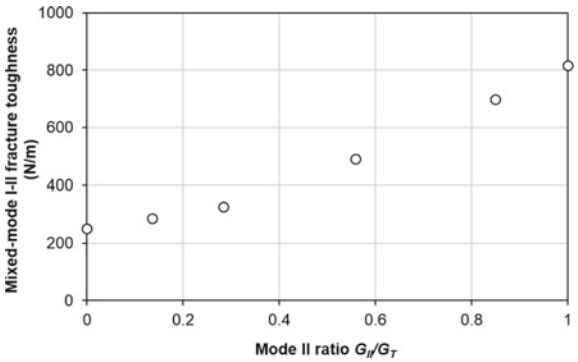

Fig. 16 Variation of mixed-mode I-II fracture toughness with respect to mode ratio for HS 160 REM carbon epoxy composite. Replotted using the data from Reference [22]

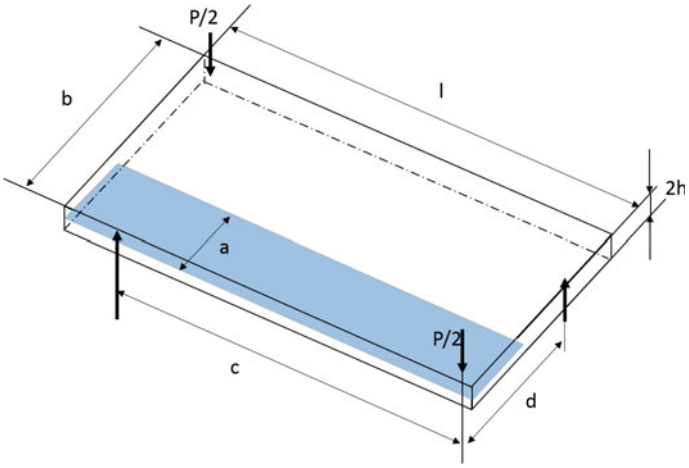

Fig. 17 Schematic diagram of the test setup for edge crack torsion (ECT) test

After that, de Morais et al. [26] determined the mode III fracture toughness G_{IIIC} of the same composite through edge crack torsion (ECT) test (Fig. 17). The stacking sequence for the ECT specimen is $[0/(\pm 0\ 45)_4/(\pm 45)_4/0]_S$, with 0-degree refers to the direction that is perpendicular to the crack front. The PTFE film was placed at the mid-thickness of the specimen. The authors reported the G_{IIIC} value to be in the range of 850–1100 N/m. The main disadvantage of ECT would be non-uniform crack propagation, which has been highlighted by some other researchers as well [27, 28]. Subsequently, de Morais and Pereira [29] proposed four-point bending plate (4PBP) test (Fig. 18) to characterise G_{IIIC}. This new test is more cost effective than ECT test. In addition to simpler test setup, 4PBP test utilises thinner specimens compared to ECT test as well. The stacking sequence for the specimens is $[(90_2/0)_{2S}/0]_S$, for which the number of plies is 26 as compared to 36 in ECT test. Also, it does not require 45-degree layers, which eases the composite preparation and reduces material waste. In addition, the crack growth is visible along the edges of the specimen. However, the crack initiation location is difficult to be predicted. In addition, the data reduction

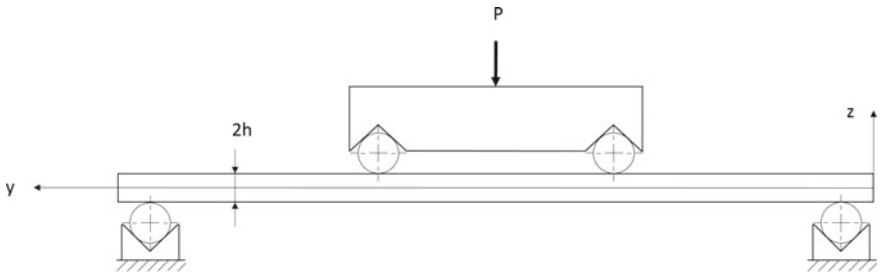

Fig. 18 Schematic diagram of the test setup for four-point bending plate (4PBP) test

method for 4PBP is not yet available, hence it requires finite element analysis (FEA) to determine the fracture toughness value. Through FEA, the fracture toughness was estimated to be $G_{IIIC} = 1550$ N/m. The authors postulated that a higher G_{IIIC} value compared to ECT was attributed to R-curve effect.

For mixed-mode I-III characterisation, Pereira and de Morais [30] developed a new eight-point bending plate (8PBP) test (Fig. 19). The stacking sequence is $[(90_2/0)_{2S}/0]_S$, which is the same as 4PBP specimens. However, the test setup is complicated. The authors tested at G_{III}/G_T of 0.22, 0.42, 0.58, 0.71 and 0.86. Figure 20 plots the variation of the mixed-mode I-III fracture toughness with respect to the mode III ratio G_{III}/G_T. It is to note that the mode I fracture toughness G_{IC} used to plot Fig. 20 is 250 N/m [22], whereas the mode III fracture toughness G_{IIIC}

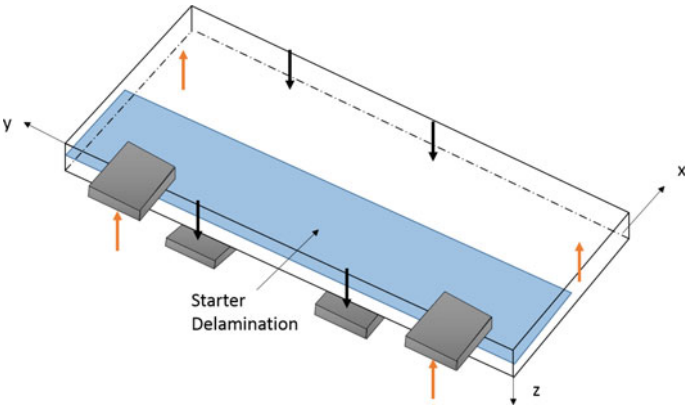

Fig. 19 Schematic diagram of the test setup for eight-point bending plate (8PBP) test

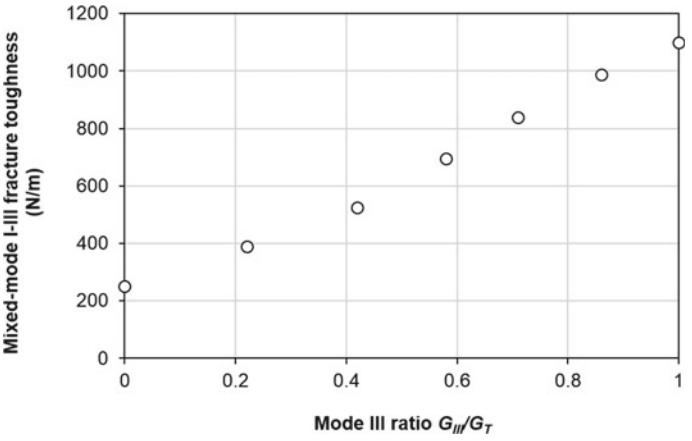

Fig. 20 Variation of mixed-mode I-III fracture toughness with respect to mode ratio for HS 160 REM carbon epoxy composite. Replotted using the data from Reference [30]

is 1100 N/m (estimated from 8PBP test) [30]. The mixed-mode fracture toughness appears to increase with the mode ratio G_{III}/G_T. It is worth to note that the experimental results show that the mixed-mode fracture toughness increases linearly with mode III ratio for $G_{III}/G_T \geq 0.42$. The mode III fracture toughness G_{IIIC} estimated through linear extrapolation is 1100 N/m, which is the same value as the upper range of the G_{IIIC} calculated through ECT test [26].

The 8PBP test has gained attention by some other researchers. For example, Miura et al. [31, 32] used 8PBP test to characterise the mixed-mode I/III delamination of G-11 woven glass/epoxy composites at cryogenic conditions under both quasi-static and fatigue loadings.

On the other hand, de Morais and Pereira [33] also developed six-point bending plate (6PBP) test (Fig. 21) to characterise mixed-mode II-III delamination. The authors used the same stacking sequence as 4PBP and 8PBP tests, which is $[(90_2/0)_{2S}/0]_S$. The authors carried out the experimental tests at G_{III}/G_T of 0.15, 0.40, 0.60, 0.75 and 0.85. Figure 22 plots the variation of the mixed-mode II-III fracture toughness with respect to the mode III ratio G_{III}/G_T. It is to note that the mode II fracture toughness G_{IIC} used is the value from ENF test ($G_{IIC} = 815$ N/m) [22]. In addition, the values plotted are the fracture toughness obtained using the peak load from the force-displacement curves. It is because the mode III fracture toughness G_{IIIC} estimated using this approach is closer to the one predicted by 8PBP test [30] and the upper limit from ECT test [26]. It is noticed that the mixed-mode fracture toughness increases with the mode ratio G_{III}/G_T. Furthermore, it is worth to note that the increasing trend of the mixed-mode II-III fracture toughness agrees with the observation from ENF [22], ECT [26] and 4PBP [29] tests, where G_{IIIC} is estimated

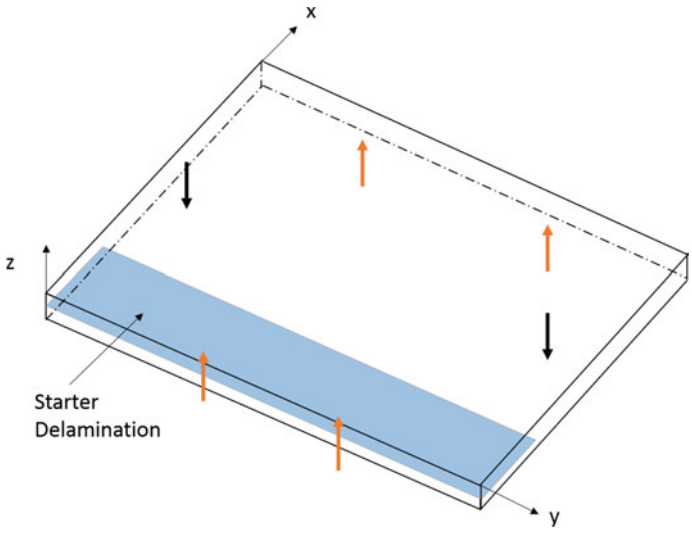

Fig. 21 Schematic diagram of the test setup for six-point bending plate (6PBP) test

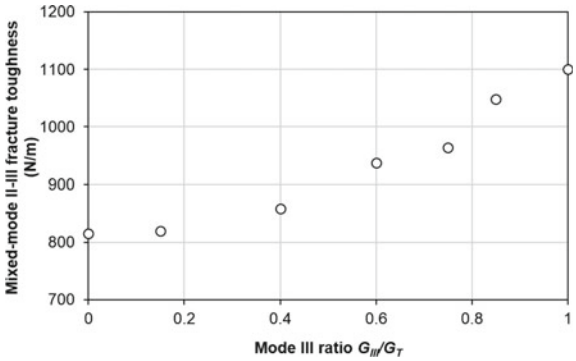

Fig. 22 Variation of mixed-mode II-III fracture toughness with respect to mode ratio for HS 160 REM carbon epoxy composite. Replotted using the data from Reference [33]

to be larger than G_{IIC}. This is similar to the observation on IM7/977-3 carbon/epoxy composite [10].

After the introduction of 6PBP test by de Morais and Pereira [33], this test has also been used by Asgari Mehrabadi to characterise the mixed-mode II-III fracture toughness of AF301 woven glass reinforced ML506 epoxy composite [34] and AD-314 epoxy adhesive bonded low carbon steel joints [35]. It has also been used by Miura et al. [36] to characterise the mixed-mode II-III delamination of G-11 woven glass/epoxy composites at cryogenic conditions. Israr et al. [37] had also used cohesive zone modelling to simulate the results by de Morais and Pereira [33] in order to understand in depth the participation of mode II and mode III during crack growth process.

Figure 23 plots the fracture envelope of the HS 160 REM carbon epoxy composite in three-dimensional form. It is apparent that the tearing mode has the highest fracture toughness (G_{IIIC}), followed by shearing mode (G_{IIC}) and the lowest value is attained at opening mode (G_{IC}). This is opposite to the trend observed in E-glass/polyester composite (Fig. 14). In addition, it is also noticed that the variation of the mixed-mode fracture toughness is not necessarily linear. Instead, it varies with a positive increasing slope in all three mixed-modes I-II, I-III and II-III. Non-linear variation is also observed in E-glass/polyester composite as shown in Fig. 14, despite the trend of variation is different. Therefore, if a three-dimensional fracture criterion is to be developed, one has to consider non-linear variation with three different fitting parameters for each two-dimensional mixed-mode plane.

Bending plate tests have the advantages of crack propagation near the edges that allows the visual inspection of the delamination. Furthermore, these tests allow mixed-mode characterisation at a wide range of mixed-mode ratio. Nevertheless, bending plate tests do not have data reduction scheme to calculate the fracture toughness. Hence, finite element analysis (FEA) is required to determine the mode ratio and fracture toughness. Not only that, the mixed-mode ratio is not uniform along the crack front. In addition, the larger specimens' size as compared to the traditional

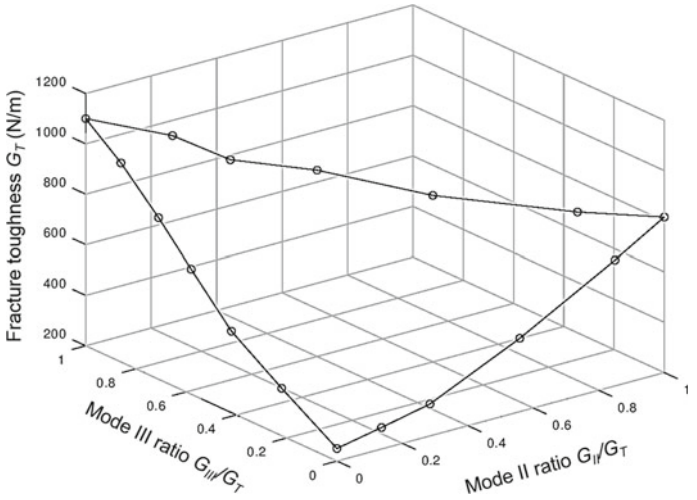

Fig. 23 Three-dimensional fracture envelope of HS 160 REM carbon epoxy composite

beam-like specimens leads to a higher cost for the materials. More works are needed to look into bending plate tests.

3 Ten-Point Bending Plate Test

Based on the literature review on bending plate tests, it is observed that 8PBP induces mixed-mode I-III through opening in the out-of-plane direction and bending about the longitudinal axis [30], whereas 6PBP utilises concurrent bending in the axial and transverse directions to induce mixed-mode II-III [33]. Inspired by 8PBP and 6PBP tests, a ten-point bending plate (10PBP) test is proposed to induce mixed-mode I-II-III delamination. Figure 24 illustrates how the specimen is loaded. Pins 1-4 are responsible for mode I (opening), pins 5-8 are for mode II (shearing) component, whereas pins 9-10 are meant to induce mode III (tearing) delamination. Figure 25 shows the entire assembly of the jig design for 10PBP test.

To evaluate the applicability of 10PBP test, experiments were conducted using a carbon/epoxy composite. This unidirectional carbon/epoxy prepreg has a nominal ply thickness of 0.15 mm. The average fibre volume fraction is 65.7 ± 6.3%, while the carbon fibre has an average diameter of 6.8 μm. Figure 26 shows the scanning electron micrograph of the cross-section of the composite. Firstly, a unidirectional composite plate with $[(90/0)_{3S}/0]_S$ was fabricated using hand lay-up technique. To generate the pre-crack, a 15 μm Teflon film was placed at the mid-thickness location of the plate. The composite was then hot-pressed and has an average thickness 2 h of 3.9 mm upon curing. After that, it was cut into specimens of 180 mm × 144 m size using a computer numerical control (CNC) machine. All specimens were prepared

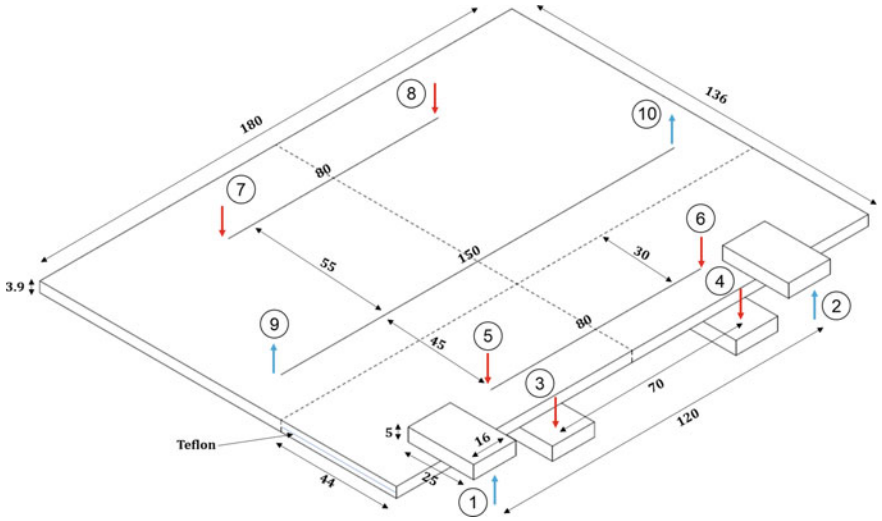

Fig. 24 Schematic diagram for the test setup of ten-point bending plate (10PBP) test

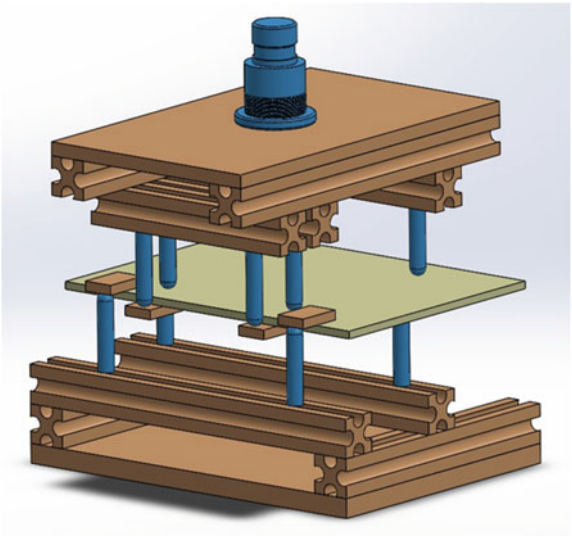

Fig. 25 Jig design for mixed-mode I-II-III delamination using ten-point bending plate test

and supplied by X Plas Singapore. This composite material has been successfully used in the previous study to characterise mode I delamination with displacement rate effect [38].

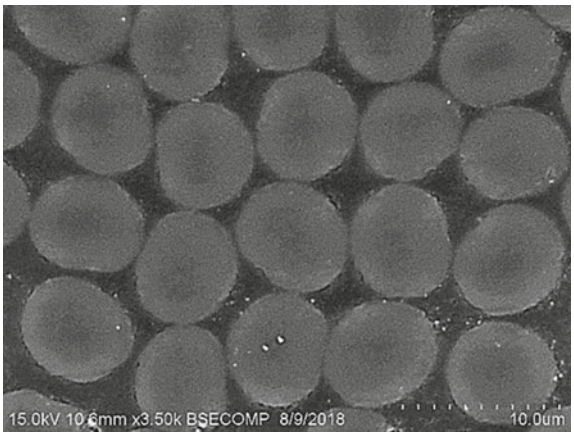

Fig. 26 Cross-sectional micrograph of the carbon/epoxy composite used in this study

Figure 27 shows the experimental setup of 10PBP test. The edges of the specimens were applied by a layer of white paint to facilitate the visual inspection of the crack propagation. It is apparent that the crack has successfully propagated during the test.

Figure 28 depicts the force displacement curves from the 10PBP tests. All four curves show comparatively good repeatability. Upon loading, the force increases

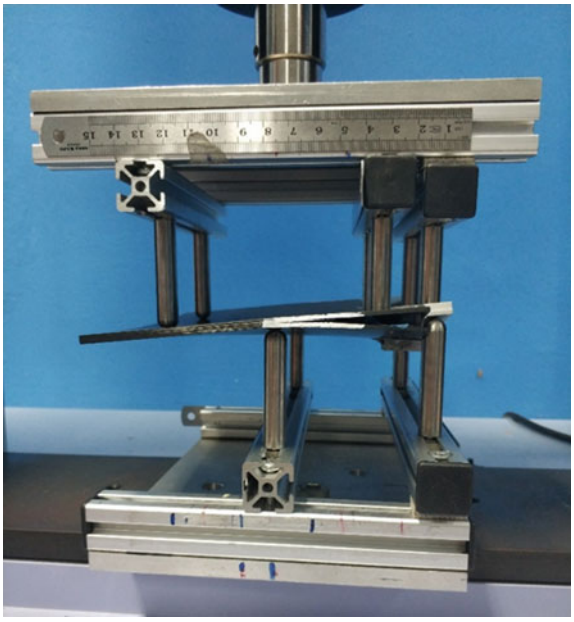

Fig. 27 Experiment test setup of ten-point bending plate test

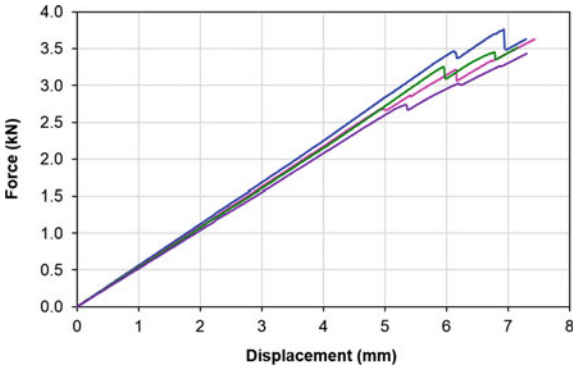

Fig. 28 Experimental force-displacement curves from 10PBP test

linearly with the displacement. At the force of approximately between 2.7 and 3.5 kN, a slight drop in the force is noticed. The difference in the first load drop among the specimens is believed to be attributed to the experimental scatter. The first load drop is an indication of the initiation of crack propagation. During the experiment, it was also accompanied by cracking sound and visual inspection of crack growth along the mid-edges of the specimens. Subsequently, the force increases gradually. This could be an indication of fibre bridging, which was postulated by Pereira and de Morais [30] in mixed-mode I-III delamination using 8PBP test. Further work is required to quantify the participation of each mode during the initiation of crack propagation through finite element analysis.

4 Conclusions and Future Perspectives

The chapter reviews the shear-torsion-bending and pre-stressed beam tests, which are the two testing methods available in the open literature to characterise mixed-mode I-II-III delamination of laminated composites. Subsequently, bending plate tests are also discussed. Inspired by bending plate tests, a ten-point bending plate test (10PBP) is proposed to characterise mixed-mode I-II-III delamination. The experimental observations show that the specimens failed under delamination prior to other types of damage mechanisms. This has partially validated the concept of 10PBP test. Finite element analysis is needed to determine the mixed-mode fracture toughness, quantify the participation of each mode and simulate the crack growth behaviour.

Acknowledgements This work was supported by Universiti Teknologi Malaysia through UTMShine Grant No. 09G16 and Transdisciplinary Research (UTM-TDR) Grant No. 05G22.

References

1. Soutis, C.: Carbon fiber reinforced plastics in aircraft construction. Mater. Sci. Eng., A **412**, 171–176 (2005)
2. Soutis, C.: 'Fibre reinforced composites in aircraft construction. Prog. Aerosp. Sci. **41**, 143–51 (2005b)
3. Johar, M., Chong, W.W.F., Kang, H.S., Wong, K.J.: Effects of moisture absorption on the different modes of carbon/epoxy composites delamination. Polym. Degrad. Stab. **165**, 117–125 (2019)
4. Johar, M., Low, K.O., Israr, H.A., Wong, K.J.: Mode I and mode II delamination of a chopped strand mat E-glass reinforced vinyl ester composite. Plast., Rubber Compos. **47**, 391–397 (2018)
5. Johar, M., Israr, H.A., Low, K.O., Wong, K.J.: Numerical simulation methodology for mode II delamination of quasi-isotropic quasi-homogeneous composite laminates. J. Compos. Mater. **51**, 3955–3968 (2017)
6. Rajendran, T.S., Johar, M., Low, K.O., Abu Hassan, S., Wong, K.J.: Interlaminar fracture toughness of a plain weave flax/epoxy composite. Plast., Rubber Compos. **48**, 74–81 (2019)
7. ASTM D5528: Standard test method for mode I interlaminar fracture toughness of unidirectional fiber-reinforced polymer matrix composites. In: 2007. West Conshohocken, Pennsylvania, United States: ASTM International
8. ASTM D7905: Standard test method for determination of the mode II interlaminar fracture toughness of unidirectional fiber-reinforced polymer matrix composites. In: 2014. West Conshohocken, Pennsylvania, United States: ASTM International
9. ASTM D6671: Standard test method for mixed mode I-mode II interlaminar fracture toughness of unidirectional fiber reinforced polymer matrix composites. In: 2006. West Conshohocken, Pennsylvania, United States: ASTM International
10. Davidson, B.D., Sediles, F.O.: Mixed-mode I-II–III delamination toughness determination via a shear–torsion-bending test. Compos. A Appl. Sci. Manuf. **42**, 589–603 (2011)
11. Szekrényes, A.: Prestressed fracture specimen for delamination testing of composites. Int. J. Fract. **139**, 213–237 (2006)
12. O'Brien, T.K., Johnston, N.J., Morris, D.H., Simonds, R.A.: Determination of interlaminar fracture toughness and fracture mode dependence of composites using the edge delamination test. In: Feest, T. (ed.), TEQC83, Butterworth-Heinemann (1983)
13. Reeder, J.R.: 3D mixed mode delamination fracture criteria - an experimentalist's perspective. In: Proceedings of American Society for Composites, 21st Annual Tehnical Conference. Dearborn, MI, US (2006)
14. Szekrényes, A.: Prestressed composite specimen for mixed-mode I/II cracking in laminated materials. J. Reinf. Plast. Compos. **29**, 3309–3321 (2010)
15. Szekrényes, A.: Improved analysis of the modified split-cantilever beam for mode-III fracture. Int. J. Mech. Sci. **51**, 682–693 (2009)
16. Szekrényes, A.: The influence of crack length and delamination width on the mode-III energy release rate of laminated composites. J. Compos. Mater. **45**, 279–294 (2011)
17. Szekrényes, A.: Interlaminar fracture analysis in the GI–GIII plane using prestressed transparent composite beams. Compos. A Appl. Sci. Manuf. **40**, 1621–1631 (2009)
18. Szekrényes, A.: Delamination fracture analysis in the GII–GIII plane using prestressed transparent composite beams. Int. J. Solids Struct. **44**, 3359–3378 (2007)
19. Szekrényes, A., Vicente, W.M.: Interlaminar fracture analysis in the GII–GIII plane using prestressed transparent composite beams. Compos. A Appl. Sci. Manuf. **43**, 95–103 (2012)
20. Szekrényes, A.: Application of prestressed transparent composite beams in fracture mechanics. Periodica Polytech. **51**, 89–97 (2007)
21. Szekrényes, A.: Interlaminar fracture analysis in the G I—G II—G III space using prestressed transparent composite beams. J. Reinf. Plast. Compos. **30**, 1655–1669 (2011)
22. Pereira, A.B., de Morais, A.B.: Mixed mode I + II interlaminar fracture of carbon/epoxy laminates. Compos. A Appl. Sci. Manuf. **39**, 322–333 (2008)

23. Pereira, A.B., de Morais, A.B.: Mode I interlaminar fracture of carbon/epoxy multidirectional laminates. Compos. Sci. Technol. **64**, 2261–2270 (2004)
24. Pereira, A.B., de Morais, A.B., Marques, A.T., de Castro, P.T.: Mode II interlaminar fracture of carbon/epoxy multidirectional laminates. Compos. Sci. Technol. **64**, 1653–1659 (2004)
25. Bensadoun, F., Verpoest, I., Van Vuure, A.W.: Interlaminar fracture toughness of flax-epoxy composites. J. Reinf. Plast. Compos. **36**, 121–136 (2017)
26. de Morais, A.B., Pereira, A.B., de Moura, M.F.S.F., Magalhães, A.G.: Mode III interlaminar fracture of carbon/epoxy laminates using the edge crack torsion (ECT) test. Compos. Sci. Technol. **69**, 670–676 (2009)
27. Israr, H.A., Wong, K.J., Tamin, M.N.: Cohesive zone modelling of mode III delamination using the edge crack torsion test. J. Mech. Eng. Sci. **11**, 2526–2538 (2017)
28. Wong, K.J., Israr, H.A., Tamin, M.N.: Crack length dependence of mode III delamination using edge crack torsion test. Int. J. Mech. Eng. Rob. Res. **6**, 219–225 (2017)
29. de Morais, A.B., Pereira, A.B.: Mode III interlaminar fracture of carbon/epoxy laminates using a four-point bending plate test. Compos. A Appl. Sci. Manuf. **40**, 1741–1746 (2009)
30. Pereira, A.B., de Morais, A.B.: Mixed-mode I + III interlaminar fracture of carbon/epoxy laminates. Compos. A Appl. Sci. Manuf. **40**, 518–523 (2009)
31. Miura, M., Shindo, Y., Takeda, T., Narita, F.: Cryogenic interlaminar fracture properties of woven glass/epoxy composite laminates under mixed-mode I/III loading conditions. Appl. Compos. Mater. **20**, 587–599 (2013)
32. Miura, M., Shindo, Y., Takeda, T., Narita, F.: Mixed-mode I/III fatigue delamination growth in woven glass/epoxy composite laminates at cryogenic temperatures. J. Compos. Mater. **48**, 1251–1259 (2013)
33. de Morais, A.B., Pereira, A.B.: Mixed mode II + III interlaminar fracture of carbon/epoxy laminates. Compos. Sci. Technol. **68**, 2022–2027 (2008)
34. Asgari Mehrabadi, F.: Analysis of pure mode III and mixed mode (III + II) interlaminar crack growth in polymeric woven fabrics', Mater. Des. **44**, 429–37 (2013)
35. Asgari Mehrabadi, F.: The use of ECT and 6PBP tests to evaluate fracture behavior of adhesively bonded steel/epoxy joints under mode-III and mixed mode III/II. Appl. Adhes. Sci. **2**, 18 (2014)
36. Miura, M., Shindo, Y., Takeda, T., Narita, F.: Interlaminar fracture characterization of woven glass/epoxy composites under mixed-mode II/III loading conditions at cryogenic temperatures. Eng. Fract. Mech. **96**, 615–625 (2012)
37. Israr, H.A., Wong, K.J., Tamin, M.N.: Numerical simulations of mixed-mode II + III delamination in carbon/epoxy composite laminate. In: Mohamed Ali, M.S., Wahid, H., Mohd Subha, N.A., Sahlan, S., Md. Yunus, M.A., Wahap, A.R. (eds.) Modeling, Design and Simulation of Systems, pp. 560–68. Springer Singapore, Singapore (2017b)
38. Low, K.O., Teng, S.M., Johar, M., Israr, H.A., Wong, K.J.: Mode I delamination behaviour of carbon/epoxy composite at different displacement rates. Compos. B Eng. **176**, 107293 (2019)

Fracture Analysis of Fused Deposition Modelling of Bio-composite Filaments

G. S. Sivagnanamani, P. Ramesh, Mohit Hemanth Kumar, and V. Arul Mozhi Selvan

Abstract In the past decades, Additive manufacturing (AM) and its application are increased rapidly due to advanced improvement in the AM process. FDM is a widely used AM process at affordable prices compared to other methods. FDM consumes polymers to develop 3D models into 3D products in a simple way. Due to the weak nature of pure polymer strength, composite-based materials were designed to enhance the life span of FDM's products. This chapter presents a review of biocomposite filaments, and its mechanical strength is explained.

Keywords Fused deposition modeling · Additive manufacturing · Bio composite

Nomenclature

FDM	Fused Deposition Modeling
AM	Additive Manufacturing
CAD	Computer Aided Design
3DP	Three-dimensional printing
PLA	Poly Lactic Acid
PBS	Polybutylene succinate
PBAT	Polybutylene adipate terephthalate
PHA	Polyhydroxyalkanoates

G. S. Sivagnanamani
Department of Mechanical Engineering, Anna University, Chennai, India

P. Ramesh (✉)
Department of Production Engineering, National Institute of Technology, Tiruchirappalli, India
e-mail: rameshbillie@gmail.com

M. H. Kumar
Center for Nanoscience, Composite Research Center, Chennai 600053, Tamil Nadu, India

V. Arul Mozhi Selvan
Department of Mechanical Engineering, National Institute of Technology, Tiruchirappalli, India

S. Mavinkere Rangappa et al. (eds.), *Fracture Failure Analysis of Fiber Reinforced Polymer Matrix Composites*, Engineering Materials,
https://doi.org/10.1007/978-981-16-0642-7_4

ABS	Acrylonitrile butadiene styrene
TMP	Thermo Mechanical Pulp
WF	Wood Flour
WPC	Wood Plastic Composite
EBM	Electron Beam Melting
SLS	Selective Laser Sintering

1 Introduction

The additive manufacturing (AM) process is a material addition process by layer by layer with the help of numerical control of CAD data. AM process is divided into three categories based on processing material types such as solid, liquid, and powder. FDM is a solid based AM process, and it uses thermoplastics as feedstock material. Recently fiber-reinforced composites are used as feedstock material for FDM based AM process. Fiber-reinforced polymer composites are applied wide range in automobile, construction, etc. However, conventional composite manufacturing methods require molds. The advantage of the AM process eliminates additional tools such as molds, fixtures, jigs. Fabrication of polymer composite feedstock for the FDM based AM process is done with the material extrusion process. Unlike the traditional subtractive manufacturing method, AM allows users to fabricate prototypes or functional products with complex shapes at a low manufacturing cost [13]. Recent studies show that pure polymeric based feedstocks show lesser strength compared to composite parts. So, fiber-reinforced polymer composite feedstocks are gaining attention in the AM process with enhanced durability. From this, bio-based polymer composites are sustainable and had reasonable strength compared to pure polymer materials. The right combination of polymers and bio-based reinforcement with an enhanced life span of product fabrication is achievable using the FDM-based AM process [5]. This chapter is presenting a review of biocomposite filaments and mechanical properties of the FDM based AM process. This chapter is organized as follows, review methodology, an overview of the FDM process, fabrication methods of composite filaments for the FDM process, literature study, and discussion.

2 Review Methodology

In the last decades, much researches have been conducted to improve the strength of FDM products. In this regard, analyses developed composites based filaments (bio-based and synthetic) for the FDM process. In this chapter, only bio-based biocomposite filaments were considered for review. In this regard, thirteen articles were found in the FDM based AM process related to bio-composite filaments.

3 Fused Deposition Modeling (FDM)

FDM is one AM technique that converts 3D CAD data into 3D products. It develops 3D products by the addition of materials by layer by layer. FDM based AM process uses thermoplastics as a feedstock material for product development. FDM is one of the cheapest AM processes compared to other methods such as Electron Beam Melting (EBM), Selective Laser Sintering (SLS), etc., FDM is the most common 3D printing technology and has excellent reliability, affordability and operates with minimal waste [11]. FDM has wide popularity in industry due to ease of operation methods. Enterprises are using FDM for prototyping making as well as for real-time product development. FDM eliminates additional tools such as jigs and fixtures. FDM process consists of several working parts such as filament feeder, printing head, build time, control panels, etc.

The critical process parameters are print speed, print direction (45/-45), build orientation, printing temperature, raster angle, raster width, infill density, and infill pattern. This thermoplastics feedstock material is called a filament, which is commercially available in 1.75 and 3 mm diameter. Acrylonitrile butadiene styrene (ABS) and Polylactic Acid (PLA) are widely used materials. Recently fiber-reinforced polymer composite feedstocks are gaining more importance in many fields to improve the FDM product's strength. Many studies have been done with natural (plant fibers) and synthetic fiber (glass fiber, carbon fiber, etc.) to improve FDM products' strength. The natural fibers based composites are eco-friendly and had lesser cost compared to synthetic fiber-based polymer composite. Natural fibers such as sisal, jute, hemp, bamboo, and wood fibers are derived for nature and reinforced with natural polymers (PLA, TPS, etc.) to improve FDM's sustainability products. Industries are utilizing bio-based composites in their products [5].

4 Fabrication Methods of Composite Filaments

A commonly known filament fabrication method is the extrusion process. Graduated pellets are dropped into the hopper and allowed to pass the screws in the barrel. The melting temperature is fixed in heating elements, and pellets are melted and drawn into wire form. For the filament extruding process, single screw and twin-screw extruders are widely used. Figure 1 depicts the twin-screw extruder setup for the filament extrusion process (CIPET Chennai). Figure 2 illustrates the CAD model of a single screw extruder.

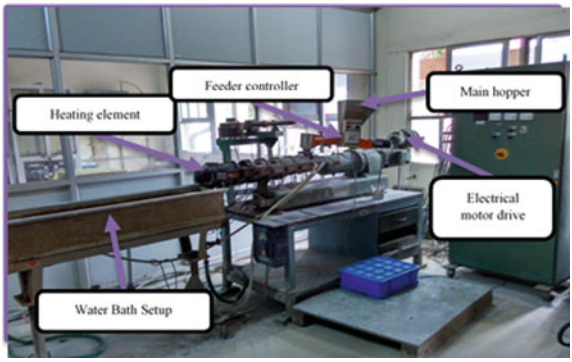

Fig. 1 Twin screw extruder setup

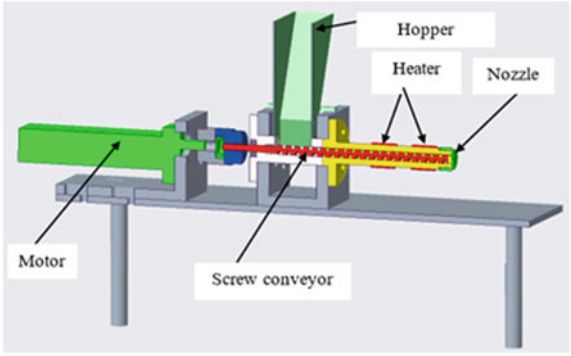

Fig. 2 CAD diagram of single screw extruder

5 Literature Study

Le Duigou et al. [7] developed a wood fiber-based biocomposite and studied mechanical properties. PLA and wood fiber were used to fabricate the biocomposite filament to develop a bilayer microstructure. Wood fiber filled PLA filament with 2.85 diameters is used to print the samples at longitudinal, transverse orientations with 100, 200, 300% of printing width. Compressed filaments are used to compare the hygroscopic and hygromorph dynamic properties of the filament, and printed samples were observed for the water intake test. 100% PLA is compared with 10 to 20% of wood fiber-based composite. Infill density of 100% was set, standard 0.4 mm nozzle is used by varying the width. The thickness of the sample is 3 mm and print speed of 18 mm/s and printed with Longitudinal direction. Compressed filament shows similar tensile properties in transversely printed samples. SEM image shows 16.5% porosity in filament was as after printing porosity at longitudinal direction is high than the transversely printed samples. This is due to close packing in 90 degrees and quickly pass. Mechanical properties strongly depend upon the print orientation

and printing width. The water intake and swelling increases depend upon the diameter and porosity. This is because of the anisotropic hygro elastic property of the composite.

Tao et al. [11] fabricated wood flour based biocomposite for 3D printing applications, where PLA and wood flour (WF) based biocomposite filament is examined for physical and mechanical properties. PLA with 5% wood flour filament is prepared, and mechanical, thermal properties of 3D printed samples were considered. The wood flour (mean particle size of 14 μm) contains 95% of PLA and compared with 100% PLA. 100% infill density is maintained for all samples. The default nozzle diameter of 0.4 is used for printing the samples. Microstructure analysis shows a clear gap in certain areas between interfaces because of the hydrophobic and hydrophilic behavior of the PLA and WF. The thermal degradation of the material at starting is decreased slightly, and the residual ratio is increased since wood is added maximum decomposition takes place at 330 °C. DSC results show that there is a decrease in glass transient temperature from 65 to 67 °C due to poor compatibility of WF and Clear gaps are Observed in certain places and weak bonding between wood and PLA, which lowers the strength. XRD results show that the interface compatibility is low between the composites. Tensile stress is increased as strength is dropped compared to neat PLA.

Stoof et al. [10] developed PLA, Hemp, and Harakeke based biocomposites using the FDM based AM process and studied mechanical properties of fabricated composites. Chemical treated hemp, harakeke fiber mixed with PLA, and printed with 1 mm nozzle. Surface and mechanical properties were investigated for fabricated biocomposites. Fiber content added with varying percentages of 10, 20 and 30 and PLA with a weight ratio of 90, 80, 70%. Filaments were fabricated with a diameter of 3 mm.

100% infill density with concentric layer setting is used to print the sample. 1 mm layer thickness is maintained with 1 mm nozzle. Hemp fiber is treated with 5% NaOH and harakeke fiber with 5% NaOH and 2% sodium sulfite and alkali solution for better digestion to reduce the dimension of the fiber. The optical microscopic image confirms the reduction of diameter after ingestion. From SEM analysis, it is observed that pores and fiber pull out was observed, resulting in poor adhesion between fiber matrix, which also reduces the strength of the printed part 30 wt% and has a weak surface finish compared to other composition. Tensile strength of the harakeke with 20% fiber content and 10% hemp fiber had good tensile strength compared to neat PLA. Young's modulus of harakeke fiber tends to increase with an increase in fiber content because of the fine fibers. Interline voids and interlayer voids were noted in the fracture surface reason is an insufficient fusion of layers.

Kariz et al. [5] investigated mechanical and rheological property for wood-based biocomposite. Different weight ratios of wood from 0 to 50% was used to study the mechanical and rheological property fabricated bio-composite material. Beech Wood particles with even particle size are mixed with PLA to manufacture a 1.75 mm diameter wood composite filament. The fabricated filament was compared with neat commercial PLA and ABS filament. The biocomposite composition is 10/90, 20/80, 30/70, 40/60, 50/50% of wood to PLA, respectively. Fabricated filament diameters are 1.45–1.75 mm. An increase in wood content decreases the density of the filament. The

results show that high wood content produces inferior parts due to uneven filament diameter, and nozzle clogging was observed.

The tensile strength of the part is increased slightly with 10% composition, and resistance is dropped with higher ratios. Due to the weak bonding of wood particles, durability is reduced. When Increasing the wood percentage, it is observed that voids are increased, and poor surface finish is observed. The young's modulus of the material is low compared to neat PLA, and 33% is decreased. Also, 10–20% of after wood content shows better young's modulus than neat PLA, and no significant change is observed in the glass transient temperature of the material between 65 and 66 °C.

Filgueira et al. [4] fabricated PLA based Thermo Mechanical Pulp (TMP) fibers composite filaments and tested for physical and mechanical properties. Raw TMP and two differently (octyl gallate (OG) lauryl gallate (LG)) chemically treated fibers with 10, 20 wt% are reinforced with PLA to manufacture a bio-based filament of diameter 2.2 ± 0.1 mm. Three fibers treated octyl gallate OG treated, and LG treated were mixed with 10 and 20% weight ratio to PLA, forming six different samples and neat PLA is used for comparison. A nozzle of diameter 0.4 mm was used to print the samples, and 15 mm/s print speed was set for all samples. TMP fibers were milled to a 30 mesh size, and an average fiber length of TMP and ground TMP 1.5 and 0.4 diameter of 33 and 38 μm is achieved.

OG and LG Chemical treatment changed the fiber surface property from hydrophilic to Hydrophobic, which reduces the water-absorbing capacity of the composites. Untreated TMP fibers show the high hydrophilic property in the water contact angle test. A water absorption study shows that untreated fiber absorbs more water, and OG treated 10% fiber has low intake. However, 20% of fiber samples exhibit secondary water absorption compared to 10%, which leads to micro cracks. With 20% of OG treated fibers, PLA had good mechanical strength compared to other compositions. That is, modified fiber promotes better adhesion with the PLA matrix, and also the strength of the composite is low compared to the plain PLA. This is due to porosity and weak adhesion of fibers in the filament. Fibre agglomeration and the protrusion are noticed in the fractured area, which shows the poor distribution of fibers.

Liu et al. [8] fabricated PLA and sugarcane bagasse fiber-based biocomposites in FDM and examined for morphological, mechanical, and thermal properties. Raw sugarcane bagasse fiber (SCBF) and chemical treated SCBF mixed with PLA and printed with different raft angle using a 0.6 mm diameter nozzle. Pure PLA is compared by varying the fiber to PLA ratio by 3–15%. 100% infill density with different orientation of printing was done. 0.4 mm layer thickness set for all the parts and print speed of 40 mm/s.

FTIR results show there is no change in before and after chemical treatment of cellulose peaks were as hemicellulose and lignin completely disappeared. XRD shows there is no change in the crystalline morphology of the cellulose. From SEM studies, it is found that lots of impurities and debris at the surface of the fibers before treated. Fibers show clear texture on the surface; deep interline voids and porosities are noted in SCBF/PLA than RSCBF/PLA composite. The chemical treatment

removes the organic compounds and impurities, thereby modifying the fiber's surface property, which increases the strength when compared to the raw fiber default voids during the FDM process, and reduced interfacial filler matrix reduces the strength. When compared to the neat PLA whereas 6-wt% has prominent tensile strength, out of different orientations. Default cross parallel and vertical orientation give the worst strength. However, cross and parallel printing obtain an optimum value due to the presence of interline, interlayer voids, and pulled out fibers, which causes poor flow. Thermal properties show that SCBF is capable of promoting the crystallization of PLA.

Martikka et al. [9] evaluated mechanical properties for wood plastics composite. PLA and wood fiber composites are fabricated, and mechanical properties were analyzed and compared with pure PLA. Pure PLA and wood composite (30% WF and 70% PLA) are compared. Density, Tensile, impact tests were carried out to check the mechanical properties of the printed samples and also compared with pure PLA. 100% PLA is compared with the fiber weight content of 30–70% 40–60% wood fibers with 1.75 mm filament diameter. Infill density of 23, 55, 100% with a shell thickness of 0.4 mm is printed. 0.4 mm layer thickness was set with a nozzle diameter of 0.5 mm is used to print the samples. Print speed is set to a minimum of 1 mm/s. The density of the WF filament is estimated as 0.2 g/cm density of the printed WF samples shows decreases in density with an increase in infill density. Charpy Impact results show that the lower percentage of wood fiber increases the impact strength of the sample were as higher the infill reduces the impact strength.

Coppola et al. [2] investigated the mechanical and rheological factors for PLA and hemp-based composites. PLA with hemp is used as a filler for FDM, and mechanical and rheological experiments were conducted. PLA with different hemp compositions was fabricated with a 2.85 mm diameter. The weight percentage of hemp is 1, 2 and 3% and mixed with PLA with a weight percentage of 99, 98 and 97% and compared with pure PLA. A layer thickness of 0.1 mm, nozzle temperature of 180 °C, and a print speed of 20 mm/s for all samples. The rheological analysis shows there is a decrease in complex viscosity at the high fiber content. Tensile strength and elastic modulus increase at high fiber content when compared to neat PLA.

Yang [13] studied physico-mechanical properties for unidirectional wood-based biocomposite using FDM. PLA and wood fiber-based biocomposite filament fabricated with the reinforcement of 40 wt% of wood. The Physico-chemical and mechanical properties were investigated for fabricated biocomposites. The fabricated filament was printed with different temperatures. A commercially available 60% PLA and 40% Cedar fibers filament are used for comparison. Infill percentage of 100 is set for all the printed samples, and 0.2 mm layer thickness was established with a nozzle diameter of 0.4 mm, and 30 mm/s print speed was set for all printed samples.

Thermal property study shows that the degradation of wood fibers occurs at 200–230 °C, and the weight loss was high above 240 °C. Physical properties show that there is a change in color as the temperature increases; also, there is a change in weight with an increase in temperature, but volume remains the same; this is due to the increase in viscosity. The water absorption of the samples varies between 2.6 and 3.1%, and the thickness of the swelling rate ranges from 0.8 to 1.1%. It is mainly due

to the hydrophilic nature of the wood fibers and the kind of gap present during the FDM process. Mechanical properties show a decrease in tensile with an increase in temperature due to the formation of acidic products at high temperatures. Good fiber bonding is noticed between PLA and wood fibers at high temperatures. However, because of thermal degradation, the strength of the thread is low.

Le Duigou et al. [6] fabricated flax fiber-reinforced biocomposites by varying percentages of fiber content. PLA and continuous flax fiber filament are fabricated and analyzed for mechanical properties. Continuous flax fiber composite filament is manufactured by twisting the yarn with PLA and printed with 1.8 mm nozzle diameter at the longitudinal and transverse direction to check the mechanical properties and porosity content. 100% infill density is printed in the longitudinal and transverse rectilinear pattern. The layer thickness of 252 ± 22 μm is observed in microstructural analysis for the samples. The print speed of 6 mm/s is set for all the prints. Irregular filament cross-section and dispersion are found in the microstructural analysis and low porosity within the fibers. The deviation of fiber is observed in the cross-section of the filaments. In print parts, reinforcement is homogeneous, and compression of the print reduces the thickness and increase the width there by the porosity of the region is reduced and also regular as well as overlapping loops are observed in print due to mismatch in nozzle and filament diameter. The mechanical property of continuous flax fiber PLA has gained 4.5 times of tensile strength and tensile stiffness compared to the neat PLA.

Badouard et al. [1] studied the mechanical properties of fully compostable flax reinforced composite. PLLA, PBS, PBAT, and flax fibers are mixed at different compositions and tested for printing. PLLA, PLLA/PBS, PBAT flax fibers, and shives are mixed with 0, 10, 20, 30-wt%, and extruded with 2.85 diameter filaments. Samples printed with 1 mm nozzle and compared with Injection Moulded (IM) samples. The composition mixed proportion are, PLLA with 10% flax fibres, PLLA50% PBS 50%with 10% flax fibres, PLLA 50% PBS 50% with 10% flax shives, PBAT 90% with 10% flax fibres, PBAT 80% with 20%flax fibres, PBAT 70% with 30% flax fibres. 100% infill density is set to all samples and compared to IM parts. They are printing speed for all samples varied between 0.8 m/min to 1.5 m/min. Particle size analyzer shows that Flax shives have a mean diameter of 162 μm were as flax fiber has a different peak of 20, 125, and 650 μm. Processing of filament with 10% composition is easy compared to high fiber content 20, and 30% shows poor flow resulting in sharkskin phenomenon since pores were present in the 3D Printed parts. 3D printed parts strength is low when compared to the IM parts.

Depuydt et al. [3] developed and analyzed characterization for bamboo and flax fiber-based biocomposite. PLA, bamboo, and flax fibers are mixed along with two types of plasticizers, and physical, thermal, and mechanical were found. Bamboo fibers were measured by image processing algorithm before and after compounding to examine the fiber changes during extrusion and compared with the commercial PLA/bamboo fiber. The filament composition of 75% PLA and 10% plasticizer cPLA1 and cPLA2 with 15% fibers were mixed to form a 3 mm filament. Plasticizer had a good impact on Glass transient temperature, and the tensile strength of

the composite is low compared to neat PLA. However, PLA with flax fiber had good strength when compared to bamboo fiber composite.

Xiao et al. [12] developed sustainable biocomposite using PLA and hemp. PLA Hemp hurd (HH) is used as filament for FDM. Rheological, mechanical, thermal, and morphological tests were conducted to study the properties of the material 87 and 13% of PLA/PBAT with ethylene-methyl acrylate-glycidyl methacrylate terpolymer (EGMA) used as toughening agent. Printed parts compared with injection-molded samples. Hemp Hurd with 10, 20, 30 and 40 wt% is mixed with PLA/PBHAT and using EGMA as a compatibilizer pure PLA/PBHAT/EGMA with 87/13 weight percentage is mixed, and the filament is fabricated with a diameter of 1.75 mm. Infill density of 100% and the layer thickness of 0.15 mm is set to all the samples. An average print speed of 60 mm/s is set to print the specimens. Rheological behavior shows slight shear thinning behavior in the examples, because of weak interparticle interaction in lower HH percentage. The crystallinity of the polymer increased with an increase in HH percentage, and uniform distribution of fibers is observed in SEM with no particular orientation. Agglomeration of HH particles is seen at a higher rate of the polymer matrix. SEM images show brittle fracture without any plastic deformation in injection molded parts. FDM parts have higher impact strength over injection molded parts on impact strength. Dimensional accuracy and roughness of the filament are increased with an increase of HH in composite samples. Table 1 represents, list of materials used, and machine type used for filament extrusion of previous studies.

6 Discussions

Fused deposition modeling is one of the AM processes and widely used due to ease of operation. With less working skills using the FDM based AM process can develop new products with lesser cost. Thermoplastics are used as feedstock material to establish 3D products. Nowadays, composite-based materials are available for the FDM process with enhanced strength. Fiber-reinforced composite filaments are gaining considerable attention among researchers and industrialists and using biopolymers and bio-based materials for reinforcing, environmentally friendlier, and economically beneficial for the product developers. Industries and researchers are trying to improve the quality and reliability of composite filaments application in many fields. From a literature study, it is found that pure polymer feedstocks show lesser mechanical strength compared to composite filaments. There are many difficulties observed from the literature survey during composite filament fabrication. Such as Surface quality, improve fiber orientation, fiber pull out, voids, uneven filament diameter, etc. When using fibers in composites, fiber orientation is essential for the final product properties [5]. Mechanical properties strongly depend upon the print orientation and printing width [7]. The following inferences are derived from the literature study.

Table 1 Literature analysis of previous studies

S. No.	Authors	Material		Machine type
		Polymer	Fibres	
1.	Yang [13]	PLA	Cedar fibres	Commercial filament
2.	Kariz et al. [5]	PLA	Beech wood (*Fagus sylvatica* L.)	Single screw extruder
3.	Tao et al. [11]	PLA	Aspen wood flour	Single screw extruder
4.	Le Duigou et al. [7]	PLA, PHA	Wood fibre	Commercial filament
5.	Stoof et al. [10]	PLA	Hemp fibre	Twin screw extruder
6.	Filgueira et al. [4]	PLA	Spruce thermo mechanical pulp fibres	Single screw extruder
7.	Liu et al. [8]	PLA	Raw Sugarcane bagasse fibre (RSCB) and Sugarcane bagasse fibre (SCB)	Twin screw extruder
8.	Martikka et al. [9]	PLA	Wood fibres	Commercial filament
9.	Coppola et al. [2]	PLA	Hemp powder	Twin screw extruder
10.	Duigou et al. [7]	PLA	Continuous flax fibre	Extrusion coating technique
11.	Badouard et al. [1]	PLLA, PBS, PBAT	Flax fibres and Flax shieves	Twin screw extruder
12.	Depuydt et al. [3]	PLA	Bamboo and Flax fibres	Twin screw extruder
13.	Xiao et al. [12]	PLA, PBAT	Hemp hurd	Twin screw extruder

7 Inferences Based on Fibre Content

Sisal, jute, hemp, and wood fibers are widely used bio-based materials to make composite materials. The purpose of alternate material like composite is used to enhance the strength of the final product. There is some limitations observed form the literature during part fabrication and filament fabrication. Uneven filament diameter mostly occurs in composite filaments due to inferior fibers distribution and fibers present in the top surface of the filament. Irregular flow of polymer is disturbed due to various parameters such as clogging, temperature, etc. Poor distribution of fibers in the filament is based on the use of compatibilizer and coating techniques,

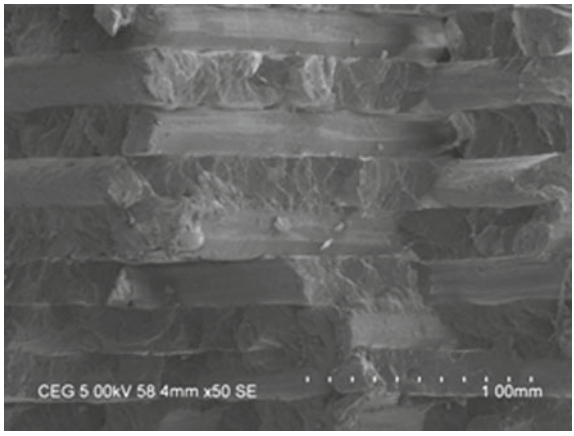

Fig. 3 SEM image of layer arrangement of FDM sample

leading to the formation of a fiber cluster in the matrix. Figure 3 represents the layer arrangement of the FDM component in the SEM study. The layer is arranged 45/-45° orientation.

Uneven l/d ratio of fibers causes poor sieving and grinding of fibers and produce clogging in the nozzle and affects the surface finish of the part. Weak bonding of fibers with polymer matrix: fibers won't attach to the polymer blend that is due to the smooth surface of fibers pretreatment will improve the adhesion. Agglomeration of fibers is a group of fibers that get deposited in a particular area resulting in fractured surfaces. The component color becomes dark when the extrusion temperature is increased [13]. Layer adhesion is defined as the bonding of one layer above the other it mostly depends upon the temperature and contact surface area between the layers. An increase in fiber content leads to poor adhesion in layers, and the mechanical party is affected [5, 9].

8 Inferences Based on Voids

Voids are unoccupied space in a polymer matrix in default. FDM produces voids since it's a layer by layer manufacturing. Interlayer voids are the gap between the layers; these occur due to weak fusion of layers. Interline or intralayer voids are present inside the layer (cross-section of the layer). Interfacial voids are often happening due to thin layer deposition that is due to the uneven flow of polymer. Voids are a significant problem in composite material manufacturing as well as product manufacturing. During composite filament manufacturing porosity, voids are observed in the composite filaments. Voids may be presented inside or surface of the filament.

Figure 4 depicts an SEM image of composite filament, and it is found that uneven surface and protrusion are observed in the outer side of the filament. Some fibers are come out from the filament during the extrusion process, and the protrusion is found

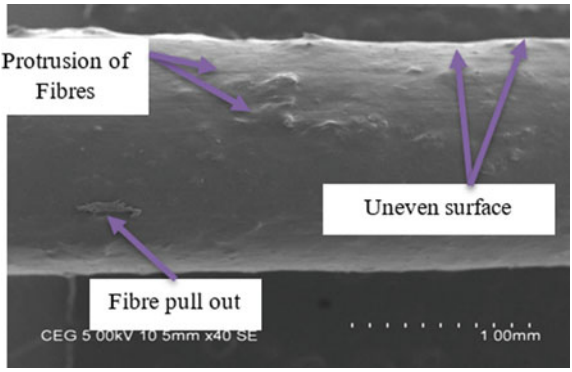

Fig. 4 SEM image of bio composite filament

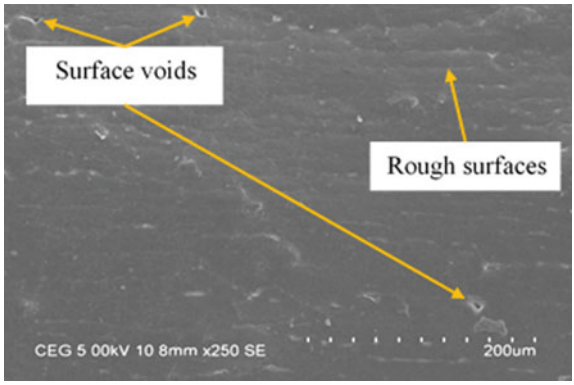

Fig. 5 SEM image of filament

at the surface of the filament. The protrusion may lead to making nozzle clogging. Figure 5 depicts surface voids in the surface of biocomposite filament. Kariz et al. [5] study observed that uneven surface and protrusion cause nozzle clogging. Nozzle clogging occurs due to fiber agglomeration irregular diameter of the filament and low melting of filament. Fiber pullout is the overhanging of fiber in the filament or print surface that is observed in fiber composites due to the weak binding of fiber with polymers. Due to the percentage of wood content increase in the filament, voids are generated during filament fabrication. The presence of voids in filament causes weak strength in mechanical property and increases voids in fabricated products [5, 10].

9 Inferences Based on Chemical Treatment

Chemical treatment is used to improve the fiber strength and to remove unwanted impurities from the fibers. Chemical treatment modifies the fiber's surface and

enhances the strength compared to raw fiber. At the same time, chemical treatment removed the organic component and impurities from the fiber [8]. From Filgueira et al. [4] study, untreated fibers absorb more water in water absorption study. There is no change before and after the chemical treatment of cellulose peaks in the characterization study [8].

10 Conclusions

This chapter summarized fused deposition modeling biocomposite filaments and their mechanical property. Many authors focused on enhancing the mechanical properties of composite filaments. The following inferences are observed from the review.

- Mechanical property is decreasing when fiber content increasing.
- Due to an increase in fiber content layer adhesion problem is occurred.
- The uneven surface of the filament, nozzle clog is observed.
- Voids are observed inside and outside of the filament.
- Due to voids presence, fabricating parts also have voids.
- Fiber pulls out are observed during the fabrication of filament.
- The chemical treatment removes organics components from fibers.

References

1. Badouard, C., Traon, F., Denoual, C., Mayer-Laigle, C., Paës, G., Bourmaud, A.: Exploring mechanical properties of fully compostable flax reinforced composite filaments for 3D printing applications. Ind. Crops Prod. **135**, 246–250 (2019)
2. Coppola, B., Garofalo, E., Di Maio, L., Scarfato, P., Incarnato, L.: Investigation on the use of PLA/hemp composites for the fused deposition modelling (FDM) 3D printing. In AIP Conference Proceedings, vol. 1981, No. 1, p. 020086. AIP Publishing LLC (2018, July)
3. Depuydt, D., Balthazar, M., Hendrickx, K., Six, W., Ferraris, E., Desplentere, F., Van Vuure, A.W.: Production and characterization of bamboo and flax fiber reinforced polylactic acid filaments for fused deposition modeling (FDM). Polym. Compos. **40**(5), 1951–1963 (2019)
4. Filgueira, D., Holmen, S., Melbø, J.K., Moldes, D., Echtermeyer, A.T., Chinga-Carrasco, G.: Enzymatic-assisted modification of thermomechanical pulp fibers to improve the interfacial adhesion with poly (lactic acid) for 3D printing. ACS Sustain. Chem. Eng. **5**(10), 9338–9346 (2017)
5. Kariz, M., Sernek, M., Obućina, M., Kuzman, M.K.: Effect of wood content in FDM filament on properties of 3D printed parts. Mater. Today Commun. **14**, 135–140 (2018)
6. Le Duigou, A., Barbé, A., Guillou, E., Castro, M.: 3D printing of continuous flax fibre reinforced biocomposites for structural applications. Mater. Des. **180**, 107884 (2019)
7. Le Duigou, A., Castro, M., Bevan, R., Martin, N.: 3D printing of wood fibre biocomposites: from mechanical to actuation functionality. Mater. Des. **96**, 106–114 (2016)
8. Liu, H., He, H., Peng, X., Huang, B., Li, J.: Three-dimensional printing of poly (lactic acid) bio-based composites with sugarcane bagasse fiber: effect of printing orientation on tensile performance. Polym. Adv. Technol. **30**(4), 910–922 (2019)

9. Martikka, O., Kärki, T., Wu, Q.L.: Mechanical properties of 3D-printed wood-plastic composites. In: Key Engineering Materials, vol. 777, pp. 499–507. Trans Tech Publications Ltd. (2018)
10. Stoof, D., Pickering, K., Zhang, Y.: Fused deposition modelling of natural fibre/polylactic acid composites. J. Compos. Sci. **1**(1), 8 (2017)
11. Tao, Y., Wang, H., Li, Z., Li, P., Shi, S.Q.: Development and application of wood flour-filled polylactic acid composite filament for 3D printing. Materials **10**(4), 339 (2017)
12. Xiao, X., Chevali, V.S., Song, P., He, D., Wang, H.: Polylactide/hemp hurd biocomposites as sustainable 3D printing feedstock. Compos. Sci. Technol. **184**, 107887 (2019)
13. Yang, T.C.: Effect of extrusion temperature on the physico-mechanical properties of unidirectional wood fiber-reinforced polylactic acid composite (WFRPC) components using fused deposition modeling. Polymers **10**(9), 976:1–11 (2018)

Experimental Evaluation of Laminated Carbon Composite Step Lap Repair Through Static and Fatigue Compression Loading

H. Sreedhara, H. Dineshkumar, and V. R. Ranganath

Abstract The static compression test is performed on various carbon fiber reinforced plastic (CFRP) epoxy-based laminate panels manufactured with the vacuum enhanced resin infusion technology (VERITy) process. These tests are conducted for establishing the compression strength and evaluation of the step-lap repaired method effectiveness. The barely visible impact damage (BVID) is simulated experimentally by impacting with low energy. The response of the pristine, impact-damaged, and step-lap repaired composite panels are captured experimentally through the online strain measurement during the testing at various locations. The predicted strain response from the finite element analysis is validated with that of the experiment for all of the specimen configuration. Reasonable good agreement is observed between the predicted and the experimental strain values in terms of their magnitude and the trend. It is observed that both of the strength and the stiffness are regained in the composite panels after the step-lap repair scheme is implemented. Constant amplitude fatigue behavior of pristine and step-lap repaired composite panels are tested under compression-compression fatigue loads. It is observed that the stiffness of both of these panels is not significantly degraded over a testing period of million fatigue cycles.

Keywords Step-lap composite repair · Verity process · Static compression · Constant amplitude fatigue · Finite element analysis · CFRP

H. Sreedhara (✉)
Knowledge and Technology Management Division, CSIR-National Aerospace Laboratories, Bengaluru, Karnataka, India
e-mail: hsreedhara@nal.res.in

H. Dineshkumar
Department of Aerospace Engineering, Indian Institute of Science, Bengaluru, Karnataka, India
e-mail: harursampath@gmail.com

V. R. Ranganath
Structural Technologies Division, CSIR-National Aerospace Laboratories, Bengaluru, Karnataka, India
e-mail: ranga.xnal@gmail.com

S. Mavinkere Rangappa et al. (eds.), *Fracture Failure Analysis of Fiber Reinforced Polymer Matrix Composites*, Engineering Materials,
https://doi.org/10.1007/978-981-16-0642-7_5

1 Introduction

The use of advanced composite materials, and in particular of CFRP material, has become a common factor even in the conservative, economy driven design environment of today's civil aircraft. Just like metallic materials, fiber-reinforced composite materials are hampered by particular inherent weaknesses, which must be understood and accounted for in the design of a structure. The dominant gap of this layered material configuration is the impact damage, introduced accidentally during the manufacture, the operation, or the maintenance of the aircraft.

In the presence of any such impact damage in the structure made up of the composite material, when it is subjected to the in-plane compression loads, the damage may lead to catastrophe depending on the nature and extent of the damage and also its location [1].

In the case of the repairable damages, it is important to develop suitable repair methodology depending upon the extent, its location, and the accessibility of the damaged part in the structure. A damaged part of the structure is repaired to restore the original strength and stiffness. It is also necessary to establish the reference values for the original strength and stiffness of the similar healthy (pristine) structure or panel without any damage or repair. The data on the pristine panel serves as reference values of strength and stiffness for assessing that of the repaired panel [2].

The major area of the impact study involves BVID, which is the measurement of a property after impact and the impacting of the stresses bodies. BVID occurs when an object, such as a tool, is dropped accidentally onto a composite structure [3]. A thin shell-like, highly stressed aircraft component such as composite wing is particularly vulnerable in this regard. The danger is that the damage is so slight it is not readily noticed by the naked eye, but nevertheless, there is a reduction in the load-carrying capacity of the component. Since many of the crucial aircraft components made up of composite materials such as CFRP are stressed in compression, it is important to evaluate the compression strength after the impact [4].

To repair the dominant weakness of this layered material configuration is impact damage, introduced accidentally during manufacture, operation or maintenance of the aircraft leads to delamination between the layers in addition to matrix cracks and fiber fractures and simultaneously to increase the load-carrying capacity of the CFRP specimen by improving the material property of the impacted zone.

Our main aim of the present study is to repair the BVID created by impacting the specimens with an impactor at low velocity. The impactor mass and height of drop are chosen to result in an impact energy of 10 J, which would produce a BVID for that laminate.

In order to understand the compression behavior completely, it is important to evaluate the compression behavior [5] of the laminates with and without impact damage and then evaluate a suitable repair method in order to recover the desired strength and stiffness [6]. Further, it is important to develop a suitable numerical model simulating [7] the impact damage and repair method to understand the state of the stress and strain for assessing the effectiveness of the repair technique [8].

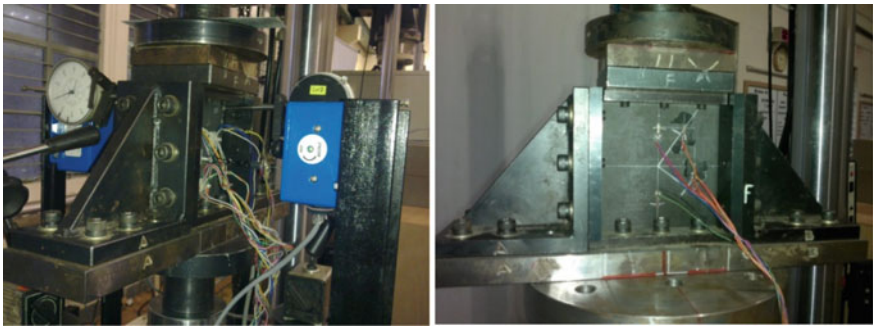

(a) With complete set-up (b) Showing panel

Fig. 1 Experimental set-up for the static and fatigue compression test on the different test panels

Hence the present study is towards the experimental and numerical evaluation of the compression behavior [9] of the laminates are made up of CFRP material fabricated with the VERITy process [10].

2 Experimental Set-Up

In a compression test, it is important to prevent or eliminate the global buckling so that the test panel experience the compression load only. Buckling in the compression test leads to significant errors in the assessment of the compression strength of the test panel.

Figure 1 shows a photograph of the experimental set up along with the test panel in a computer-controlled servo-hydraulic test machine.

3 Test Fixture

The compression test fixture in accordance with the ASTM standard, ASTM D7137 (2007) [11, 12] is shown in Fig. 2. The test fixture consists of left side knife edges, right side knife edges as well as the top-loading block which has two flat edges for holding the top portion of the test panel. Each of these knives and/or flat edges are adjustable independently to align the pristine test panel in the loading line and/or loading plane. The left side and right side knife edges together serve as an anti-buckling guide mechanism to prevent global buckling of the test panel during the compression testing. Flat edges of the top-loading block help in holding the top edge of the test panel during the compression testing and also responsible for keeping the loading plane and/or axis in-line with the mid-plane of the test panel.

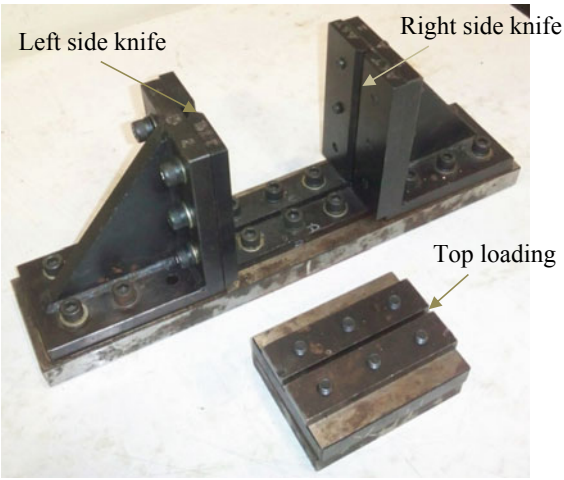

Fig. 2 Photograph showing the details of the test fixture

Similarly, the left side and the right side knife edges of the anti-buckling guides are required to align with the mid-plane of the test panel synchronously. In addition to this, the top-loading block also needs to be synchronous with the anti-buckling guides.

4 Test Matrix and Specimen

The material used for the current study is a CFRP with epoxy-based composite laminate produced by the VERITy process.

In this process, the unidirectional (UD) carbon (Hex*force*-G0827-S1040-HP03-1F) fabric of size (600 × 400) mm^2 is laid up in quasi-isotropic layup sequence on a flat metallic mold, and the epoxy resin (Epolam 2063) is infused into it under vacuum, followed by curing. The properties of this material are given in Table 1. The resulting laminate is cut into the required size for various specimen configurations such as pristine (without damage), impacting (with impact damage), and step-lap repaired test panels and a typical size of each test panel is illustrated in Table 2.

Table 1 Typical mechanical properties of the CFRP material

Modulus in normal directions (GPa)			In-plane shear modulus (GPa)	Transverse modulus (GPa)		Poisson's ratio		
E_{11}	E_{22}	E_{33}	G_{12}	G_{23}	G_{13}	υ_{12}	υ_{23}	υ_{13}
130	8	8	3	3.5	3	0.32	0.27	0.30

Table 2 Specification of the test panel for pristine, impact damaged, and repaired configurations

Test panel length (mm)	150
Test panel width (mm)	150
Test panel thickness (mm)	4.20
No. of plies	24 layers
Layup sequence (angle in degrees)	Quasi-isotropic $[(45, 0, -45, 90)_3]_s$
Ply thickness (mm)	0.175

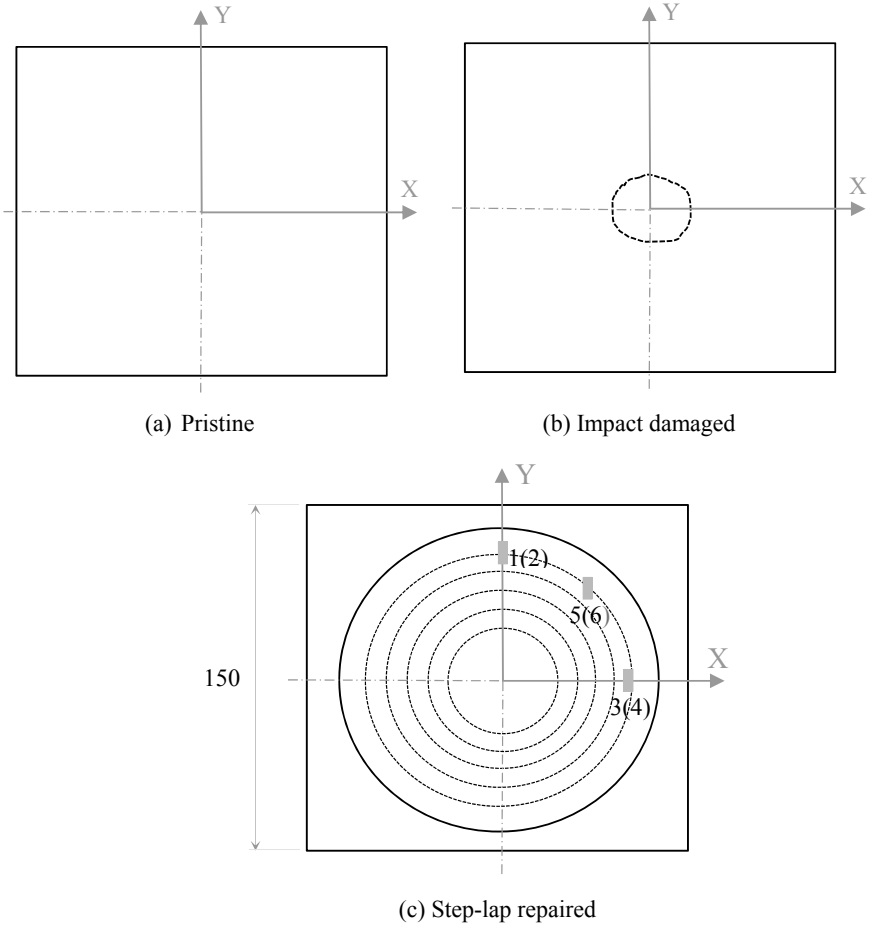

Fig. 3 Schematic of the compression test panel configurations

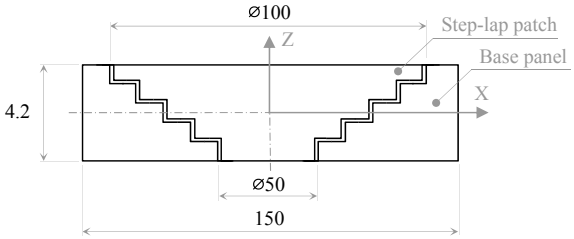

Fig. 4 Schematic of a cross-section of the step-lap repaired test panel

Figure 3 shows a schematic diagram of typical test panel configurations such as pristine, impact-damaged, and step-lap repaired laminates, and the positive Y-direction indicates the direction of the 0° for the plies. The direction of the compression load application is also in the Y-direction. A typical cross-sectional view of the step-lap repair indicating various steps from diameter 50 mm to diameter 100 mm in 5 steps, as shown in Fig. 4.

Each of these steps is having an incremental diameter of 10 mm in diameter with the layer of epoxy around 0.175 mm in each step between the base panel and step-lap repair patch. The coordinate locations of each of the six strain gauges from G1 to G6, as shown in Fig. 3c, are tabulated in Table 3 for pristine, impact-damaged, and step-lap repaired laminates. The origin of the Cartesian coordinate system is located at the center of the test panel laminate, as shown in Figs. 3 and 4.

Impact damage is induced at the center of the pristine test panel subjected to a low-velocity impact with an impact energy of 10 J. While impacts on the test panel, adequate care is taken to prevent multiple impacts on the same laminate through an appropriate anti-rebounding system. The extent of the impact damage is quantified using non-destructive techniques such as Ultrasound C-scan and A-Scan. The ultrasound signal is being attenuated at the location where there is impact damage compared to that of the rest of the test panel laminate [13]. The size of the impact damage is clearly visible as a white spot at the center of the test panel on either side (front and rear) in a typical C-scan image as shown in Fig. 5.

Table 3 Location of the strain gauges on various compression test panels

Strain gauge number	Strain gauge notation	Coordinate location in mm (origin is at the center of test panel)		
		X	Y	Z
1	G1	0	45	2.10
2	G2	0	45	− 2.10
3	G3	45	0	2.10
4	G4	45	0	−2.10
5	G5	30	30	2.10
6	G6	30	30	−2.10

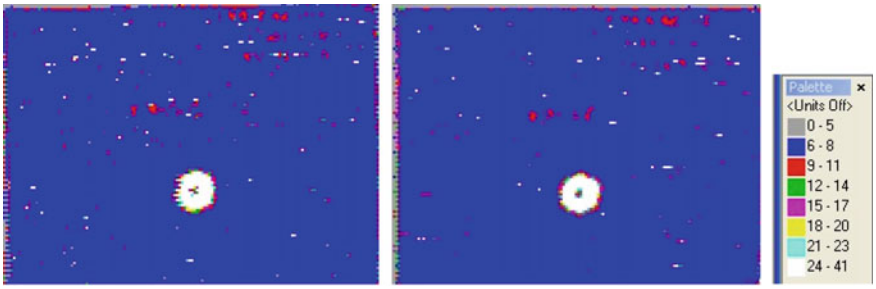

(a) Front side (b) Rear side

Fig. 5 Typical ultrasound C-Scan image of an impacted test panel with 10 J impact energy

Figure 6 shows photographs of various test panel configurations along with the direction of the 0° for plies before subjected to compression tests. The pristine and impact damaged test panel configurations are shown in Fig. 6a, b, respectively. The step-lap repair patch bonded to the base laminate is shown on either side (Front and Rear) of the laminate from Fig. 7.

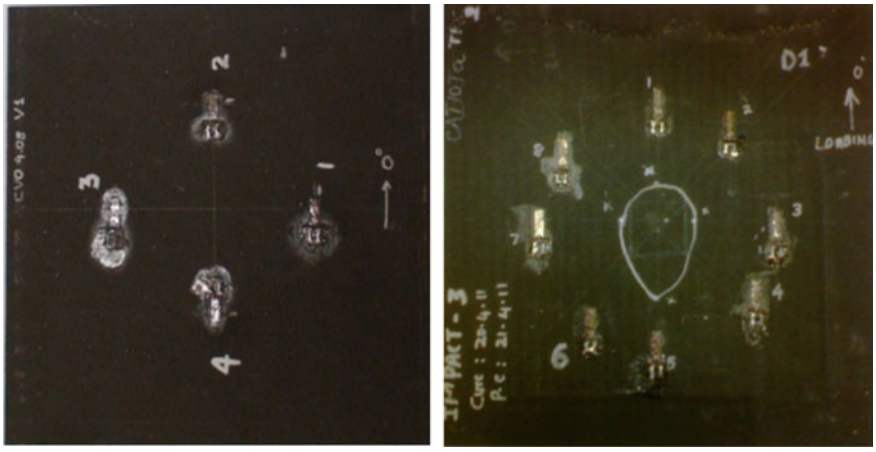

(a) Pristine panel (b) Impact-damaged panel

Fig. 6 Photograph of pristine and impact damaged compression test panel configurations

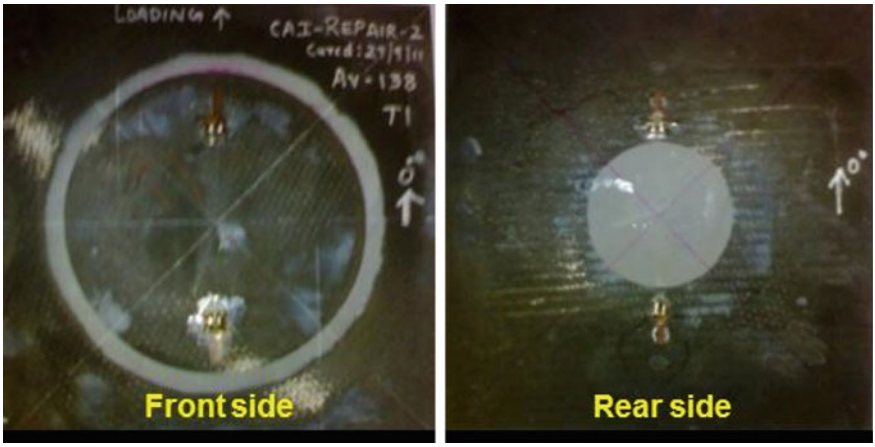

Fig. 7 Photograph of step-lap repaired compression test panel configuration

5 Static and Fatigue Testing

For conducting the static and fatigue compression testing, a computer-controlled closed-loop servo-hydraulic universal testing machine is used with a capacity of 500 kN with a 100 mm stroke. Resistance strain gauges having gauge resistance of 120 Ω with a gauge factor of 2.14 are bonded on various test panels at appropriate locations (as indicated in Table 3) for capturing strain response in loading direction (that is Y-direction) during the static and fatigue testing. The data acquisition system, System 5000 make, is adapted, which is having a capacity of 1–50 sample(s) recording simultaneously up to 20 channels is used for online real-time data acquisition during the testing.

The strain gauges are fixed to the test panels in the loading direction, which is the direction of the 0° plies as well for each of the test laminate. Static compression tests are conducted under the stroke-control mode, at a loading rate of 0.02 mm/min and tested until the failure. The applied load, stroke, and strain values are recorded continuously. Alternate method of monitoring is dealt by authors [14].

The manufacturing process adapted for the composite repair is VERITy, and no base data is available to have a pure compression strength. Hence, to establish base compression strength data, coupon level tests are conducted using the IITRI (Illinois Institute of Technology Research Institute) test fixture as per ASTM standard, ASTM D3410 (2008) [15] subjected to a pure static compression loading on quasi-isotropic laminates fabricated with VERITy manufacturing process. The typical experimental set-up is shown in Fig. 8, with a fixture in the computer-controlled servo-hydraulic test machine.

The size of the specimens is (140 mm × 25 mm × 2.08 mm), and the material is CFRP. Ten numbers of specimens are tested with static compression load while making sure that there is no global buckling during the test. In each of the specimens,

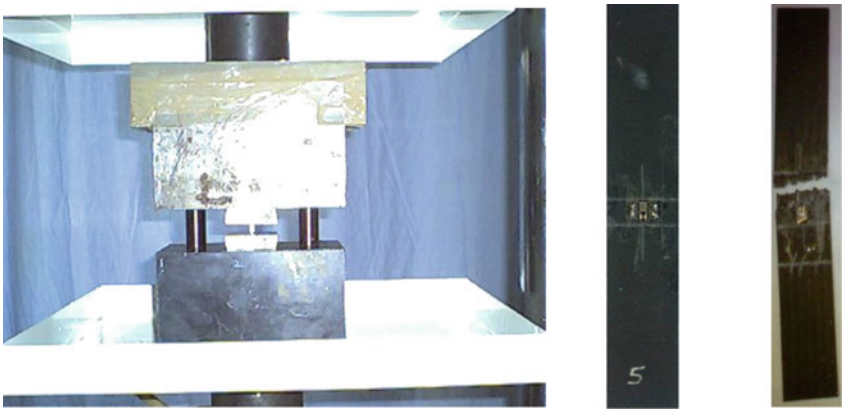

(a) Test set-up (b) Before test (c) After a test

Fig. 8 Experimental set-up with the IITRI fixture and specimen before and after the test

linear strain gauges are mounted on the front and rear side of the specimen at the study section, which is at the center. During the test, strains are measured through an online data acquisition system. The test is conducted up to the failure of the specimen. The static compression failure strength is computed for each of the ten specimens. The test coupon before and after the compression test is shown in Fig. 8b, c along with the failure mode and its location. The value of the average normalised static compression strength obtained experimentally is 1.46.

Similarly, at the test panel size level of 150 mm × 150 mm × 4.2 mm, a reference compression strength and stiffness data need to be established by evaluating pristine (healthy) laminates subjected to static and fatigue compression tests in order to assess the effectiveness of the step-lap repair scheme. In addition, it is also required to have a compression strength value for the impact-damaged laminate. The effectiveness of the step-lap repair is evaluated by comparison of the strength values obtained with the reference (pristine) strength and that of the impact damaged panels. For static compression tests, each of these test panel configurations (Pristine, Impacted, and Repaired), a minimum of three numbers of samples are tested.

The failure location in the pristine test panel is nearly close to the compression loading edge, whereas, in the case of the impact damaged test panel, the laminate failed at the center of the panel as it is evident from the fact that laminated is weakened by the impact damage. But in the case of the step-lap repaired test panel, there bonding between step-lap repair patch location is weaker, and hence the failure mode is to de-bonding of the patch from the base laminate as shown in Fig. 9.

The fatigue testing is conducted in load controlled mode at 0.1 Hz frequency on pristine and step-lap repaired test laminates subjected constant amplitude compression-compression fatigue loads with a stress ratio of 0.1, [16] as shown in Fig. 10. The minimum and maximum loads applied on the pristine and step-

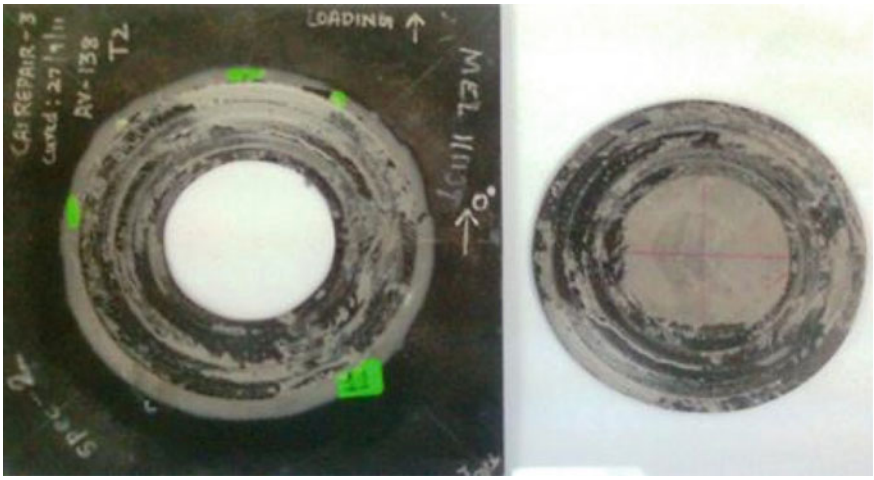

(a) Base plate (b) Repair patch

Fig. 9 Step-lap repaired CFRP panel after compression test

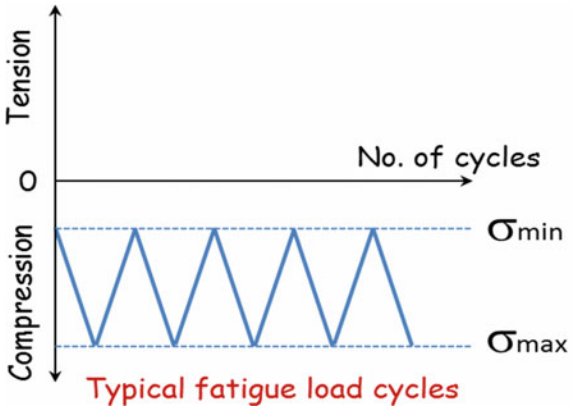

Fig. 10 Typical compression-compression fatigue load cycles

lap repaired panels expressed in terms of normalized stress values using the static compression strength value of the pristine panel are −0.32 and −0.032, respectively.

The purpose of the fatigue testing on the pristine laminate is to have reference data to compare with that of the repaired panel. Each of these two test panels is subjected to 1 million load cycles during the compression-compression fatigue test. Strain response is captured during every one lakh load cycles to check for any stiffness degradation due to fatigue loads.

6 Finite Element Analysis (FEA)

A static geometrically nonlinear three-dimensional (3-D) finite element analyses of the pristine, impact damaged step-lap repaired CFRP laminates subjected to the static compression loads [17] and appropriate boundary conditions using commercially available finite element package [18]. Figure 11 shows a typical finite element model of a complete step-lap repair panel indicating the base plate and the step-lap repair patch with the simulated step-laps.

Taking advantage of the symmetry, and only the quarter model is simulated and analyzed subjected symmetric boundary conditions [16] as shown in Fig. 12. The 10 J impact damage is quantified with the help of Ultrasound A- and C-scans of the laminate. The quantified impact damage is simulated appropriately in the finite element modeling for the impact damaged panel. Uniformly distributed compression loads are applied on the laminate in the Y-direction in adequate number of load steps in order to have data for comparing with that of the experimental data sufficiently and up to laminate failure.

Figure 13 shows a typical deformation pattern when subjected to in-plane compression loads [19]. The out-of-the plane displacement pattern is shown through the exploded view at the center of the impact-damaged laminate panel, as shown in Fig. 13b due to the simulated impact damage.

A typical stress variation pattern with a step-lap repaired laminate panel is shown in Fig. 14, where maximum stress occurs at the step-lap patch area, which is indicated in red color contour.

(a) Base plate with patch (b) Base-plate (c) Step-lap patch

Fig. 11 Finite element model of a step-lap repaired composite laminate

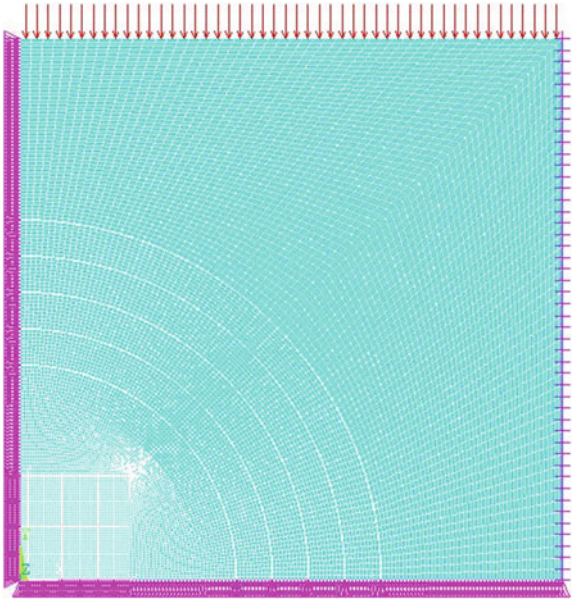

Fig. 12 Typical finite element model for test panel showing load and boundary conditions

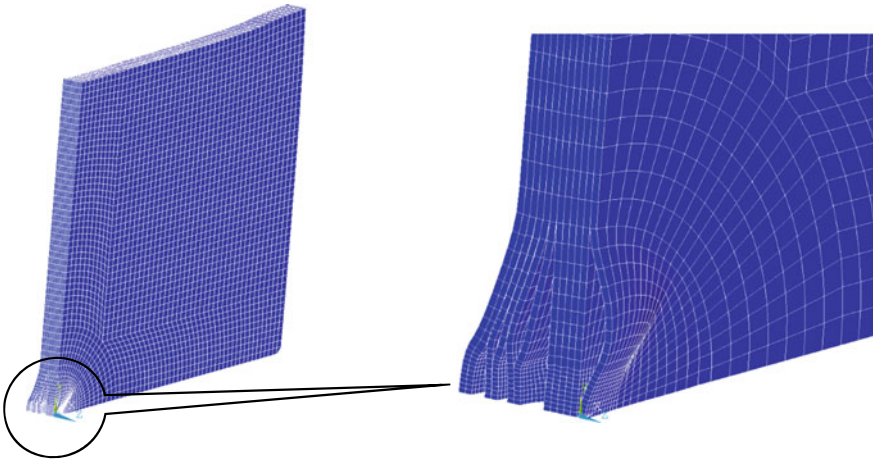

(a) Overall displacement pattern (b) Exploded view around the impact damage

Fig. 13 Typical overall displacement pattern of the impact damaged test panel

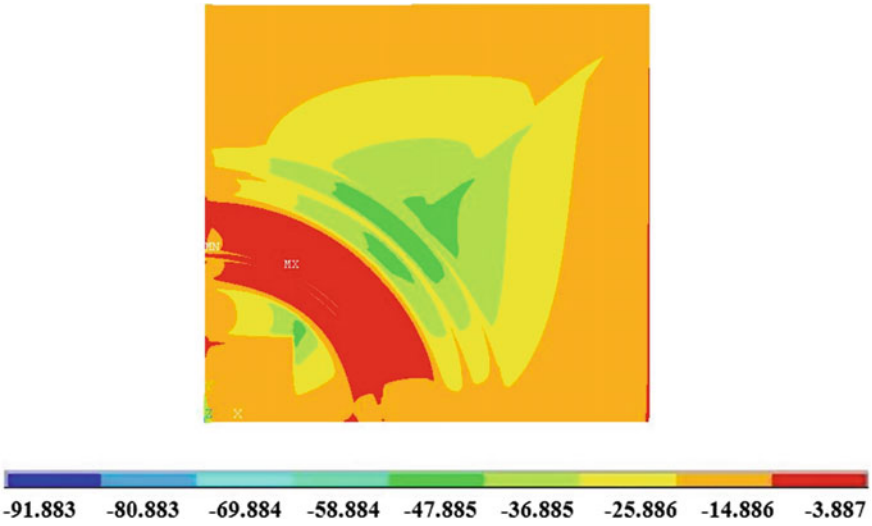

Fig. 14 The typical finite element model shows the pattern of the stress developed

7 Results and Discussion

7.1 Strain Response for Global Anti-buckling Check

In the compression test, it is very important to ensure there is no global buckling. For each of the panel configurations, good anti-buckling is achieved through proper adjustment of the test fixture. The applied compression loads are normalized using static compression failure strength value of the pristine panel. Figure 15 shows the graph of applied static compression load in normalized stress versus strain obtained in micro strains, in the loading direction on the different test panels.

The strain measurement is obtained at the front and rear location on the test panels during the static compression test to verify the effects of the global buckling. In the pristine panel, a good anti-buckling effect is observed, as it is evident from Fig. 15a.

But in the case of impact damaged and step-lap repaired panels, there is a considerable deviation of the strain response between the front and rear strain locations. The deviation observed in the impact damaged and repaired panel is attributed to the local buckling. As far as the global buckling is concerned, there is a good anti-buckling up to a normalized stress value of −0.12, as it is evident from Figs. 15b, c. The deviation is due to the possible asymmetry of the impact damage in the impact damaged panel. Due to this asymmetry, there is an eccentricity in the loading plane of the impact damaged panel. This eccentricity increases as the damage inside the laminate open up with the loading, and it is evident from Fig. 15b. Similar load plane eccentricity exists due to the improper bonding of the step-lap repair patch to the base laminate. Hence there is a considerable deviation in the strain response between the

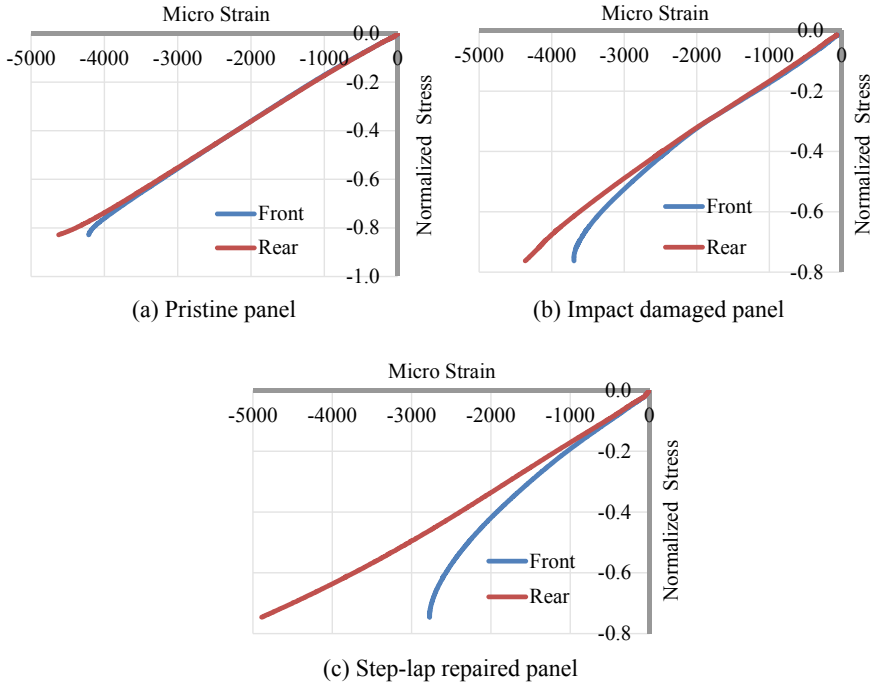

Fig. 15 Typical strain comparison between front and rear on the different test panels for the anti-buckling check

front and rear strain locations on the step-lap repaired laminate, as shown in Fig. 15c. The primary reason for this deviation is due to non-uniformity in the bond thickness between the step-lap repair patch and the base laminate.

7.2 Validation of Strain Response FEA with Experiment

The strain response at different strain gauge locations is computed from FEA and compared with that of the experiments [19].

Figures 16, 17 and 18 show the typical strain comparison between test and FEA for the pristine, impact-damaged, and step-lap repaired laminates, respectively. At the strain gauge location G1 on the pristine test panel, the strain deviation between FEA and test values starts somewhere around a normalized stress value of −0.32, and thereafter it is increasing with the increase in the applied load. There is good agreement between the strain values between test and FEA at the location G2 up to a normalized stress value, −0.64, as shown in Fig. 16. The strain gauges G1 and G2 are located on either side of the test panel and very close to the loading edge. For the same applied load, there is a considerable between the strain values measured

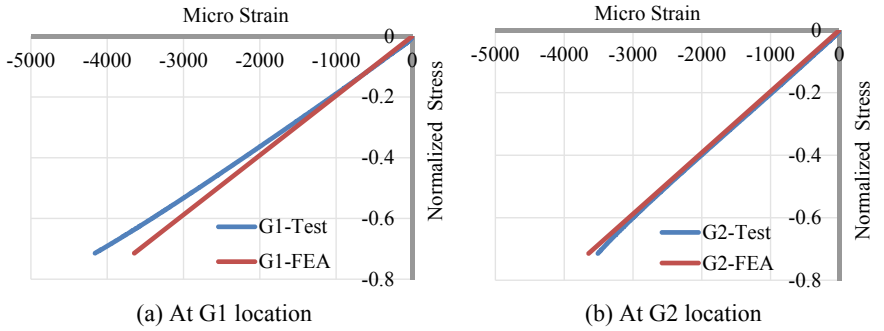

Fig. 16 Comparison of strain values between the test and the FEA for pristine laminate

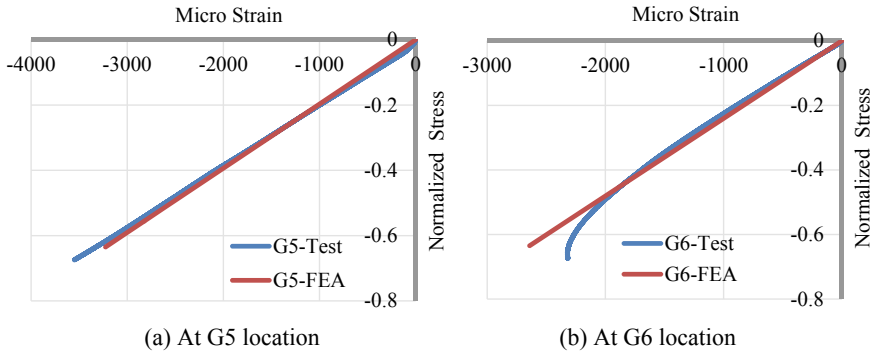

Fig. 17 Comparison of strain values between the test and the FEA for impact damaged laminate

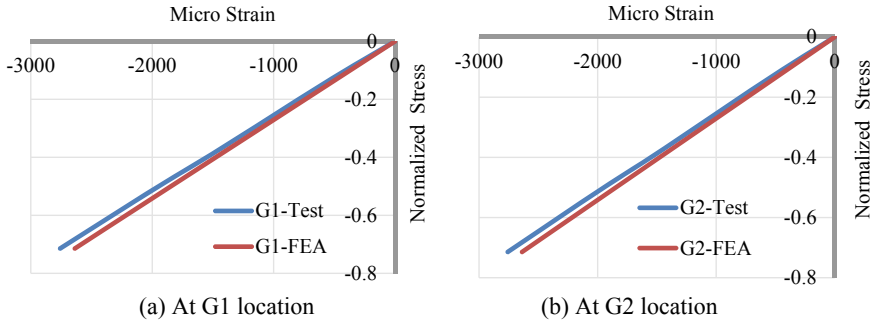

Fig. 18 Comparison of strain values between the test and the FEA for step-lap repaired laminate

at G1 and G2. This difference of strain values suggests there is a local buckling taking place. The final failure for the pristine test panel happening is very close to the loading edge.

In the case of impact damaged test laminate, the final failure occurs at the center section because of the impact damage is present at the central section of the laminate. There is a good agreement in the strain response between test and FEA values up to a normalized stress of −0.64 at G5 and up to a normalized stress of −0.48 at G6 locations, as shown in Fig. 17.

Similarly, there is a good match between test and FEA values on the step-lap repaired test panel up to an applied normalized stress value of −0.71, as shown in Fig. 18.

Overall, the FEA predicted strain values match well at most of the strain gauge locations in terms of magnitude and trend. The strain response curves predicted by FEA start deviating from that of the test value when the test panel is likely undergoing an initiation of the final failure.

7.3 Evaluation of Step-Lap Repair Against Static Loading

The experimentally obtained failure loads are tabulated, and then the failure strength values are computed. The average static compression failure strength for each panel configurations is tabulated in Table 4. The normalized static compression strength obtained through pure compression strength using the IITRI test fixture is 1.46 times that of the pristine panel, which is higher than that of the pristine test panel due to the absence of buckling. In the case of a pristine test panel, it undergoes a considerable amount of local buckling at the section where final failure occurs.

It is observed that there is a 19% reduction in the strength due to the impact damage on the CFRP panel with respect to that of the pristine panel. The step-lap repaired panel is observed to recover around 14.5% of the strength in comparison with that of the impact damage, and there is a 4.5% reduction in the strength observed when compared with that of the pristine panel. Therefore, a good amount of recovery of the static compression strength is seen experimentally with the step-lap repair method.

The experimental strain response obtained from the pristine, impact-damaged, and repaired panels is analyzed. The typical experimental strain responses are plotted

Table 4 Comparison of strength values between different test panel configurations

Panel configuration	Normalized compression failure strength	Reduction in load carrying capacity (%)
IITRI coupon	1.460	Pure compression
Pristine	1.000	Reference
Impact damaged	0.810	19
Step-lap repaired	0.955	4.5

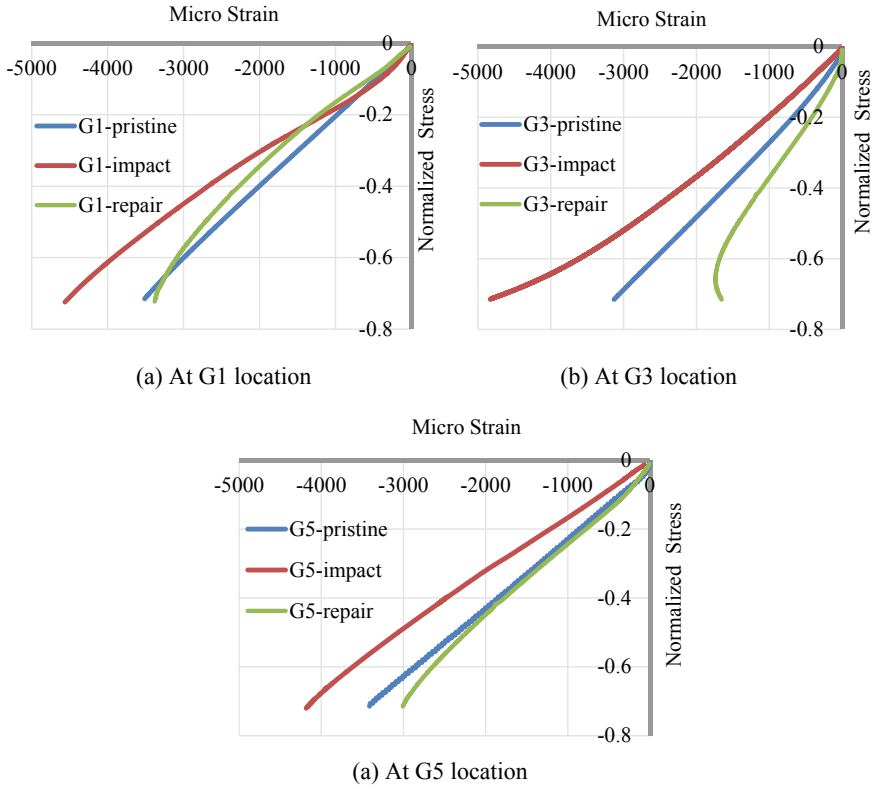

Fig. 19 Experimental strain comparison between pristine, impact damaged and repaired panels

against applied load in in terms of normalized stress, as shown in Fig. 19 for each of the test panel configurations at G1, G2, and G3 locations. The stress-strain curve, which is closer to the vertical axis of the graph in Fig. 19, indicates the test panel is stiffer, and the stress-strain curve, which is closer to the horizontal axis indicates the in the reduction in the stiffness when compared to that of the pristine test panel. With this, it is evident from the graphs that the step-lap repair panel is stiffer compared to that of the impact damaged panel and closer to that of the pristine (reference) panel at both of the strain gauge locations. Therefore, the repair method is capable of recovering the stiffness as well.

In summary, the static compression strength and stiffness are recovered with the step-lap repair method in terms of the magnitude and the trend.

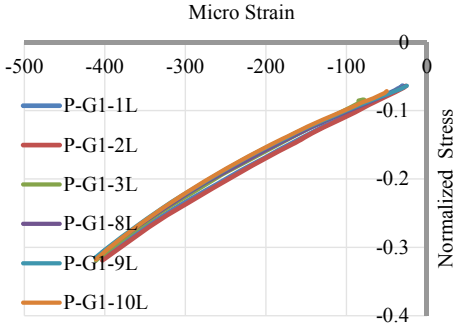

Fig. 20 Experimental stress-strain response for the pristine panel at G1 location during the compression-compression fatigue test

7.4 Evaluation of Step-Lap Repair Against Fatigue Loading

During the fatigue testing, the strain responses at G1 to G6 location are recorded at the interval of one lakh (1L) fatigue load cycles up to one million (10L) load cycles.

These strain responses, thus computed, are plotted in a graph against the remote fatigue compression stress cycle. Figures 20 and 21 show the stress–strain diagram for the pristine and step-lap repaired panels from 1 to 10L load cycles, respectively. The slopes of the curves in Fig. 20 are observed to be almost constant between each other at 1L to 10L load cycles, and the strain deviation is around 1%. A similar trend in the slope is also observed with the step-lap repaired test panel as it can be seen from Fig. 21 at strain locations such as G1, G3, G4, and G5, but there is a slight deviation at locations G2 and G6. The shift of each curve in Fig. 21 is due to the various start and stop of the fatigue test since the duration of the one fatigue test is around 60 working days approximately. Due to this, their stress–strain curves are shifted by maintaining the same or approximately constant slopes at each of these curves at various locations, G1 to G6, and at various recording intervals between 1 and 10L number of fatigue cycles.

The strain values at G1 to G6 locations corresponding to a load point say normalized stress value of −0.48, which is closest to the highest load in the fatigue load cycle, are tabulated, and the percentage of deviation of the strain values are computed in Table 5.

The highest strain deviation percentage observed is around 25% at G1 and 20% at G5 locations, respectively, with the step-lap repaired laminate. At the rest of the locations such as G2, G3, G4, and G6, the percentage of deviation is below 10%. Due to the negligible change in the slopes of the stress-strain curves from 1 to 10L of applied load cycles for each of these strain gauge locations G1 to G6 on the step-lap repaired test laminate, the local changes in the strain values are attributed to the local buckling [20].

The strain gauges G1, G3, G5, are located on the step-lap patch whereas G2, G4, G6 are located on the base panel at identical locations respectively on the laminate. A

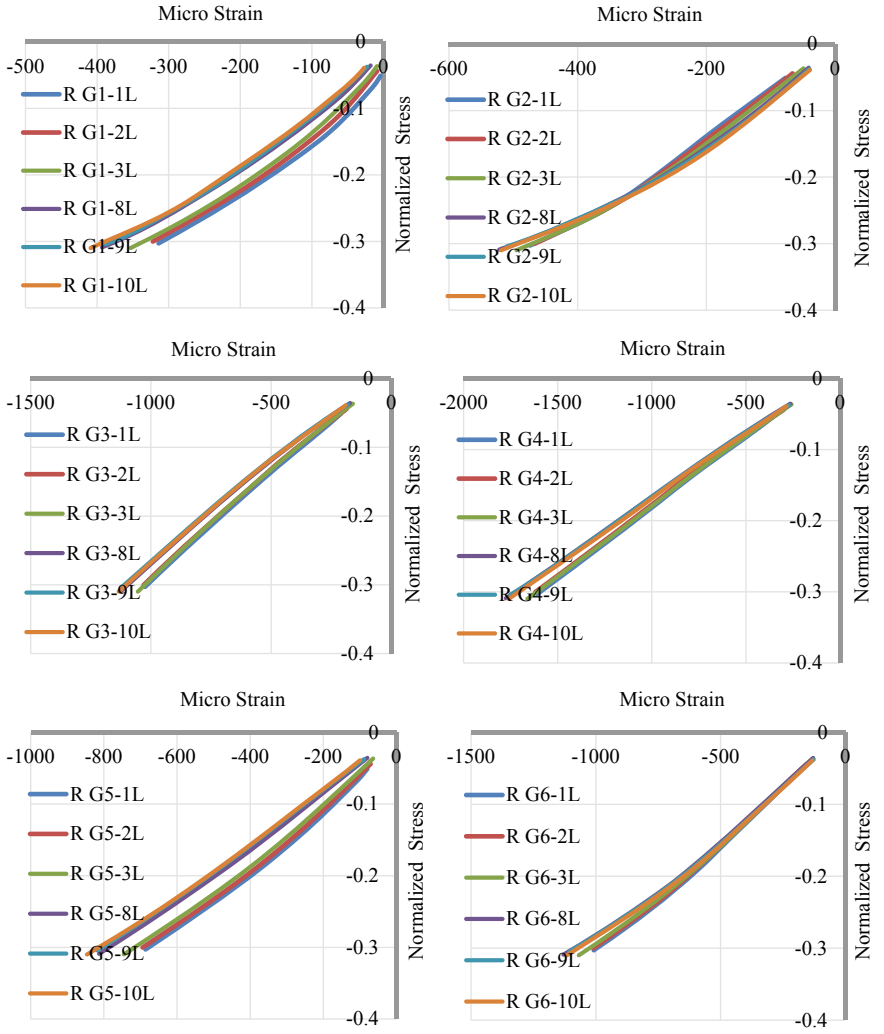

Fig. 21 Experimental stress-strain response for the step-lap repaired panel during the compression-compression fatigue test

small non-uniform application of adhesive for bonding the step-lap repair patch leads in inducing an eccentricity in the loading plane, which is, in turn, local buckling, and hence it gets reflected by the proportionate increase in the strain values with increase in the applied load.

This phenomenon of induced eccentricity is observed by calculating the difference in strain values between the front and rear strain gauges that are tabulated in Table 6. The percentage of deviation of the strain values at G1 and G2 is 33.8% and 21.2%

Table 5 Deviation of strains at various strain gauge locations on step-lap repaired test panels

Strain gauge location	Compression strain at a normalized stress of −0.48		Deviation (%)
	At 1 lakh cycles (1L)	At 10 lakh cycles (10L)	
G1	−314	−394	25
G2	−474	−500	5.5
G3	−1024	−1111	8.5
G4	−1608	−1720	7
G5	−686	−823	20
G6	−1008	−1084	7.5

Table 6 Deviation of strains at between front and rear locations on the step-lap repaired test panel

Front and rear strain gauge pairs	Percentage of strain deviation (%) at a normalized stress of −0.48 load level	
	At 1 lakh cycles (1L)	At 10 lakh cycles (10L)
G1 and G2	33.8	21.2
G3 and G4	36.3	35.4
G5 and G6	31.9	24.1

at the end of 1L and 10L load cycles, respectively. A similar trend of deviation is observed with G3 and G4, along with G5 and G6 pairs, as shown in Table 6.

This deviation serves as a measure of the amount of eccentricity induced primarily due to the non-uniformity of bonding of the step-lap repair patch to the base laminate while adopting a particular repair method and manufacturing process.

8 Conclusions

The static compression tests on the various specimen configurations such as pristine, impact damaged, and step-lap repaired test panel laminates manufactured with the VERITy process are carried out till failure to establish the static compression strength. The pure compression strength experimentally obtained using the IITRI fixture is compared with that of the pristine test panel. The strain response of these test panels is captured through the online strain measurement at various locations on the laminates. The strain gauges on either side of the test panels also serve as feedback for proper alignment adjustment in order to ensure that there is no global buckling. This ensured the compression loading is in-plane with the mid-plane of the test panels during the test.

Constant amplitude fatigue on pristine and step-lap repaired test panels are tested with compression-compression load cycles with a stress ratio of 0.1 up to one million load cycles. The strain response at various intervals of applied cycles is recorded and

compared. It is observed that there is no failure occurred with the pristine and step-lap repaired panels even after 1 million load cycles. There is a reasonable degradation of the stiffness observed with the step-lap repaired test panels and is attributed primarily to the load eccentricity because of the non-uniform bonding of the step-lap repair patch. This happens even due to the way the bonding process of the step-lap repair patch on the base laminate is carried out. If the uniformity in the bonding and bonding thickness is maintained along with continuous non-stop fatigue testing till 10L load cycles, then there would be a negligible variation of strain values and the slopes of each of the stress-strain curves at various strain locations at the end of each completed 1L to 10L number of fatigue cycles.

3-D finite element analyses are performed by modeling above three test panel laminate configurations at various load levels for capturing the state of stress in and around the impact damage and step-lap repair patch with the base laminate. The typical strain responses predicted from FEA are validated with that of the experiment for all of the test panel configurations.

The impact damage impacted with a 10 J impact energy, thus quantified using non-destructive techniques, is successfully simulated. And the predicted strain response from FEA is validated with that of the test results. Similarly, step-lap repair details are also simulated along with the validation of FEA results with that of the test. The predicted strain response from the FEA is reasonably in good agreement with that of the experiment in terms of their magnitudes and trend at most of the strain locations, although there is a reasonable amount of deviation when strain reaches closer to the compression failure.

The step-lap repair scheme for repairing CFRP laminates fabricated with the VERITy process is successfully experimentally evaluated under static compression and compression-compression fatigue loads to qualify the repair method. It is observed that the repair method is capable of recovering the strength and the stiffness under compression loads.

Acknowledgements The authors express thanks to the staff of ACD, CSIR-NAL, who have provided the composite laminate panels for this study.

References

1. Duong, C.N., Wang, C.H.: Composite Repair: Theory and Design, 1st edn. Elsevier Publications, Great Britain (2007)
2. Panigrahi, S.K.: Modeling of an aircraft skin with cut-out repaired by a bonded composite patch using variational asymptotic method. In: Modelling and Simulation in Computational Mechanics: Engineering Applications, pp. 106–120. Lambert Academic Publishing AG & Co. KG. (2008)
3. Reid, S.R., Zhou, G.: Impact Behaviour of Fibre-reinforced Composite Materials and Structures. Woodhead Publishing Ltd. (2000)
4. Abrate, S.: Impact on Composite Structures. Cambridge University Press (1998)
5. Soutis, C.: Measurement of the static compression strength of carbon-fiber/epoxy laminates. Compos. Sci. Technol. **42**, 373–392 (1991)

6. Lee, J., Soutis, C.: Thickness effect on the compressive strength of T800/924C carbon fiber-epoxy laminates. Compos. A Appl. Sci. Manuf. **36**, 213–227 (2005)
7. Soutis, C., Smith, F.C., Matthews, F.L.: Predicting the compressive engineering performance of carbon fiber-reinforced plastics. Compos. A Appl. Sci. Manuf. **37**, 531–536 (2000)
8. Yokozeki, T., Ogasawara, T., Ishikawa, T.: Nonlinear behavior and compressive strength of unidirectional and multidirectional carbon fiber composite laminates. Compos. A Appl. Sci. Manuf. **37**, 2069–2079 (2006)
9. Lee, J., Soutis, C.: A study on the compression strength of thick carbon fiber-epoxy laminates. Compos. Sci. Technol., 2015–2026 (2007)
10. Verma, K.K., Dinesh, B.L., Singh, K., Gaddikeri, K.M., Srinivasa, V., Kumar, R., Sundaram, R.: Development of vacuum enhanced resin infusion technology (VERITy) process for manufacturing of primary aircraft structures. J. Indian Inst. Sci. **3**(4), 621–634 (2013)
11. Standard Test Method for Compressive Residual Strength Properties of Damaged Polymer Matrix Composite Plates (2017), ASTM D7137/D7137M-17
12. Linke, M., Flugge, F., Olivares-Ferrer, A.J.: Design and validation of a modified compression-after-impact testing device for thin-walled composites plates. J. Rein. Plastics. Compos. (4–126), 2–16 (2020)
13. Tuo, H., Lu, Z., Ma, X., Zhang, C., Chen, S.: An experimental and numerical investigation on low-velocity impact damage and compression-after-impact behaviour of composite laminates, composites. Part B: Eng. **167**, 329–341 (2019)
14. Li, Y., Zhang, W., Ming, A., Yang, Z., Tian, G.: A new way for revealing the damage evolution of impacted CFRP laminate under compression-compression fatigue load based on thermographic images. Compos. Struct. **176**, 1–8 (2017)
15. Standard Test Method for Compressive Properties for the Polymer Matrix Composite materials with Unsupported Gage Section by Shear Loading (2008), ASTM D3410/D3410M-03
16. Souza, A., Gomes, G.F., Peres, E.P.: Jose claudio isaias and antonio carlos ancelotti Jr. A numerical-experimental evaluation of the fatigue strain limits of CFRP subjected to dynamic compression loads. Int. J. Adv. Manufact. Technolo. **103**, 219–237 (2019)
17. Abdulhamid, H., Bouvet, C., Michel, L., Aboissiere, J., Minot, C.: Numerical simulation of impact and compression after impact of asymmetrically tapered laminated CFRP. Int. J. Impact Eng. **95**, 154–164 (2016)
18. Abir, M.R., Tay, T.E., Ridha, M., Lee, H.P.: Modelling damage growth in composites subjected to impact and compression after impact. Compos. Struct. **168**, 13–25 (2017)
19. Tan, W., Falzon, B.G., Chiu, L.N.S., Price, M.: Predicting low velocity impact damage and compression-after-impact (CAI) behaviour of composite laminates. Compos.: Part A **71**, 212–226 (2015)
20. Stojkovic, N., Folic, R., Pasternak, H.: Mathematical model for the prediction of strength degradation of composites subjected to constant amplitude fatigue. Int. J. Fatigue **103**, 478–487 (2017)

Fracture Behavior and Toughness of Fiber Reinforced Thermoset Composites

Alak Kumar Patra and Indrajit Ray

Abstract The fiber reinforced polymer composites (FRPC) are being widely used in several advanced engineering structures ranging from civil infrastructure to aircraft, spacecraft, ships, cars and in many other outdoor and household applications. The major advantage is its high specific strength, stiffness, and durability leading to sustainable applications. Thermoset resins have advantages of retaining shape and strength at a higher temperature and harsh environment and lower life-cycle cost compared to thermoplastic resins. However, the knowledge of their behaviors during fracture failures are essential to properly evaluate the performance of thermoset composites. This chapter is divided into following five sections: Sect. 1 provides the introduction; Sect. 2 discusses the fracture mechanism of FRP's from micromechanics and global response of components or structure as a whole. The detailed information on general fracture mechanics approach including different modes of fracture, fracture failure procedures, fracture mechanics approach in FRC problems, fracture under compression, and failures at different scales will be provided. Section 3 elaborates on various failure theories such as micromechanical failure of FRP with UD lamina, anisotropic failure theory including theory of maximum stress, maximum strains, deviatoric strain energy theory, theory of tensor polynomial, failure for damage mechanism, failures under creep, fatigue and rupture, high strain rate failures. Section 4 covers the various modes of experimental investigations on FRPC including mode I, mode II, mode III, and mixed mode fracture toughness.

Keywords Fiber reinforced composites · Fracture behavior · Fracture failure theory · Thermoset composites · Toughness

A. K. Patra (✉)
Department of Civil Engineering, Advanced Composite Research Centre, SRM Institute of Science and Technology, Kattankulathur, Chennai 603203, India
e-mail: AlakPatra19@gmail.com

I. Ray
Department of Civil and Environmental Engineering, University of the West Indies, St. Augustine, Trinidad and Tobago
e-mail: IndrajitRay29@gmail.com

S. Mavinkere Rangappa et al. (eds.), *Fracture Failure Analysis of Fiber Reinforced Polymer Matrix Composites*, Engineering Materials,
https://doi.org/10.1007/978-981-16-0642-7_6

1 Introduction

Fracture behavior of FRPCs includes the behavior of FRPCs in the course of their fractures. The behavior can be described in different ways. Fracture failure is the focal point of all these exercises. Inability of the element of structure to withstand against load or loss of material integrity can be defined as failure [29]. Failure of FRPC is a complicated phenomenon and a continuous growing field of research for its importance. There are obvious reasons behind it. The FRPCs are stronger in the direction of fiber in comparison to other directions. It is evident that the failures of FRPCs depend on the direction of stresses. FRPCs fail in much lower stresses in the direction normal to the fiber than that required to cause failure in the direction of fiber. Failure under tensile load is governed by the strength of the fiber and controlled by the bond strength between the fiber and the polymer matrix and the matrix-strength in the direction perpendicular to the fiber direction. But the failure in an angular direction other than the 0° or 90° depends on the direct stresses in 0° and 90° directions with respect to fibers and the shear stress also. It becomes an important point of investigation that under which stress (direct/shear) or stress combination the FRPC will fail. Matrix materials in FRPCs may be ductile or brittle. In case of ductile polymer matrix, the material may fail due to disruption in load transfer mechanism from matrix to fiber under large strain of matrix. Polymer composites with brittle matrices may exhibit numerous cracks about the fibers or in between the fibers causing disturbances in the transfer mechanism of the load to the fibers from the matrices leading to failures. Buckling or enormous deformation of fibers may cause the failure of FRPCs under compressive loads. Most of the times, failure is an ultimate result of initiation and maturity of a combination of more than one of these mechanisms which is a complex and intricate event. FRPCs are not only multi-phase materials but also multi-layered and may be composed of fibers in multiple directions which may be subjected to a variety of loads. Even if the failure of unidirectional (UD) lamina of FRPC is considered, it becomes difficult to understand for the dissimilarities in stress distribution in different phases and interfaces. This is because in UD lamina, matrix and fibers are of different strengths, interface behaves differently from the matrix and the manufacturing defects or flaws. It is now obviously understandable why failure of FRPCs is a complicated topic and why it is studied by so many researchers and groups of researchers till today. Instead of the importance of understanding the failure mechanisms in FRPCs, it is not possible to realize the details of every state of failure. From practical point of view, it is important to know for the safety of the structure whether a stress level or combination of stresses or that of strains are below some critical limit or not. Establishing a fracture criterion for the improvement in precision of predictability of a fracture behavior is essential [46]. Another important point is that the criteria of failure should not be much conservative without compromising its safety against failure, must be understandable and verifiable through experiments. At base, all these criteria are either maximum stress or maximum strain criteria or interaction between them, sometimes are modified by some specific observations obtained from

experimental investigations. The objective of all these straight or intricate approaches is to predict the failure through some failure criteria. The significance of so many criteria is that instead of immense efforts, none of them is able to explain the failure behaviors of all the FRPCs subjected to any kind of loading system. The issue is same for isotropic materials also; some fail due to yielding while some others' failure is of brittle nature. Many criteria may be acceptable when the criteria are considered for indication, not for prediction of failures under all conditions.

Fracture behaviors of FRPCs can be assessed from the criteria for fracture [51]. The mechanisms from crack initiation to propagation is not clear for complicated relation between the material's microstructure and the stress field at macroscopic level [56]. One approach followed in fracture mechanics calculates critical rate of release of strain energy from macroscopic displacements and applied forces. A look into the cracks at microscopic level reveals that the strain energy induced in the location of crack supplies the energy required for the newly generated surfaces from the formation of cracks, heat, some additional release of elastic energy as well as energy required for plastic deformation. Instead of significant advancement in fracture mechanics, much insights are yet to be gained on the extension in front region of the crack tip as well as on the kinetic and kinematic instabilities in the displacement field around the crack tip [17, 76]. Reason is straightforward, it is very difficult to investigate directly on propagation of crack starting from the nucleation for the speed of propagation of cracks in solids.

Fracture behaviors of brittle thermoset polymers (mostly epoxy resins) were started to be addressed through kinetic approach to explain the fracture in thermoset polymers as ruptures of bonds [21, 80, 81]. In a latter approach [67, 68], the micro-level stresses have been taken into account to address the kinetics of polymer fracture. The kinetic theory is much applicable to the initiation of fracture in brittle polymer and cannot be efficiently used for the crack propagation especially for non-brittle polymers with deformations consisting of inelastic and/or plastic components [37]. There are some other approaches also for explanation of fractures in polymers like molecular fracture etc. [37]. Thermoset polymers are well known brittle materials. These thermosets are reinforced with toughners and/or fibers to improve its characteristics and toughness against fracture. Consequently, the fracture behavior of thermoset FRPCs are often studied by application of fracture mechanics. Though detailed scientific criteria to address the failures of all FRPCs under all conditions are not available, phenomenological procedures are there to address the failures of such materials due to formation of cracks. Mechanics of cracks or fracture mechanics is based on Griffith's and Irwin's approaches [19, 20, 30]. These approaches can be followed to describe the fracture in ceramics, polymers or metals. But for FRPCs, heterogenous ingredients of different length scales are infused into homogeneous and isotropic matrices with some other consequences for arresting, branching or deflection of cracks along with mixed mode features. Consequently, some conditions assumed in classical theories or hypotheses become insufficient for these composites. Moreover, with the advent of new varieties of matrices and fibrous materials, additional theories are being employed to explain the fracture behaviors of FRPCs. Diverse field of development of different theories are becoming important day by

day to address the fracture problems of fiber reinforced polymeric composites. These FRPCs are used in many applications for their appreciable performances in resisting fractures or fracture toughness.

2 Fracture of FRPCs

Fracture of FRPCs is a type of failure that can be explained by several approaches. One of the approaches deals with micromechanics of composites. Another approach is to estimate the global response of components or structure as a whole which is very much important to the scientists, engineers and policy makers of the world. There is one intermediate approach between the two. In this approach, the deformation or the load carrying capacity of each layer or that of the number of layers of a laminate with the interactions between the different layers of laminated composite is addressed. The topics are discussed in a little more detail in the following section.

Based on reinforcing materials, polymeric composites can be divided in to two broad classes (as described in details in first chapter): Particulate and fiber reinforced composites. Based on matrices, they are primarily divided into two types: thermoplastic and thermoset polymeric composites. The target of discussion in this chapter is the fracture behavior of the fiber reinforced thermoset polymeric composites. It is clear from the fore going discussions that fracture in FRPCs is a complicated phenomenon. Nevertheless, fibers play key roles in FRPCs. Legitimate approach is to start with the interaction between fibers and matrices during fractures. Fibers and matrices are treated as elements of separate constituents in numerous studies. The failure problem may be addressed from different points of views. One of such views of addressing this problem is studying the fiber-stresses, stresses in matrices holding the fibers in positions, the interface stresses, fiber breakage, matrix cracks, fiber interactions, varying distances between the fibers, influence of other fibers on the broken one, or localized yields of matrix or fibers. This view of addressing localized effects of interaction between matrices and fibers is micromechanics [32, 41]. On the other hand, different intellectuals of the world are interested in the global response of composite structures or structural components made of FRPCs. The global responses like deformation, buckling and fatigue loads, thermal behaviors, damping, energy absorbing capacity, effect of holes or similar discontinuities etc. in the components or the structure as a whole are more important to them from application point of view. Response of a layer or a number of layers are intermediate in nature between these two approaches. In this approach, the deflection or load carrying capacity of individual layer, or that of the laminates of a groups of layers along with the interactions between the different layers of laminates are studied to predict their failures. Role of fiber orientation or constituent materials in a single layer or the layers of a laminate is an active field of study due to invention and development of new constituent materials for both fibers and matrices (as mentioned in the previous section). In this technique, the responses like deformations of some element of a layer

with many fibers are addressed without going to the micromechanical responses of individual fiber, matrix and their interactions.

The next section will be dedicated to failures accompanied with fractures only as the topic of this section is fracture of FRPCs followed by much more insights from micro, meso and macro level study of failures.

2.1 General Fracture Mechanics Approach

Fracture mechanics deals with the propensity of inherent cracks of materials to grow under applied loads. The strength of component or structures is reduced due to existing flaws or cracks. If the cracks are long enough, the structure or structural component will fail much below the design loads. The defect criticality assessment for the performance of a structure is the prime objective of fracture mechanics. Moreover, fracture mechanics is applied to calculate the maximum allowable size of cracks.

The material science and applied mechanics are generally integrated in fracture mechanics to study the behaviors of materials with defects. Applied mechanics is applied to find the relationship between the stress field and deformation at the tip of a crack in a cracked material body. The resistance of the materials against fracture (due to crack) is estimated in material science applying fracture mechanics for developing more robust materials through better processing and design of materials.

The defect or flaws plays the key role in the strength exhibited by any material. These flaws are very much important in fracture failure of FRPCs [32]. The micro or macro-cracks governs the strength of the FRPCs. Thus, fracture mechanics is an essential field of study in the fracture failures of the FRPCs, be it at micro or macro levels for strength of materials approach is essential but not sufficient to explain the behaviors of FRPCs.

Three major stages are to be considered in fractures due to cracks: nucleation or initiation of microcracks, growth and coalescence and crack propagation. In the growth phase, microcracks grow stably to join with other micro cracks to form a macro crack. In the final stage, these macro cracks propagate fast leading to fracture. This happens at a stress level which is critical for unstable crack growth. While these stages are prominent in thermoplastic FRPCs, due to matrix ductility and crack arresting capability of fibers at the interface between the fibers and matrix, stage two is not prominent to be realized in thermoset FRPCs for brittle character of the thermosets. It is already mentioned that polymer composites with brittle matrices like thermoset resins are prone to exhibit numerous cracks about the fibers or in between the fibers causing disturbances in the transfer mechanism of the load to the fibers from the matrices leading to failures.

Failures may occur under one or combination of more than one of the modes of fractures. Based on applied loads, following modes of fractures are encountered in fracture mechanics.

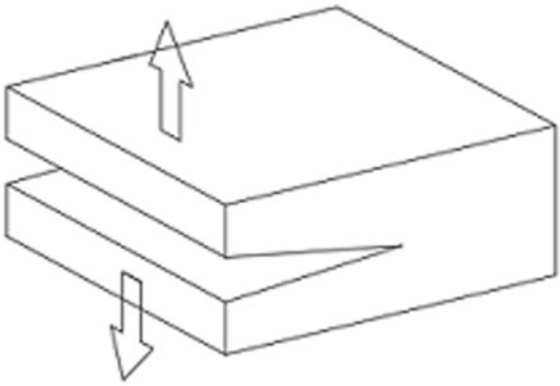

Fig. 1 Fracture under mode I loading

1. Mode I fracture
2. Mode II fracture
3. Mode III fracture failures and
4. Mixed mode fractures.

2.1.1 Mode I Fracture

In mode I, tensile load is applied perpendicular to the facture plane leading to opening mode of fracture. It is termed as opening mode for the joints between the fracture surfaces at the crack tips open like opening some page in writing pad as shown in Fig. 1.

2.1.2 Mode II Fracture

In mode II fracture, the load applied is parallel to the fracture plane and results in sliding the two newly developed fracture surfaces parallel to the crack surface and in the same direction to the crack front due to shear stress perpendicular to the crack front. The loading direction, cracked surfaces and the crack front are presented in Fig. 2. This is sometimes termed as sliding mode for the newly developed fractured surfaces which are parallel to the crack-plane, slide in directions opposite to each other as shown in figure. Definitely, in-plane shear forces play important role in this type of fracture.

2.1.3 Mode III Fracture

Mode III fracture occurs when load is applied in such a way that the shear stress is parallel to the crack front and crack plane both. The load is applied out of plane to

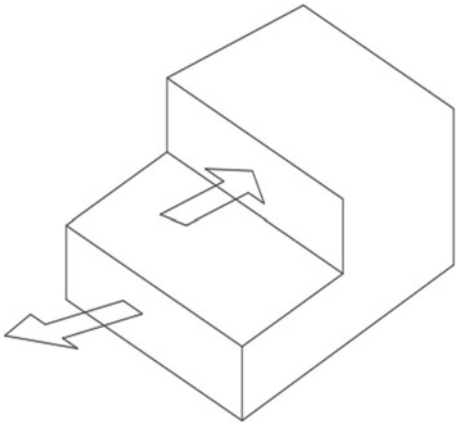

Fig. 2 Fracture under mode II loading

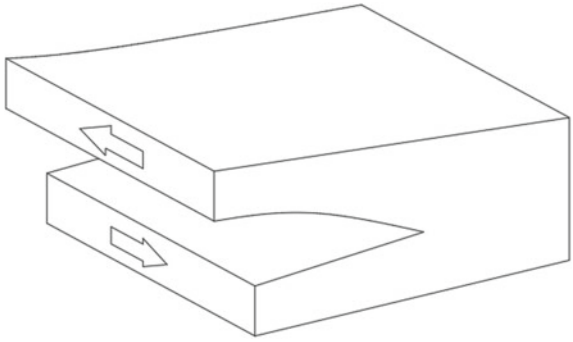

Fig. 3 Fracture under mode III loading

the shearing plane. This is called as tearing mode of fracture for this mode of fracture is often realized in tearing some component. As for example, this mode of fracture observed when a paper is torn by applying forces by two hands at one edge in reverse directions. Mode III fracture is schematically presented in Fig. 3.

2.1.4 Mixed Mode of Fractures

A combination of the different pure modes of fractures (mode I, mode II and mode III) are frequently experienced in practical cases of complex situations. This mode of fracture can be characterized by the presence of two or more modes (Mode I and mode II, Mode I and Mode III or all modes) mixed at the crack front. This mixed mode fracture is common in case of sandwich composites due to asymmetry in both material and geometry of layers and in several loading cases.

It is already mentioned that different mechanisms ultimately result in failures. Several mechanisms which finally lead to failures in FRPCs are presented in the following section.

2.2 *Fracture Failure Procedures*

Two well accepted hypotheses of fracture mechanics are:

1. There are inherent flaws in every real material, and
2. Higher stresses are induced at the location of flaws than the surrounding region of the materials which finally lead to fracture.

Several anomalies or flaws in microscales exist in FRPCs due to defects in manufacturing or other reasons [4]. These defects are the breeding points of crack-initiations leading to propagation due to the higher stress concentration at flaws than the surrounding materials. Failure in macroscopic scales within FRPCs can include the following four mechanisms.

1. Transverse cracking,
2. longitudinal cracking
3. Delamination and
4. Fiber breakage.

Based on observations, the resultant event of failure in laminated composites starts with transverse cracks which leads to series of failure events such as: cracking in longitudinal direction, delamination and breakage of fibers. The failure mechanisms in macroscopic scales mentioned above are briefly presented below.

2.2.1 Transverse Cracking

Crack in the matrix in a direction transverse to the direction of applied load is one of the mostly observed mode of damage in laminated composites [77]. The transverse cracking in laminates has been shown in aqua color in Fig. 4. Transverse crack

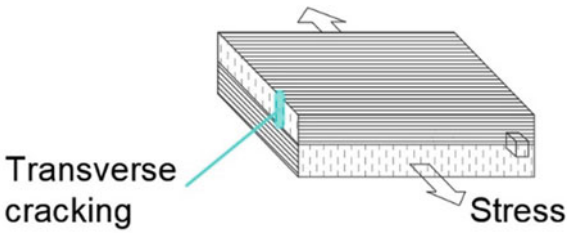

Fig. 4 Transverse cracking in FRP laminates

initiation and propagation is an enduring issue over some decades. The microcracks at 90° plies due to loads applied along plies at 0° direction are commonest form of damage [43]. Stiffness of laminates is reduced due to it followed by stress singularity at the location of crack tip along with initiation of delamination between the laminae. Delamination leads to disband between the matrix and the fibers and breakage in fibers. Finally, the integrity in the structures is lost inviting failures in structures. It is now understandable that failure of laminated composites starts with transverse cracks which can be followed by cracking in longitudinal direction, delamination and breakage of fibers. Analytical and experimental investigations on the failures of laminates have been concentrated over decades on the initiation of cracks transverse to the loading direction and their propagation in laminated composites. Finite element method was employed in a three-dimensional analysis of specimen [78] to calculate the rate of energy release for initiation and propagation of crack across the width. Behavior of neighboring plies due to transverse cracking in matrix and generalized plane strain induced delamination was studied by Yokozeki et al. [79]. Propagation of crack in the matrix of continuous carbon fiber reinforced epoxy composite was predicted [62] by another research group applying finite element method in non-linear domain.

2.2.2 Longitudinal Cracking

Investigation based on numerical analysis reveals that matrix-crack in the direction transverse to the loading direction is first damage mode and longitudinal cracking [48] is the second mode of damage. Longitudinal cracks are developed when the direction of primary loading is parallel to the direction of fibers. While longitudinal cracks are not developed in the life time of some laminates, they are observed to occur before the failure in some of the laminated composites. Sometimes, for this reason, longitudinal cracks are not taken into account in modelling laminates. But they can develop in cross-ply laminates [48]. The longitudinal cracking in laminates has been shown in aqua color in Fig. 5.

2.2.3 Delamination

In case of laminated or layered composites, delamination is separation of different laminae or layers of composites. It is a critical mechanism of failure [73] in composites made of polymeric matrix reinforced with different fibers. This is a basic difference between the behaviors of the FRPCs and metals. Delamination is resulted from higher stresses in the interfacial region accompanied with lower strength through the thickness. This is evident as the fibers provided along the plane of laminae do not render any reinforcing effect in the through-thickness direction leaving weaker matrix only to carry the loads in that direction. In addition, the tendency of delamination is increased by the matrices like brittle resins. It may occur due to failure in adhesives or glues joining the layers. Material fibers of higher strengths like carbon

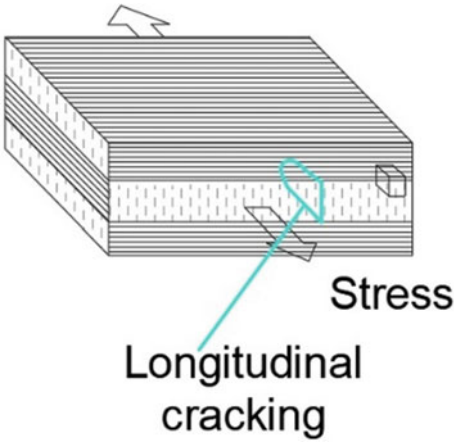

Fig. 5 Longitudinal cracking in cross-ply FRP laminates

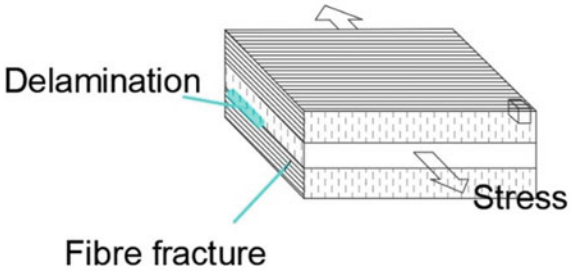

Fig. 6 Delamination and fibre fracture in FRPCs

or glass fibers are bonded together by lower strength matrices. Load applied in the direction perpendicular to the layer of higher strength or some shear force may cause fracture failure of matrix or debonding of fibers from the matrix. The separation of two layers of layered composite is schematically shown by aqua color in Fig. 6. Delamination may be there as manufacturing defect or may originate within the body of the composite component under service loads which are not visible on the exposed surfaces of the component. It may grow under applied loads or due to environmental effects finally leading to catastrophic failures and huge loss of wealth or life. This is one of the major concerns of the material scientists and engineers working with composite structures.

2.2.4 Breakage of Fibers

This mechanism finally leads to failures in fiber reinforced polymer composites. The name of the mechanism is self-explanatory. Typical breakage in fiber is schematically

shown in Fig. 6. As per fiber bundle approach, a number of fibers must break before ultimate failure under tensile loads [55]. Mechanical performance of laminated and other fiber reinforced composites can be degraded due to breakage in fibers [65]. Pullout and breakage of fibers appear to be common mechanisms of failures in the impact tests under low velocity. Due to shear force or high flexural stresses at the stress field induced in the sides opposite to the face indented or hit by the projectiles, fibers break or fail. Breakage of fibers may be caused by the high stress or instantaneous rise in temperature during indentation or experiment. High level fiber breakage may be experienced by a fibrous composite specimen at the location of impact [6]. This breakage of fibers obviously depends on many factors like fiber types, fiber volume ratio, original aspect ratio of fibers at initial stage and the stress–strain condition during manufacturing of fibers. Modelling on fiber breakage is exercised by research-group on ruptures in carbon composite [31, 42, 63] to address both the theory and applications.

2.3 Fracture Mechanics Approach in FRPC Problems

Some concepts of isotropic material approach in linear elastic fracture mechanics is difficult to implement for FRPCs for anisotropy and inhomogeneity. Anisotropy and inhomogeneity are there both in materials, and stacking sequence of laminae (i.e. several laminas in different directions) within the laminates invite complex problems.

The anisotropic materials with homogeneity can be used with fracture mechanics approach to deal with the FRPCs. Here, composite materials are assumed to be homogeneous but anisotropic. But in most of the cases FRPCs are not homogeneous revealing that this assumption is also insufficient to explain the behaviors of the FRPCs in true sense. Stress distribution around the crack tip is reported by Wu [74]. He finds that the stress intensities around the crack in affected by the properties of anisotropic materials, crack orientation with respect to the principal material axis and crack parameters. The researchers worked on the advancements in application of fracture mechanics to the problems of composite materials [10, 59, 69]. The problem is more critical in the case of fatigue. It is a complex phenomenon. Crack tends to grow parallel to the fibers in a self-similar pattern if the crack is cut in parallel to the fiber direction, whereas the crack growth is parallel to the fibers if cut at an angle to the fibers not parallel to the crack itself. In a laminate of various layers, the crack growth is much more complicated. Therefore, in reality, the growth prediction of different cracks in FRPCs is a complex problem.

2.4 Fracture in FRPCs Under Compression

Fracture and delamination in laminates may be caused by compression beyond a certain limit.

Fig. 7 Delamination of carbon fiber reinforced polymer under compression load [Courtesy: Wikimedia Commons (under free reuse license)]

This type of delamination followed by fracture due to compressive load beyond limit is presented in Fig. 7.

The crack-interactions among the cracks in orthotropic layered composites under compression were analyzed in a non-classical approach of fractures mechanics [72]. The problem was treated as transversely isotropic one with parallel fibers embedded in matrix and analyzed by finite element method. The investigators reported that the critical strain in layered materials under compressive loading not only depends on the interaction of cracks but also depends on the crack size and their mutual positions. There are several other works also on the fracture of FRPCs under compressive loads.

2.5 Fracture Failures of FRPCs in Different Scales

It is clear from the foregoing discussions that the fracture failure analysis of FRPCs is a complicated problem. Different approaches have been proposed to explain the behaviors of FRPCs subjected to fractures. Some of them are competent to explain certain behavior of particular or a group of FRPCs, but insufficient for others. This is

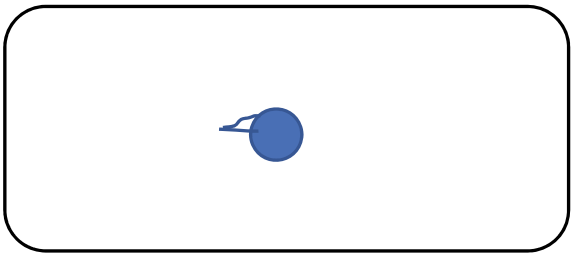

Fig. 8 Micro level flaw near a fiber in FRP

still an open field of research. To handle this complex problem of fracture failure, one such approach may be acceptable. The problem can be examined in different length scales to make it convenient for study [58]. In this context, it is logical to discuss on the failure mechanisms those occur in different scales, i.e. micro, meso and macro scales [36]. The study of fracture behaviors of fiber reinforced composites will be briefly addressed in the following section on the next page.

2.5.1 Fracture Study in Micro-scale

It is evident that there are inherent flaws within FRPCs due to manufacturing defects or some other reasons. These are the hotspots for the fracture initiation and further growths. Fracture starts at molecular or atomic levels at these hotspots. One of such flaws in the matrix at the location of a fiber is shown in Fig. 8 hiding all neighboring fibers. Crack may grow under service loads. The problem is much more complex when treated with fracture mechanics. Each of these mechanisms at micro level depends on the types of loading at macroscopic levels. How the effects of loads are distributed among these micro cracks, how they are affected is not clear till date. The bonds are damaged due to force exceeding some limits to initiate crack growth. For the uncertainties associated with these mechanisms, Monte-Carlo simulation was used by the investigators for prediction of failure [23, 35]. But there are limitations in capturing the complicacy as a whole. The diameter of the fiber (in microns) and their lengths are taken as input parameters which are much and much larger than atomistic scales which shows the incapability of this simulation in constituting microstructure explicitly. This is so much important for it permits to realize different failure mechanisms besides failure of individual ingredients. It is started with the flaws in atomistic scales at fiber location.

2.5.2 Fracture Study in Meso-scale

Meso scale is characterized by several hundred microns. Therefore, it addresses flaws extending through several fibers. One of such fractures extending through multiple

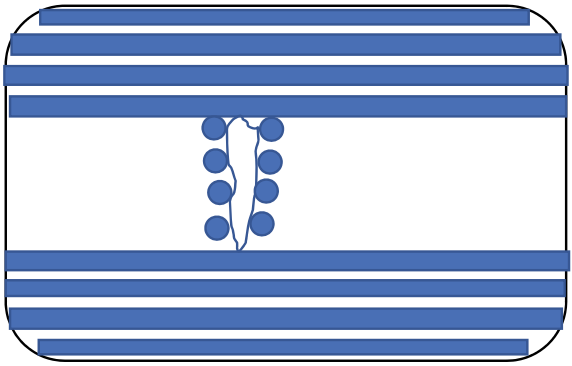

Fig. 9 Meso scale crack in FRP

fibers in a cross-ply laminate is shown in Fig. 9. In this type of fracture, the micro level mechanisms can grow and conglomerate through complicated mechanisms under external loading. Meso scale fracture study is useful for FRPCs made of fibers arranged with textile fashion for laminates with UD fibers are very weak in transvers direction with respect to the fiber direction. Laminates are often manufactured by stacking UD laminae in different directions, woven fabrics etc. Mesoscale is useful when the interactions of constituent plies of laminates in fracture is considered. Meso-scale fracture study can well address the inter-ply delamination as well as splitting. The important input parameter for the inter-ply delamination is the adhesion between the fiber and the matrix. The surfaces of fracture exhibit noticeable mutilated or hackle structures through branching and deflection of cracks [18] for increased bond strength consuming more energy for the same propagation length of relevant macroscopic crack.

If the individual ply is weak, then interlaminar crack can grow and propagate through it. But the bonding between the matrix and fiber is the key factor for delamination between the plies. Delamination may occur within a layer also if it is subjected to high stress in out-of-plane direction with rough surfaces of fracture and noticeable splitting of the layers of fibers as shown in Fig. 10.

Several plies of these laminates are subjected to different levels of stresses in axial direction. Strain coupling [57] is possible in this case if there is no interfacial damage between the laminae. The strength and elastic behaviors really depend on the orientation of the fibers at different plies with different states of stresses. Cracks between the fibers of the off-axis plies are readily observed under tension. Fracture depends on the configuration of loads and the sequence of the stack. These cracks

Fig. 10 Interlaminar delamination from inter-fiber cracks

may develop within the fibers in both the direction of loads or in a transverse direction to it. Consecutive plies with fibers in different directions may stop or halt the growth of cracks for the fibers in loading direction can avoid the matrix failure under local coupling of strains. But such cracks among the fibers may cause to more damage due to crack tip-stress concentration and lead to propagation of delamination between the layers of laminates.

Fiber bridging is another type of failures which may occur under tensile loading at mesoscopic scales due to low bonding strength between the matrix and fiber. Even after some pull out, the fibers in transverse direction to the crack propagation can resist the propagation of load to some extent.

In addition to the above some pores at mesoscopic level may exist within the laminated composites which can act as the local spot of stress concentration leading to delamination or buckling or may reduce the effective area of cross section to increase the stress level.

2.5.3 Fracture Study in Macro-scale

The scale ranges from some millimeters to meters. In this study, the laminate thickness or a whole structure can be covered. This macro-scale fracture is defined by the types of applied loads for a large range of mechanisms are covered within micro and meso scales. Fracture type inter-fiber may not result into fracture in macroscopic scales. But it may impair the stiffness. Macro level fracture may be due to an integral effect of several microscopic and mesoscopic failures. It can be observed from a test of T-pull, pattern of damage or fracture in a woven fabric composite. In fracture of woven fabric components, it is observed that through-thickness macroscopic fracture surfaces are results of branching of cracks into several mesoscopic cracks causing many inter laminar debonding, micro buckling of several layers and other micro or mesoscopic damages. On the microscale, cracks between fibers with breakage of fibers are observed. One of such macroscopic failure resulting from several micro and meso level failures may be damage due to impact. In the case of impact of low velocity, the damage may not be directly visible on the exposed surfaces but may cause serious damages in micro and meso scales causing delamination within the laminates finally leading to fractures.

3 FRPC Failure Theories

Many theories have been proposed to predict the failures of FRPCs over the decades to interlink the different microscopic and mesoscopic failure mechanisms leading to failures at macro-scales. Additionally, these vary for different type of loading and materials. The theories can be grouped under different categories based on their field of applications as follows:

1. Failure theories for static or quasi-static loads
2. Failure theories for damage mechanism, growth and degradation
3. Theories of failures under creep, fatigue and rupture due to stress
4. Theories for high strain rate failures.

Laminae are the building blocks of laminated composites. Before going to a brief review on most significant developments in this theoretical area, it will be legitimate to start with the micromechanics of UD FRPC lamina. Primarily following three modes of failures are observed at micro level [41, 66] in UD laminae made of FRPCs.

1. Failure dominated by fibers
2. Failures dominated by matrix
3. Interfacial failures or failures dominated by flaws.

Instead of failures are induced in FRPCs by the above-mentioned causes, global failures are not usually treated with them (which are considered at microlevels).

FRPCs fail gradually, stresses are redistributed among the other laminae when a particular lamina is affected by failure. Basically, in the analysis of failures. Strength is considered to be the important criterion. This strength of laminae is affected by directionality and there is significant difference between tensile and compressive strengths of UD lamina. Additionally, the direction of shear stress in comparison to the direction of fibers plays important role on the strength of UD lamina.

3.1 Micromechanical Failure of Fiber Reinforced Polymeric UD Lamina

The failure of UD FRPC lamina with their strengths with respect to the three phases (fiber, matrix and interfaces) will be briefly presented below.

3.1.1 Tension in Longitudinal Direction

The ingredient with lower ultimate strain will fail before the other for fiber and matrix exhibit different values of ultimate strains under tension. The stress in longitudinal direction of lamina is given by

$$\sigma_{1t} = \sigma_{1tf} V_f + \sigma_{1tm} V_m \tag{1}$$

where

σ_{1tf} is the average stress in fibers under uniaxial tensile load.
σ_{1tm} is the average stress in matrix under uniaxial tensile load.
V_f volume fraction of fiber present in the FRPC.
V_m volume fraction of matrix (resins or other polymers) in the FRPC.

There is a possibility of two cases.

Firstly, it is possible that the ultimate strain in matrix is greater than that of the fiber. The UD lamina will fail when strain in longitudinal direction exceeds ultimate strain in fiber. In that case, the strength of lamina in longitudinal direction is approximately given by

$$S_{1t} = S_{1tf} V_f + \sigma_{avm} V_m \tag{2}$$

where

S_{1t} is tensile strength of the lamina in longitudinal direction.
S_{1tf} is tensile strength of the fiber in longitudinal direction.
σ_{avm} is the average stress in the matrix in longitudinal direction at the time of ultimate strain in the fiber.

Secondly, the ultimate strain in fiber may be greater than that of the matrix.

The UD lamina will fail when strain in longitudinal direction exceeds ultimate strain in matrix. In that case, the strength of lamina in longitudinal direction is approximately given by

$$S_{1t} = S_{mt} V_m + \sigma_{avf} V_f \tag{3}$$

where

S_{mt} is tensile strength of the matrix.
σ_{avf} is the average stress in the fiber in longitudinal direction at the time of ultimate strain in the matrix.

This may be written in another form as

$$S_{1t} = S_{mt}\left(V_f \frac{E_{f1}}{E_m} + Vm\right) \tag{4}$$

E_{f1} is the elastic modulus of fiber in longitudinal direction.
E_m is the Modulus of elasticity of matrix material.

But the statistical distribution of the strength of fibers and matrix is not considered in above discussion [52, 53]. Strength in longitudinal direction in this case is governed by the strength of fibers.

Three different types of failures can be observed in FRPCs.

1. Transverse matrix crack for stronger interface and brittle matrix.
2. Matrix-fiber debonding for weaker interface and higher ultimate strain of fibers.
3. Failure through conical shear for stronger interface and matrix-ductility which does not occur in thermoset resins for thermosets are well known for their brittleness.

The stresses are redistributed among the other fibers when a particular fiber break. This is a localized phenomenon. A greater number of fibers break with increased loads. These localized failures result in eventual failures when they join together and interacts among them. The pattern of failure depends on the volume fractions of the constituents and their properties.

3.1.2 Compression in Longitudinal Direction

It is very difficult to verify the results of numerical analysis of UD FRPC lamina through experiment for two reasons.

Firstly, it is very difficult to arrange experimental setup for UD composite lamina through which it will be subjected to true compression only. Secondly, the experts may have the opinions that these structural components or the structures are rarely subjected to true compression. Except some special cases, instability influences the failure in these cases before failure under pure compression. Significant investigations have been exercised to address the compressive strength of FRPC [47].

Compression failure in longitudinal direction occurs due to micro-buckling or kinking of fibers. In out-of-phase micro-buckling, the compressive strength at low V_f is expressed as

$$S_{1c} \cong 2V_f \sqrt{\left[\frac{E_m E_{f1} V_f}{3(1 - V_f)}\right]} \tag{5}$$

compressive strength at higher V_f is expressed as

$$S_{1c} \cong \frac{G_m}{1 - V_f} \tag{6}$$

Expression (6) gives the compressive strength for the failure for higher V_f occurs due to in-phase or shear mode and G_m is the modulus of rigidity or shear modulus of the matrix. The compressive strength may be governed by the strength of fiber in shear also in another failure mode. In that case, compressive strength is expressed as

$$S_1 \cong 2S_{fs}\left[V_f + (1 - V_f)\frac{E_m}{E_{f1}}\right] \tag{7}$$

where

S_{fs} is the strength of the fiber in shear.

3.1.3 Tension in Transverse Direction

In case of UD lamina of FRPC, transverse tension is most critical for failure. Matrix and interphase experience very high strain or stress concentration under this loading. Distribution of stress about the fiber can be determined experimentally or theoretically. Experimentally it can be determined by photo elastic method. The methods of complex variable, finite element, boundary element or finite difference can be applied to determine the theoretical stress distribution. Primarily, the critical stress and the critical strains are developed in the interface between the fiber and the matrix.

Concept of stress concentration factor is used to determine the strength of the lamina under tension in transverse direction and that is related to the strain concentration factor as follows [14].

$$\mathrm{K_e} = \frac{e_{2\max}}{e_2} \cong K_s \left(\frac{E_{2t}}{E_m}\right) \frac{(1-\nu_m)(1-2\nu_m)}{1-V_m} \tag{8}$$

where

$\mathrm{K_e}$ is the factor of strain concentration.
$\mathrm{K_s}$ factor of stress concentration.
e_{2max} Maximum value of strain in transverse direction.
e_2 Average value of transverse strain.
ν_m Poisson's ratio for the matrix material.

Composite laminas are subjected to thermal stress in many cases. Curing of matrix induces residual stress and residual strains. The induced stresses cause difference in values of thermal coefficients in the ingredients. Failures of composite laminae subjected to thermal stresses are predicted through the linear relation between the stress and strains. If the thermal stress is considered with criterion for the maximum stress, then the tensile strength of FRPC in transverse direction can be expressed as

$$\mathrm{S_{2t}} = \frac{1}{K_s}(S_{tm} - \sigma_{mr}) \tag{9a}$$

where

σ_{mr} Maximum value of residual stress.

If the thermal stress is considered with criterion for the maximum strain, then the tensile strength of FRPC in transverse direction can be expressed as

$$\mathrm{S_{2t}} = \frac{(1-\nu_m)}{K_s(1+V_m)(1-2\nu_m)}(S_{tm} - e_{mr}E_m) \tag{9b}$$

where

e_{mr} Maximum value of residual strain.

3.1.4 Compression in Transverse Direction

Several mechanisms in UD FRPCs may result in compression failures. Stress concentration at of high magnitude at the interface under compression may lead to matrix failure or fiber failure through crushing. The transverse compressive stress of UD composite lamina is

$$S_{2C} = \frac{1}{K_s}(S_{cm} - \sigma_{mr}) \tag{10}$$

where

S_{cm} matrix-compressive-strength.

Overall shear failure may be observed at higher stress under compression for higher stress at the interface resulting in delamination or shear failure in matrix.

3.1.5 In Plane Shear

The interface between the matrix and fiber of UD lamina is the worst affected region under inplane shear. It can be fairly assumed that the matrix of UD lamina fails under inplane shear, and the predicted shear strength is given by

$$S_6 = \frac{S_{sm}}{K_\tau} \tag{11}$$

where

K_τ concentration factor for the shear strength.
S_{sm} Shear strength of the matrix.

The values of K_τ varies with the materials and V_f which can be determined by the method of finite difference [1].

3.2 Anisotropic Failure Theories

Prediction on failure initiation from micromechanical analysis is acceptable at critical points. In case of global failures, that is an approximation only. Micromechanically, laminae are anisotropic and the strength is a function of the direction of fibers. Lamina may have five parameters for in plane micromechanical strengths—S_{1t}, S_{c1}, S_{2t}, S_{2C} and S_6.

Theories of micromechanical failures of composites are adoption and extensions of isotropic theories. There is a good review on the anisotropic composite failure theories [60].

Four failure criteria are basically employed to explain failures of FRPCs.

1. Theory of maximum stress
2. Theory of maximum strain
3. Theory of deviatoric strain energy or Tsai-Hill theory
4. Theory of tensor polynomial or Tsai-Wu theory.

3.2.1 Theory of Maximum Stress

This theory states that the UD lamina fails when a stress component reaches a value of the strength in the direction of corresponding principal axis. The stresses in a complex state can be transformed into stresses in principal axes of the materials. Failure takes place when

$$\sigma_1 = \left.\begin{array}{c} S_{1t} \text{ when } \sigma_1 \text{ is positive} \\ -S_{c1} \text{ when } \sigma_1 \text{ is negative} \end{array}\right\} \tag{12a}$$

$$\sigma_2 = \left.\begin{array}{c} S_{2t} \text{ when } \sigma_2 \text{ is positive} \\ -S_{2c} \text{ when } \sigma_2 \text{ is negative} \end{array}\right\} \tag{12b}$$

$$|\sigma_6| = S_6 \tag{12c}$$

$$\begin{aligned} \sigma_1 &= \sigma_x \cos^2 \theta \\ \sigma_2 &= \sigma_x \sin^2 \theta \\ \sigma_6 &= -\sigma_x \cos\theta \sin\theta \end{aligned} \tag{13}$$

Equating strengths to corresponding stresses, strengths in off-axis direction (S_x) are determined as follows (Fig. 11).

For σ_x is tensile, i.e., $\sigma_{x,}$ is positive

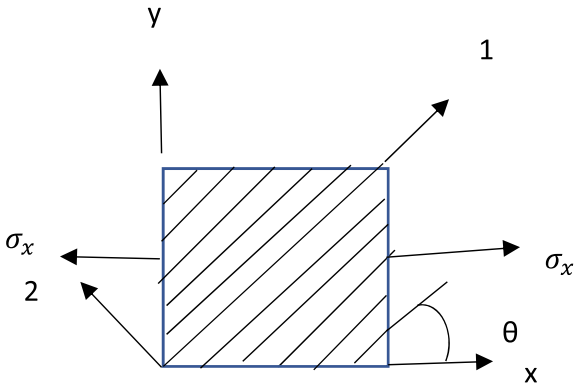

Fig. 11 Unidirectional lamina under off-axis load

$$
\begin{aligned}
S_{xt} &= \frac{S_{1t}}{\cos^2\theta} \\
S_{xt} &= \frac{S_{2t}}{\sin^2\theta} \\
S_{xt} &= \frac{S_6}{\cos\theta\,\sin\theta}
\end{aligned} \tag{14}
$$

For σ_x is compresive, i.e., $\sigma_{x,}$ is negative

$$
\begin{aligned}
S_{xc} &= \frac{S_{1c}}{\cos^2\theta} \\
S_{xc} &= \frac{S_{2c}}{\sin^2\theta} \\
S_{xc} &= \frac{S_6}{\cos\theta\,\sin\theta}
\end{aligned} \tag{15}
$$

According to theory of maximum stress, only three out of five subcriteria are applicable depending on whether σ_x is compressive or tensile. As per this theory, failure in any direction is not dependent on the stresses in its perpendicular directions. The interaction of stresses as in biaxial stresses is not considered in this theory.

3.2.2 Theory of Maximum Strains

This theory states that the UD lamina fails when a strain component reaches a value of the ultimate strain in the direction of corresponding principal axis. The stresses in a complex state can be transformed into stresses in principal axes of the materials. Failure takes place when

$$
e_1 = \left.\begin{array}{l} e_{1tu} \text{ if } e_1 \text{ is positive} \\ e_{1cu} \text{ if } e_1 \text{ is negative} \end{array}\right\} \tag{16a}
$$

$$
e_2 = \left.\begin{array}{l} e_{2tu} \text{ if } e_2 \text{ is positive} \\ e_{2cu} \text{ if } e_2 \text{ is negative} \end{array}\right\} \tag{16b}
$$

$$
e_6 = e_{6u} \tag{16c}
$$

where

e_{1tu} is ultimate tensile strain in longitudinal direction.
e_{1cu} is ultimate compressive strain in longitudinal direction.
e_{2tu} is ultimate tensile strain in transverse direction.
e_{2cu} is ultimate compressive strain in transverse direction.
e_{6u} is in plane ultimate shear strain.

In case of biaxial stresses, stresses in xy-coordinate axes are expressed in 1–2 axes (principal axes system of material) through transformation. The components of strains in 1–2 axes system can be obtained from the relation between stress and strains.

$$e_1 = \frac{1}{E_1}(\sigma_1 - \nu_{12}\sigma_2) \tag{17a}$$

$$e_2 = \frac{1}{E_2}(\sigma_2 - \nu_{21}\sigma_1) \tag{17b}$$

$$e_6 = \frac{\sigma_6}{E_6} \tag{17c}$$

The signs in principal direction of the material for the shear stresses are shown in Figs. 12 and 13.

In case of UD lamina, ultimate strains can be determined from basic parameters of the strengths.

$$e_{1tu} = \frac{S_{1t}}{E_1}$$

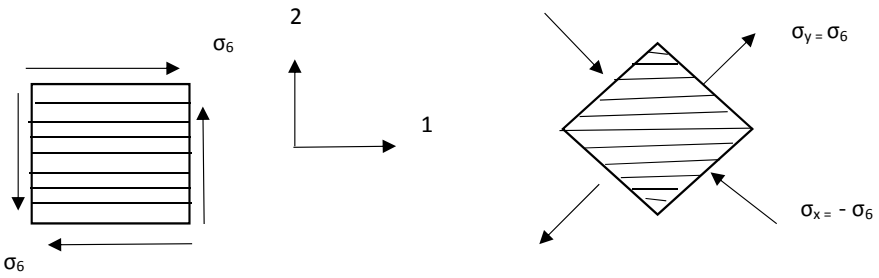

Fig. 12 Positive shear stress

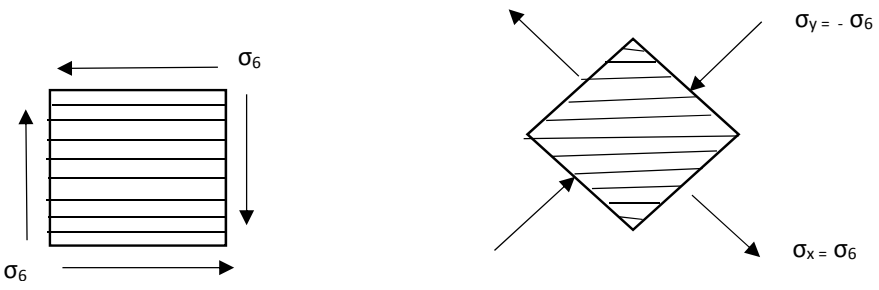

Fig. 13 Negative shear stress

$$\begin{aligned} e_{1cu} &= -\frac{S_{1c}}{E_1} \\ e_{2tu} &= \frac{S_{2t}}{E_2} \\ e_{2cu} &= -\frac{S_{2c}}{E_2} \\ e_{6u} &= \frac{S_6}{E_6} \end{aligned} \tag{18}$$

The criteria for failure in general state of biaxial stress can be written as

$$\sigma_1 - \nu_{12}\sigma_2 = \left.\begin{array}{c} S_{1t} \text{ if } e_1 \text{ is positive} \\ -S_{1c} \text{ if } e_1 \text{ is negative} \end{array}\right\} \tag{19a}$$

$$\sigma_2 - \nu_{21}\sigma_1 = \left.\begin{array}{c} S_{2t} \text{ if } e_2 \text{ is positive} \\ -S_{2c} \text{ if } e_2 \text{ is negative} \end{array}\right\} \tag{19b}$$

$$|\sigma_6| = S_6 \tag{19c}$$

According to theory of maximum strains, number of subcriteria is five. Material can experience strain in any direction without any applied stress in that direction due to Poisson's or residual thermal effects. The interaction of strains is not considered in this theory also.

3.2.3 Theory of Deviatoric Strain Energy or Tsai-Hill Theory

In three-dimensional stress field, the yield criterion proposed by von Mises for isotropic materials is expressed as

$$\sigma_1^2 + \sigma_2^2 + \sigma_3^2 - \sigma_1\sigma_2 - \sigma_2\sigma_3 - \sigma_3\sigma_1 = \sigma_{yp}^2 \tag{20}$$

where

σ_{yp} is material's yield stress.

This criterion for isotropic material was modified by Hill [24] to describe anisotropic behavior of isotropic metals for large deformation in plastic region.

$$A\sigma_1^2 + B\sigma_2^2 + C\sigma_1\sigma_2 + D\sigma_6^2 + E\sigma_3^2 + F\sigma_2\sigma_3 + G\sigma_3\sigma_1 + H\sigma_4^2 + I\sigma_5^2 = 1 \tag{21}$$

Equation (21) can be expressed as following for a two-dimensional problem

$$A\sigma_1^2 + B\sigma_2^2 + C\sigma_1\sigma_2 + D\sigma_6^2 = 1 \tag{22}$$

The constants A, B, C, etc. depend on the anisotropy of the material.

Assuming FRPCs as transversely isotropic, and 1-direction as the direction of fibers Tsai and Azzi [5] expressed the following relations for FRP composite in two-dimensional stress field from the relation (22) provided by Hill.

In case of failure under in plane shear.

$\sigma_{6u} = S_6$ and $\sigma_2 = \sigma_1 = 0$. The relation (22) is modified as

$$D = \frac{1}{S_6^2} \tag{23}$$

In case of failure under uniaxial loading in transverse direction.

$\sigma_{2u} = S_2$ and $\sigma_6 = \sigma_1 = 0$. The relation (22) is modified as

$$B = \frac{1}{S_2^2} \tag{24}$$

In case of failure under uniaxial loading in longitudinal direction.

$\sigma_{1u} = S_1$ and $\sigma_6 = \sigma_2 = 0$. The relation (22) is modified as

$$A = \frac{1}{S_1^2} \tag{25}$$

Only C is the remaining parameter which can be determined from the interaction between σ_2 and σ_1 through biaxial test. Alternately, for equal loading along both the axes, though $\sigma_6 = 0$; $\sigma_2 = \sigma_1 \neq 0$. Failure of the material can be defined by criteria of maximum stress. That is the material will fail when σ_2 reaches composite strength in transverse direction for $S_2 \ll S_1$. The relation (22) can be expressed as

$$C = -\frac{1}{S_1^2} \tag{26}$$

Then Eq. (22) can be expressed with these values of A, B, C, D as

$$\frac{1}{S_1^2}\sigma_1^2 + \frac{1}{S_2^2}\sigma_2^2 - \frac{1}{S_1^2}\sigma_1\sigma_2 + \frac{1}{S_6^2}\sigma_6^2 = 1 \tag{27}$$

where

$$S_1 = S_{1t} \text{ or } S_{1c}$$

$$S_2 = S_{2t} \text{ or } S_{2c}$$

The tensile strength is to be used for S_1 and S_2 values when the composite is subjected to tension and the compressive strength is to be used for S_1 and S_2 values when compressive load is applied on the composite.

Equation (27) can be written as

$$\frac{1}{S_1^2}\sigma_1^2 + \frac{1}{S_2^2}\sigma_2^2 - \left(\frac{\sigma_1}{S_1}\right)\left(\frac{\sigma 2}{S_2}\right) + \frac{1}{S_6^2}\sigma_6^2 = 1 \tag{28}$$

The relation can be expressed as the following one for uniaxial off-axis load (Figs. 10 and 11) using Eqs. (13) and (28).

$$\frac{1}{S_x^2} = \frac{m^4}{S_1^2} + \frac{n^4}{S_2^2} + \left(\frac{1}{S_6^2} - \frac{1}{S_1 S_2}\right)\mathrm{m}^2\mathrm{n}^2 \tag{29}$$

where $\mathrm{m} = \cos\theta$, $\mathrm{n} = \sin\theta$ and $\mathrm{S_x} = \sigma_{\mathrm{xu}}$.

For advanced composites

$\mathrm{S_1} \gg \mathrm{S_6}$, Eq. (29) is transformed to

$$\frac{1}{S_x^2} = \frac{m^4}{S_1^2} + \frac{n^4}{S_2^2} + \frac{m^2 n^2}{S_6^2} \tag{30}$$

Tsai-Hill criterion is a single criterion. This is the primary advantage of it over theories of maximum stress and maximum strain (with many criteria). Though the interaction between $\mathrm{S_1}$, $\mathrm{S_2}$ and $\mathrm{S_6}$ is considered but the tensile and compressive strengths are not separately considered in Tsai-Hill criterion.

3.2.4 Theory of Tensor Polynomial or Tsai-Wu Theory

A theory of tensor polynomial has been proposed and modified by Tsai and Wu [64] with the assumption of existence of a failure surface within stress space which can be expressed with contracted notations as follows:

$$S_i\sigma_i + S_{ij}\sigma_{ij} = 1 \tag{31}$$

S_i is second rank strength tensor.
S_{ij} is forth rank strength tensor.

Equation (31) is a very complicated one. The expanded form of Eq. (31) for an orthotropic lamina in plane stress is given by

$$S_1\sigma_1 + S_2\sigma_2 + S_6\sigma_6 + S_{11}\sigma_1^2 + S_{22}\sigma_2^2 + S_{66}\sigma_6^2 + 2S_{12}\sigma_1\sigma_2 + 2S_{16}\sigma_1\sigma_6 + 2S_{26}\sigma_2\sigma_6 = 1 \tag{32}$$

S_{12} incorporates the interaction between σ_1 and σ_2.

Tsai-Wu theory of failure is most general among all the theories discussed in Sect. 3.2.

Maximum stress criterion, maximum strain criterion, and Tsai-Wu theory have been discussed as they are the most popular criteria for strength of composites for

these are based on simple specimens subjected to tension, compression or shear. Further, these can be used to predict the failure loads of composite structures subjected to combined stress.

Important developments in the failure theories will be summarized below for the FRPCs without going to detailed discussion on complicated Tsai-Wu theory. The current developments and usage of experimentally determined input parameters of the theories will be emphasized in the following sections.

It is already mentioned in Sect. 3 that the failure theories can be grouped under four major classes:

1. Failure theories for static or quasi-static loads
2. Failure theories for damage mechanism, growth and degradation
3. Theories of failures under creep, fatigue and rupture due to stress
4. Theories for high strain rate failures.

3.2.5 Failure Theories for Static or Quasi-static Loads

Tsai-Wu-Criteria is one of the famous such failure theories [64, 75]. Hashin [22] showed that this criterion is not consistent with all the stress states of FRPCs inviting new development in the theories. Hashin adopted Mohr's criterion [39] for fracture failure of brittle materials. Hinton with the team performed a notable task to work out predictive capabilities of the failure theories [26, 27, 33]. In this series of attempts, the theories provided by Pinho et al. [45], Cuntze [12] and other two researcher groups were capable of holding best position for predicting the behaviors under 3-D state of stresses.

3.2.6 Failure Theories for Damage Mechanism, Growth and Degradation

Failure at macroscopic level through the summation of microscopic failure mechanism is experimentally challenging. In addition to it, the computational exercise in microscopic level in fact is very much intensive from computational point of view. Stress–strain relations in macro-scales, homogeneity, orthotropic symmetry with layers free from defects are considered to be acceptable for analytical analyses. In this approach, classical laminate theory (CLT) is valid. Layer-wise theory is used to predict the failures. Progress of damage within laminates with fracture mechanics concepts using strain energy of laminates subjected to triaxial loading is studied [16]. In another notable study, the capability of different criteria to predict delamination and initiation of cracks within the matrix has been compared [34] to conclude that experimental verification will be necessary to select which theory will be best in this approach to predict the behavior.

3.2.7 Theories of Failures Under Creep, Fatigue and Rupture Due to Stress

The investigations on prediction of failures due to creep, fatigue and ruptures caused by stresses are limited. As per definition [47] a strain rate less than 10^{-6} s^{-1} is considered as creep. In case of polymers reinforced with fibers creep generally cause unacceptable degradation but not always. Besides some studies, there are no much theories proposed for this type of failures of the FRPCs. In case of stress rupture, different theories produced similar results in prediction of life time. Some accelerated tests discussed [44] in literature needs further validation regarding stress-rupture. The investigation on viscoelastic materials in this field is extremely limited. Study of FRPCs under fatigue load is being continued for a long time. Behavior of FRPCs under fatigue load is extremely complicated and challenging field both from experimental as well as computational point of view. Studies are still being continued in several composite research centres. Prediction of actual point of time for initiation of cracks is really challenging. Statistical approach is essential for large number of scattered data. Nevertheless, the study and prediction of fatigue lives are essential for important structural designs. Different criteria have been proposed with their competencies and limitations.

3.2.8 Theories for High Strain Rate Failures

Currently, use of FRPCs in crash-worthy structures has been increased. This ensures the importance of studies under high strain rates. Unlike the other failures discussed in foregoing sections, the failure is sudden. A The rate of strain beyond 10^2 per second is considered as high strain rate. A strain rate of 10^6 per second can also be realized from special cases. The failure is of different nature for there is no scope of stress redistribution or relaxation etc. Instead of failure theories, several investigations have been carried out in this field with continuous refinements and developments along with the use of digital image correlation (DIC) techniques [38]. The location and the impact energy are being monitored by using sensors.

There is no criterion which is accepted universally for the failure of composites [25].

Instead of an appreciable number of failure theories has been developed, no criterion alone can accurately predict the failure of all FRPCs under all classes of loadings [29].

Large scale applicability of Tsai-Wu criteria in industrial composites is due to its capability in predicting composites' strengths reasonably. But the failure mode is not predicted through this criterion [25]. On the other hand, it is to be noted that World-Wide -Failure-Exercise concluded that no failure model predicted the failure accurately [25].

In early 1960s, the competitors of metals among FRPCs were boron or carbon fiber reinforced polymeric composites. Polymeric matrices like epoxy resins with

low toughness were not considered for determining the toughness of the composites. Improved matrices with considerable toughness were developed as per civil and military demands of applications in 1980s. Moreover, new fibers are also developed in the composite world. This resulted in improvements and development of experimental techniques for investigation on the toughness and tolerance of FRPCs against fracture/damage. New test methods were proposed and developed for testing FRPCs including different modes of fracture tests under experimental fracture mechanics. These experimental investigations will be addressed in the following section.

4 Experimental Investigations on FRPCs

Experimental mechanics, especially experimental fracture mechanics are frequently used to measure the parameters and to realize the behaviors of FRPCs for the different limitations of the mathematical prediction theories and criteria. Experimental investigation itself may suffer from errors due to error in experimental setup and different other factors. Experimental setup for advanced fiber reinforced composites is generally expensive but experimental approach is the only way where reliable input data are not available for numerical simulations or analytical studies. Recently, both the industrial and political sectors of some countries have realized the importance of research on FRPCs. Experimental investigations play a great role towards fulfilment of this demand goals of research in this field.

Numerous experiments were performed by Wu [74] on FRPC material for realizing the extent of applicability of fracture mechanics of linearly elastic materials. He investigated on UD FRPCs with central cracks for critical loads and lengths (of cracks) at the initiation of rapid extension of cracks with different crack orientation and several loadings with respect to direction of fibers. Cracks were recorded to propagate colinearly with the original cracks. In addition, the opening mode was led by the symmetric loading while sliding mode was observed under skew symmetric loadings. For tensile load $\sigma\infty$ perpendicular to the central crack parallel to fibers, the intensity factors for stress are

$$\begin{aligned} k_1 &= \sigma\infty(a)^{1/2} \\ k_2 &= 0 \end{aligned} \tag{33}$$

Critical intensity factors for stress are

$$\begin{aligned} k_{1c} &= \sigma_c\infty(a_c)^{1/2} \\ k_{2c} &= 0 \end{aligned} \tag{34}$$

where

$\sigma_c\infty$ is defined as critical stress and the half crack length at the point of initiation of fast crack extension is denoted by a_c. Equation (34) can be written as

$$\log k_{1c} = \log \sigma_c \infty + \frac{1}{2} \log a_c \tag{35a}$$

$$\text{i.e., } \log \sigma_c \infty = -\frac{1}{2} \log a_c + \log k_{1c} \tag{35b}$$

Equation (35b) indicates that a plot of $\log \sigma_c \infty$ versus $\log a_c$ will be a straight line with a slope of $-(1/2)$ if k_{1c} is considered as a constant expressing material property. In fact, the slope is determined to be -0.49 [18] which shows that the theory is applicable to orthotropic thin lamina with cracks in principal direction of the material, i.e., in the direction parallel to the fibers. Numerous works of researchers through decades have advanced the level of knowledge on application of fracture mechanics to the fracture problems of FRPCs.

4.1 Fracture Toughness of FRPCs

Selection of a materials for an application is based on its toughness.

Fracture toughness (FT) indicates the resistance of a material against the growth of a crack which is measured in terms of intensity factor for stress or rate of release of the strain energy G_c at critical stage of crack growth. In anisotropic FRPCs, the highest fracture toughness is measured during in-plane fracture. This in-plane fracture is associated with pull-out or breakage of fibers. Lowest fracture toughness is recorded in interlaminar delamination. Fracture toughness of wood or fiber reinforced such other natural composites also reflect the anisotropic characters. This parameter largely depends on the properties of constituent materials of the FRPCs. The toughness of FRPCs against fracture can be improved through materials modifications like toughening matrices or by structural modifications like stitching, pinning etc. Additionally, many factors (Wu proposes seven factors) influence the resistance of the materials against fracture. Dr. Hyer demonstrated that none of the prediction models are capable of predicting the fracture behaviors of the each FRP composites under all conditions. In addition, the most general one, i.e., Tsai-Wu criteria is a very involved one with its limitations. Experimental investigations on mode I, mode II, mode III and mixed mode fractures are frequently used for determination of fracture toughness of FRPCs under quasi static loads for understanding the fracture behaviors. Numerous investigations on fracture behaviors of FRPCs under fatigue loads have been undertaken through decades. The uncertainties associated with fracture of FRPCs needs rigorous statistical approaches for determining a most probable fracture and fracture toughness under fatigue loadings. To introduce the readers first with the fracture events under quasi static loads will be briefly introduced in the following sections before addressing complicated fatigue behaviors of FRPCs.

4.2 Experimental Investigations on Fracture Toughness of FRPCs

A majority of the research works on FRPCs from early 1970s has focused on application of LEFM or linear elastic fracture mechanics in determining the fracture toughness. In case of thermoset polymeric composites, with randomly oriented short fibers more or less 0.5 mm long, the inelastic zone in front of crack tip is small enough to apply LEFM on the crack initiation and propagation. But the inelastic region ahead of the crack tip for long fibers (>25 mm) is sufficiently extended and the assumption of small yielding required for application of LEFM is no longer valid. In that case, some alternative procedure like that based on tension-softening plot or fracture mechanics applicable to non-linear characters are more acceptable to determine the fracture toughness of FRPCs [40].

As already stated in Sect. 2.1, fracture mechanics is the mechanics of cracks which includes the mechanisms from initiation to propagation of cracks and is applied in analysis and design of composites materials and structures. One of the primary objectives of analysis through fracture mechanics is prediction of initiation of crack and its growth in a material body with a cracks-size. LEFM is applicable to cracks in some composites [71] and in UD composites of brittle matrices [70]. The state of crack can be understood from the elastic stress intensity in the field about the crack tip. It is realized from the investigations that stress singularity is a function of—$(r_e)^{1/2}$ at a distance r_e from crack tip in homogeneous and isotropic or orthotropic materials [2]. If the plane of crack follows any plane of symmetry of orthotropic materials, the intensity factors for stress can be calculated [61]. Loadings at crack tip can be partitioned into three modes of fractures as shown in Figs. 1, 2 and 3. Mode I, Mode II and mode III [8].

It is becoming a common tendency to investigate interfacial cracks applying the concept of rate of energy release G. It is derived from energy considerations, defined mathematically and can be measured experimentally. It is based on original Griffith's criterion of fracture which considers the energy required for extension of crack from the available energy.

Potential of elastic energy in a body with crack can be expressed as

$$V = W_e - U_i \tag{36}$$

where

W_e is the work done by external forces,
U_i is the strain energy due to strain of the body.

The energy required for creation of unit area of crack (G_c) due to crack growth is given by

$$\delta V \geq Gc\delta A \tag{37}$$

In which, increase in the area of crack is given by δA.

At critical condition, the net energy is used to just balance the energy required for creation of unit area of crack (G_c). The condition can be expressed as

$$\delta V = Gc\delta A \tag{38}$$

The crack grows when the equilibrium is disturbed. i.e.,

$$\delta V > G_c\delta A \tag{39}$$

The rate of release of energy G is given by

$$\mathrm{G} = \frac{\delta V}{\delta A} \tag{40}$$

Then, the fracture criteria can be expressed as

$$\mathrm{G} > G_c \tag{41}$$

This can be demonstrated through Fig. 14 for a body which is linearly elastic with initial crack size "a". It is assumed that the growth of crack occurs at fixed load or constant displacement (grip is fixed).

In case of fixed load,

$$\delta U_i = {}^1\!/_2(\mathrm{F}\delta\mathrm{x}) \tag{42}$$

$$\delta W_e = \mathrm{F}\delta\mathrm{x} \tag{43}$$

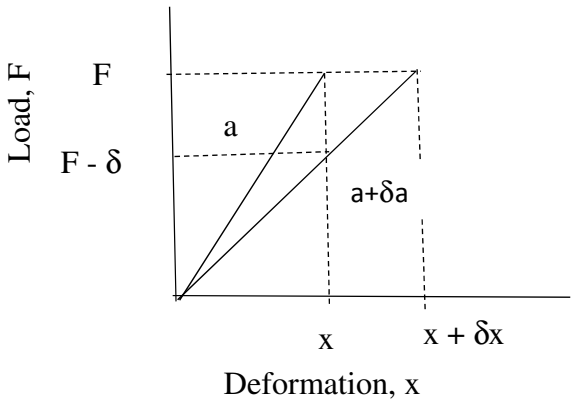

Fig. 14 Load deformation plot for crack size a and a + δa

From Eq. (36),

$$\delta V = F\delta x - {}^1/_2(F\delta x) = {}^1/_2(F\delta x) \tag{44}$$

Then, Eq. (40) can be written as

$$G = {}^1/_2(F\delta x/\delta A) \tag{45}$$

In case of *constant displacement*, i.e., when the grip is fixed, the W_e is zero and

$$\delta V = {}^1/_2(x\delta F) \tag{46}$$

Stiffness is reduced due to crack extension, for that, the δF is negative.

$$G = -{}^1/_2(x\delta F/\delta A) \tag{47}$$

As the material is linearly elastic, therefore,

$$x = CF \tag{48}$$

In Eq. (48), compliance is denoted by C.
Using the Eqs. (48) and (45) for fixed load,

$$G = {}^1/_2F^2(\delta C/\delta A) \tag{49}$$

In case of *fixed displacement*, i.e., when the grip is fixed, substituting F = x/C in Eq. (47)

$$G = \frac{x^2}{2C^2}\frac{\partial C}{\partial A} = \frac{F^2}{2}\frac{\partial C}{\partial A} \tag{50}$$

It is clear from Eqs. (49) and (50) that both for fixed load and fixed displacement cases, the rate of energy release G is given by same expression.

If a crack in principal plane of material is considered, it can be decomposed into three modes of cracks shown in Figs. 1, 2 and 3. That is

$$G = G_I + G_{II} + G_{III} \tag{51}$$

where

G_I rate of energy release due to mode I component of crack,
G_{II} rate of energy release due to mode II component of crack and
G_{III} rate of energy release due to mode III component of crack.

Theoretically, the above components can be determined from Irwin's concept which states that the energy release for a small crack is equal to the energy required

to close the crack for the same length. To maintain the direction of this section, the experimental methods for determining these components will be discussed in the following section.

4.2.1 Experimental Investigations on Mode I Fracture Toughness of FRPCs

Method of mode I interlaminar fracture toughness of unidirectional fiber-reinforced polymer matrix composites is specified in ASTM D 5528-13 [3]. The schematic of the specimen is shown in Fig. 15. The initial delamination in DCB testing of composites is placed symmetrically at mid-plane as shown in Fig. 15. The two cantilever limbs on both top and bottom of pre-crack is assumed to be firmly supported at the remaining portion of the specimen. Load is applied through the hinge tab fixed at top of the upper cantilever limb of the sample while the advancement of crack is recorded with the load displacement data of the experiment. Determination of global compliance (C) as a function of crack length (a) is typically obtained in the analysis of fracture test specimens. The energy release rate G is obtained by differentiating C with respect to a and is given by the following equation,

$$G = \frac{P^2}{2b}\frac{dC}{da} \tag{52}$$

where b is the specimen width and P is the applied load. C is the compliance given by

$$\mathrm{C} = \delta/\mathrm{P} \tag{53}$$

and δ is the displacement of the loading point.

At critical condition,

$$G_c = \frac{P_c^2}{2b}\frac{dC}{da} \tag{54}$$

and

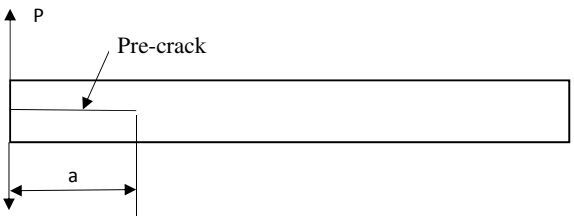

Fig. 15 Double cantilever beam specimen

$$C_c = \frac{\delta_c}{P_c} \tag{55}$$

Analytical solution of compliance (C) as a function of crack length, C(a) is possible in some specimen with simpler geometry, loading and support conditions. The energy release rate (G) is obtained by differentiation of C(a) with respect to crack length (a) as per Eq. (52). Experimentally, compliance versus crack length data of the DCB specimen is fitted to a power function of crack length as

$$C = C_0 a^n \tag{56}$$

From Eqs. (54) and (56),

$$G = \frac{nP\delta}{2ab} \tag{57}$$

Under critical condition like crack initiation point in DCB test

$$G_c = \frac{nP_c\delta_c}{2ab} \tag{58}$$

The value of parameter n can be determined by curve fitting to the experimental compliance (C) versus crack length (a) plot. Once the value of n is experimentally determined, the energy release rate G can be calculated from Eq. (58) for each crack length (a).

4.2.2 Experimental Investigations on Mode II Fracture Toughness of FRPCs

End notch flexure (ENF) test specimen used for mode II fracture characterization originally developed for wooden beam and applied to laminated composite by Russell [54] as shown in Fig. 16 who used this specimen as an end-delaminated three-point bend specimen to measure the Mode II interlaminar fracture energy of graphite/epoxy laminates. This specimen is used for mode II test in which the element of monolithic composites at crack tip is subjected to shear stress due to this experimental setup.

4.2.3 Experimental Investigations on Mode III Fracture Toughness of FRPCs

In spite of numerous works in mode I, mode II or mixed mode (mode I and mode II) testing, the study on mode III testing of sandwich is remarkably less due to presence of unwanted mode II component at the crack tip caused by in-plane bending moment higher near the edge. Among the test methods for mode III, Split Cantilever Beam (SCB) test set up shown in Fig. 17is most commonly used which is first used by

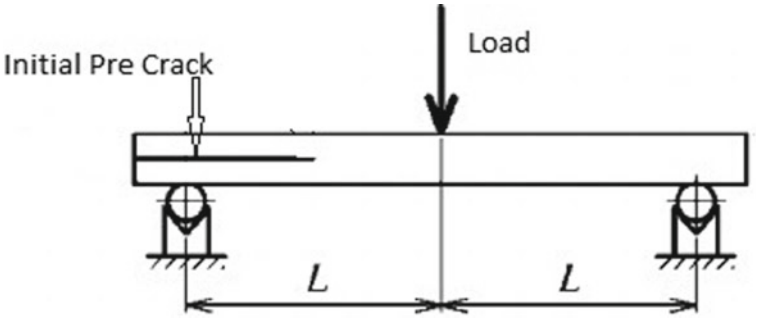

Fig. 16 End notch flexure test (ENF) specimen for mode II test

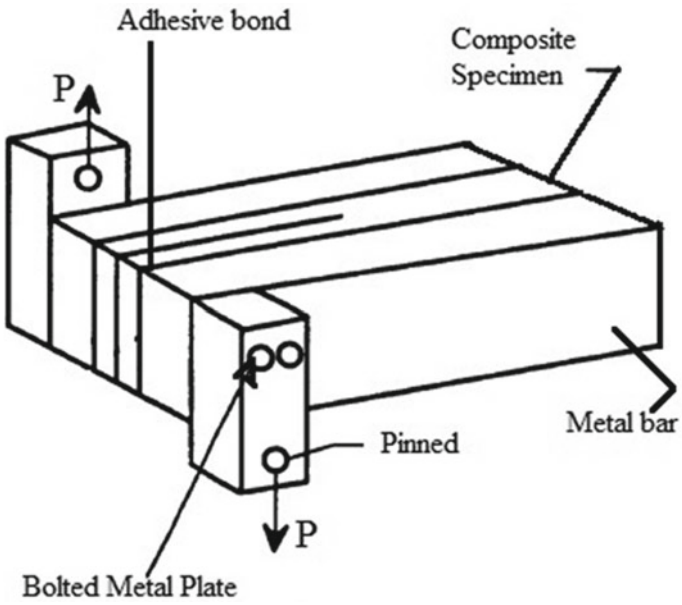

Fig. 17 Split cantilever beam test configuration

Donaldson [15]. Robinson and Song [50] modified the split cantilever beam setup by introducing additional loading points to reduce the unwanted mode II component.

4.2.4 Experimental Investigations on Mixed Mode Fracture Toughness of FRPCs

In a number of cases, failure due to delamination is associated with mixed mode loading (i.e. mixed mode I, mode II and /or mode III loading). In laminated composites, initiation of crack or its propagation is caused by influence of both mode I (causing normal stress) and shear stresses (mode II). The procedure of test for delamination under mixed-mode loading was executed by combining setup of loading DCB specimens for mode I test and the setup of loading ENF specimens for mode II test of UD laminates. A single load (F) applied through a lever can induce both mode I and mode II components of loading on the specimen as shown in Fig. 18. Delamination under combined normal and shear stresses was experimentally investigated by Crews [11] and Reeder [49]. Experimentally, laminated composite specimens are tested with mixed mode bending (MMB) apparatus. Loading in MMB apparatus can be considered as the combined mode I and mode II loadings [3, 4].

The test can be executed for different mode ratios (G_I/G_{II}) by changing the positions of load applications on the lever. The standard testing procedure for MMB

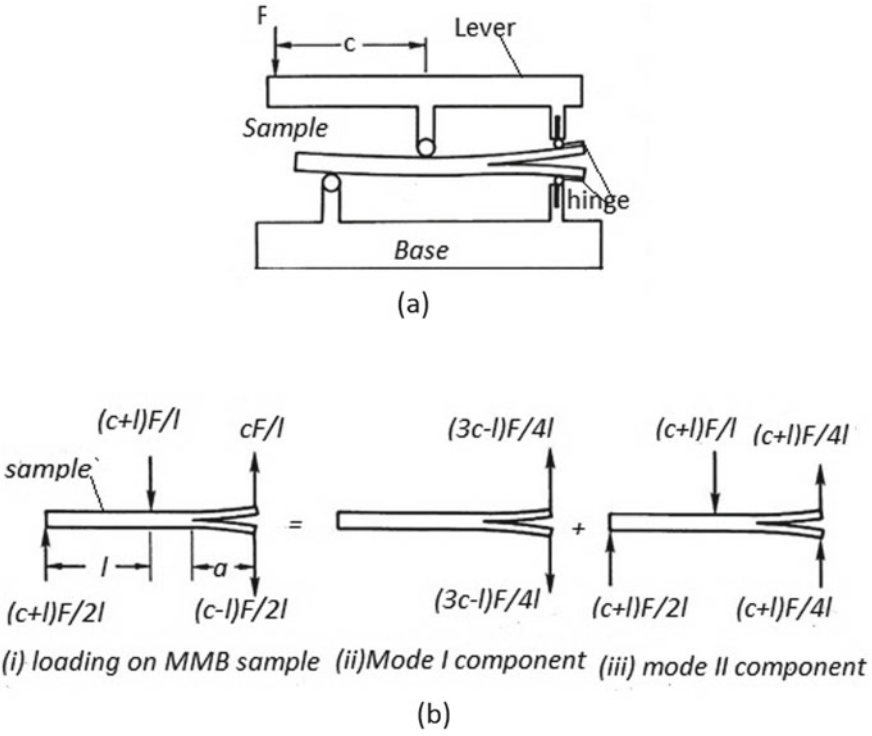

Fig. 18 MMB apparatus: **a** Mixed mode apparatus with laminate specimen, **b** components of mixed mode

fracture of UD fiber reinforced laminated samples is demonstrated in ASTM standard [28]. In the interest of conciseness, the first author requests to accept apologies for restricting the discussions on laminated composites only without going through the analysis of sandwich composites. Advanced learners are requested to go through the references [4, 7–9, 11, 13, 28, 49] for the detailed theoretical analysis and experimental investigations.

5 Conclusions and Future Perspective

The chapter started with an introduction to fracture behaviors and toughness of fiber reinforced polymer matrix composites (FRPCs). Fracture failure mechanisms in different length scales (micro, meso and macro) are addressed. The primary failure theories for fiber reinforced thermoset composites have been discussed. Failures of UD lamina under different loading conditions have been addressed from micromechanical approaches. Anisotropic failure theories applicable to FRPCs have also been presented in this chapter. Damage mechanisms, and theories of failures under creep, fatigue and high strain rates are briefly presented. The fracture behaviors of thermoset composites under different modes of fractures are theoretically discussed. Finally, the fracture behaviors and toughness of fiber reinforced thermoset polymer reinforced composites are addressed through the procedures of experimental fracture mechanics. Existing research gaps have been indicated in different sections.

References

1. Adams, D.F., Doner, D.R.: Longitudinal shear loading of a unidirectional composite. J. Compos. Mater. **1**(1), 4–17 (1967)
2. Anderson, D.D., Rosakis, A.J.: Comparison of three real time techniques for the measurement of dynamic fracture initiation toughness in metals. Eng. Fract. Mech. **72**(4), 535–555 (2005)
3. ASTM, D. 5528-13: Standard test method for mode I interlaminar fracture toughness of unidirectional fiber-reinforced polymer matrix composites. In: Annual Book of ASTM Standards, 30 (2013)
4. ASTM, D. 6671/D 6671M-06: Standard test method for mixed mode I-mode II interlaminar fracture toughness of unidirectional fiber reinforced polymer matrix composites. ASTM International, West Conshohocken PA, USA (2006). https://doi.org/10.1520/D6671-D6671M-06
5. Azzi, V.D., Tsai, S.W.: Anisotropic strength of composites. Exp. Mech. **5**(9), 283–288 (1965)
6. Bandaru, A.K., Patel, S., Sachan, Y., Alagirusamy, R., Bhatnagar, N., Ahmad, S.: Low velocity impact response of 3D angle-interlock Kevlar/basalt reinforced polypropylene composites. Mater. Des. **105**, 323–332 (2016)
7. Carlsson, L.A., Kardomateas, G.A.: Structural and Failure Mechanics of Sandwich Composites, vol. 121. Springer Science & Business Media, Berlin (2011)
8. Carlsson, L.A., Adams, D.F., Pipes, R.B.: Experimental Characterization of Advanced Composite Materials. CRC Press, Boca Raton (2014)
9. Chatterjee, S.N., Dick, W.A., Pipes, R.B.: Mixed-mode delamination fracture in laminated composites. Compos. Sci. Technol. **25**(1), 49–67 (1986)

10. Corton, H.T.: Micromechanics and fracture behavior of composites. Mod. Compos. Mater. 27–105 (1967)
11. Crews Jr, J.H., Reeder, J.R.: A mixed-mode bending apparatus for delamination testing (1988)
12. Cuntze, R.G.: Comparison between experimental and theoretical results using Cuntze's "failure mode concept" model for composites under triaxial loadings—part B of the second world-wide failure exercise. J. Compos. Mater. **47**(6–7), 893–924 (2013)
13. Daniel, I.M.: Mixed-mode failure of composite laminates with cracks. Exp. Mech. **25**(4), 413–420 (1985)
14. Daniel, I.M.: Photoelastic investigations of composites. Mech. Compos. Mater. 433 (2016)
15. Donaldson, S.L., Mall, S., Lingg, C.: The split cantilever beam test for characterizing Mode III interlaminar fracture toughness. J. Compos. Tech. Res. **13**(1), 41–47 (1991)
16. Doudican, B.M., Zand, B., Amaya, P., Butalia, T.S., Wolfe, W.E., Schoeppner, G.A.: Strain energy based failure criterion: comparison of numerical predictions and experimental observations for symmetric composite laminates subjected to triaxial loading. J. Compos. Mater. **47**(6–7), 847–866 (2013)
17. Frid, V., Rabinovitch, A., Bahat, D.: Fracture induced electromagnetic radiation. J. Phys. D Appl. Phys. **36**(13), 1620 (2003)
18. Greenhalgh, E.: Failure Analysis and Fractography of Polymer Composites. Elsevier, Amsterdam (2009)
19. Griffith, A.: The theory of rupture. In: First International Congress for Applied Mechanics, pp. 55–63 (1924)
20. Griffith, A.A.: VI. The phenomena of rupture and flow in solids. Philos. Trans. R. Soc. Lond. Ser. A Containing Pap. Math. Phys. Charact. **221**(582–593), 163–198 (1921)
21. Halpin, J.C.: Fracture of amorphous polymeric solids: time to break. J. Appl. Phys. **35**(11), 3133–3141 (1964)
22. Hashin, Z.: Failure criteria for unidirectional fiber composites (1980)
23. He, F., Tan, C.M., Zhang, S., Cheng, S.: Monte Carlo simulation of fatigue crack initiation at elevated temperature. In: 13th Conference on Fracture, pp. 1–10 (2013)
24. Hill, R.: A theory of the yielding and plastic flow of anisotropic metals. Proc. R. Soc. Lond. Ser. A Math. Phys. Sci. **193**(1033), 281–297 (1948)
25. Hinton, M.J.K.A., Soden, P.D., Kaddour, A.S. (eds.): Failure Criteria in Fiber Reinforced Polymer Composites: The World-Wide Failure Exercise. Elsevier, Amsterdam (2004)
26. Hinton, M.J., Kaddour, A.S.: The background to part b of the second world-wide failure exercise: evaluation of theories for predicting failure in polymer composite laminates under three-dimensional states of stress. J. Compos. Mater. **47**(6–7), 643–652 (2013)
27. Hinton, M.J., Kaddour, A.S.: Triaxial test results for fiber-reinforced composites: the second world-wide failure exercise benchmark data. J. Compos. Mater. **47**(6–7), 653–678 (2013)
28. Hutchinson, J.W., Suo, Z.: Mixed mode cracking in layered materials. In: Advances in Applied Mechanics, vol. 29, pp. 63–191. Elsevier, Amsterdam (1991)
29. Hyer, M.W., White, S.R.: Stress Analysis of Fiber-Reinforced Composite Materials. DEStech Publications, Inc., USA (2009)
30. Irwin, G.R.: Analysis of stresses and strains near the end of a crack traversing a plate (1997)
31. Jain, A., Upadhyay, C., Mohite, P.: Fiber breaking damage model for unidirectional fibrous composites using micromechanics. In: Proceedings of the 16th National Seminar on Aerospace Structures (NASAS), Mumbai, India, pp. 19–20 (2009)
32. Jones, R.M.: Mechanics of Composite Materials (2018)
33. Kaddour, A.S., Hinton, M.: Maturity of 3D failure criteria for fiber-reinforced composites: comparison between theories and experiments: part B of WWFE-II. J. Compos. Mater. **47**(6–7), 925–966 (2013)
34. Kaddour, A.S., Hinton, M.J., Smith, P.A., Li, S.: A comparison between the predictive capability of matrix cracking, damage and failure criteria for fiber reinforced composite laminates: part A of the third world-wide failure exercise. J. Compos. Mater. **47**(20–21), 2749–2779 (2013)
35. Kermode, J.R., Albaret, T., Sherman, D., Bernstein, N., Gumbsch, P., Payne, M.C., et al.: Low-speed fracture instabilities in a brittle crystal. Nature **455**(7217), 1224–1227 (2008)

36. Kimura, M., Watanabe, T., Takeichi, Y., Niwa, Y.: Nanoscopic origin of cracks in carbon fiber-reinforced plastic composites. Sci. Rep. **9**(1), 1–9 (2019)
37. Kinloch, A.J.: (ed.): Fracture Behavior of Polymers. Springer Science & Business Media, Berlin (2013)
38. Koerber, H., Xavier, J., Camanho, P.P.: High strain rate characterisation of unidirectional carbon-epoxy IM7-8552 in transverse compression and in-plane shear using digital image correlation. Mech. Mater. **42**(11), 1004–1019 (2010)
39. Mohr, O.: Welche Umstände bedingen die Elastizitätsgrenze und den Bruch eines Materials. Z. Ver. Dtsch. Ing. **46**(1524–1530), 1572–1577 (1900)
40. Mower, T.M., Li, V.C.: Fracture characterization of random short fiber reinforced thermoset resin composites. Eng. Fract. Mech. **26**(4), 593–603 (1987)
41. Mukhopadhyay, M.: Mechanics of Composite Materials and Structures. Universities Press (2005)
42. Murthy, P.L., Phoenix, S.L., Grimes-Ledesma, L.: Fiber breakage model for carbon composite stress rupture phenomenon: theoretical development and applications (2010)
43. Nairn, J.A.: Matrix microcracking in composites. Polym. Matrix Compos. **2**, 403–432 (2000)
44. Nakada, M., Okuya, T., Miyano, Y.: Statistical prediction of tensile creep failure time for unidirectional CFRP. Adv. Compos. Mater **23**(5–6), 451–460 (2014)
45. Pinho, S.T., Vyas, G.M., Robinson, P.: Material and structural response of polymer-matrix fiber-reinforced composites: Part B. J. Compos. Mater. **47**(6–7), 679–696 (2013)
46. Qian, L., Wang, X., Sun, C., Dai, A.: Correlation of macroscopic fracture behavior with microscopic fracture mechanism for AHSS sheet. Materials **12**(6), 900 (2019)
47. Ramesh, K.T.: High strain rate and impact testing. In: Springer Handbook of Experimental Solid Mechanics, pp. 929–960. Springer, NY (2008)
48. Rebière, J.L.: Matrix cracking and delamination evolution in composite cross-ply laminates. Cogent Eng. **1**(1), 943547 (2014)
49. Reeder, J.R., Crews Jr, J.H.: Nonlinear analysis and redesign of the mixed-mode bending delamination test (1991)
50. Robinson, P., Song, D.Q.: The development of an improved mode III delamination test for composites. Compos. Sci. Technol. **52**(2), 217–233 (1994)
51. Rolfe, S.T., Barsom, J.M.: Fracture and Fatigue Control in Structures: Applications of Fracture Mechanics. ASTM International, USA (1977)
52. Rosen, B.W.: Tensile failure of fibrous composites. AIAA J. **2**(11), 1985–1991 (1964)
53. Rosen, B.W.: Mechanics of composite strengthening (1965)
54. Russell, A.J.: On the Measurement of Mode II Interlaminar Fracture Energies. Defence Research Establishment Pacific (1982)
55. Safri, S.N.A.B., Sultan, M.T.H., Jawaid, M.: Damage analysis of glass fiber reinforced composites. In: Durability and Life Prediction in Biocomposites, Fiber-Reinforced Composites and Hybrid Composites, pp. 133–147. Woodhead Publishing, UK (2019)
56. Sause, M.G.: In Situ Monitoring of Fiber-Reinforced Composites: Theory, Basic Concepts, Methods, and Applications, vol. 242. Springer, Berlin (2016)
57. Schürmann, H.: Design with Fiber-Plastic Composites, vol. 2. Springer, Berlin (2005)
58. Shukla, S., Choudhuri, D., Wang, T., Liu, K., Wheeler, R., Williams, S., et al.: Hierarchical features infused heterogeneous grain structure for extraordinary strength-ductility synergy. Mater. Res. Lett. **6**(12), 676–682 (2018)
59. Sih, G.C., Chen, E.P.: Fracture analysis of unidirectional composites. J. Compos. Mater. **7**(2), 230–244 (1973)
60. Sih, G.C., Skudra, A.M.: Handbook of Composites. Failure Mechanics of Composites, vol. 3. Elsevier Science Publishers BV, Amsterdam (1985)
61. Sih, G.C., Paris, P.C., Irwin, G.R.: On cracks in rectilinearly anisotropic bodies. Int. J. Fract. Mech. **1**(3), 189–203 (1965)
62. Sirivedin, S., Fenner, D.N., Nath, R.B., Galiotis, C.: Viscoplastic finite element analysis of matrix crack propagation in model continuous-carbon fiber/epoxy composites. Compos. A Appl. Sci. Manuf. **37**(11), 1922–1935 (2006)

63. Thionnet, A., Bunsell, A.R.: Fiber break failure processes in unidirectional composites: evaluation of critical damage states. Philos. Trans. R. Soc. A Math. Phys. Eng. Sci. **374**(2071), 20150270 (2016)
64. Tsai, S.W., Wu, E.M.: A general theory of strength for anisotropic materials. J. Compos. Mater. **5**(1), 58–80 (1971)
65. Vieille, B., Casado, V.M., Bouvet, C.: About the impact behavior of woven-ply carbon fiber-reinforced thermoplastic-and thermosetting-composites: a comparative study. Compos. Struct. **101**, 9–21 (2013)
66. Vinson, J.R., Sierakowski, R.L.: The Behavior of Structures Composed of Composite Materials, vol. 105. Springer, Berlin (2006)
67. von Schmeling, H.K.: Recent developments in the kinetic theory of fracture of polymers. Kolloid-Zeitschrift Und Zeitschrift Für Polymere **236**(1), 48–58 (1970)
68. von Schmeling, H.K.B., Hsiao, C.C.: Behavior of elastic networks of various degrees of orientation in the kinetic theory of fracture. J. Appl. Phys. **39**(11), 4915–4919 (1968)
69. Waddoups, M.E., Eisenmann, J.R., Kaminski, B.E.: Macroscopic fracture mechanics of advanced composite materials. J. Compos. Mater. **5**(4), 446–454 (1971)
70. Wang, A.S.D., Crossman, F.W.: Initiation and growth of transverse cracks and edge delamination in composite laminates Part 1. An energy method. J. Compos. Mater. **14**(1), 71–87 (1980)
71. Wilkins, D.J., Eisenmann, J.R., Camin, R.A., Margolis, W.S., Benson, R.A.: Characterizing delamination growth in graphite-epoxy. In: Damage in Composite Materials: Basic Mechanisms, Accumulation, Tolerance, and Characterization. ASTM International (1982)
72. Winiarski, B., Guz, I.A.: The effect of the interaction of cracks in orthotropic layered materials under compressive loading. Philos. Trans. R. Soc. A Math. Phys. Eng. Sci. **366**(1871), 1841–1847 (2008)
73. Wisnom, M.R.: The role of delamination in failure of fiber-reinforced composites. Philos. Trans. Roy. Soc. A Math. Phys. Eng. Sci. **370**(1965), 1850–1870 (2012)
74. Wu, E.M.: Application of fracture mechanics to anisotropic plates (1967)
75. Wu, E.M.: Phenomenological anisotropic failure criterion. Mech. Compos. Mater. **2**, 353–431 (1974)
76. Yamada, I., Masuda, K., Mizutani, H.: Electromagnetic and acoustic emission associated with rock fracture. Phys. Earth Planet. Inter. **57**(1–2), 157–168 (1989)
77. Ye, J., Lam, D., Zhang, D.: Initiation and propagation of transverse cracking in composite laminates. Comput. Mater. Sci. **47**(4), 1031–1039 (2010)
78. Yokozeki, T., Aoki, T., Ishikawa, T.: Transverse crack propagation in the specimen width direction of CFRP laminates under static tensile loadings. J. Compos. Mater. **36**(17), 2085–2099 (2002)
79. Yokozeki, T., Aoki, T., Ishikawa, T.: Consecutive matrix cracking in contiguous plies of composite laminates. Int. J. Solids Struct. **42**(9–10), 2785–2802 (2005)
80. Zhurkov, S.N.: Kinetic concept of the strength of solids. Int. J. Fract. Mech. **1**, 311–323 (1965)
81. Zhurkov, S.N., Tomashevsky, E.E.: Physical basis of yield and fracture. In: Conference Proceedings. Institute of Physics London, UK (1966)

Dimensional Analysis for Predicting the Fracture Behavior of Particulate Polymer Composite Under the Effect of Impact Loading

Vinod Kushvaha and Aanchna Sharma

Abstract In the current study, a methodology of dimensional analysis based on Buckingham-pi theorem is presented to determine the dynamic fracture behavior of glass filled epoxy composites. Rod shaped glass fillers having an aspect ratio of 80 have been used to reinforce the epoxy matrix. These glass fillers were used in the volume fraction of 0%, 5%, 10% and 15%. Dynamic fracture toughness index for crack-opening mode (mode-I) is proposed to find out the fracture toughness of the Particulate Polymer Composites (PPCs) under different strain rate conditions of impact loading. The legitimacy of the proposed methodology is supported with the limited experimental results of dynamic fracture test which was conducted for varying filler concentration. The influence of various governing factors on the fracture toughness of the particulate polymer composites is also discussed and shear wave speed is found to have the most pronounced effect on the dynamic fracture toughness of the resulting composite.

Keywords Buckingham-pi theorem · Dynamic fracture toughness index · Dimensional analysis · Impact loading · Particulate polymer composite

1 Introduction

Composite materials have recently grown into the most appropriate alternative materials to be used by several industries like automobile, marine, aerospace, biomedical and electrical [5, 13, 20, 31, 48] etc. due to the combination of excellent properties such as high strength to weight ratio, corrosion resistance, chemical resistance, adhesion and dielectric properties [2, 10, 12, 24]. Depending upon the choice of reinforcement material, there are different types of composites that exist. Among these different types, Particulate Polymer Composites (PPCs) are easiest to manufacture and the most common type of composites [34, 36]. PPCs are made up of two or more constituent materials in which polymer serves as the matrix and some inorganic

V. Kushvaha (✉) · A. Sharma
Department of Civil Engineering, Indian Institute of Technology Jammu, Jammu, J&K, India
e-mail: vinod.kushvaha@iitjammu.ac.in

S. Mavinkere Rangappa et al. (eds.), *Fracture Failure Analysis of Fiber Reinforced Polymer Matrix Composites*, Engineering Materials,
https://doi.org/10.1007/978-981-16-0642-7_7

particles serve as the reinforcement. Mica, alumina, zirconia, silica etc. can be used to reinforce the polymer matrix. The fabrication of PPCs is also relatively cheaper along with the advantage of achieving tailored properties of the resulting composite by selecting the suitable filler reinforcement (in terms of type, size and shape), its volume fraction and the manufacturing process. Another aspect that makes PPCs one of the most appropriate materials for mechanical structural design is the macroscopic isotropy that these composites possess. The interfacial strength between the filler and the matrix is one of the key parameters that determine the overall performance of the resulting composite [9, 19, 37]. Hence, understanding the role of volume fraction of the filler and it's interfacial strength with the polymer matrix in determining the mechanical properties like strength, stiffness and toughness of the resulting PPC is critical for strategic engineering applications [21, 23, 41]. Investigating the mechanical behavior of composites corresponding to different design parameters and varying loading conditions experimentally is a very cumbersome and time consuming task. This has motivated researchers to look for alternative techniques in order to characterize the composite behavior with limited experimentation when subjected to different loading conditions [7, 8, 22, 38, 44, 45].

One such technique is the dimensional analysis, more precisely the Buckingham-π theorem which has been recognized as a very promising methodology for handling the intricacies of various physical concepts [4, 28]. This methodology offers certain process steps in order to develop compatible and meaningful dimensionless factors using the available set of parameters. The flexibility of the Buckingham-pi theorem lies in the fact that the characteristic relation between the parameters does not need to be known. This methodology has an ingrained physical basis because of which it has been extensively utilized in numerous engineering applications [11, 27]. The appropriate dependent and independent parameters obtained from physical experimentation are selected and using the technique of dimensional analysis, a functional relationship is established between the dimensionless quantities. Buckingham-π theorem has proven to be a very powerful scaling method and engrossed many scientists and engineers in the field for designing the practical problems. A numerical electroosmotic flow model was developed by making use of Buckingham-pi theorem in order to find a correlation between different physiochemical factors [32]. Another research group [6] performed an analysis of the roller bearings by means of Buckingham-pi theorem. A full scale test specimen of a simply supported beam made up of isotropic material was designed based on Buckingham-π theorem [46]. A research group [30] studied the characteristics of multiple bearing parameters when exposed to different temperature conditions and used dimensional analysis to determine the most significant factor affecting the bearing system. Another group [14] conducted a parametric study based on Buckingham-pi theorem to investigate the different system geometries of a composite slab.

In an attempt to solve a problem, analytical relations are usually established but it becomes very difficult to solve them as the number of parameters increases with increase in the intricacy of the problem. While in the laboratories, performing experiments that involve impact loading in order to study the fracture response of the composite materials, is very expensive and laborious [15, 16, 47]. In addition, it is

a well-established fact that the fracture behavior of composites is non-linear in both pre- and post-crack initiation stages.

Owing to the potential of Buckingham-pi theorem to predict the material behavior, it has been implemented in various studies by different researchers. A group of researchers [39] came up with a model so as to find out the strain analogue to a very small biaxial loading condition. They derived conditions for the strain analogue to large biaxial loading by using Buckingham-pi theorem. Another research group [40] developed a mathematical model again by using Buckingham-pi theorem and studied the correlation between the different parameters influencing the tribological performance of the cutting tool. A study [17] was conducted to investigate the wear behavior of polymer composites reinforced with chopped fibres using the approach of dimensional analysis. A group of researchers [3] used the methodology of dimensional analysis to comprehend the micromechanics of particulate composites based on the macroscopic fracture toughness.

In this view, it is desirable to make use of dimensional analysis using the approach of Buckingham-pi theorem which is a powerful tool for better understanding of the fracture behavior under impact loading with limited experimentation. A lot of experimental work has been reported in the purview of dynamic fracture toughness of particulate polymer composites but the prediction of this dynamic behavior as a function of filler volume fraction is still ambiguous and requires attention.

Therefore the current work presents an integrated approach to illustrate the fracture behavior of particulate polymer composites under the effect of impact loading at varying strain rates. This approach is ingrained based on a similarity condition which is denoted as 'dynamic fracture toughness index'. This index represents various factors like strain rate, material density, filler volume fraction, longitudinal wave speed and shear wave speed that can affect the crack initiation fracture toughness. This index is very useful for designing materials which have high resistance to impact load and hence can be utilized in numerous engineering applications.

The current study focuses on using Buckingham-pi theorem as a powerful tool of dimensional analysis in order to develop a model which will be used to evaluate the correlation between the crack-initiation fracture behavior and the dynamic fracture toughness index. This analysis utilizes the values of stress intensity factor analogue to different volume fractions of glass fillers obtained through lab experiments. Dynamic fracture toughness index is determined corresponding to different conditions of strain rate so as to widen the scope of utilizing the developed model to encounter various practical problems. Detailed methodology of the determination of this toughness index is reported elsewhere [18].

2 Experimental Procedure

In the current study, rod-shaped glass fillers of length 800 μm with a diameter of 10 μm (refer to Fig. 3) were used to reinforce the polymer matrix. Epoxy of low viscosity (Bisphenol-A) was used as the polymer matrix and glass fillers with an

aspect ratio of 80 were used in a volume fraction of 0%, 5%, 10% and 15%. First of all, glass-filled epoxy sheets were cast and cured for seven days. Then these sheets were cut into rectangular test specimens of dimensions 60 mm × 30 mm × 9 mm. A notch of length, 6 mm was made at the middle of each test specimen with the help of a circular saw. The density, longitudinal wave speed and shear wave speed for neat epoxy composite (0% glass fillers) is 1146 kg/m^3, 2481 m/s and 1128 m/s respectively. The material properties of glass filled epoxy composite corresponding to different volume fraction of the glass fillers is given in Table 1. The detailed procedure of measuring those material properties is reported in another study [19].

The setup used to conduct the dynamic fracture test is shown in Fig. 1. The projectile impacted the test specimen at a velocity of around 16 m/s. Three different values of strain rate (3.7 s^{-1}, 10.7 s^{-1} and 40 s^{-1}) were used in the present study.

The in-plane deformation of the test specimen was measured by using the technique of Digital Image Correlation (DIC). The deformed and undeformed states of the test specimen were examined by means of a black and white speckled pattern on

Table 1 Material properties of glass filled epoxy composite

Particle type	Density, D (kg/m^3)	Longitudinal wave speed, C_L (m/s)	Shear wave speed, C_S (m/s)	Fiber volume fraction, V_f (%)
Rod shaped glass fillers	1226	2534	1188	5
	1285	2534	1243	10
	1375	2598	1286	15

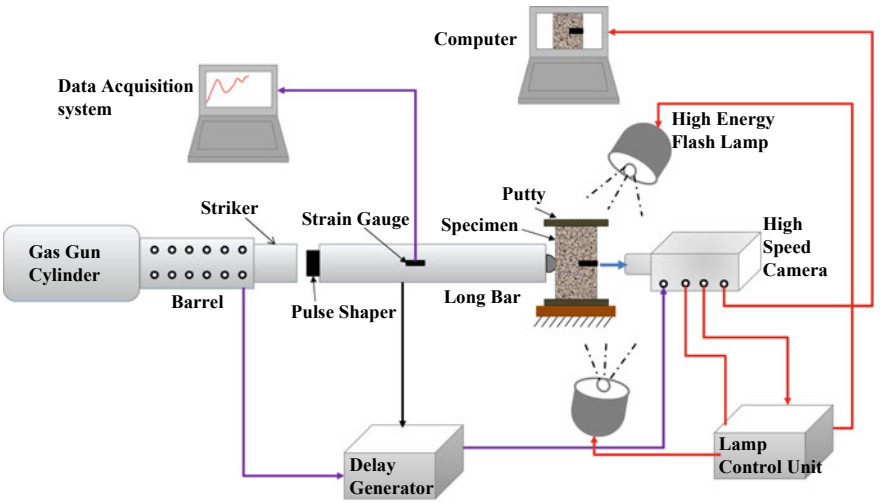

Fig. 1 Schematic of the setup used for dynamic fracture test [35]

the surface of the specimen. Further in order to extract the dynamic fracture toughness in terms of stress intensity factor, displacement fields obtained from Williams expressions were used. The detailed description of the experimental procedure is reported in a previous study [20].

When Buckingham-pi theorem is used to solve a problem having "x" variables and "y" dimensions then the variables can be reorganized into "x-y" independent dimensionless variables. This study deals with using Buckingham-pi theorem so as to establish the necessary functional relationships [1, 25, 33, 42, 43].

The functional relationship between the governing parameters which significantly affect the crack-opening mode (mode-I) dynamic fracture toughness under the effect of impact loading is given in Eq. (1).

$$K_I^d = f(\rho, C_s \text{ or } C_L, V_f, v, \gamma, \dot{\varepsilon}) \tag{1}$$

where K_I^d is the dynamic fracture toughness, ρ is the density of the material, v is the velocity of the crack, C_S is the shear wave speed, C_L is the longitudinal wave speed, γ is the Poisson ratio, V_f is the volume fraction of the glass fillers and, $\dot{\varepsilon}$ is the strain rate.

Using the Buckingham-pi theorem,

$$\pi_0 = f(\pi_1, \pi_2, \pi_3) \tag{2}$$

Out of the six governing parameters, C_S or C_L, $\dot{\varepsilon}$, ρ, γ, V_f and v, three parameters viz. $\dot{\varepsilon}$, v and ρ have independent dimensions. Therefore the dimensions of C_S or C_L, γ, and V_f are given as:

$$\pi_1 = [C_\mathrm{S} \text{ or } C_\mathrm{L}] = [v] \tag{3}$$

$$\pi_2 = [\gamma] = [1] \tag{4}$$

$$\pi_3 = [V\mathrm{f}] = [1] \tag{5}$$

$$\pi_0 = K_I^{index} = K_I^d \cdot (\dot{\varepsilon}^{0.5}/(\rho \cdot (C_\mathrm{L} \text{ or } C_\mathrm{S})^{2.5}) \tag{6}$$

where, K_I^{index} is the dynamic fracture toughness index and $v^{index} = v/C_s$ or v/C_L is the crack velocity index.

3 Results and Discussion

In order to investigate the fracture behavior of particulate polymer composites, a mathematical relationship between the dynamic fracture toughness index and crack velocity index is presented using the approach of dimensional analysis.

When a composite specimen is subjected to impact loading, the material experiences two different types of stress waves namely, longitudinal stress wave and shear stress wave [20]. Therefore the longitudinal and shear wave speed are included in the development of the mathematical relationship so as to account for the contribution of these stress waves in assessing the fracture toughness of the composite.

Figure 2a shows the variation in dynamic fracture toughness with respect to the crack velocity index for neat epoxy and glass-filled epoxy ($V_f = 10\%$) composite. This graph is corresponding to three different strain rates and the longitudinal wave speed has been used as one of the parameters in the above mentioned mathematical model. Figure 2b represents the same variation but by utilizing shear wave speed in the developed model. The variation corresponding to both, the shear wave speed and longitudinal wave speed is found to be linear. Both the figures clearly show that the glass filled epoxy possesses a higher value of dynamic fracture toughness index compared to the neat epoxy composite. This is attributed to the fact that glass fillers improve the overall strength of the resulting composite.

The slope in the first case corresponding to Fig. 2a is approximately 50 and the same corresponding to Fig. 2b is around 155, which clearly indicates that the influence of shear wave speed is much more pronounced on the fracture behavior of the composite compared to the longitudinal wave speed.

For better understanding of the failure mechanism due to the dynamic fracture, fractographic examination was done by means of scanning electron microscopy. Figure 3 shows the fractograph of the glass filled epoxy composite which clearly demonstrates the crack interaction with the filler reinforcement. Various failure modes like cracking of matrix, filler breakage and filler pullout are shown in Fig. 3. Each of these failure modes dissipate energy which consequently enhances the overall fracture toughness of the composite. At the crack tip, the presence of a substantial component of the in-plane shear resulted in filler matrix interface separation which further led to matrix cracking and hence matrix cracking was found to be the most dominating mode of failure. Similar filler-matrix interface separation as a failure mode has been reported for PPCs [26].

Figure 4 shows the relationship between the fracture toughness index and the crack velocity index at a constant strain rate, corresponding to the different filler volume fraction (5%, 10% and 15%). It was observed that increase in the concentration (volume fraction) of glass fillers, increases the dynamic fracture toughness of the composite. But this effect is not as much pronounced as it was due to the shear wave speed and this can be attributed to the fact that increase in the overall density and shear wave speed suppresses the effect of filler volume fraction. However, the contribution of filler concentration can be ascribed to increase the density of the resulting composite which ultimately makes the composite stiffer and stronger [29].

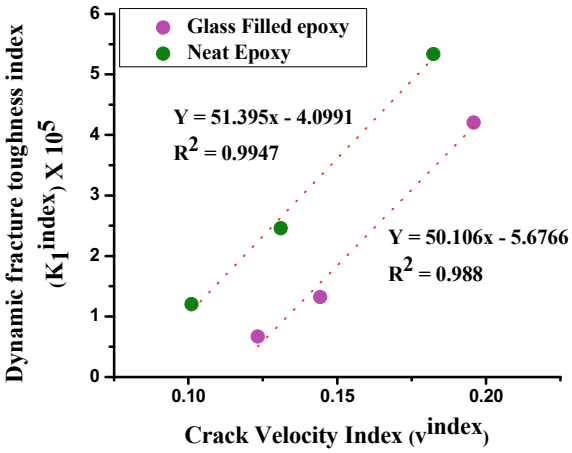

(a)

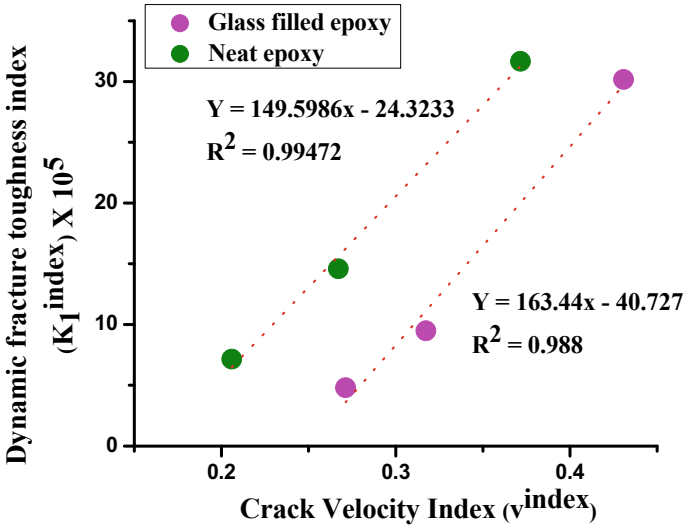

(b)

Fig. 2 Variation in dynamic fracture toughness index with respect to the crack velocity index **a** with longitudinal wave speed, **b** with shear wave speed

During the event of impact, shear stress wave interacts with the matrix and the fillers at a very high speed and this interaction directs the fracture behavior of the overall polymer composite. The filler pullout and breakage as shown in Fig. 3 is also attributed to the shear wave interaction with the fillers present in the glass filled epoxy composite.

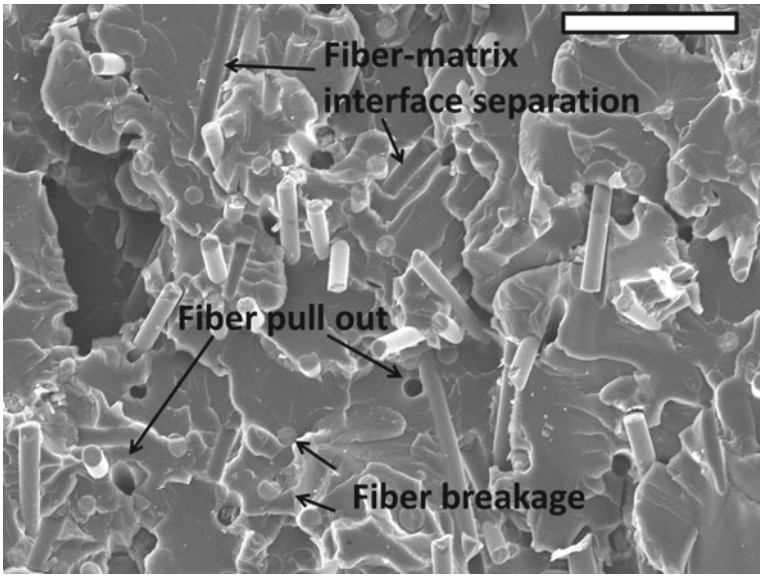

Fig. 3 Fractograph of rod-shaped glass-filled epoxy composite (scale bar = 100 μm)

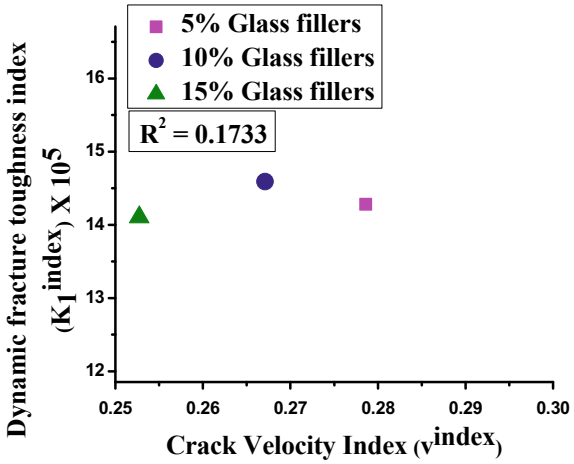

Fig. 4 Variation of dynamic fracture toughness index with respect to the crack velocity index for glass-filled epoxy

Finally, the developed functional relationship between the dynamic fracture toughness index and the crack velocity index was used to predict the fracture toughness for glass filled epoxy composites with three different volume fractions of the glass fillers (5%, 10% and 15%). These predicted results were compared with the experimental ones and the values were found to be close enough. Figure 5 shows

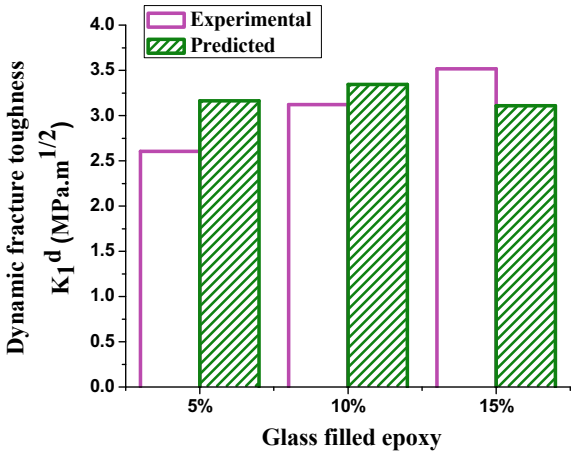

Fig. 5 Predicted versus experimental results for dynamic fracture toughness

a good agreement between the two results which encourages to further explore the possibility of using the proposed approach for predicting dynamic fracture toughness of PPCs with limited experimentation.

4 Conclusion and Future Perspective

The current study presents a technique to predict the dynamic fracture toughness of the glass filled epoxy composites under the effect of high strain rate impact loading by using dimensional analysis based on Buckingham pi-theorem. The legitimacy of the proposed methodology is supported with the limited experimental results of dynamic fracture test which was conducted for varying filler concentration. Shear wave speed is found to have the most significant effect on the dynamic fracture toughness of particulate polymer composite. The proposed dimensional analysis is found to be a very reliable and potential methodology to predict the dynamic fracture behavior of PPCs which is otherwise very tedious to investigate through multiple experiments. Furthermore, since the methodology has been observed to perform fairly efficiently, the same can be further extended to investigate the fracture behavior of composites using biofillers. This would assist in selection of a more efficient material and development of a robust composite with superior potential to resist fracture under dynamic loading.

References

1. Barenblatt, G.I.: Dimensional Analysis. CRC Press (1987)
2. Bharath, K.N., Madhu, P., Gowda, T.G.Y., Sanjay, M.R., Kushvaha, V., Siengchin, S.: Alkaline effect on characterization of discarded waste of *Moringa oleifera* fiber as a potential eco-friendly reinforcement for biocomposites. J. Polym. Environ. (2020). https://doi.org/10.1007/s10924-020-01818-4
3. Bouché, G.A., Akono, A.-T.: Micromechanics-based estimates on the macroscopic fracture toughness of micro-particulate composites. Eng. Fract. Mech. **148**, 243–257 (2015). https://doi.org/10.1016/j.engfracmech.2015.09.037
4. Buckingham, E.: On physically similar systems; illustrations of the use of dimensional equations. Phys. Rev. **4**(4), 345–376 (1914). https://doi.org/10.1103/PhysRev.4.345
5. Davies, P.:. Composites for marine applications. In Soares, C.A.M., Soares, C.M.M., Freitas, M.J.M. (eds.) Mechanics of Composite Materials and Structures, pp. 235–248. Springer, Netherlands (1999). https://doi.org/10.1007/978-94-011-4489-6_12
6. Desavale, R.G., Venkatachalam, R., Chavan, S.P.: Experimental and numerical studies on spherical roller bearings using multivariable regression analysis. J. Vib. Acoust. **136**(2), 021022–021022-10 (2014). https://doi.org/10.1115/1.4026433
7. Garg, A., Huang, H., Kushvaha, V., Madhushri, P., Kamchoom, V., Wani, I., Koshy, N., Zhu, H.-H.: Mechanism of biochar soil pore–gas–water interaction: gas properties of biochar-amended sandy soil at different degrees of compaction using KNN modeling. Acta Geophys. **68**(1), 207–217 (2020). https://doi.org/10.1007/s11600-019-00387-y
8. Garg, A., Reddy, N.G., Huang, H., Buragohain, P., Kushvaha, V.: Modelling contaminant transport in fly ash–bentonite composite landfill liner: mechanism of different types of ions. Sci. Rep. **10**(1), 11330 (2020). https://doi.org/10.1038/s41598-020-68198-6
9. Gowda, V.A.Y., Gupta, M.K., Jamil, M., Kushvaha, V., Siengchin, S.: Novel Muntingia Calabura bark fiber reinforced green-epoxy composite: a sustainable and green material for cleaner production. J. Clean. Prod. 126337 (2021). https://doi.org/10.1016/j.jclepro.2021.126337
10. Gowda, Y.T.G., Madhu, V.A.P., Kushvaha, V., Siengchin, S.M.R.S.: A new study on flax-basalt-carbon fiber reinforced epoxy/bioepoxy hybrid composites. Wiley (2021). https://doi.org/10.1002/pc.25944
11. Hadjileontiadis, L.J., Douka, E., Trochidis, A.: Fractal dimension analysis for crack identification in beam structures. Mech. Syst. Signal Process. **19**(3), 659–674 (2005). https://doi.org/10.1016/j.ymssp.2004.03.005
12. Hemath, M., Mavinkere Rangappa, S., Kushvaha, V., Dhakal, H.N., Siengchin, S.: A comprehensive review on mechanical, electromagnetic radiation shielding, and thermal conductivity of fibers/inorganic fillers reinforced hybrid polymer composites. Polym. Compos. (2020). https://doi.org/10.1002/pc.25703
13. Javid, S., Kushvaha, V., Karami, G., McEligot, S., Dragomir-Daescu, D.: Cadaveric femoral fractures in a fall on the hip configuration. In: Barthelat, F., Zavattieri, P., Korach, C.S., Prorok, B.C., Grande-Allen, K.J. (eds.) Mechanics of Biological Systems and Materials, vol. 4, pp. 53–57. Springer International Publishing (2014)
14. Kohrmann, M., Buchschmid, M., Greim, A., Müller, G., Schanda, U.: Vibroacoustic characteristics of light-weighted slabs—Part 1: Aspects of Numerical Modeling, Model Updating and Parametric Studies using the Buckingham Pi-Theorem (2013)
15. Koppula, S., Kaviti, A.K., Namala, K.K.: Experimental investigation of fibre reinforced composite materials under impact load. IOP Conf. Ser. Mater. Sci. Eng. **330**, 012047 (2018). https://doi.org/10.1088/1757-899X/330/1/012047
16. Korneeva, N.V., Kudinov, V.V., Krylov, I.K., Mamonov, V.I.: Properties and destruction of anisotropic composite materials under static deformation and impact loading conditions. J. Phys: Conf. Ser. **1134**, 012028 (2018). https://doi.org/10.1088/1742-6596/1134/1/012028

17. Kumar, S., Kachhap, R.K., Satapathy, B.K., Patnaik, A.: Wear performance forecasting of chopped fiber-reinforced polymer composites: a new approach using dimensional analysis. Tribol. Trans. **60**(5), 873–880 (2017). https://doi.org/10.1080/10402004.2016.1224962
18. Kushvaha, V., Anandkumar, S., Madhushri, P.: Dynamic fracture toughness index: a new integrated methodology for mode-I fracture behaviour of polymer composite under impact loading. Mater. Res. Express (2019). https://doi.org/10.1088/2053-1591/ab4e35
19. Kushvaha, V., Tippur, H.: Effect of filler shape, volume fraction and loading rate on dynamic fracture behavior of glass-filled epoxy. Compos. B Eng. **64**, 126–137 (2014). https://doi.org/10.1016/j.compositesb.2014.04.016
20. Kushvaha, V.: Synthesis, Processing and Dynamic Fracture Behavior of Particulate Epoxy Composites with Conventional and Hierarchical Micro-/Nano-fillers (2016). https://etd.auburn.edu/handle/10415/5468
21. Kushvaha, V., Branch, A., Tippur, H.: Effect of loading rate on dynamic fracture behavior of glass and carbon fiber modified epoxy. In: Song, B., Casem, D., Kimberley, J. (eds.) Dynamic Behavior of Materials, vol. 1, pp. 169–176. Springer International Publishing (2014). https://doi.org/10.1007/978-3-319-00771-7_21
22. Kushvaha, V., Kumar, S.A., Madhushri, P., Sharma, A.: Artificial neural network technique to predict dynamic fracture of particulate composite. J. Compos. Mater., 0021998320911418 (2020). https://doi.org/10.1177/0021998320911418
23. Kushvaha, V., Tippur, H.: Effect of filler particle shape on dynamic fracture behavior of glass-filled epoxy. In: Chalivendra, V., Song, B., Casem, D. (eds.) Dynamic Behavior of Materials, vol. 1, pp. 513–522. Springer New York (2013). https://doi.org/10.1007/978-1-4614-4238-7_66
24. McGarry, F.J.: Polymer composites. Annu. Rev. Mater. Sci. **24**(1), 63–82 (1994). https://doi.org/10.1146/annurev.ms.24.080194.000431
25. Miles, J.W.: Dimensional Analysis for Engineers (Taylor, E.S., ed.). Oxford University Press (1974). 162 pp. £5.75. J. Fluid Mech. **68**(2), 416–416. https://doi.org/10.1017/S0022112075210900
26. Moloney, A.C., Kausch, H.H., Kaiser, T., Beer, H.R.: Parameters determining the strength and toughness of particulate filled epoxide resins. J. Mater. Sci. **22**(2), 381–393 (1987). https://doi.org/10.1007/BF01160743
27. Paul, S.N., Karambelkar, V.V., Rao, S.N., Ekhe, J.D.: The application of Buckingham π theorem to modeling polypyrrole synthesis done by chemical oxidative polymerization. Indian J. Sci. Technol. **8**(35) (2015)
28. Pescetti, D.: Dimensional analysis and qualitative methods in problem solving. Eur. J. Phys. **29**(4), 697–707 (2008). https://doi.org/10.1088/0143-0807/29/4/005
29. Qiao, Y.: Fracture toughness of composite materials reinforced by debondable particulates. Scripta Mater. **49**(6), 491–496 (2003). https://doi.org/10.1016/S1359-6462(03)00367-1
30. Reddy, G.M., Reddy, V.D.: Theoretical investigations on dimensional analysis of ball bearing parameters by using Buckingham Pi-theorem. Procedia Eng. **97**, 1305–1311 (2014). https://doi.org/10.1016/j.proeng.2014.12.410
31. Rossman, T., Kushvaha, V., Dragomir-Daescu, D.: QCT/FEA predictions of femoral stiffness are strongly affected by boundary condition modeling. Comput. Methods Biomech. Biomed. Eng. **19**(2), 208–216 (2016). https://doi.org/10.1080/10255842.2015.1006209
32. Saini, R., Kenny, M., Barz, D.P.J.: Electroosmotic flow through packed beds of granular materials. Microfluid. Nanofluid. **19**(3), 693–708 (2015). https://doi.org/10.1007/s10404-015-1594-0
33. Sedov, L.I.: Similarity and Dimensional Methods in Mechanics. CRC Press (2018). https://doi.org/10.1201/9780203739730
34. Sharma, A., Kushvaha, V.: Predictive modelling of fracture behaviour in silica-filled polymer composite subjected to impact with varying loading rates using artificial neural network. Eng. Fract. Mech. **239**, 107328 (2020). https://doi.org/10.1016/j.engfracmech.2020.107328
35. Sharma, A., Subramaiyan, A.K., Kushvaha, V.: Effect of aspect ratio on dynamic fracture toughness of particulate polymer composite using artificial neural network. Eng. Fract. Mech. **228**, 106907 (2020). https://doi.org/10.1016/j.engfracmech.2020.106907

36. Sharma, A., Khan, V.C., Balaganesan, G., Kushvaha, V.: Performance of nano filler reinforced composite overwrap system to repair damaged pipelines subjected to quasi-static and impact loading (2020). https://doi.org/10.1007/s11668-020-01013-6
37. Sharma, A., Madhushri, P., Kushvaha, V., Subramaniyan, A.K.: Prediction of the fracture toughness of silicafilled epoxy composites using K-nearest neighbor (KNN) method. In: 2020 International Conference on Computational Performance Evaluation (ComPE), pp. 194–198 (2020). https://doi.org/10.1109/ComPE49325.2020.9200093
38. Sharma, A., Munde, Y., Kushvaha, V.: Representative volume element based micromechanical modelling of rod shaped glass filled epoxy composites. SN Appl. Sci. *3*, 232 (2021). https://doi.org/10.1007/s42452-021-04261-9
39. Shehadeh, M., Shennawy, Y., El-Gamal, H.: Similitude and scaling of large structural elements: case study. Alexandria Eng. J. **54**(2) (2015). https://cyberleninka.org/article/n/571725
40. Singh, R., Khamba, J.S.: Mathematical modeling of tool wear rate in ultrasonic machining of titanium. Int. J. Adv. Manuf. Technol. **43**(5), 573–580 (2009). https://doi.org/10.1007/s00170-008-1729-5
41. Song, S.G., Shi, N., Iii, G.T.G., Roberts, J.A.: Reinforcement shape effects on the fracture behavior and ductility of particulate-reinforced 6061-Al matrix composites. Metall. Mater. Trans. A **27**(11), 3739–3746 (1996). https://doi.org/10.1007/BF02595465
42. Sonin, A.A.: The Physical Basis of Dimensional Analysis, 2nd edn. Department of Mechanical Engineering (2001)
43. Tan, Q.-M.: Dimensional Analysis: With Case Studies in Mechanics. Springer-Verlag (2011). https://www.springer.com/gp/book/9783642192333
44. Wani, I., Kumar, H., Rangappa, S.M., Peng, L., Siengchin, S., Kushvaha, V.: Multiple regression model for predicting cracks in soil amended with pig manure biochar and wood biochar. J. Hazard. Toxic Radioactive Waste **25**(1), 04020061 (2021). https://doi.org/10.1061/(ASCE)HZ.2153-5515.0000561
45. Wani, I., Sharma, A., Kushvaha, V., Madhushri, P., Peng, L.: Effect of pH, volatile content, and pyrolysis conditions on surface area and O/C and H/C ratios of biochar: towards understanding performance of biochar using simplified approach. J. Hazard. Toxic Radioactive Waste **24**(4), 04020048 (2020). https://doi.org/10.1061/(ASCE)HZ.2153-5515.0000545
46. Wool, R.P., Sun, X.S.: Bio-Based Polymers and Composites. Elsevier (2005)
47. Zuhudi, N.Z.M., Jayaraman, K., Lin, R.J.T., Nur, N.M.: Impact resistance of bamboo fabric reinforced polypropylene composites and their hybrids. IOP Conf. Ser. Mater. Sci. Eng. **370**, 012047 (2018). https://doi.org/10.1088/1757-899X/370/1/012047
48. Zweben, C.: Advanced composites for aerospace applications: a review of current status and future prospects. Composites **12**(4), 235–240 (1981). https://doi.org/10.1016/0010-4361(81)90011-2

Evaluation of Strength of Laminates in Four-Bar Mechanism Using Tsai-Wu-Hahn Failure Criterion

Hemaraju Pollayi and Dineshkumar Harursampath

Abstract The objective of this chapter is to evaluate the component-laminate load-carrying capacity, i.e., to calculate the loads that cause the failure of the individual layers and the component-laminate as a whole in four-bar mechanism. The component-laminate load-carrying capacity is evaluated using the Tsai-Wu-Hahn failure criterion for various layups. The reserve factor of each ply in the component-laminate is calculated by using the maximum resultant force and the maximum resultant moment occurring over an entire period of rotation at the joints of the mechanism. The nonlinear through-the-thickness stress and strain distributions are reported at different points. The Tsai-Wu-Hahn failure criterion is used to predict the first-ply-failure and the mechanism as a whole.

Keywords Composite sandwich · Geometrically non-linear · Dimensional reduction · VAM · FMA

1 Introduction

During the recent years, many researches focus on the damage and failure analyzes of fiber-reinforced composites due to the increase of demand for composite structures in industries. As an example [1–3], in the construction of each new-generation aircraft, the aerospace industry uses a higher proportion of advanced composite materials every year. For the past 30-years, weight percentage of these materials to whole weight of the aircraft has significantly increased. For Boeing 787, these materials account for nearly 5% of the total weight of the aircraft structure and for Airbus A380,

H. Pollayi (✉)
Advanced Composite Structures Laboratory, Department of Civil Engineering, GITAM University, Hyderabad, Telangana 502329, India
e-mail: dpollayi@gitam.edu

D. Harursampath
Nonlinear Multifunctional Composites Analysis and Design Laboratory, Department of Aerospace Engineering, Indian Institute of Science, Bengaluru, Karnataka 560012, India
e-mail: dineshkumar@iisc.ac.in

S. Mavinkere Rangappa et al. (eds.), *Fracture Failure Analysis of Fiber Reinforced Polymer Matrix Composites*, Engineering Materials,
https://doi.org/10.1007/978-981-16-0642-7_8

these materials make up about 2% of the total airframe [4]. Damage mechanics of these composites deals with quantitative descriptions of the physical events (such as initiation, propagation, and fracture) that alter composite materials when it is subjected to mechanical loads and aging (long-term performance of composites). The mechanisms that lead to failure of composite materials are not fully understood yet, even after the World-Wide Failure Exercise (WWFE). WWFE concluded that most of the criteria were unable to capture some of the trends in the failure envelopes of the experimental results and most of the expressions proposed to predict each failure mode are still to some extent empirical. These physical damage modes should establish suitably when failure takes place in composite structures, and also describe the post-failure behavior of composite structures for better performance. The need for predicting failure in composites has led to the proposal of several failure criteria in the literature.

Failure criteria are used to assess the possibility of failure of a material in mechanisms. A number of phenomenological failure criteria for anisotropic materials have been developed which essentially provide a practical basis for the design. These phenomenological criteria can be roughly divided into two categories: (1) Stress-based criteria (such as maximum stress criterion), and (2) Strain-based criteria (such as the maximum strain criterion). These two criteria predict physically different failure envelopes. The strain-based criteria for anisotropic materials have not received the same degree of attention as that of the stress-based criteria because of the difficulties in measuring strains to failure. Amongst the stress-based criteria, one of the most rationally developed interactive failure criteria is the stress tensor polynomial criterion of Tsai and Wu [5] which allows for the interaction of anisotropic stresses on failure. The most commonly used stress-based failure criteria i.e., the Tsai-Wu-Hahn failure criterion [6] is used in the present work for failure analysis.

Failure criteria associated with a lamina can be divided into two categories:

1. Failure criteria not directly associated with failure modes
   (a) Tsai-Hill
   (b) Tsai-Wu
   (c) Modified Tsai-Wu
   (d) All polynomial, tensorial, or parametric criteria
2. Failure criteria associated with failure modes
   (a) Maximum strain or stress
   (b) Hashin and Rotem
   (c) Yamada and Sun
   (d) Hashin
   (e) Hart-Smith
   (f) Puck
   (g) Kriging

Polynomial Criterion of Failure Tensor

A simple form-invariant expression is extensively used for the failure tensor polynomial function. The theoretical predictions may or may not seriously effect because of the rank of the tensors and the number of terms appearing in the respective equation. The following is the failure function by considering tensor polynomial coefficients up to the fourth rank:

$$f(\sigma) = \sigma \cdot H \cdot \sigma + h \cdot \sigma - 1 = 0 \tag{1}$$

With an appropriate definition of the Cartesian components of the fourth- and second-rank tensors H and h, respectively, many anisotropic failure criteria can be written in the form of above relation. The stress differential effect second-rank tensor h, as well as the diagonal components of failure fourth-rank tensor H. H and h are uniquely determined for the criteria assuming the general form of the above equation. Differences arising only in the definition of off-diagonal components $H_{ij}(i \neq j)$ express the various phenomenological conjectures of these criteria.

$H_{ij} = 0(i \neq j)\ for\ Tsai-Wu\,(TW)\,Criterion$

$H_{ij} = -\frac{1}{2}\left(H_{ii}H_{jj}\right)^{\frac{1}{2}}\ for\ Tsai-Hahn\,(TH)\,Criterion$

$H_{ij} = \frac{1}{2}\left(H_{kk} - H_{ii} - H_{jj}\right)\ (i, j, k \leq 3; i \neq j \neq k)\ for\ Elliptic\ Paraboloid\ Failure\ Surface\,(EPFS)\,Criterion$

The quadratic stress tensor polynomial failure criterion for anisotropic materials can be represented, using the usual contracted matrix notation, as

$$F_i\sigma_i + F_{ij}\sigma_i\sigma_j = 1 \quad (i, j = 1, 2, \ldots, 6) \tag{2}$$

where F_i and F_{ij} are strength tensors of the second and fourth rank, respectively, and the recovered 3-D stress tensor, σ_i, are given below:

$$F_i^T = \begin{bmatrix} F_1 & F_2 & F_3 & F_4 & F_5 & F_6 \end{bmatrix} \tag{3}$$

$$F_{ij} = \begin{bmatrix} F_{11} & F_{12} & F_{13} & F_{14} & F_{15} & F_{16} \\ & F_{22} & F_{23} & F_{24} & F_{25} & F_{26} \\ & & F_{33} & F_{34} & F_{35} & F_{36} \\ & & & F_{44} & F_{45} & F_{46} \\ & sym & & & F_{55} & F_{56} \\ & & & & & F_{66} \end{bmatrix} \tag{4}$$

$$\sigma_i^T = \begin{bmatrix} \sigma_1 & \sigma_2 & \sigma_3 & \sigma_4 & \sigma_5 & \sigma_6 \end{bmatrix} = \begin{bmatrix} \sigma_{11} & \sigma_{22} & \sigma_{33} & \sigma_{23} & \sigma_{31} & \sigma_{12} \end{bmatrix} \tag{5}$$

Expanding Normal Components of Failure Tensor

$$F_{11} = \frac{1}{\sigma_{T1}\sigma_{C1}},\ F_{22} = \frac{1}{\sigma_{T2}\sigma_{C2}},\ F_{33} = \frac{1}{\sigma_{T3}\sigma_{C3}} \tag{6}$$

$$\begin{aligned} F_1 &= \frac{1}{\sigma_{T1}} - \frac{1}{\sigma_{C1}} = (\sigma_{C1} - \sigma_{T1})F_{11} \\ F_2 &= \frac{1}{\sigma_{T2}} - \frac{1}{\sigma_{C2}} = (\sigma_{C2} - \sigma_{T2})F_{22} \\ F_3 &= \frac{1}{\sigma_{T3}} - \frac{1}{\sigma_{C3}} = (\sigma_{C3} - \sigma_{T3})F_{33} \end{aligned} \tag{7}$$

where σ_{Ti} is Tension (T) failure stress in i-direction ($i = 1, 2, 3$) and σ_{Ci} is Compression (C) failure stress in i-direction ($i = 1, 2, 3$).

Expanding Shear Components of Failure Tensor

$$F_{44} = \frac{1}{\sigma_{S4}^{+}\sigma_{S4}^{-}},\ F_{55} = \frac{1}{\sigma_{S5}^{+}\sigma_{S5}^{-}},\ F_{66} = \frac{1}{\sigma_{S6}^{+}\sigma_{S6}^{-}} \tag{8}$$

$$\begin{aligned} F_4 &= \tfrac{1}{\sigma_{S4}^{+}} - \tfrac{1}{\sigma_{S4}^{-}} = \left(\sigma_{S4}^{-} - \sigma_{S4}^{+}\right)F_{44} \\ F_5 &= \tfrac{1}{\sigma_{S5}^{+}} - \tfrac{1}{\sigma_{S5}^{-}} = \left(\sigma_{S5}^{-} - \sigma_{S5}^{+}\right)F_{55} \\ F_6 &= \tfrac{1}{\sigma_{S6}^{+}} - \tfrac{1}{\sigma_{S6}^{-}} = \left(\sigma_{S6}^{-} - \sigma_{S6}^{+}\right)F_{66} \end{aligned} \tag{9}$$

where σ_{Si}^{+} is $+$ve shear (S) strength in i-plane ($i = 4, 5, 6$) and σ_{Si}^{-} is $-$ve shear (S) strength in i-plane ($i = 4, 5, 6$).

Expanding $F_{ij}(i \neq j)$

$$\begin{aligned} &F_{12} = -\frac{1}{2}(F_{11}F_{22})^{\frac{1}{2}},\ F_{13} = -\frac{1}{2}(F_{11}F_{33})^{\frac{1}{2}},\ F_{14} = -\frac{1}{2}(F_{11}F_{44})^{\frac{1}{2}} \\ &F_{15} = -\frac{1}{2}(F_{11}F_{55})^{\frac{1}{2}},\ F_{16} = -\frac{1}{2}(F_{11}F_{66})^{\frac{1}{2}} \\ &F_{23} = -\frac{1}{2}(F_{22}F_{33})^{\frac{1}{2}},\ F_{24} = -\frac{1}{2}(F_{22}F_{44})^{\frac{1}{2}},\ F_{25} = -\frac{1}{2}(F_{22}F_{55})^{\frac{1}{2}} \\ &F_{26} = -\frac{1}{2}(F_{22}F_{66})^{\frac{1}{2}} \\ &F_{34} = -\frac{1}{2}(F_{33}F_{44})^{\frac{1}{2}},\ F_{35} = -\frac{1}{2}(F_{33}F_{55})^{\frac{1}{2}},\ F_{36} = -\frac{1}{2}(F_{33}F_{66})^{\frac{1}{2}} \\ &F_{45} = -\frac{1}{2}(F_{44}F_{55})^{\frac{1}{2}},\ F_{46} = -\frac{1}{2}(F_{44}F_{66})^{\frac{1}{2}} \\ &F_{56} = -\frac{1}{2}(F_{55}F_{66})^{\frac{1}{2}} \end{aligned} \tag{10}$$

Non-dimensionalization of Tsai-Wu-Hahn Criterion

The equation for non-dimensionalization of Tsai-Wu-Hahn failure criterion is derived by using the following definitions:

$$\begin{aligned}
\widetilde{\sigma_L} &\triangleq \sqrt{F_{11}}\sigma_L; \quad \widetilde{F_1} \triangleq \tfrac{F_1}{\sqrt{F_{11}}} \\
\widetilde{\sigma_T} &\triangleq \sqrt{F_{22}}\sigma_T; \quad \widetilde{F_2} \triangleq \tfrac{F_2}{\sqrt{F_{22}}} \\
\widetilde{\sigma_{T'}} &\triangleq \sqrt{F_{33}}\sigma_{T'}; \quad \widetilde{F_3} \triangleq \tfrac{F_3}{\sqrt{F_{33}}} \\
\widetilde{\sigma_{TT'}} &\triangleq \sqrt{F_{44}}\sigma_{TT'}; \quad \widetilde{F_4} \triangleq \tfrac{F_4}{\sqrt{F_{44}}} \\
\widetilde{\sigma_{LT'}} &\triangleq \sqrt{F_{55}}\sigma_{LT'}; \quad \widetilde{F_5} \triangleq \tfrac{F_5}{\sqrt{F_{55}}} \\
\widetilde{\sigma_{LT}} &\triangleq \sqrt{F_{66}}\sigma_{LT}; \quad \widetilde{F_6} \triangleq \tfrac{F_6}{\sqrt{F_{66}}}
\end{aligned} \tag{11}$$

Reserve factor, R can be defined as a common factor by which all of the stresses applied on a lamina need to be multiplied by for the lamina to just fail. The ply in the component-laminate resists the combination of stresses without failure if $R > 1$.

Non-dimensionalization and substitution in non-dimensional form of Tsai-Wu-Hahn failure criterion implies a quadratic equation, quadratic in reserve factor, R, and is as follows:

$$AR^2 + BR - 1 = 0 \tag{12}$$

where

$$\begin{aligned}
A = {} & \widetilde{\sigma_L}^2 + \widetilde{\sigma_T}^2 + \widetilde{\sigma_{T'}}^2 + \widetilde{\sigma_{TT'}} + \widetilde{\sigma_{LT'}}^2 + \widetilde{\sigma_{LT}}^2 \\
& - \big[\widetilde{\sigma_L}\widetilde{\sigma_T} + \widetilde{\sigma_L}\widetilde{\sigma_{T'}} + \widetilde{\sigma_L}\widetilde{\sigma_{TT'}} + \widetilde{\sigma_L}\widetilde{\sigma_{LT'}} + \widetilde{\sigma_L}\widetilde{\sigma_{LT}} + \widetilde{\sigma_T}\widetilde{\sigma_{T'}} \\
& + \widetilde{\sigma_T}\widetilde{\sigma_{TT'}} + \widetilde{\sigma_T}\widetilde{\sigma_{LT'}} + \widetilde{\sigma_T}\widetilde{\sigma_{LT}} + \widetilde{\sigma_{T'}}\widetilde{\sigma_{TT'}} + \widetilde{\sigma_{T'}}\widetilde{\sigma_{LT'}} + \widetilde{\sigma_{T'}}\widetilde{\sigma_{LT}} \\
& + \widetilde{\sigma_{TT'}}\widetilde{\sigma_{LT'}} + \widetilde{\sigma_{TT'}}\widetilde{\sigma_{LT}} + \widetilde{\sigma_{LT'}}\widetilde{\sigma_{LT}}\big] \\
B = {} & \widetilde{F_1}\widetilde{\sigma_L} + \widetilde{F_2}\widetilde{\sigma_T} + \widetilde{F_3}\widetilde{\sigma_{T'}} + \widetilde{F_4}\widetilde{\sigma_{TT'}} + \widetilde{F_5}\widetilde{\sigma_{LT'}} + \widetilde{F_6}\widetilde{\sigma_{LT}}
\end{aligned}$$

The reserve factor of each ply in the component-laminate is calculated by using the maximum resultant force, $F_r = \sqrt{F_1^2 + F_2^2 + F_3^2}$ and the maximum resultant moment, $M_r = \sqrt{M_1^2 + M_2^2 + M_3^2}$ instead of choosing either maximum of $\{F_1, F_2, F_3\}$ or maximum of $\{M_1, M_2, M_3\}$. The positive root for R shows the failure stress level with loads in the same direction as the initial values and the negative root shows the failure stress level with all loads reversed.

2 Elastic Constitutive Equations for Mechanism

The closed-form analytical analysis is restricted to thin rectangular cross-sections for generally anisotropic composites. Figure 1 shows the sketch of an initially twisted

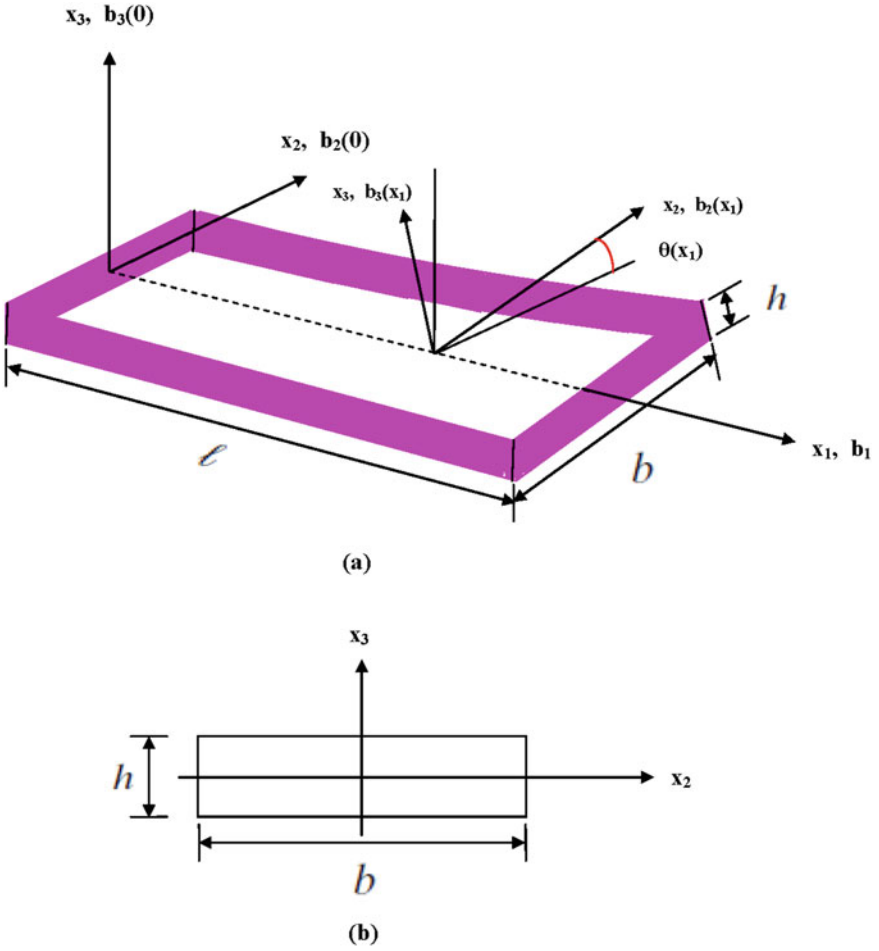

Fig. 1 Sketch of **a** initially twisted strip configuration and coordinate system and **b** its cross-section

and curved strip configuration, coordinate system and cross-section. When the strip is first reduced from a 3-D to a 2-D elastic body, its strain energy density (i.e. energy per unit middle surface area) is given by:

$$\bigcup_{2D} = \frac{1}{2} \begin{Bmatrix} \varepsilon_{11} \\ \varepsilon_{22} \\ 2\varepsilon_{12} \\ \rho_{11} \\ \rho_{22} \\ 2\rho_{12} \end{Bmatrix}^{T} \begin{bmatrix} A & B \\ B^{T} & D \end{bmatrix} \begin{Bmatrix} \varepsilon_{11} \\ \varepsilon_{22} \\ 2\varepsilon_{12} \\ \rho_{11} \\ \rho_{22} \\ 2\rho_{12} \end{Bmatrix} \tag{13}$$

where $\varepsilon_{\alpha\beta}$ and $\rho_{\alpha\beta}(\alpha, \beta = 1, 2)$ are the 2-D strain measures, and A, B, and D are the membrane, coupling, and bending (3×3) stiffness matrices, respectively, appropriately corrected for initial twist and curvature. The beam strain energy density (per unit length of the strip) is given by:

$$\bigcup_{1D} = \left\langle \bigcup_{1D} \right\rangle \tag{14}$$

where the notation

$$\langle \cdot \rangle \equiv \int_{-\frac{b}{2}}^{\frac{b}{2}} (\cdot) dx_2 \tag{15}$$

is used here where b is the width of the strip being considered and x_2 is a Cartesian coordinate along the width, with origin at the geometric center of the cross-section. Minimizing the strain energy functional, $\bigcup_{1D}$, subject to appropriate constraints results in the unknown 3-D warping field at any given order of approximation in the VAM. The final expression for the first order strain energy per unit length (or 1-D strain energy density) of the curved and twisted beam component is:

$$\begin{aligned} \bigcup_{1D} = {} & \frac{1}{2}\varepsilon_\ell^T [S_\ell]\varepsilon_\ell + \varepsilon_\ell^T [S_{\ell n}]\varepsilon_n + \frac{1}{2}\varepsilon_n^T [S_n]\varepsilon_n + \frac{k_2}{2}\varepsilon_\ell^T \left[S_\ell^{c1}\right]\varepsilon_\ell \\ & + \frac{k_2^2}{2}\varepsilon_\ell^T \left[S_\ell^{c2}\right]\varepsilon_\ell + k_2 \varepsilon_\ell^T \left[S_{\ell n}^{c}\right]\varepsilon_n \end{aligned} \tag{16}$$

where k_1 is pre-twist per unit length, k_2 is initial curvature in flat-wise direction of strip, $[S_\ell]$ is the linear stiffness matrix, $[S_{\ell n}]$ is the non-symmetric non-linear stiffness matrix, $[S_n]$ is the symmetric non-linear stiffness matrix, $[S_\ell^{c1}]$ is correction to the linear stiffness matrix, $[S_\ell^{c2}]$ is correction to the symmetric linear stiffness matrix, $[S_{\ell n}^{c}]$ is correction to the non-symmetric non-linear stiffness matrix, and the linear and non-linear 1-D strain vectors, ε_ℓ and ε_n respectively, are defined as follows:

$$\begin{aligned} \varepsilon_\ell &= \left[\, \overline{\gamma_{11}} \;\; \overline{\kappa_1} \;\; \overline{\kappa_2} \;\; \overline{\kappa_3} \,\right]^T \\ \varepsilon_n &= \left[\, \overline{\kappa_1}^2 \;\; \overline{\kappa_2}^2 \;\; \overline{\kappa_2\gamma_{11}} \;\; \overline{\kappa_2\kappa_3} \;\; \overline{\kappa_2\kappa_1} \,\right]^T \end{aligned} \tag{17}$$

Here, the barred quantities $\overline{\gamma_{11}}$, $\overline{\kappa_1}$, $\overline{\kappa_2}$ and $\overline{\kappa_3}$ relate to their unbarred counterparts as

$$\overline{(\cdot)} = (\cdot)|_{2\gamma_{12}} = 2\gamma_{13} = 0 \tag{18}$$

The cross-sectional stiffness matrix is obtained by expressing the resultant forces on the beam cross-section as:

$$\underline{f}^* \triangleq \frac{1}{2}\begin{Bmatrix} F_1 \\ F_2 \\ F_3 \\ M_1 \\ M_2 \\ M_3 \end{Bmatrix}^T = \begin{Bmatrix} \frac{\partial \bigcup_{1D}}{\partial \gamma_{11}} \\ \frac{1}{2}\frac{\partial \bigcup_{1D}}{\partial \gamma_{12}} \\ \frac{1}{2}\frac{\partial \bigcup_{1D}}{\partial \gamma_{13}} \\ \frac{\partial \bigcup_{1D}}{\partial \kappa_1} \\ \frac{\partial \bigcup_{1D}}{\partial \kappa_2} \\ \frac{\partial \bigcup_{1D}}{\partial \kappa_3} \end{Bmatrix} \tag{19}$$

This is the most general form of the cross-sectional analysis for class S and class T beams defined by Hodges [7]. The coefficients of the nonlinear stiffness matrix, S^{NL}, obtained from the nonlinear analysis of the beam cross-section is defined in the Appendix A [8]. All the 1-D stiffness matrices and their corrections are defined in the work of Harursampath [9].

3 Dynamic Analysis of Mechanism

The dynamic response of non-linear, flexible multi-body beam-systems is simulated within the framework of energy-preserving and energy-decaying time integration schemes. These schemes provide unconditional stability for non-linear systems. The kinematic description of bodies and joints in their undeformed and deformed configurations adopted here follows Bauchau [10] and makes use of three orthogonal triads. Figure 2 shows the beam in the undeformed and deformed configurations. First, an inertial triad, S_I, is used as a global reference for the system with unit vectors, i_1, i_2, and i_3. A second triad, S_O, is attached to the body and defines its orientation in the reference configuration with unit vectors, e_{o1}, e_{o2}, and e_{o3}. Finally, a third triad, S^*, defines the orientation of the body in its deformed configuration with unit vectors, e_1, e_2, and e_3. The components of vector $(\cdot)$ measured in S_I and S^* are denoted by $\underline{(\cdot)}$ and $\underline{(\cdot)}^*$, respectively. For completeness, we outline the relevant portions of Bauchau [10].

The kinetic and strain energies of the beam are:

$$\mathrm{K} = \frac{1}{2}\int_0^\ell \underline{v}^{*T} M^* \underline{v}^* dx_1; \bigcup = \int_0^\ell \bigcup_{1D} (\overline{\gamma_{11}}, \overline{\kappa_1}, \overline{\kappa_2}, \overline{\kappa_3}) dx_1 \tag{20}$$

respectively, where ℓ is the length of the beam; x_1 is the curvilinear coordinate along the reference curve; M^* and $\underline{v}^*$ are the sectional inertia matrix and velocity vector, respectively. The superscript $(\cdot)^*$ is used to denote tensor components measured in deformed configuration.

The equations of motion of the beam can be derived from the Hamilton's principle as follows:

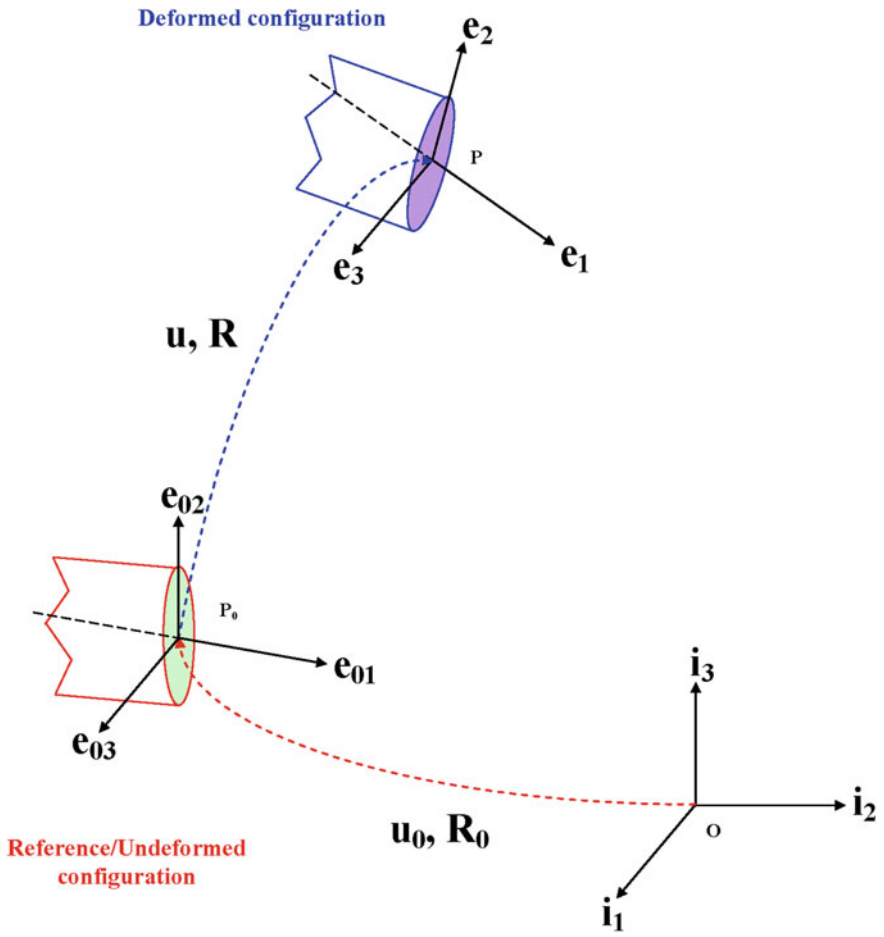

Fig. 2 Beam in the undeformed and deformed configurations [10]

$$\int_{t_i}^{t_f}\int_{0}^{\ell}\left(\delta\underline{v}^{*T}M^{*}\underline{v}^{*}-\delta\bigcup_{1D}(\overline{\gamma_{11}},\overline{\kappa}_1,\overline{\kappa_2},\overline{\kappa_3})+\delta W^{a}\right)dx_1dt=0 \tag{21}$$

where $\delta\underline{v}^{*}$ are the virtual variations in sectional velocities, $\delta\bigcup_{1D}$ is the variation of 1-D strain energy density, and δW^{a} is the virtual work done by the externally applied forces. The final form of the equations of motion of the beam is as follows:

$$\left(\Re\Re_0\underline{p}^{*}\right)^{\cdot}+\bigcup[\tilde{\tilde{u}}]\Re\Re_0\underline{p}^{*}-\left(\Re\Re_0\underline{f}^{*}\right)^{\prime}-\bigcup[\overline{u_0}^{\prime}+\tilde{u}^{\prime}]\Re\Re_0\underline{f}^{*}=\underline{q} \tag{22}$$

where u_0 is the displacement vector from a global reference for the system to body attached reference configuration; u is the displacement vector from body attached

reference configuration to deformed configuration; the sectional momenta and elastic forces are defined as $\underline{p}^* = M^* \underline{v}^*$; as before, $\underline{f}^* = S^{NL} \underline{e}^*$; and $\underline{q}$ is a column matrix containing components of the external forces.

3.1 Computational Scheme

An energy-preserving discretization of these equations of motion, Eq. (22), is performed. The inertial and elastic forces are discretized to yield the following discretized equations of motion:

$$\frac{\Re_f \Re_0 \underline{p}_f^* - \Re_i \Re_0 \underline{p}_i^*}{\Delta t} + \bigcup \left[\frac{\tilde{u}_f - \tilde{u}_i}{\Delta t} \right] \Re_a \Re_0 \frac{\underline{p}_f^* + \underline{p}_i^*}{2} - \left(\Re_b \Re_0 \underline{f}_m^* \right)' - \bigcup \left[\widetilde{u_0}' + \widetilde{u_m}' \right] \Re_b \Re_0 \underline{f}_m^* = \underline{q}_m \tag{23}$$

where $(\cdot)_m = \left((\cdot)_f + (\cdot)_i\right)/2$; Subscripts $(\cdot)_i$, $(\cdot)_f$, and $(\cdot)_m$ are used to indicate the value of a quantity at times t_i, t_f and $t_m = \left(t_f + t_i\right)/2$, and all the rotation operators and the discretization of finite rotations are defined in Appendix A and B of Bauchau [10].

In the formulation of flexible joint elements, the strain energy in a given flexible joint is defined as follows:

$$v = \frac{1}{2} \underline{s}^{*T} C^* \underline{s}^* \tag{24}$$

where C^* are the components of the flexible joint stiffness tensor and $\underline{s}^*$ are the induced deformations in the flexible joint in terms of relative displacements $\left(\underline{u} = \underline{u}^k - \underline{u}^\ell\right)$ and relative rotations $\left(\underline{\delta\psi} = \underline{\delta\psi}^k - \underline{\delta\psi}^\ell\right)$ of the two bodies $(\cdot)^k$ and $(\cdot)^\ell$. The energy-preserving formulation for flexible joints consists of the elastic force discretization together with the following constitutive laws:

$$\underline{f}_m^* = C^* \left(\underline{s}_f^* + \underline{s}_i^* \right)/2 \tag{25}$$

3.2 System Constraints: Modeling of Joints

Figure 3 shows the revolute joint in the reference and deformed configurations. For the case of revolute joint elements, the two kinematic constraints, $C_1 = 0$ and, $C_2 = 0$ are defined in the deformed configuration utilizing the condition of no relative displacements and the third constraint, $C_3 = 0$, obtained from the definition

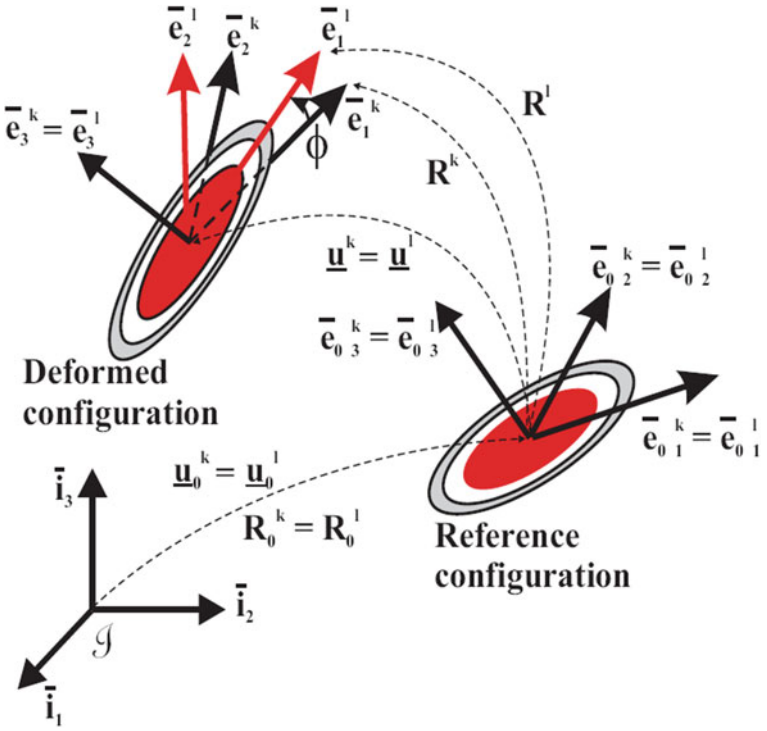

Fig. 3 Revolute joint in the reference and deformed configurations [10]

of the relative rotation ϕ between the two bodies where $C_i (i = 1, 2, 3)$ are defined as follows:

$$C_1 = g_{31} = \underline{e}_3^{kT} \underline{e}_1^{\ell} = 0 \tag{26}$$

$$C_2 = g_{32} = \underline{e}_3^{kT} \underline{e}_2^{\ell} = 0 \tag{27}$$

$$C_3 = g_{11} \sin\phi + g_{12} \cos\phi = 0 \tag{28}$$

where $g_{11} = \underline{e}_1^{kT} \underline{e}_1^{\ell}$ and $g_{12} = \underline{e}_1^{kT} \underline{e}_2^{\ell}$. Here $(\underline{e}_1, \underline{e}_2, \underline{e}_3)$ form ortho-normal bases in the deformed configurations for two bodies k and ℓ. The above formulation is explained in Pollayi and Harursampath [11].

4 Numerical Example

The benchmark problem adopted but generalized from Bauchau [10] deals with a four-bar mechanism problem depicted in Fig. 4.

Bar-1, (AB) is of length $\ell_1 = 0.12$ m and is connected to the ground at point A by means of a revolute joint. Bar-2, (BC) is of length $\ell_2 = 0.24$ m and is connected to bar-1 at point B with a revolute joint. Finally, bar-3, (CD) is of length $\ell_3 = 0.12$ m and is connected to bar-2 and the ground at points C and D, respectively, by means of two revolute joints. Table 1 shows the definition of the six joints. Here "Yes" or "No" indicate that the corresponding relative motion is allowed or prohibited, respectively. For the screw joint, p is the screw pitch. These 6-joints are called lower pairs and are used for practical applications. All these joints imposes constraints on the relative motion of the different bodies of the multi-body system. Figure 5 shows the different types of four-bar linkages where s is the shortest link, and l is the longest link.

At time, $t = 0$, in the undeformed configuration, the bars of this mechanism intersect each other at 90° angles. However, the axes of rotation of all the revolute joints are at non-zero angles with respect to the normal to the plane of the mechanism to simulate initial defects and/or additional design variables in the mechanism. Such initial defects and/or additional design variables shall be defined in the form of initial

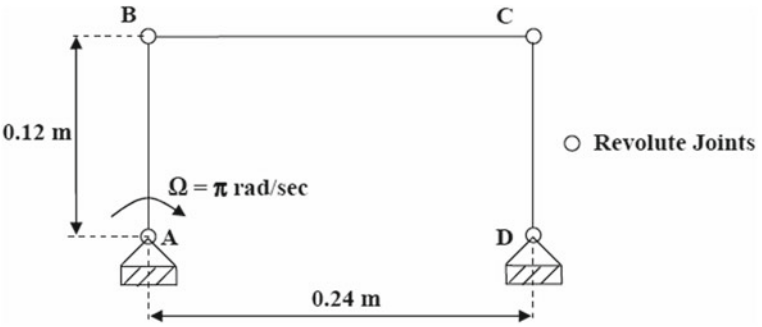

Fig. 4 The four-bar mechanism problem

Table 1 Definition of six joints

Joint type	Relative displacements			Relative rotations		
	d_1	d_2	d_3	θ_1	θ_2	θ_3
Revolute	No	No	No	No	No	Yes
Prismatic	No	No	Yes	No	No	No
Screw	No	No	$=p\,\theta_3$	No	No	Yes
Cylindrical	No	No	Yes	No	No	Yes
Planar	Yes	Yes	No	No	No	Yes
Spherical	No	No	No	Yes	Yes	Yes

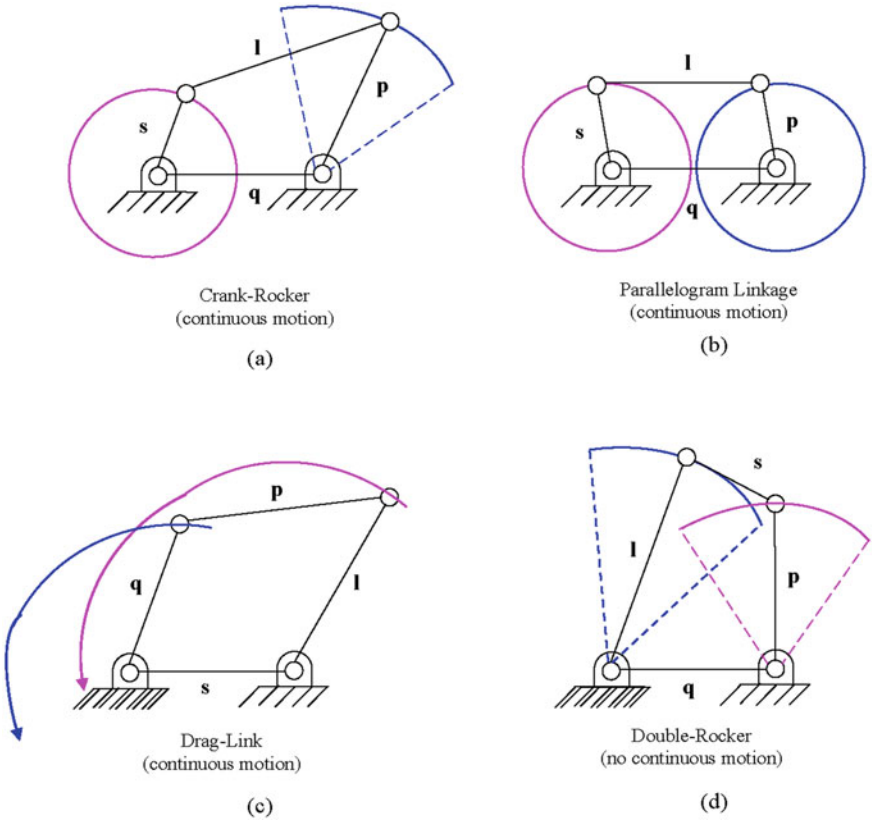

Fig. 5 Different types of four-bar linkages: **a** $s + \ell \leq p + q$ **b** $s + \ell \leq p + q$ **c** $s + \ell \leq p + q$ and **d** $s + \ell \leq p + q$

twists (k_1) and curvatures (k_2) of all the three bars. A torque is applied on bar-1 at point A so as to enforce a constant angular velocity $\Omega = \pi \ \frac{\text{rad}}{\text{s}}$. If the four-bars were infinitely rigid, no motion would be possible as the mechanism locks and this was also observed by simulating using available commercial software (I-DEAS + NASTRAN + ADAMS). For elastic bars, complete motion becomes possible, but generates large internal forces.

The four-bar mechanisms are simulated using the available commercial software (I-DEAS + NASTRAN + ADAMS) to see the practical applicability by arranging the beams in the mechanisms in distinctly different orientations. The two-different ways of arranging the beams in the mechanism, found in the literature, are shown in Fig. 6. Figure 6a shows the CAD drawing of the synthesized mechanism [12]. Figure 6b shows the proposed two-DOF wing mechanism translating and rotating a folded polymer wing using two independently actuated parallel four-bar structures, and its kinematic and force parameters [13].

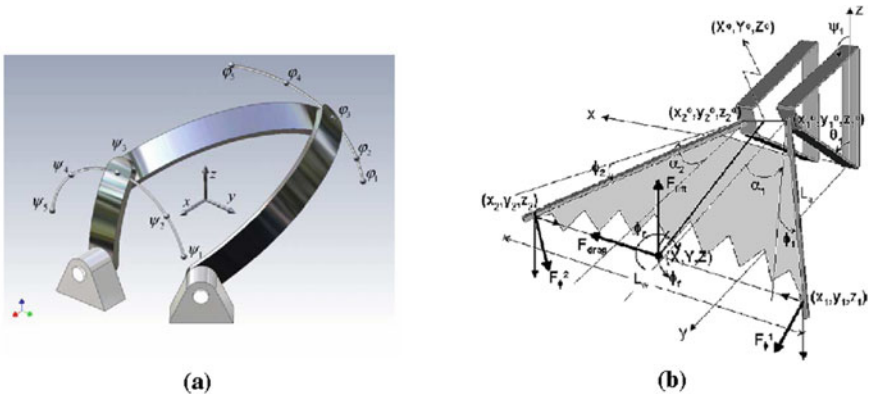

Fig. 6 Two-different ways of arranging the beams

VAM requires identification of small parameters in the present four-bar mechanism problem. Each bar is modeled as a laminated strip-beam. The wavelength of deformation along the strip-beam is denoted by ℓ. The width and thickness of the strip-beam are denoted by b and h, respectively. From the geometry of the strip-beam, the natural small parameters are the thickness-to-width ratio $\delta_h = h/b$; the width-to-length ratio $\delta_b = b/\ell$; the width times pre-twist per unit length $\delta_\ell = bk_1$. As an example, the authors have chosen dimensions such that $\delta_\ell = \delta_b = 0.1$ for bar-1 and bar-3; $\delta_h = \delta_b = 0.05$ for bar-2 for the present four-bar mechanism problem, as observable from Table 2.

Table 2 Material properties and dimensions of all three bars in the mechanism

Property (dimension)	Bar-1	Bar-2	Bar-3
E_L (GPa)	135.6	132.2	132.2
$E_T = E_{T'}$ (GPa)	9.9	10.75	10.75
$G_{LT} = G_{LT'}$ (GPa)	4.2	5.65	5.65
$G_{TT'}$ (GPa)	3.3	5.65	5.65
$\upsilon_{LT} = \upsilon_{LT'}$	0.3	0.239	0.239
$\upsilon_{TT'}$	0.5	0.4	0.4
ℓ (m)	0.12	0.24	0.12
b (m)	0.012	0.012	0.012
h (m)	0.0012	0.0006	0.0012
Ply thickness (mm)	0.075	0.075	0.075
$\rho\,(\mathrm{kg/m^3})$	1520.6	1530.8	1530.8
k_1(rad/m)	−0.7275	−0.3638	−0.7275
k_2(rad/m)	0.291	0.1455	0.291

The laminated composite strip of bar-1 is similar to that considered by Armanios et al. [14] which was fabricated from ICI Fiberite T300/954-3 Graphite/Cyanate material system, whereas the laminated composite strips of bar-2 and bar-3 are similar to those considered by Kosmatka [15] which were made of T300/5208 Graphite/Epoxy material system. In a previous work of Pollayi and Harursampath [11], the present authors had considered, for the same problem, the stacking sequence $[20_2/-70_4/20_2/-20_2/70_4/-20_2]_T$ for bar-1 and bar-3 and $[20/-70_2/20/-20/70_2/-20]_T$ for bar-2. On the other hand, the current work investigates various types of stacking sequences including those in [11]. Ply thickness in all bars is identical and listed in Table 2. The specific type of anti-symmetrical layup used in the previous work for all the bars ensures hygro-thermal stability of the laminates [16] and eliminates initial warping that results from the curing stresses while exhibiting extension-twist coupling, useful for certain applications. Thus all the three bars were anti-symmetric laminates and thus had the following properties:

$$A_{16} = A_{26} = 0;\ B_{11} = B_{22} = B_{66} = B_{12} = 0;\ D_{16} = D_{26} = 0 \tag{29}$$

Exploring Different Stacking Sequences

The behavior of the four-bar mechanism problem is studied for the following stacking sequences:

1. Anti-Symmetric
2. Symmetric
3. Cross-Ply
4. Quasi-Isotropic

The analytic sensitivity of the described four-bar mechanism to stacking sequences is thus observed. The specific candidate lay-ups for each component bar are tabulated in Table 3. In the second case, all the three bars are symmetric laminates and have the following properties:

$$B_{ij} = 0(\forall i,\ j = 1, 2, 6) \tag{30}$$

In the third case, all the three bars are symmetric cross-ply laminates and have the following properties:

$$A_{16} = 0 = A_{26};\ D_{16} = 0 = D_{26};\ B_{ij} = 0(\forall i,\ j = 1, 2, 6) \tag{31}$$

In the fourth case, all the three bars are symmetric quasi-isotropic laminates and have the following properties:

$$A_{11} = A_{22};\ A_{16} = 0 = A_{26};\ 2A_{66} = A_{11} - A_{12};\ D_{16} = D_{26};\ B_{ij} = 0(\forall i,\ j = 1, 2, 6) \tag{32}$$

Table 3 Different stacking sequences in all component bars of the four-bar mechanism

S. No.	Stacking sequences
1	For B1 and B3: $[\alpha_2/(\alpha-90)_4/\alpha_2/-\alpha_2/(90-\alpha)_4/-\alpha_2]_T$ For B2: $[\alpha/(\alpha-90)_2/\alpha/-\alpha/(90-\alpha)_2/-\alpha]_T$
2	For B1 and B3: $[\alpha_2/(\alpha-90)_4/\alpha_2/\alpha_2/(90-\alpha)_4/-\alpha_2]_T$ For B2: $[\alpha/(\alpha-90)_2/\alpha/\alpha/(90-\alpha)_2/\alpha]_T$
3	For B1 and B3: $[0/90]_{4S}$ For B2: $[0/90]_{2S}$
4 (i)	For B1 and B3: $[0/+45/-45/90]_{2S}$ For B2: $[0/+45/-45/90]_S$
4 (ii)	For B1 and B3: $[0/+45/90/-45]_{2S}$ For B2: $[0/+45/90/-45]_S$

Performing a study on sensitivity towards ply-angle, α, by varying from $\alpha = 0°$ to 90° in increments of 5° in both cases 1 and 2 provides a better understanding of critical system dynamic parameters for the four-bar mechanism. As a combinatorial effect of the misalignments described earlier, design choices and laminate manufacturing/handling induced-defects, each strip is modeled with a uniformly distributed pre-twist of −5° about its longitudinal reference curve and initial flat-wise curvature causing an angle of 2° between its ends. The physical characteristics of the three bars are tabulated in Table 2. The subscripts L, T, and T' suffixing E'^s, G'^s and υ'^s denote the principal material axes.

For comparing linear stiffnesses from FE code VABS with the results from analytical expressions for non-linear stiffnesses, the cross-sections of bar-1 and bar-3 are divided into 160 eight-noded quadrilateral finite elements with 10-elements each along the width direction and 16-elements along the thickness direction. Similarly, bar-2 is divided into 80 eight-noded quadrilateral finite elements with 10-elements along the width direction and 8-elements along the thickness direction. Thus in the thickness direction, each ply constitutes an element. The sectional mass properties are given in Table 4 for all three bars.

Here μ is the mass per unit length, i_2 is the mass moment of inertia about the direction along the width, and i_3 is the mass moment of inertia about the direction along the thickness. The stiffness matrices obtained from the linear cross-sectional analyses of bars-1, -2, and -3 using anti-symmetric, symmetric, quasi-isotropic, and cross-ply laminates are given in Tables 5, 6, 7, 8 and 9 in bold-face and kept inside brackets. Here the correlation between the row/column number in the 6 × 6 stiffness

Table 4 The sectional mass properties of all three bars in the mechanism

Property	Bar-1	Bar-2	Bar-3
μ (kg/m)	0.2189E−01	0.1102E−01	0.2204E−01
i_2 (kg m^2/m)	0.2628E−08	0.3307E−09	0.2645E−08
i_3 (kg m^2/m)	0.2628E−06	0.1323E−06	0.2645E−06

Table 5 Stiffness coefficients of all three bars in the mechanism using anti-symmetric laminates @$\alpha = 20°$

Stiffness	Present work		
	Bar-1	Bar-2	Bar-3
S_{11}^{NL} (10^6 N)	0.8113 (**0.7723**)	0.4053 (**0.3996**)	0.8107 (**0.7848**)
S_{14}^{NL} (N m)	158.8 +9.735 κ_1 (**151.6**)	36.54 +4.864 κ_1 (**38.14**)	146.1 +9.728 κ_1 (**143.8**)
S_{15}^{NL} (N m)	0 (**0.05956**)	0 (**0.0003808**)	0 (**0.04814**)
S_{16}^{NL} (N m)	0 (**0.0**)	0 (**0.0**)	0 (**0.0**)
S_{44}^{NL} (N m^2)	0.09468 +9.735 γ_{11} +0.005513 κ_1 +0.000008575 κ_2 +0.0003154 $\kappa_1{}^2$ +0.00002949 $\kappa_2{}^2$ (**0.0877**)	0.0127 +4.864 γ_{11} +0.00115 κ_1 +0.000001853 κ_2 +0.0001576 $\kappa_1{}^2$ +0.00001271 $\kappa_2{}^2$ (**0.0127**)	0.1016 +9.7281 γ_{11} +0.005057 κ_1 +0.000007412 κ_2 +0.0003152 $\kappa_1{}^2$ +0.00002549 $\kappa_2{}^2$ (**0.09564**)
S_{45}^{NL} (N m^2)	−0.000006248 +0.000008575 κ_1 −0.00004294 κ_2 −0.0002658 κ_3 +0.00005898 κ_1 κ_2 (−**0.0002549**)	−0.0000006752 +0.000001853 κ_1 −0.000009282 κ_2 −0.0002574 κ_3 +0.00002549 κ_1 κ_2 (−**0.00003071**)	−0.000005402 +0.000007412 κ_1 −0.00003713 κ_2 −0.0002574 κ_3 +0.00005099 κ_1 κ_2 (−**0.0002318**)
S_{46}^{NL} (N m^2)	−0.0002658 κ_2 (**0.0**)	−0.0002574 κ_2 (**0.0**)	−0.0002574 κ_2 (**0.0**)
S_{55}^{NL} (N m^2)	0.07402 −0.00004294 κ_1 +0.00001627 κ_2 +0.00002949 $\kappa_1{}^2$ +0.00005592 $\kappa_2{}^2$ −0.0009134 $\kappa_3{}^2$ (**0.1069**)	0.0102 −0.000009282 κ_1 +0.000003043 κ_2 +0.00001275 $\kappa_1{}^2$ +0.00002091 $\kappa_2{}^2$ −0.001769 $\kappa_3{}^2$ (**0.01371**)	0.08161 −0.00003713 κ_1 +0.00001217 κ_2 +0.00002549 $\kappa_1{}^2$ +0.00004183 $\kappa_2{}^2$ −0.0008844 $\kappa_3{}^2$ (**0.1082**)
S_{56}^{NL} (N m^2)	−0.0002658 κ_1 −0.001827 κ_2 κ_3 (**0.0**)	−0.0002574 κ_1 −0.003538 κ_2 κ_3 (**0.0**)	−0.0002574 κ_1 −0.001769 κ_2 κ_3 (**0.0**)
S_{66}^{NL} (N m^2)	9.735 −0.0009134 $\kappa_2{}^2$ (**8.532**)	4.864 −0.001769 $\kappa_2{}^2$ (**4.676**)	9.728 −0.0008844 $\kappa_2{}^2$ (**8.910**)

matrix and the deformation modes are as follows: 1—Extension, 4—Torsion, 5—Flatwise Bending, 6—Edgewise Bending. The bold-faced values in brackets are from the linear cross-sectional analysis using FE code VABS with refined Timoshenko-like beam model. The non-linear cross-sectional stiffness matrix has strong extension-twist coupling, as expected.

Table 6 Stiffness coefficients of all three bars in the mechanism using symmetric laminates @$\alpha = 20°$

Stiffness	Present work		
	Bar-1	Bar-2	Bar-3
S_{11}^{NL} (10^6 N)	0.4073 (**0.6938**)	0.2461 (**0.3656**)	0.4922 (**0.7298**)
S_{14}^{NL} (N m)	−3.556 +4.888 κ_1 (−**13.45**)	−1.074 +2.953κ_1 (−**2.792**)	−4.297 +5.906 κ_1 (−**10.08**)
S_{15}^{NL} (N m)	0 (−**8.841**)	0 (−**1.357**)	0 (−**4.573**)
S_{16}^{NL} (N m)	0 (**0.0**)	0 (**0.0**)	0 (**0.0**)
S_{44}^{NL} (N m^2)	0.09987 +4.888 γ_{11} −0.0002213 κ_1 −1.17E−05 κ_2 +0.0001584 ${\kappa_1}^2$ +9.5E−06 ${\kappa_2}^2$ +3.122E−05 κ_1 κ_2 (**0.08784**)	0.01333 +2.953 γ_{11} −0.0001367 κ_1 −3.327E−06 κ_2 +9.568E−05 ${\kappa_1}^2$ +5.232E−06 ${\kappa_2}^2$ +1.759E−05 κ_1 κ_2 (**0.01271**)	0.1067 +5.906 γ_{11} −0.0002682 κ_1 −1.33E−05 κ_2 +0.0001913 ${\kappa_1}^2$ +1.048E−05 ${\kappa_2}^2$ +3.518E−05 κ_1 κ_2 (**0.09584**)
S_{45}^{NL} (N m^2)	−0.07792 −1.17E−05 κ_1 −8.61E−06 κ_2 −5.37E−05 κ_3 +1.56E−05 ${\kappa_1}^2$ +4.79E−06 ${\kappa_2}^2$ +1.90E−05 κ_1 κ_2 (**0.06870**)	−0.009054 −3.327E−06 κ_1 −2.45E−06 κ_2 −7.88E−05 κ_3 +8.79E−06 ${\kappa_1}^2$ +2.50E−06 ${\kappa_2}^2$ +1.048E−05 κ_1 κ_2 (**0.008642**)	−0.07243 −1.33E−05 κ_1 −9.79E−06 κ_2 −7.88E−05 κ_3 +1.759E−05 ${\kappa_1}^2$ +5.01E−06 ${\kappa_2}^2$ +2.097E−05 κ_1 κ_2 (**0.06523**)
S_{46}^{NL} (N m^2)	−5.368E−05 κ_2 (**0.0**)	−7.88E−05 κ_2 (**0.0**)	−7.88E−05 κ_2 (**0.0**)
S_{55}^{NL} (N m^2)	0.1118 −8.61E−06 κ_1 +1.93E−06 κ_2 +9.50E−06 ${\kappa_1}^2$ +6.616E−06 ${\kappa_2}^2$ −0.0001845 ${\kappa_3}^2$ +9.57E−06 κ_1 κ_2 (**0.1046**)	0.01392 −2.45E−06 κ_1 +5.01E−07 κ_2 +5.24E−06 ${\kappa_1}^2$ +3.443E−06 ${\kappa_2}^2$ −0.0005417 ${\kappa_3}^2$ +5.01E−06 κ_1 κ_2 (**0.01365**)	0.1114 −9.79E−06 κ_1 +2.00E−06 κ_2 +1.048E−05 ${\kappa_1}^2$ +6.885E−06 ${\kappa_2}^2$ −0.0002708 ${\kappa_3}^2$ +1.00E−05 κ_1 κ_2 (**0.1065**)
S_{56}^{NL} (N m^2)	−5.368E−05 κ_1 −0.0003689 κ_2 κ_3 (**0.0**)	−7.88E−05 κ_1 −0.001083 κ_2 κ_3 (**0.0**)	−7.88E−05 κ_1 −0.0005417 κ_2 κ_3 (**0.0**)
S_{66}^{NL} (N m^2)	4.8878 −0.0001845 ${\kappa_2}^2$ (**4.8417**)	2.9530 −0.0005417 ${\kappa_2}^2$ (**2.9485**)	5.9059 −0.0002708 ${\kappa_2}^2$ (**5.8613**)

Table 7 Stiffness coefficients of all three bars in the mechanism using quasi-isotropic type-1 laminates

Stiffness	Present work		
	Bar-1	Bar-2	Bar-3
S_{11}^{NL} (10^6 N)	0.7468 (**0.7422**)	0.3761 (**0.3744**)	0.7521 (**0.7491**)
S_{14}^{NL} (N m)	−6.5196 +8.9615 κ_1 (**−5.9543**)	−1.6415 +4.5127 κ_1 (**−1.6043**)	−6.5661 +9.0254 κ_1 (**−6.1160**)
S_{15}^{NL} (N m)	0 (**−0.04307**)	0 (**−0.004245**)	0 (**−0.03996**)
S_{16}^{NL} (N m)	0 (**0.0**)	0 (**0.0**)	0 (**0.0**)
S_{44}^{NL} (N m^2)	0.1295 +8.9615 γ_{11} −0.0004279 κ_1 +1.479E−05 κ_2 +0.0002903 ${\kappa_1}^2$ +1.916E−05 ${\kappa_2}^2$ −1.875E−05 κ_1 κ_2 (**0.1102**)	0.01396 +4.5127 γ_{11} −0.0001106 κ_1 +9.381E−06 κ_2 +0.0001462 ${\kappa_1}^2$ +1.420E−05 ${\kappa_2}^2$ −2.889E−05 κ_1 κ_2 (**0.01317**)	0.1332 +9.0254 γ_{11} −0.0004308 κ_1 +1.409E−05 κ_2 +0.0002924 ${\kappa_1}^2$ +1.777E−05 ${\kappa_2}^2$ −1.814E−05 κ_1 κ_2 (**0.1172**)
S_{45}^{NL} (N m^2)	−0.005797 +1.479E−05 κ_1 −2.883E−05 κ_2 −0.0002277 κ_3 −9.373E−06 ${\kappa_1}^2$ −4.08E−06 ${\kappa_2}^2$ +3.832E−05 κ_1 κ_2 (**−0.004911**)	−0.001092 +9.381E−06 κ_1 −1.034E−05 κ_2 −0.0003654 κ_3 −1.444E−05 ${\kappa_1}^2$ −8.051E−06 ${\kappa_2}^2$ +2.840E−05 κ_1 κ_2 (**−0.001036**)	−0.005928 +1.409E−05 κ_1 −2.668E−05 κ_2 −0.0002302 κ_3 −9.071E−06 ${\kappa_1}^2$ −3.637E−06 ${\kappa_2}^2$ +3.554E−05 κ_1 κ_2 (**−0.005234**)
S_{46}^{NL} (N m^2)	−0.0002277 κ_2 (**0.0**)	−0.0003654 κ_2 (**0.0**)	−0.0002302 κ_2 (**0.0**)
S_{55}^{NL} (N m^2)	0.1185 −2.883E−05 κ_1 +7.115E−06 κ_2 +1.916E−05 ${\kappa_1}^2$ +2.445E−05 ${\kappa_2}^2$ −0.0007826 ${\kappa_3}^2$ −8.16E−06 κ_1 κ_2 (**0.1181**)	0.01865 −1.035E−05 κ_1 +2.938E−06 κ_2 +1.42E−05 ${\kappa_1}^2$ +2.019E−05 ${\kappa_2}^2$ −0.002512 ${\kappa_3}^2$ −1.61E−05 κ_1 κ_2 (**0.01864**)	0.1185 −2.668E−05 κ_1 +6.08E−06 κ_2 +1.777E−05 ${\kappa_1}^2$ +2.089E−05 ${\kappa_2}^2$ −0.000791 ${\kappa_3}^2$ −7.27E−06 κ_1 κ_2 (**0.1183**)
S_{56}^{NL} (N m^2)	−0.0002277 κ_1 −0.001565 κ_2 κ_3 (**0.0**)	−0.0003654 κ_1 −0.005023 κ_2 κ_3 (**0.0**)	−0.0002302 κ_1 −0.001582 κ_2 κ_3 (**0.0**)
S_{66}^{NL} (N m^2)	8.9614 −0.0007826 ${\kappa_2}^2$ (**8.8022**)	4.5126 −0.002512 ${\kappa_2}^2$ (**4.4541**)	9.0253 −0.000791 ${\kappa_2}^2$ (**8.9204**)

Table 8 Stiffness coefficients of all three bars in the mechanism using quasi-isotropic type-2 laminates

Stiffness	Present work		
	Bar-1	Bar-2	Bar-3
S_{11}^{NL} (10^6 N)	0.7468 (**0.7434**)	0.3761 (**0.3748**)	0.7521 (**0.7498**)
S_{14}^{NL} (N m)	−6.5196 +8.9615 κ_1 (−**6.0195**)	−1.6415 +4.5127 κ_1 (−**1.6101**)	−6.5661 +9.0254 κ_1 (−**6.1609**)
S_{15}^{NL} (N m)	0 (−**0.0123**)	0 (−**0.001543**)	0 (−**0.01768**)
S_{16}^{NL} (N m)	0 (**0.0**)	0 (**0.0**)	0 (**0.0**)
S_{44}^{NL} (N m^2)	0.1120 +8.9615 γ_{11} −0.0004307 κ_1 +1.839E−05 κ_2 +0.0002903 ${\kappa_1}^2$ +1.514E−05 ${\kappa_2}^2$ −2.823E−05 κ_1 κ_2 (**0.09645**)	0.01086 +4.5127 γ_{11} −0.0002175 κ_1 +9.773E−06 κ_2 +0.0001462 ${\kappa_1}^2$ +1.005E−05 ${\kappa_2}^2$ −3.262E−05 κ_1 κ_2 (**0.01033**)	0.1169 +9.0254 γ_{11} −0.0004335 κ_1 +1.773E−05 κ_2 +0.0002924 ${\kappa_1}^2$ +1.412E−05 ${\kappa_2}^2$ −2.750E−05 κ_1 κ_2 (**0.1036**)
S_{45}^{NL} (N m^2)	−0.01205 +1.839E−05 κ_1 −2.236E−05 κ_2 −0.0001959 κ_3 −1.411E−05 ${\kappa_1}^2$ −4.636E−06 ${\kappa_2}^2$ +3.0285E−05 κ_1 κ_2 (−**0.01053**)	−0.002443 +9.773E−06 κ_1 −6.441E−06 κ_2 −0.0002753 κ_3 −1.631E−05 ${\kappa_1}^2$ −5.552E−06 ${\kappa_2}^2$ +2.0181E−05 κ_1 κ_2 (−**0.00232**)	−0.01204 +1.773E−05 κ_1 −2.079E−05 κ_2 −0.0001993 κ_3 −1.375E−05 ${\kappa_1}^2$ −4.181E−06 ${\kappa_2}^2$ +2.825E−05 κ_1 κ_2 (−**0.0108**)
S_{46}^{NL} (N m^2)	−0.0001959 κ_2 (**0.0**)	−0.0002753 κ_2 (**0.0**)	−0.000199 κ_2 (**0.0**)
S_{55}^{NL} (N m^2)	0.1190 −2.236E−05 κ_1 +4.052E−06 κ_2 +1.514E−05 ${\kappa_1}^2$ +1.392E−05 ${\kappa_2}^2$ −0.0006732 ${\kappa_3}^2$ −9.273E−06 κ_1 κ_2 (**0.1186**)	0.01887 −6.441E−06 κ_1 +1.096E−06 κ_2 +1.009E−05 ${\kappa_1}^2$ +7.53E−06 ${\kappa_2}^2$ −0.001892 ${\kappa_3}^2$ −1.11E−05 κ_1 κ_2 (**0.01884**)	0.1184 −2.079E−05 κ_1 +3.496E−06 κ_2 +1.412E−05 ${\kappa_1}^2$ +1.20E−05 ${\kappa_2}^2$ −0.000685 ${\kappa_3}^2$ −8.36E−06 κ_1 κ_2 (**0.1181**)
S_{56}^{NL} (N m^2)	−0.0001959 κ_1 −0.001346 κ_2 κ_3 (**0.0**)	−0.0002753 κ_1 −0.003784 κ_2 κ_3 (**0.0**)	−0.000199 κ_1 −0.00137 κ_2 κ_3 (**0.0**)
S_{66}^{NL} (N m^2)	8.9614 −0.0006732 ${\kappa_2}^2$ (**8.8426**)	4.5127 −0.001892 ${\kappa_2}^2$ (**4.4668**)	9.0253 −0.000685 ${\kappa_2}^2$ (**8.943**)

Table 9 Stiffness coefficients of all three bars in the mechanism using cross-ply laminates

Stiffness	Present work		
	Bar-1	Bar-2	Bar-3
S_{11}^{NL} (10^6 N)	1.0528 (**1.0525**)	0.5163 (**0.5163**)	1.0327 (**1.0326**)
S_{14}^{NL} (N m)	−9.1909 +12.63333 κ_1 (**−8.9357**)	−2.2539 +6.1962 κ_1 (**−2.2375**)	−9.0157 +12.3925 κ_1 (**−8.7672**)
S_{15}^{NL} (N m)	0 (**−0.06389**)	0 (**−0.004178**)	0 (**−0.0579**)
S_{16}^{NL} (N m)	0 (**0.0**)	0 (**0.0**)	0 (**0.0**)
S_{44}^{NL} (N m^2)	0.02917 +12.6333 γ_{11} −0.0005955 κ_1 +7.52E−07 κ_2 +0.000409 ${\kappa_1}^2$ +2.928E−06 ${\kappa_2}^2$ +1.9E−07 κ_1 κ_2 (**0.02727**)	0.0049 +6.1962 γ_{11} −0.0002921 κ_1 +2.03E−07 κ_2 +0.000201 ${\kappa_1}^2$ +1.506E−06 ${\kappa_2}^2$ +8.57E−08 κ_1 κ_2 (**0.004773**)	0.03919 +12.3925 γ_{11} −0.0005842 κ_1 +6.38E−07 κ_2 +0.0004015 ${\kappa_1}^2$ +2.518E−06 ${\kappa_2}^2$ +1.81E−07 κ_1 κ_2 (**0.03682**)
S_{45}^{NL} (N m^2)	−4.77E−06 +7.52E−07 κ_1 −4.297E−06 κ_2 −0.0003 κ_3 +9.5E−08 ${\kappa_1}^2$ +4.6E−09 ${\kappa_2}^2$ +5.856E−06 κ_1 κ_2 (**−0.34E−06**)	−3.56E−07 +2.03E−07 κ_1 −1.14E−06 κ_2 −0.00036 κ_3 +4.3E−08 ${\kappa_1}^2$ +2.3E−09 ${\kappa_2}^2$ +3.106E−06 κ_1 κ_2 (**−0.56E−07**)	−2.32E−06 +6.38E−07 κ_1 −3.70E−06 κ_2 −0.00029 κ_3 +9.0E−08 ${\kappa_1}^2$ +3.9E−09 ${\kappa_2}^2$ +5.035E−06 κ_1 κ_2 (**−0.206E−06**)
S_{46}^{NL} (N m^2)	−0.0003 κ_2 (**0.0**)	−0.00036 κ_2 (**0.0**)	−0.000294 κ_2 (**0.0**)
S_{55}^{NL} (N m^2)	0.1468 −4.30E−06 κ_1 +1.3E−07 κ_2 +2.93E−06 ${\kappa_1}^2$ +4.32E−07 ${\kappa_2}^2$ −0.001032 ${\kappa_3}^2$ −9.3E−09 κ_1 κ_2 (**0.1468**)	0.0204 −1.14E−06 κ_1 +3.6E−08 κ_2 +1.55E−06 ${\kappa_1}^2$ +2.48E−07 ${\kappa_2}^2$ −0.002491 ${\kappa_3}^2$ −4.5E−09 κ_1 κ_2 (**0.02042**)	0.1437 −3.70E−06 κ_1 +9.5E−08 κ_2 +2.518E−06 ${\kappa_1}^2$ +3.26E−07 ${\kappa_2}^2$ −0.0010095 ${\kappa_3}^2$ −7.7E−09 κ_1 κ_2 (**0.1436**)
S_{56}^{NL} (N m^2)	−0.0003 κ_1 −0.002064 κ_2 κ_3 (**0.0**)	−0.00036 κ_1 −0.004982 κ_2 κ_3 (**0.0**)	−0.0002938 κ_1 −0.002019 κ_2 κ_3 (**0.0**)
S_{66}^{NL} (N m^2)	12.633 −0.001032 ${\kappa_2}^2$ (**12.6286**)	6.1962 −0.002491 ${\kappa_2}^2$ (**6.1956**)	12.3924 −0.0010095 ${\kappa_2}^2$ (**12.389**)

Figure 7 shows the noticeable snap-shots of the deformation shapes of the four-bar mechanism problem about 1000 frames in 1.0 s for three complete rotations of beam-1 about point *A*. It was observed that beam-1 makes a full rotation about point *A* and beam-3 oscillates back and forth, never completing an entire turn. Only beam-2 undergoes large deformations and large rotations. Noticeable deformations of beam-2 start at about $t = 0.098$ s for the first rotation. The maximum deformation

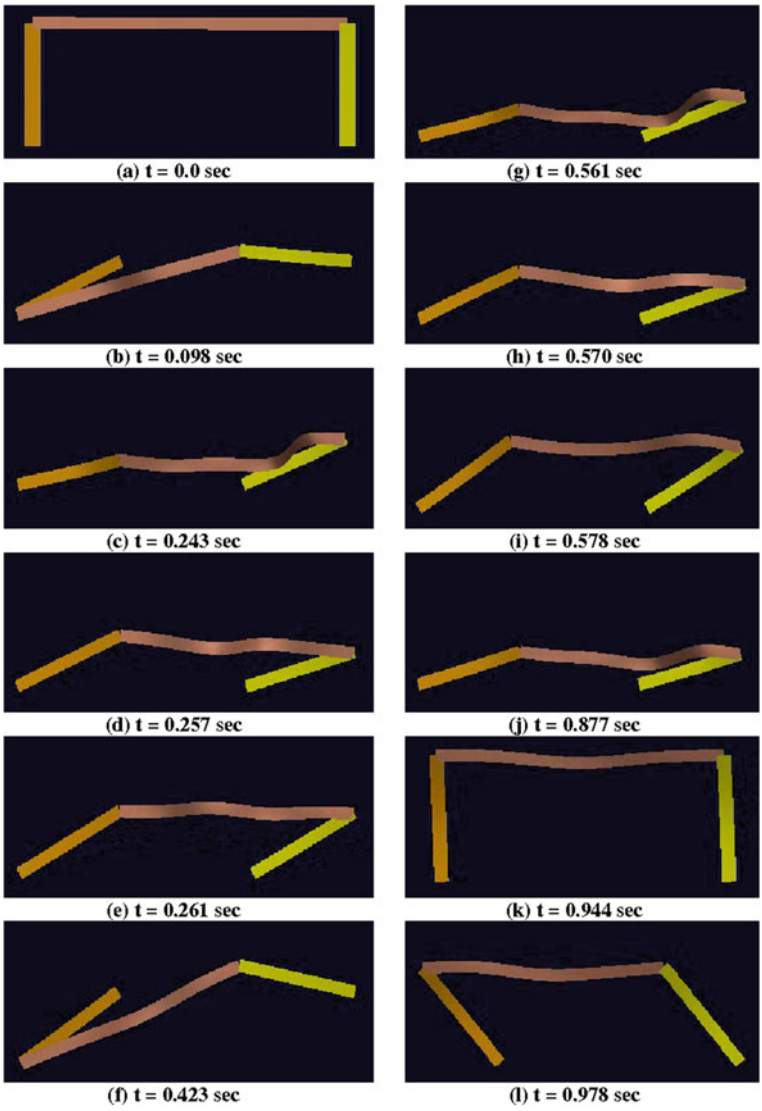

Fig. 7 Snap-shots of the deformation shapes of the four-bar mechanism about 1000 frames in 1.0 s

of beam-2 occurred about $t = 0.243$ s in the first rotation. Figure 8 shows the snap-shots of the deformation shapes of the four-bar mechanism problem for one complete rotation of beam-1 sampled in steps of 40° about point *A*.

The component-laminate strength properties are given in Table 10 and these values are used to evaluate the component-laminate load-carrying capacity in the present four-bar mechanism problem. The point-wise reserve factor of component-laminates

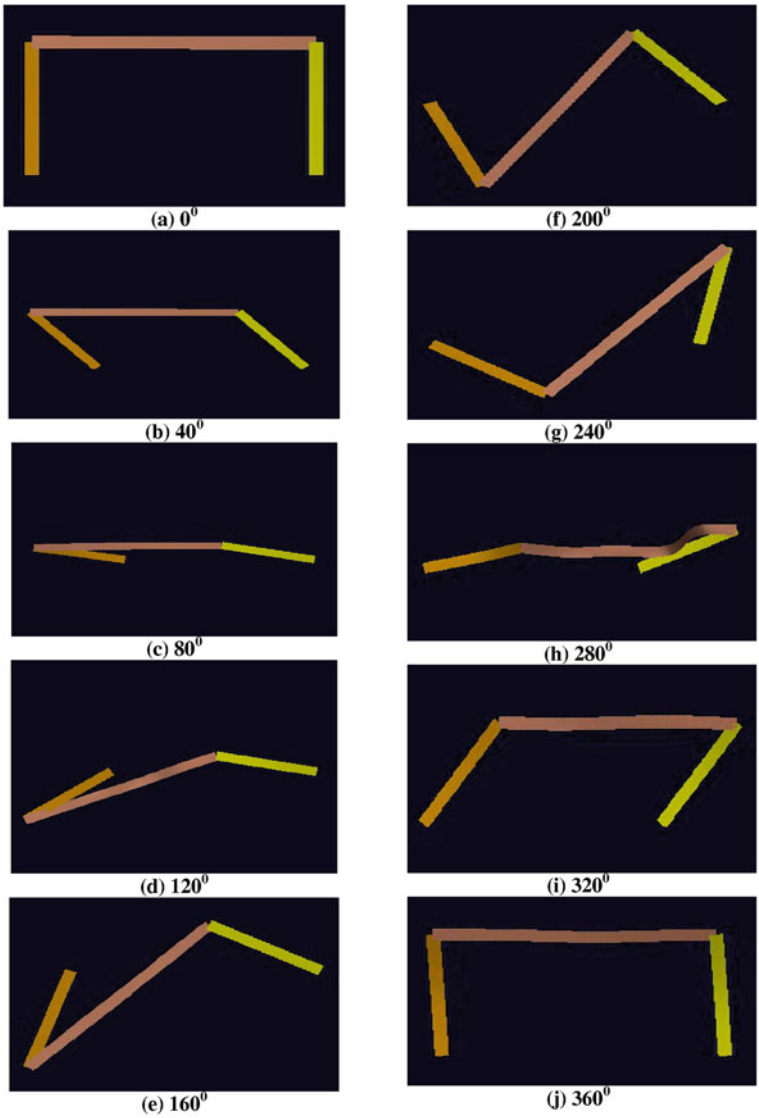

Fig. 8 Snap-shots of the deformation shapes of the four-bar mechanism for one complete rotation

Table 10 T300/954-3 and T300/5208 carbon/epoxy ply strengths

Material	Strength parameters (MPa)				
	σ_{T1}	σ_{C1}	σ_{T2}	σ_{C2}	$\sigma_{S6}^{+} = \sigma_{S6}^{-}$
T300/954-3	1314	1220	43	168	48
T300/5208	1500	1500	40	246	68

Table 11 Reserve factors (R) of component-laminates of the present four-bar mechanism

Point	F_r	R (clock)	R (anti-clock)	M_r	R (clock)	R (anti-clock)
A (AB)	**38.03 N** (1.51 s)	85.24	−44.28	**0.47 N m** (0.005 s)	**14.86**	−8.89
B (AB)	38.08 N (1.51 s)	771.22	−1474.13	0.03 N m (0.0005 s)	224.42	−325.04
B (BC)	38.08 N (1.51 s)	400.24	−215.62	0.1005 N m (0.00056 s)	35.06	−14.46
C (BC)	38.29 N (1.51 s)	63.44	−36.57	0.083 N m (0.0038 s)	28.89	−51.15
C (CD)	38.16 N (1.51 s)	172.81	−211.8	0.041 N m (1.49 s)	150.39	−188.9
D (CD)	38.21 N (1.51 s)	124.65	−146.43	0.122 N m (0.0002 s)	63.29	−51.02

As the four-bar mechanism is rotating about the joint 'A', the mechanism as a whole fails due to maximum resultant moment, $M_r = 0.47$ Nm by considering the least reserve factor and the corresponding resultant force, $F_r = 38.03$ N

in the present four-bar mechanism are given in Table 11. The above mentioned complete analysis is depicted as a flow-chart in Fig. 9.

The Procedure

The following is the step-wise procedure used to predict the first-ply-failure and the failure of present mechanism as a whole.

1. $\left[F \;\; M \right]^T$ = The stress resultants obtained from 1-D global beam(s) analysis as distributions w.r.t. time and all three beam reference curves coordinates.
2. Find $F_{r_{\max}}$ and $M_{r_{\max}}$ (available @ different times).
3. Input $\left[F \;\; M \right]^T$ twice (for $F_{r_{\max}}$ and $M_{r_{\max}}$) to cross-sectional analysis software based on current work by keeping Recovery Flag = True to obtain recovered 3-D strain and hence stress results.
4. Determine stresses in the principal material directions using the above recovered 3-D stresses by applying the following stress transformation relations:

$$\begin{Bmatrix} \sigma_L^{(n)} \\ \sigma_T^{(n)} \\ \sigma_{LT}^{(n)} \end{Bmatrix} = \begin{bmatrix} \cos^2\alpha^{(n)} & \sin^2\alpha^{(n)} & \sin 2\alpha^{(n)} \\ \sin^2\alpha^{(n)} & \cos^2\alpha^{(n)} & -\sin 2\alpha^{(n)} \\ -\sin\alpha^{(n)}\cos\alpha^{(n)} & \sin\alpha^{(n)}\cos\alpha^{(n)} & \cos 2\alpha^{(n)} \end{bmatrix} \begin{Bmatrix} \sigma_{11} \\ \sigma_{22} \\ \sigma_{12} \end{Bmatrix} \quad (33)$$

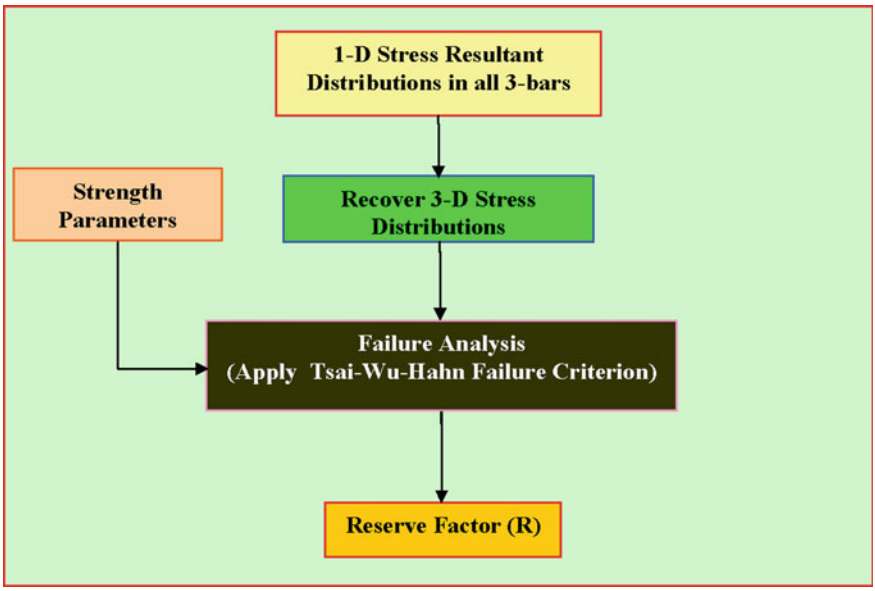

Fig. 9 Flow-chart for finding the failure stress level in laminates of four-bar mechanisms

$$\begin{Bmatrix} \sigma_{LT'}^{(n)} \\ \sigma_{TT'}^{(n)} \\ \sigma_{T'}^{(n)} \end{Bmatrix} = \begin{bmatrix} \cos\alpha^{(n)} & \sin\alpha^{(n)} & 0 \\ -\sin\alpha^{(n)} & \cos\alpha^{(n)} & 0 \\ 0 & 0 & 1 \end{bmatrix} \begin{Bmatrix} \sigma_{13} \\ \sigma_{23} \\ \sigma_{33} \end{Bmatrix} \tag{34}$$

Here $\alpha^{(n)}$ denotes the ply-angle of nth ply.

5. Determine strains in the principal material directions are determined using the above recovered 3-D strains by applying the following strain transformation relations:

$$\begin{Bmatrix} \varepsilon_{L}^{(n)} \\ \varepsilon_{T}^{(n)} \\ \varepsilon_{LT}^{(n)} \end{Bmatrix} = \begin{bmatrix} \cos^2\alpha^{(n)} & \sin^2\alpha^{(n)} & \sin 2\alpha^{(n)} \\ \sin^2\alpha^{(n)} & \cos^2\alpha^{(n)} & -\sin 2\alpha^{(n)} \\ -\sin\alpha^{(n)}\cos\alpha^{(n)} & \sin\alpha^{(n)}\cos\alpha^{(n)} & \cos 2\alpha^{(n)} \end{bmatrix} \begin{Bmatrix} \varepsilon_{11} \\ \varepsilon_{22} \\ \varepsilon_{12} \end{Bmatrix} \tag{35}$$

$$\begin{Bmatrix} \varepsilon_{LT'}^{(n)} \\ \varepsilon_{TT'}^{(n)} \\ \varepsilon_{T'}^{(n)} \end{Bmatrix} = \begin{bmatrix} \cos\alpha^{(n)} & \sin\alpha^{(n)} & 0 \\ -\sin\alpha^{(n)} & \cos\alpha^{(n)} & 0 \\ 0 & 0 & 1 \end{bmatrix} \begin{Bmatrix} \varepsilon_{13} \\ \varepsilon_{23} \\ \varepsilon_{33} \end{Bmatrix} \tag{36}$$

Here $\alpha^{(n)}$ denotes the ply-angle of nth ply.

6. Calculate reserve factor (R) in each ply by applying Tsai-Wu-Hahn 3-D failure criterion using above calculated stresses in the principal material directions i.e.

$$\left[\sigma_{L}^{(n)}\ \sigma_{T}^{(n)}\ \sigma_{LT}^{(n)}\ \sigma_{LT'}^{(n)}\ \sigma_{TT'}^{(n)}\ \sigma_{T'}^{(n)}\right]^{T}.$$

7. Then $R_{\text{Laminate}} = \min . \, of \, \{R_1, R_2, R_3, \ldots, R_n\}$ for each of the three bars in the mechanism.

Figure 10 shows the strain distribution through-the-laminate-thickness at A of bar-1 (AB) for maximum resultant force, $F_r = 38.03$ N which occurs at $t = 1.51$ s. Figure 11 shows the stress distribution through-the-laminate-thickness at A of bar-1 (AB) for maximum resultant force, $F_r = 38.03$ N which occurs at $t = 1.51$ s. The distributions are significantly affected by cross-sectional non-linearity. Here it can be observed that the layer orientation influences the stress distribution of the component-laminate and it is also very important to determine the location of highly stressed regions in the component-laminate and the stress values in all the layers of the system. Stresses σ_L and σ_{LT} reach their maximum values at the bottom of the laminate of bar-1 (AB) whereas stress σ_T is maximum at 0.4 mm from the bottom of the same laminate. The highest stress, as expected, is σ_L due to bending in this laminate. Figure 12 shows the reserve factor, R, in each ply at A of the laminate AB for the applied clockwise constant angular velocity, $\Omega = \pi \frac{\text{rad}}{\text{s}}$. In this case, ply-1 of bar-1 is predicted to fail first for maximum F_r and its $R = +85.24$. For maximum F_r and with reversal of the applied constant angular velocity, ply-3 of bar-1 is predicted to fail first and its $R = -44.28$ as observed from Fig. 13.

Figure 14 shows the strain distribution through-the-laminate-thickness at A of bar-1 (AB) for the case of maximum resultant moment, $M_r = 0.47$ N m occurring at $t = 0.005$ s. Figure 15 shows the corresponding stress distribution through-the-laminate-thickness at A of bar-1 (AB). In this case also, the stress and strain distributions are significantly affected by cross-sectional nonlinearities. Stresses σ_L and σ_{LT} reach their maximum values at the bottom of the laminate of bar-1 (AB) whereas stress σ_T is maximum at 0.4 mm from the bottom of the laminate. The highest stress, as expected, is σ_L due to bending in this laminate. Figure 16 shows

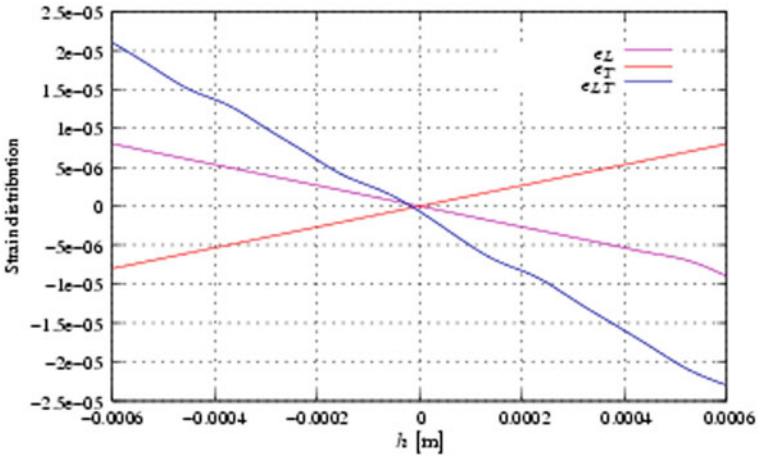

Fig. 10 Strain distribution through-the-laminate-thickness (@A of AB) for max. resultant force, $F_r = 38.03$ N @ t = 1.51 s

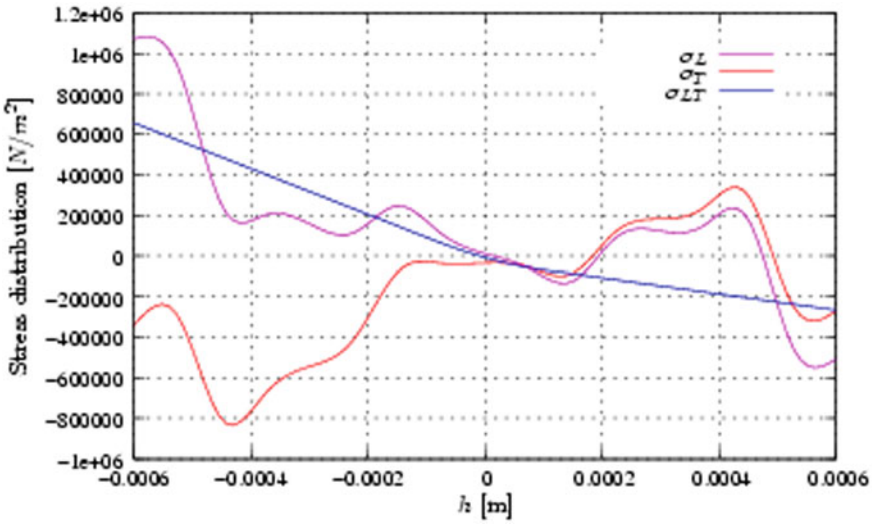

Fig. 11 Stress distribution through-the-laminate-thickness (@A of AB) for max. resultant force, $F_r = 38.03$ N @ t = 1.51 s

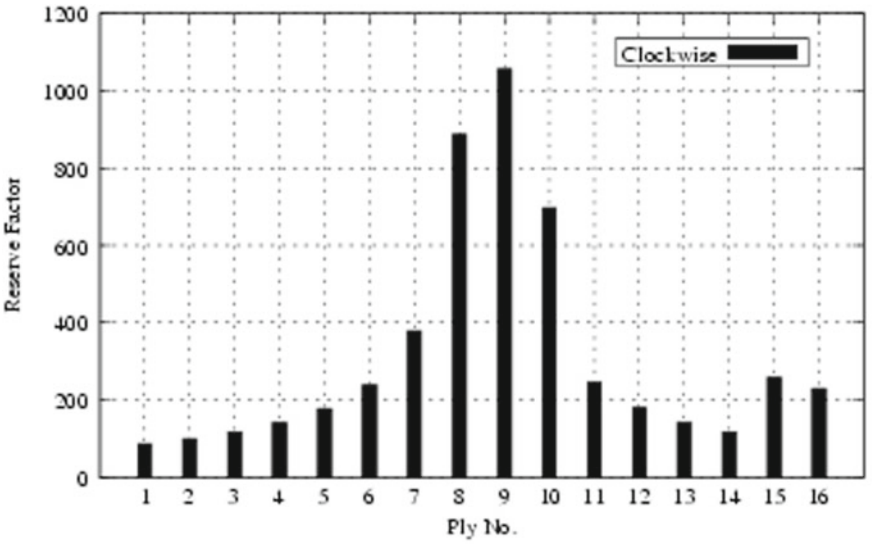

Fig. 12 Reserve factor (R) in each ply ($R_{Laminate} = +85.24$)

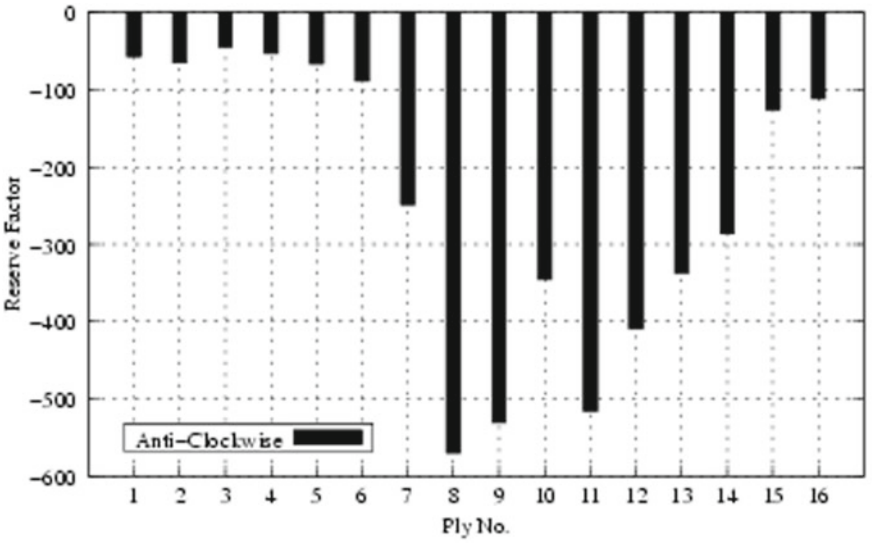

Fig. 13 Reserve factor (R) in each ply ($R_{Laminate} = -44.28$)

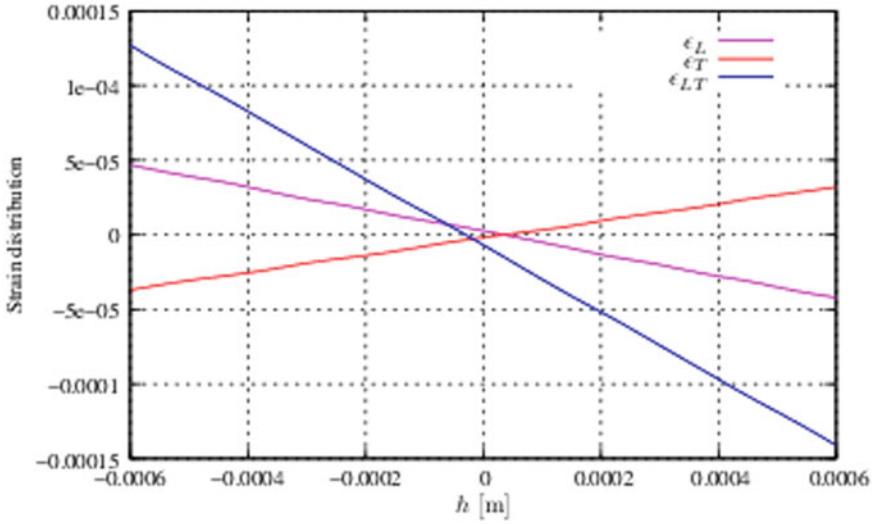

Fig. 14 Strain distribution through-the-laminate-thickness (@A of AB) for max. resultant moment, $M_r = 0.47$ N m @ t = 0.005 s

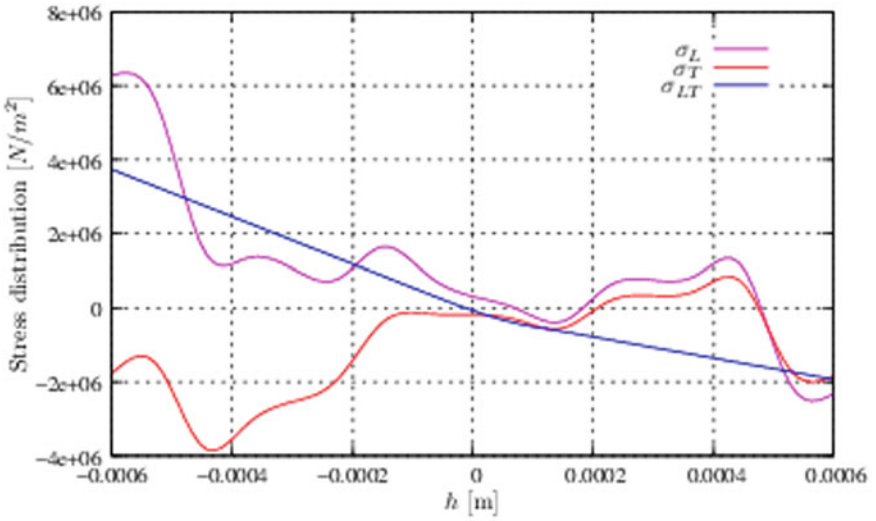

Fig. 15 Stress distribution through-the-laminate-thickness (@A of AB) for max. resultant moment, $M_r = 0.47$ N m @ t = 0.005 s

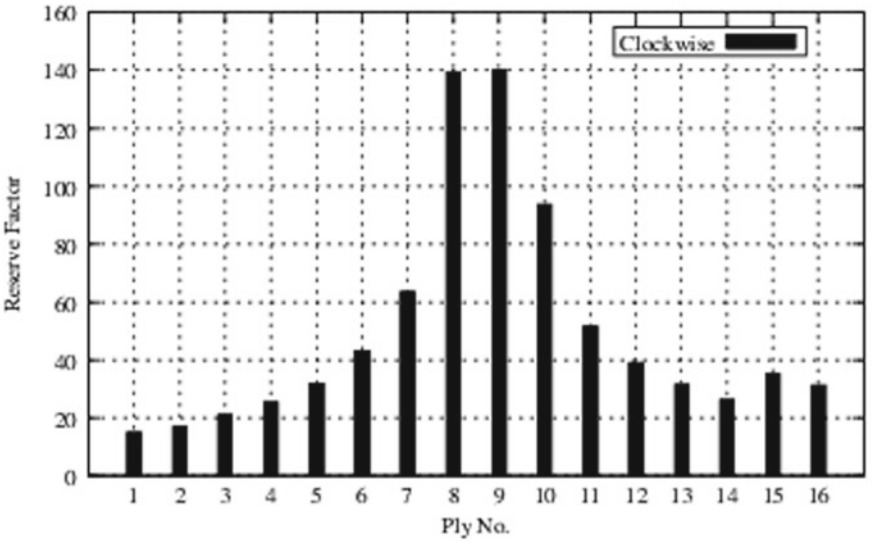

Fig. 16 Reserve factor (R) in each ply ($R_{Laminate} = +14.86$)

the reserve factor, R, in each ply at A of the laminate AB for the applied clockwise constant angular velocity, $\Omega = \pi \frac{\text{rad}}{\text{s}}$. In this case also, ply-1 of bar-1 is predicted to fail first for maximum M_r and its $R = +14.86$. For maximum M_r and with the reversal of the applied constant angular velocity, ply-3 of bar-1 is predicted to fail first and its $R = -8.89$ as observed from Fig. 17.

Similarly, Figs. 18 and 19 show the strain and stress distributions, respectively, through-the-laminate-thickness at B of bar-1 (AB) for maximum resultant force, $F_r = 38.08$ N occurs at $t = 1.51$ s. Figures 20 and 21 show the reserve factor, R, in each ply at B of the laminate AB for the applied clockwise and with the reversal of the applied constant angular velocity, $\Omega = \pi \frac{\text{rad}}{\text{s}}$, respectively. Figures 22 and 23 show the strain and stress distributions, respectively, through-the-laminate-thickness at B of bar-1 (AB) for maximum resultant moment, $M_r = 0.03$ N m occurs at $t = 0.005$ s. Figures 24 and 25 show the reserve factor, R, in each ply at B of the laminate AB for the applied clockwise and with the reversal of the applied constant angular velocity, $\Omega = \pi \frac{\text{rad}}{\text{s}}$, respectively.

For bar-2 (BC) at B, the strain and stress distributions through-the-laminate-thickness for maximum resultant force, $F_r = 38.08$ N occurs at $t = 1.51$ s are shown in Figs. 26 and 27, respectively. At the same B, the reserve factor, R, in each ply of the laminate BC for the applied clockwise and with the reversal of the applied constant angular velocity are shown in Figs. 28 and 29, respectively. At the same point, B, for maximum resultant moment, $M_r = 0.1005$ N m occurs at, $t = 0.00056$ s the

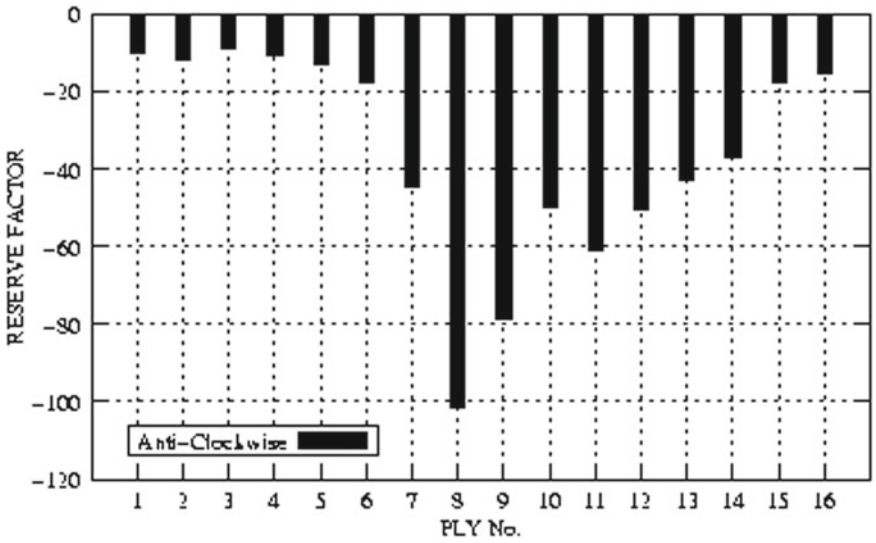

Fig. 17 Reserve factor (R) in each ply ($R_{\text{Laminate}} = -8.89$)

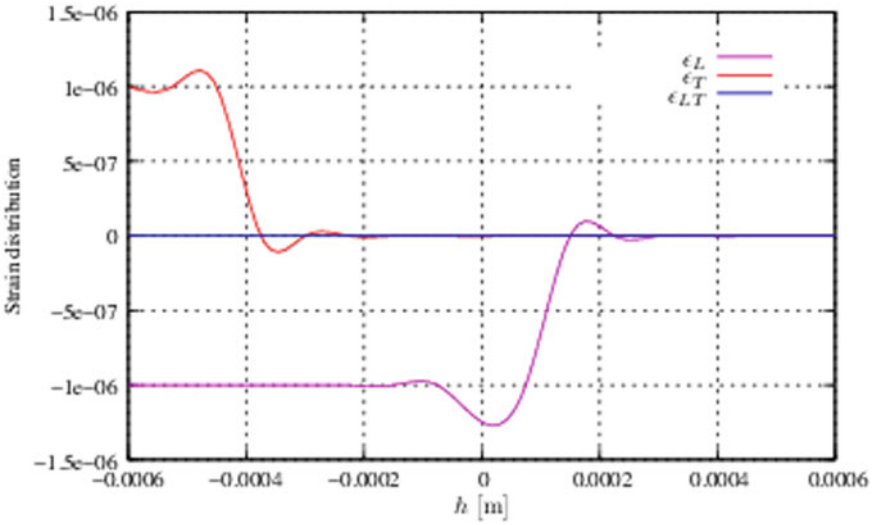

Fig. 18 Strain distribution through-the-laminate-thickness (@B of AB) for max. resultant force, $F_r = 38.08$ N @ t = 1.51 s

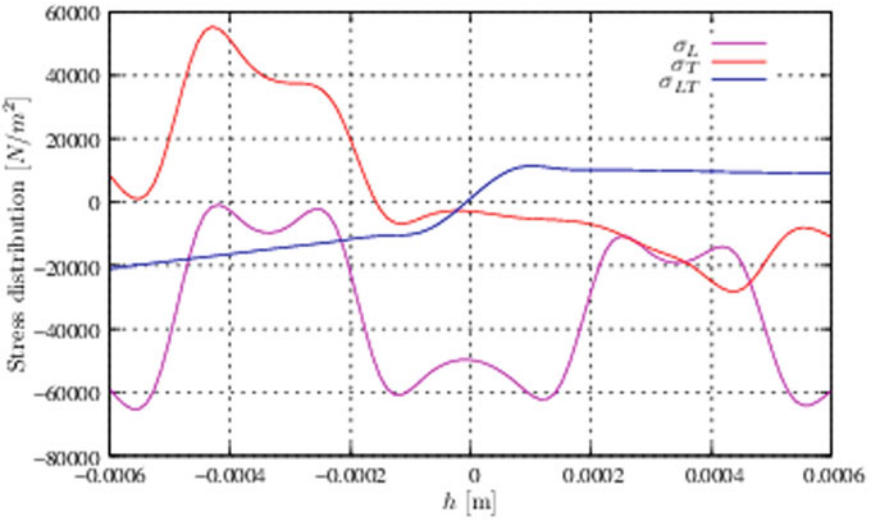

Fig. 19 Stress distribution through-the-laminate-thickness (@B of AB) for max. resultant force, $F_r = 38.08$ N @ t = 1.51 s

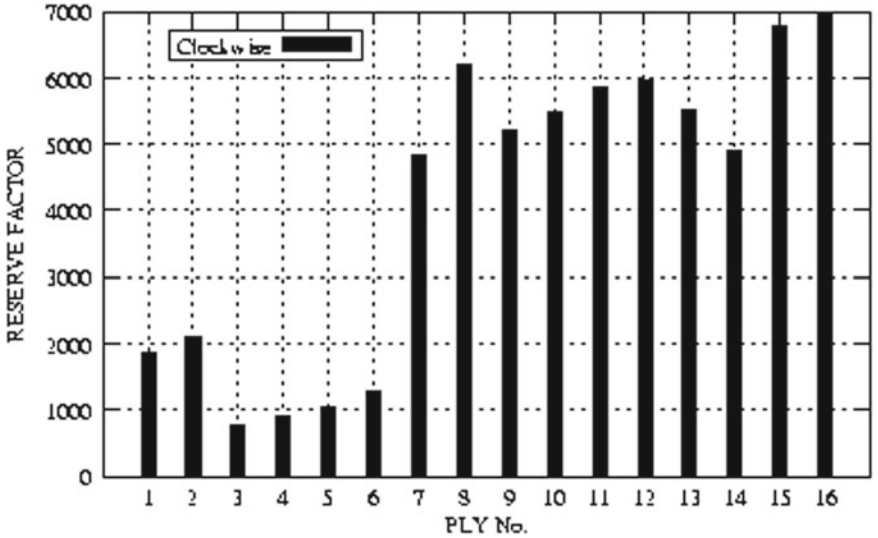

Fig. 20 Reserve factor (R) in each ply ($R_{Laminate} = +771.22$)

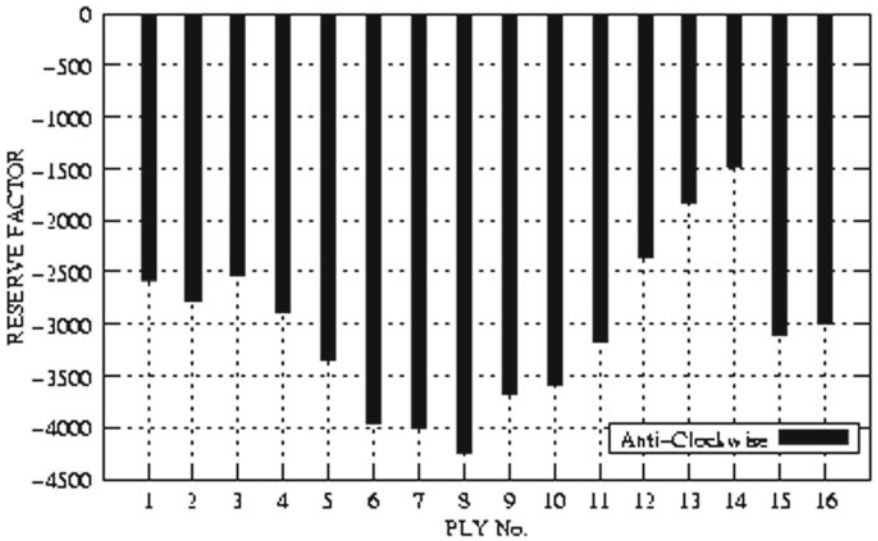

Fig. 21 Reserve factor (R) in each ply ($R_{Laminate} = -1474.13$)

strain and stress distributions are shown in Figs. 30 and 31, respectively. The Reserve Factor, R, in each ply at B of the laminate BC for the applied clockwise and with the reversal of the applied constant angular velocity are shown in Figs. 32 and 33, respectively.

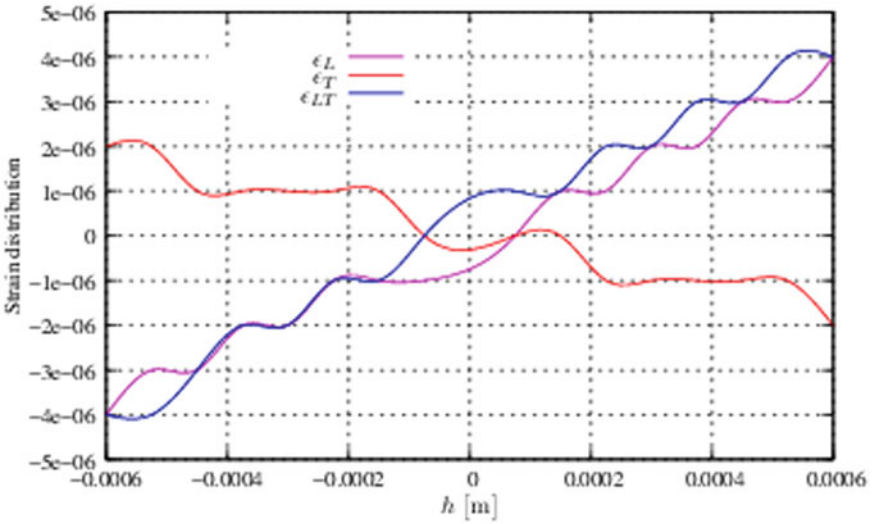

Fig. 22 Strain distribution through-the-laminate-thickness (@B of AB) for max. resultant moment, $M_r = 0.03$ N m @ t = 0.0005 s

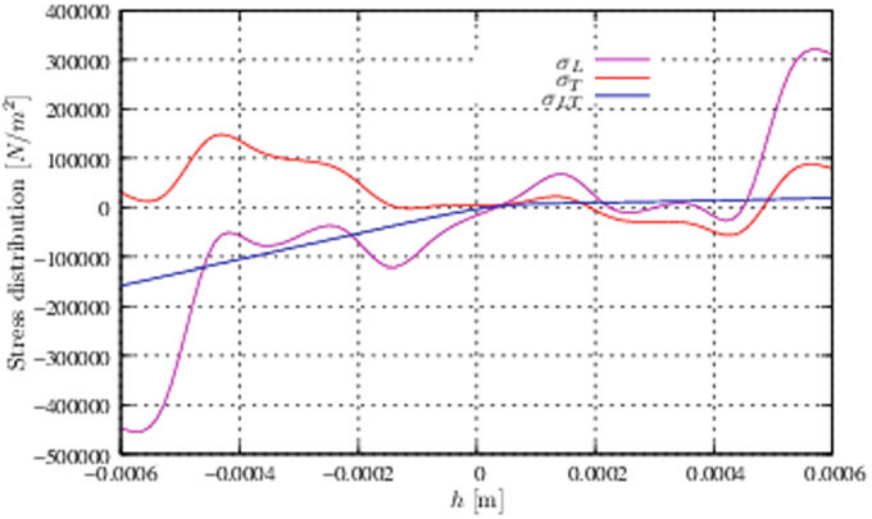

Fig. 23 Stress distribution through-the-laminate-thickness (@B of AB) for max. resultant moment, $M_r = 0.03$ N m @ t = 0.0005 s

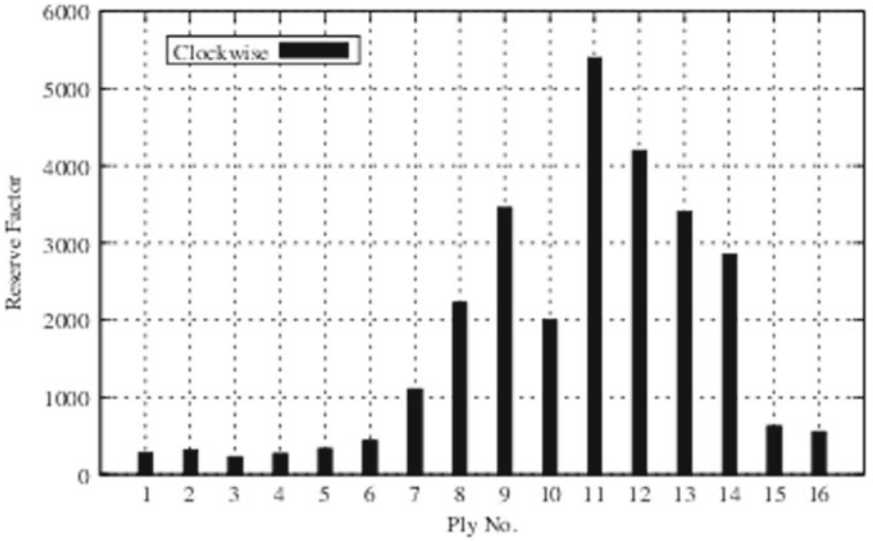

Fig. 24 Reserve factor (R) in each ply ($R_{Laminate} = +224.42$)

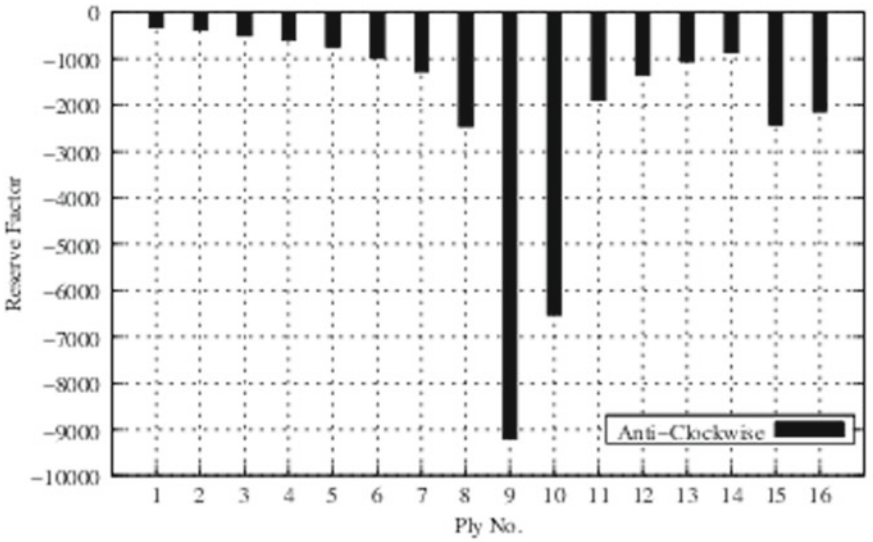

Fig. 25 Reserve factor (R) in each ply ($R_{Laminate} = -325.04$)

Figures 34, 35, 36 and 37 shows the strain distribution, stress distribution, the reserve factor, R, in each ply for the applied clockwise and with the reversal of the applied constant angular velocity, respectively, at C of bar-2 (BC) for maximum resultant force, $F_r = 38.29$ N occurs at $t = 1.51$ s. Figures 38, 39, 40 and 41 shows

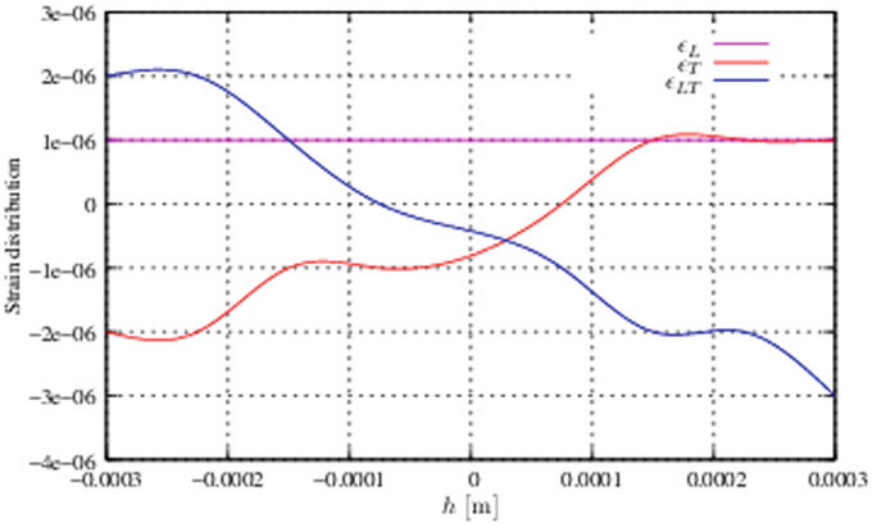

Fig. 26 Strain distribution through-the-laminate-thickness (@B of BC) for max. resultant force, $F_r = 38.08$ N @ t = 1.51 s

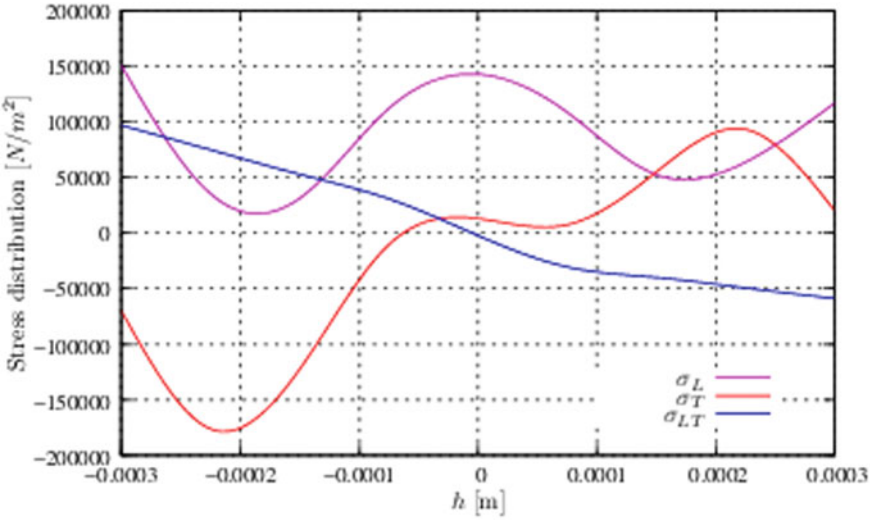

Fig. 27 Stress distribution through-the-laminate-thickness (@B of BC) for max. resultant force, $F_r = 38.08$ N @ t = 1.51 s

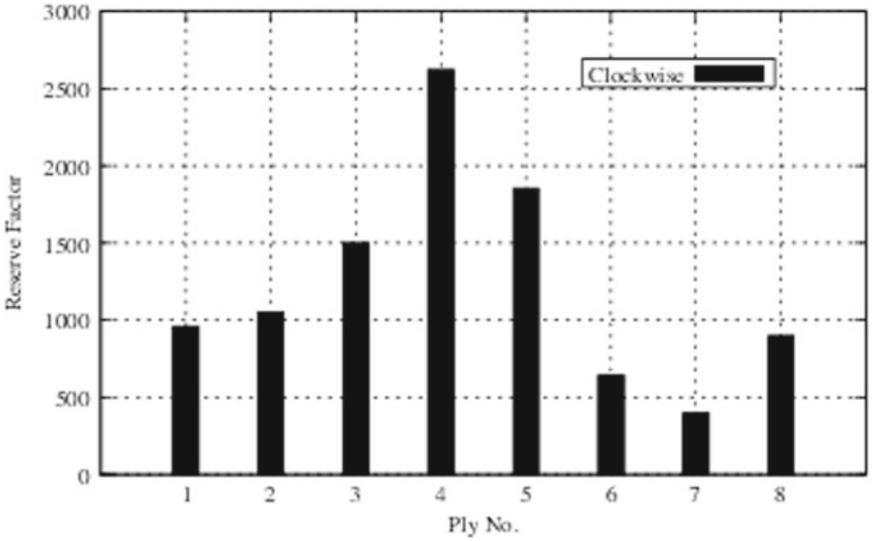

Fig. 28 Reserve factor (R) in each ply ($R_{Laminate} = +400.24$)

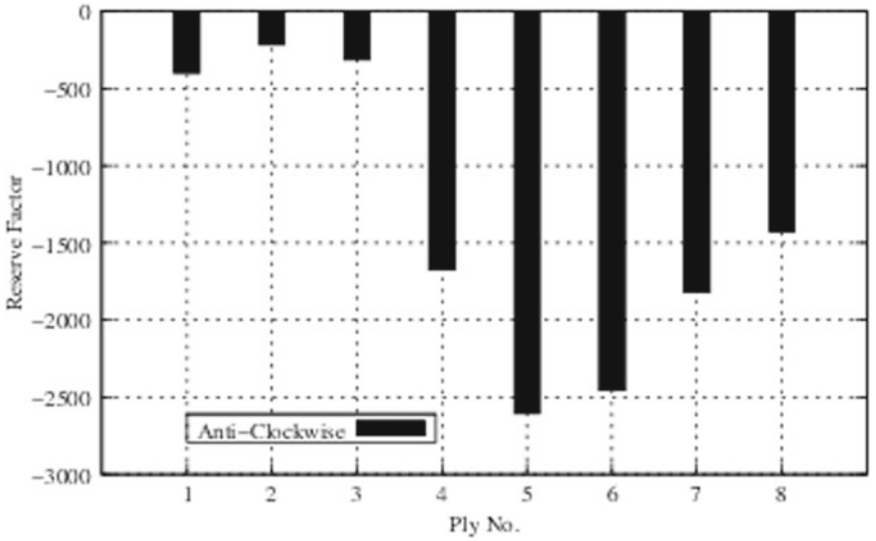

Fig. 29 Reserve factor (R) in each ply ($R_{Laminate} = -215.62$)

the corresponding strain and stress distributions, reserve factors, R, at C of bar-2 (BC) for maximum resultant moment, $M_r = 0.083$ N m occurs at $t = 0.0038$ s. At C of bar-3 (CD), for maximum resultant force, $F_r = 38.16$ N occurs at $t = 1.51$ s and for maximum resultant moment, $M_r = 0.041$ N m occurs at, $t = 1.49$ s the strain-stress

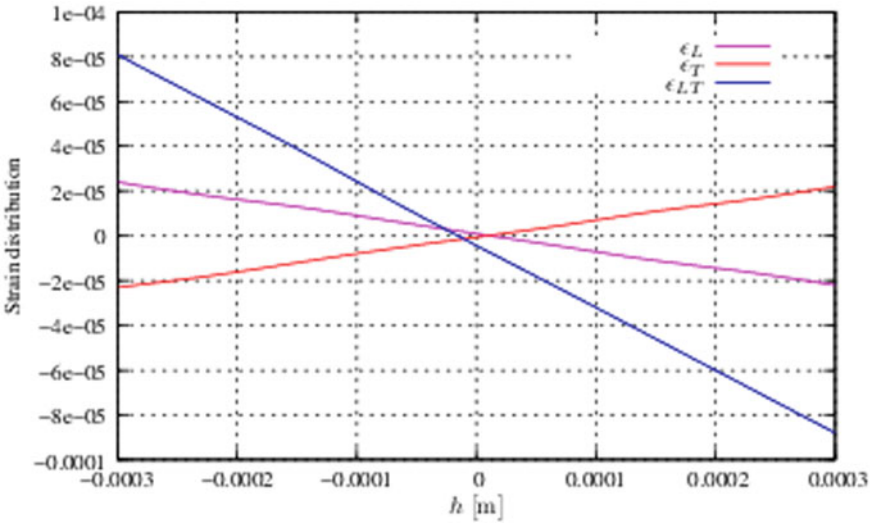

Fig. 30 Strain distribution through-the-laminate-thickness (@B of BC) for max. resultant moment, $M_r = 0.1005$ N m @ t = 0.00056 s

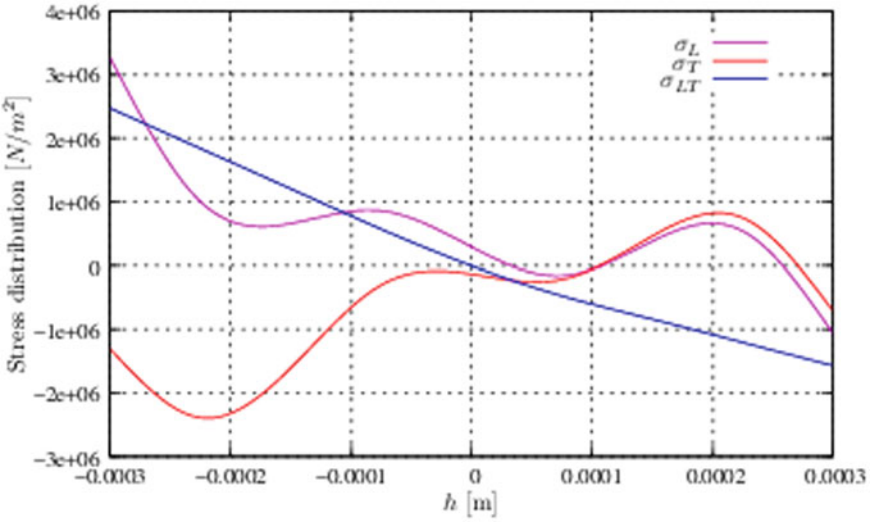

Fig. 31 Stress distribution through-the-laminate-thickness (@B of BC) for max. resultant moment, $M_r = 0.1005$ N m @ t = 0.00056 s

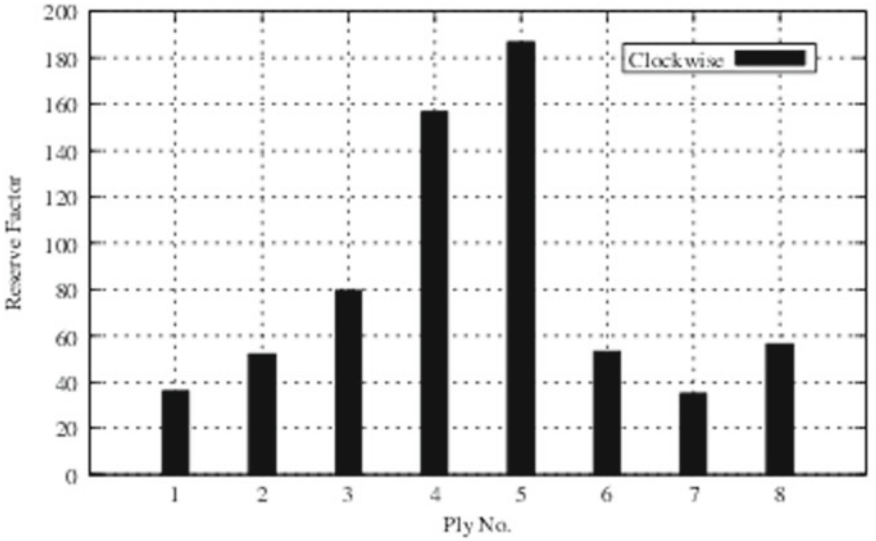

Fig. 32 Reserve factor (R) in each ply ($R_{Laminate} = +35.06$)

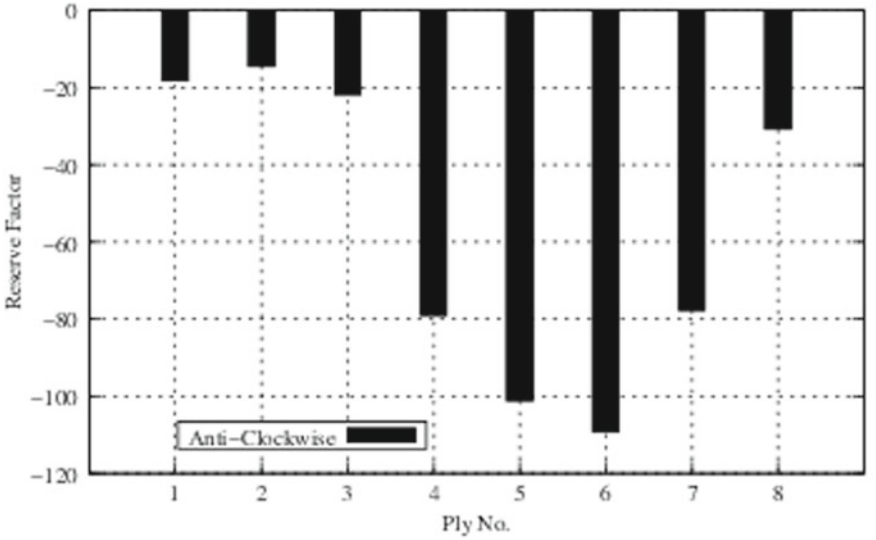

Fig. 33 Reserve factor (R) in each ply ($R_{Laminate} = -14.46$)

distributions and the reserve factors, R, in each ply are shown in Figs. 42, 43, 44, 45, 46, 47, 48 and 49. At D of bar-3 (CD), for maximum resultant force, $F_r = 38.21$ N occurs at $t = 1.51$ s and for maximum resultant moment, $M_r = 0.122$ N m occurs at, $t = 0.0002$ s the strain-stress distributions and the reserve factors, R, in each ply

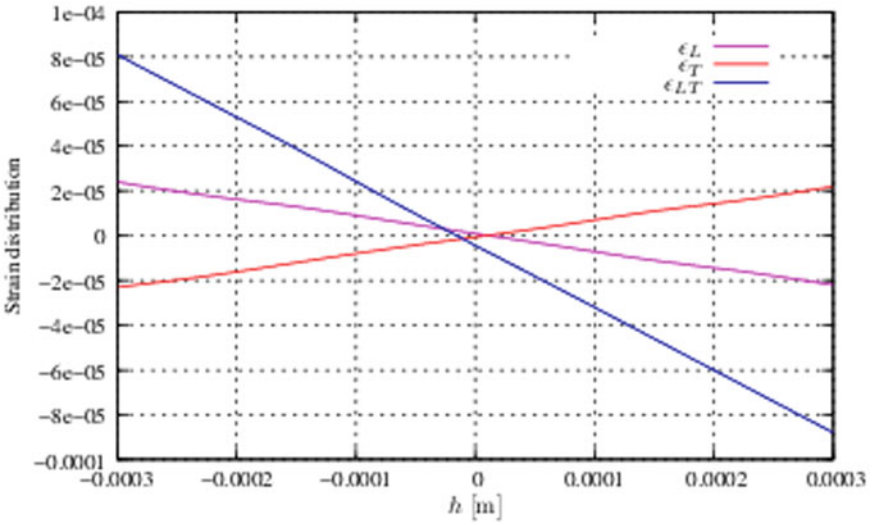

Fig. 34 Strain distribution through-the-laminate-thickness (@C of BC) for max. resultant force, $F_r = 38.29$ N @ t = 1.51 s

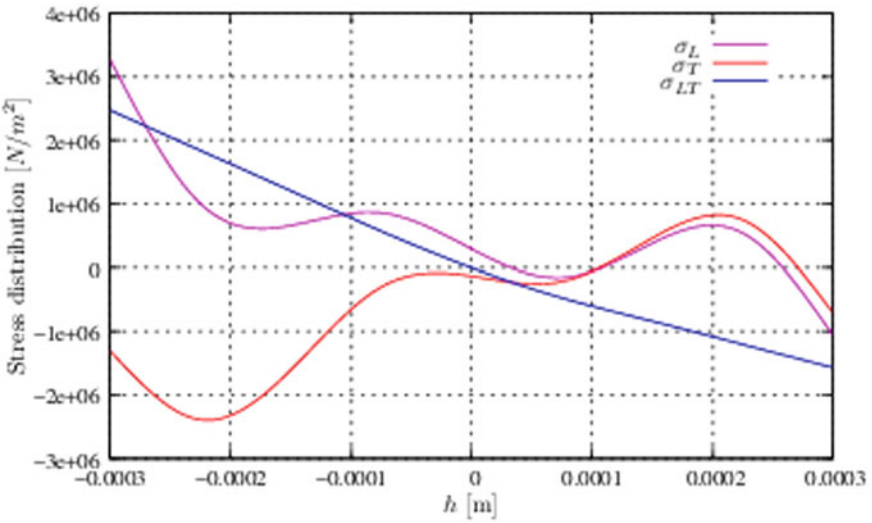

Fig. 35 Stress distribution through-the-laminate-thickness (@C of BC) for max. resultant force, $F_r = 38.29$ N @ t = 1.51 s

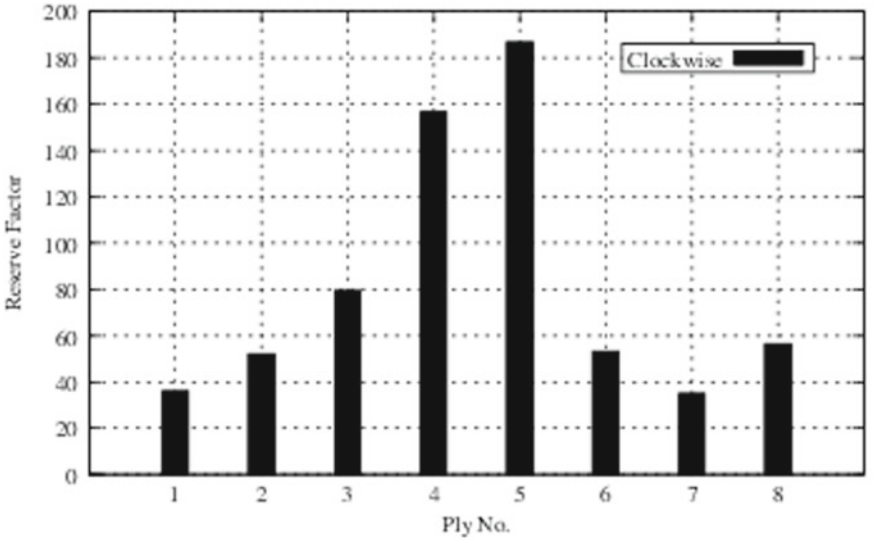

Fig. 36 Reserve factor (R) in each ply ($R_{Laminate} = +63.44$)

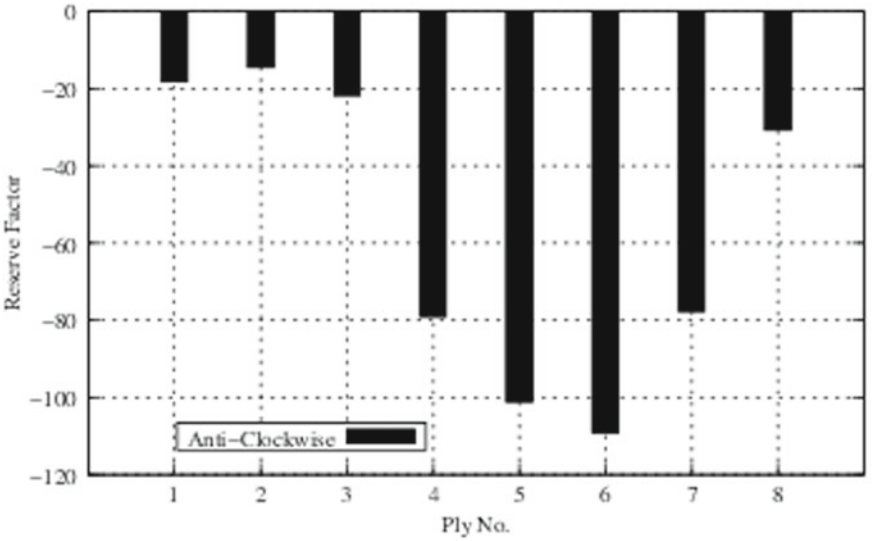

Fig. 37 Reserve factor (R) in each ply ($R_{Laminate} = -36.57$)

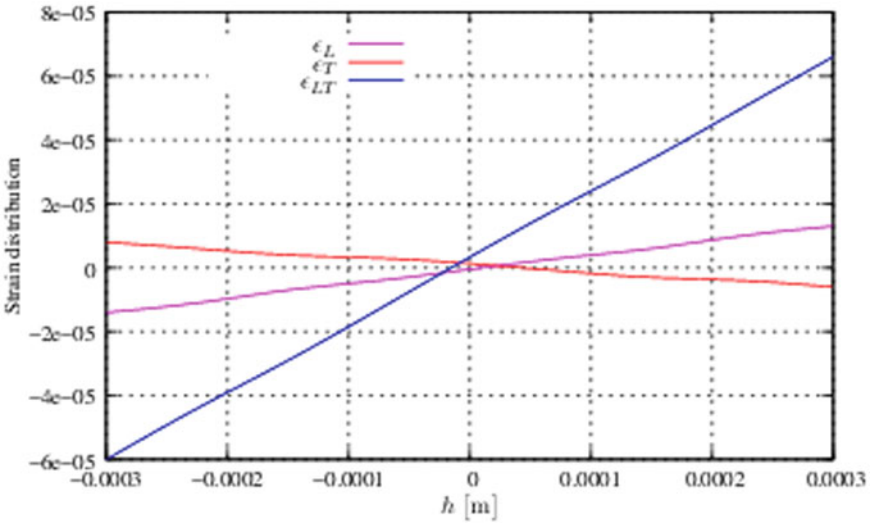

Fig. 38 Strain distribution through-the-laminate-thickness (@C of BC) for max. resultant moment, $M_r = 0.083$ N m @ t = 0.0038 s

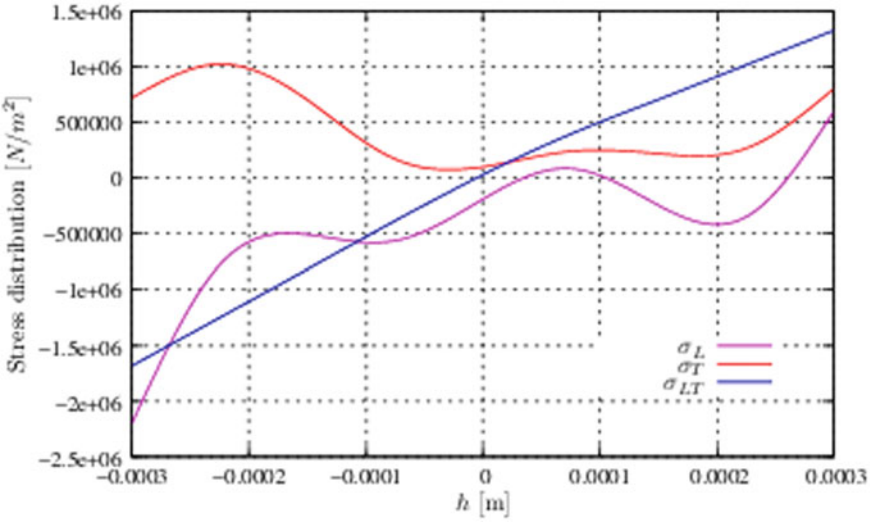

Fig. 39 Stress distribution through-the-laminate-thickness (@C of BC) for max. resultant moment, $M_r = 0.083$ N m @ t = 0.0038 s

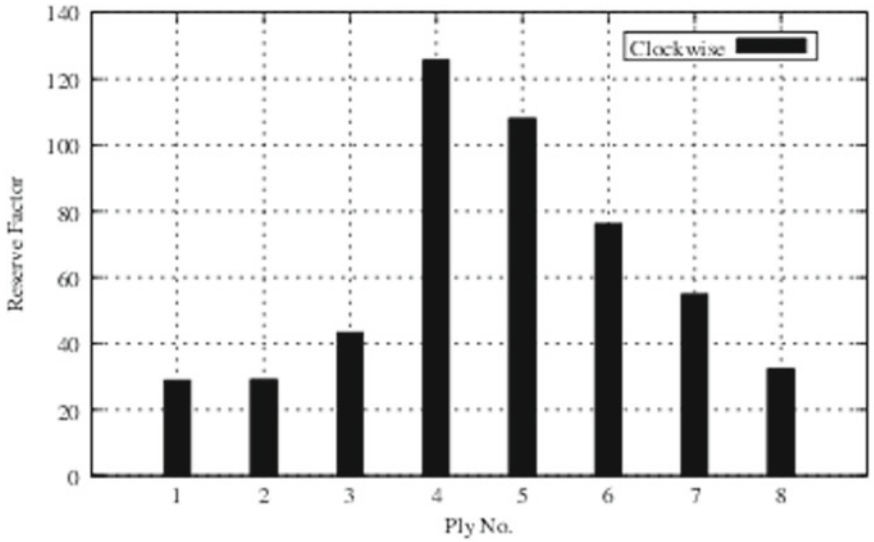

Fig. 40 Reserve factor (R) in each ply ($R_{Laminate} = +28.89$)

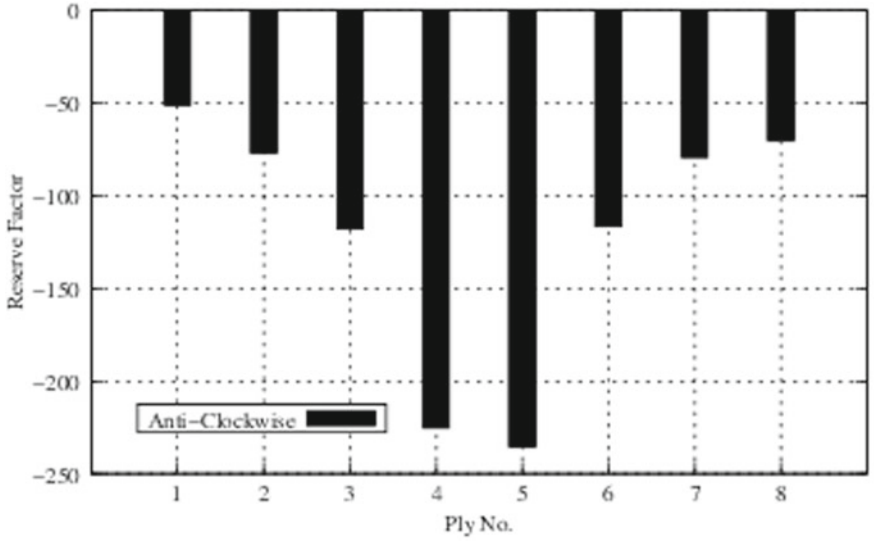

Fig. 41 Reserve factor (R) in each ply ($R_{Laminate} = -51.15$)

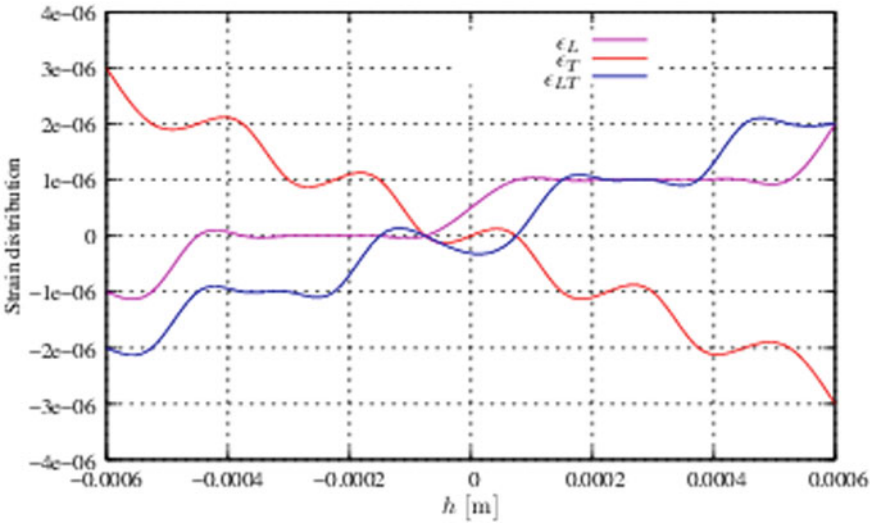

Fig. 42 Strain distribution through-the-laminate-thickness (@C of CD) for max. resultant force, $F_r = 38.16$ N @ t = 1.51 s

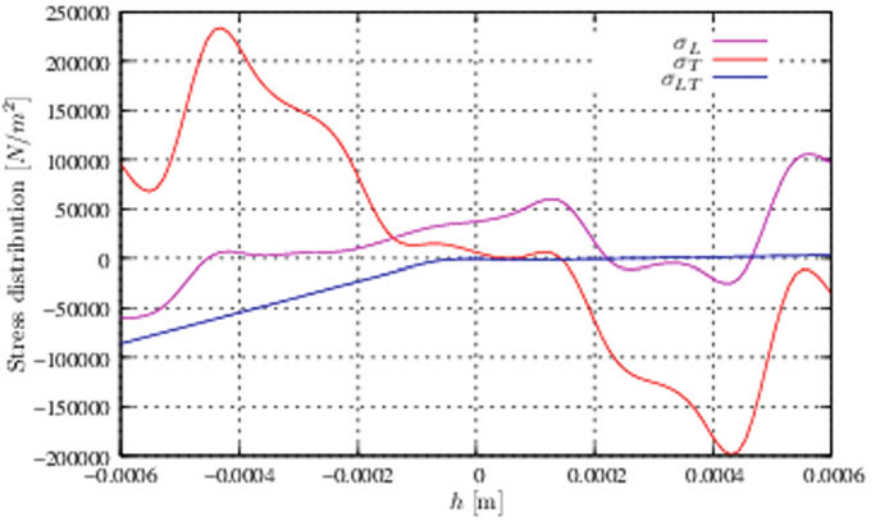

Fig. 43 Stress distribution through-the-laminate-thickness (@C of CD) for max. resultant force, $F_r = 38.16$ N @ t = 1.51 s

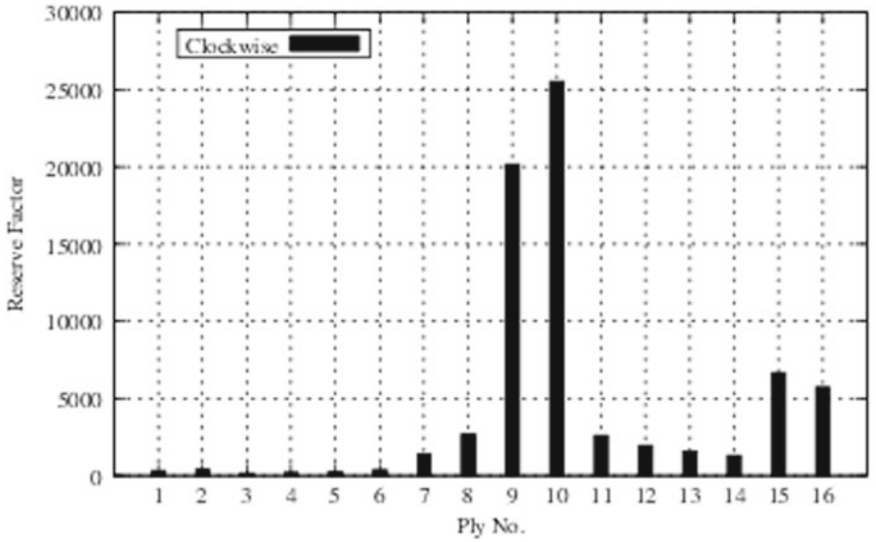

Fig. 44 Reserve factor (R) in each ply ($R_{Laminate} = +172.81$)

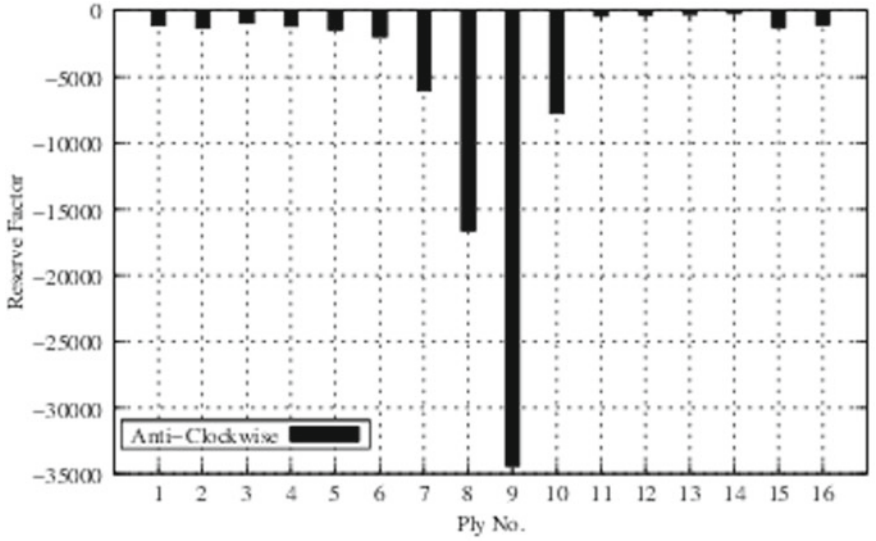

Fig. 45 Reserve factor (R) in each ply ($R_{Laminate} = -211.8$)

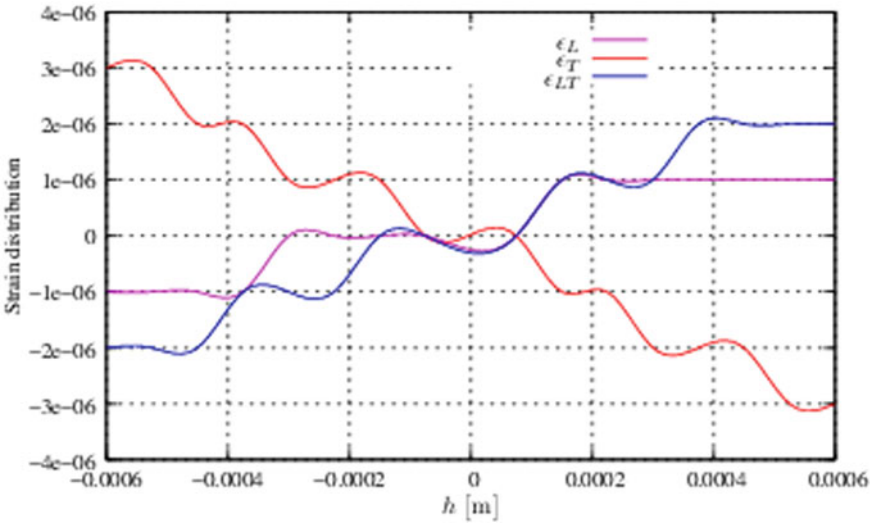

Fig. 46 Strain distribution through-the-laminate-thickness (@C of CD) for max. resultant moment, $M_r = 0.041$ N m @ t = 1.49 s

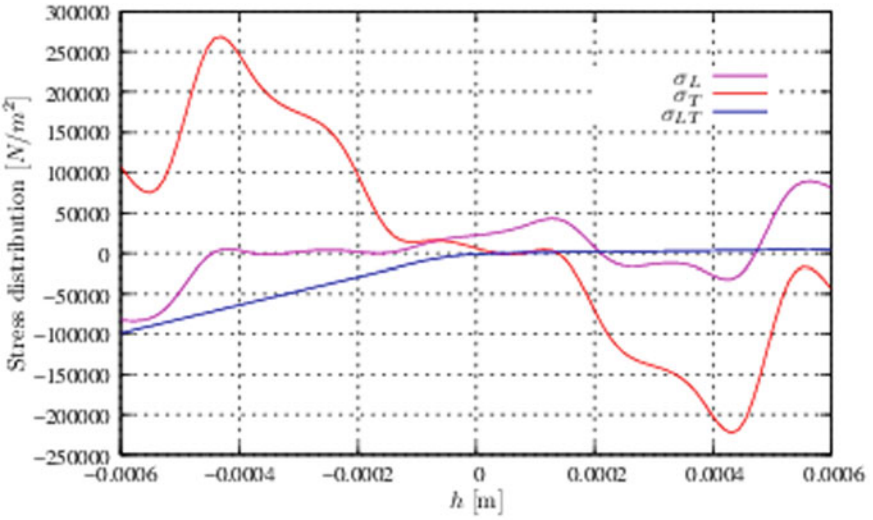

Fig. 47 Stress distribution through-the-laminate-thickness (@C of CD) for max. resultant moment, $M_r = 0.041$ N m @ t = 1.49 s

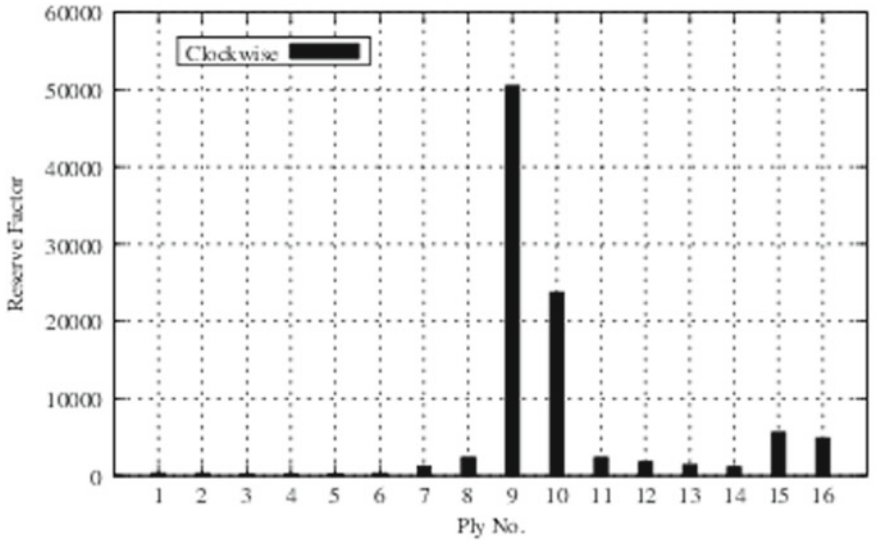

Fig. 48 Reserve factor (R) in each ply ($R_{Laminate} = +150.39$)

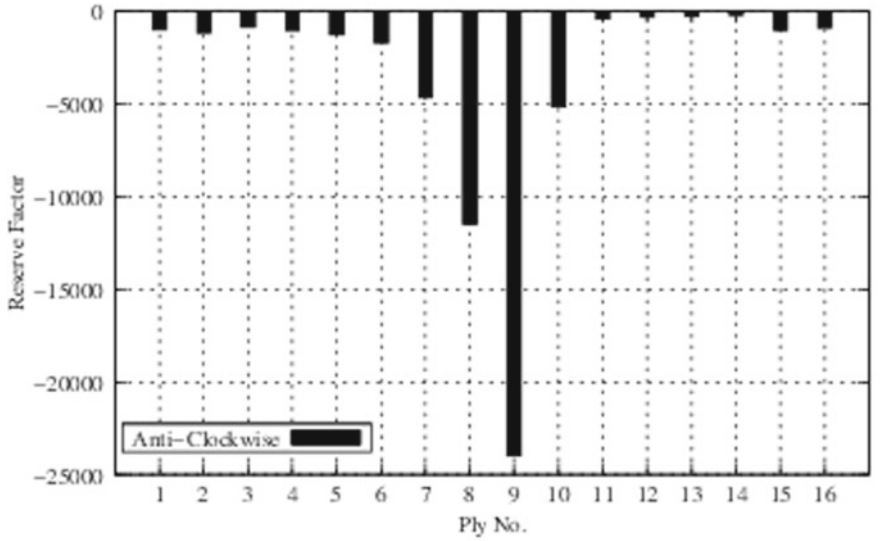

Fig. 49 Reserve factor (R) in each ply ($R_{Laminate} = -188.9$)

are shown in Figs. 50, 51, 52, 53, 54, 55, 56 and 57. F_r and M_r are evaluated at the joints and along the reference curves of all the component-laminates and tabulated in the Table 11. It is observed that the mechanism as a whole fails due to maximum resultant moment, $M_r = 0.47$ N m which occurs at $t = 0.005$ s.

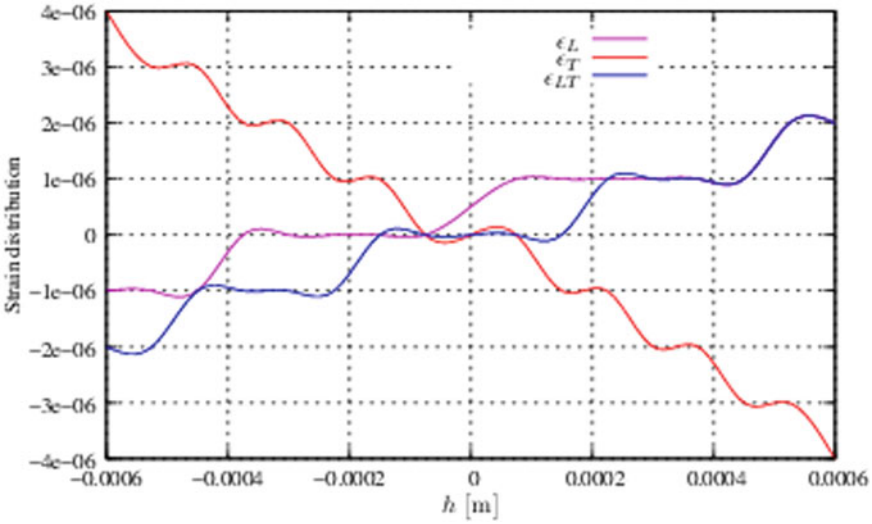

Fig. 50 Strain distribution through-the-laminate-thickness (@D of CD) for max. resultant force, $F_r = 38.21$ N @ t = 1.51 s

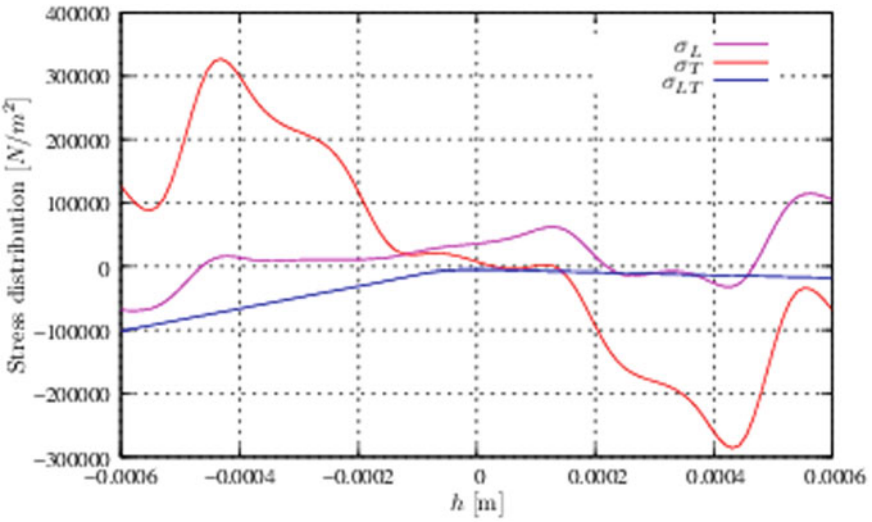

Fig. 51 Stress distribution through-the-laminate-thickness (@D of CD) for max. resultant force, $F_r = 38.21$ N @ t = 1.51 s

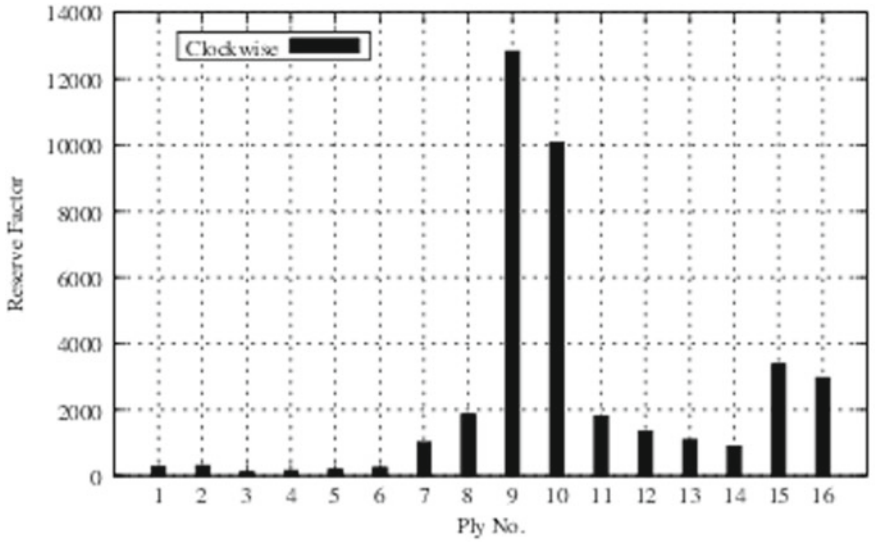

Fig. 52 Reserve factor (R) in each ply ($R_{Laminate} = +124.65$)

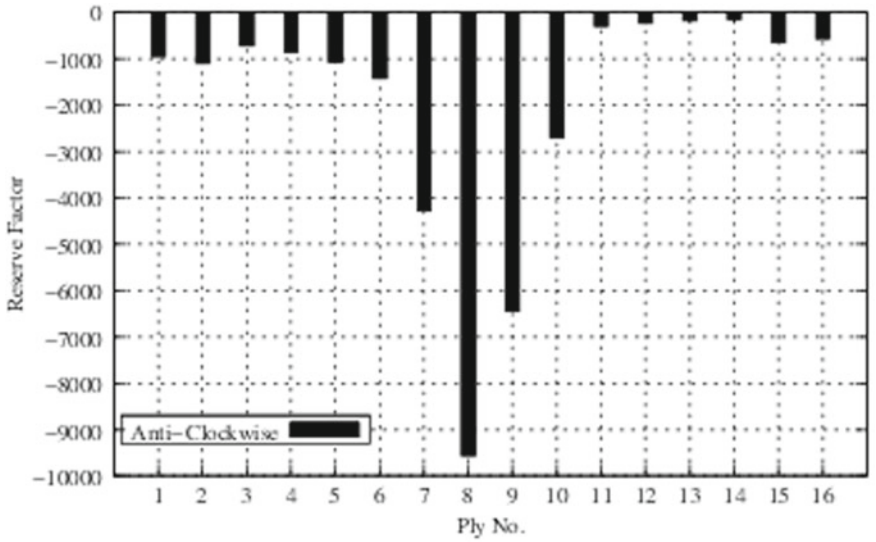

Fig. 53 Reserve factor (R) in each ply ($R_{Laminate} = -146.43$)

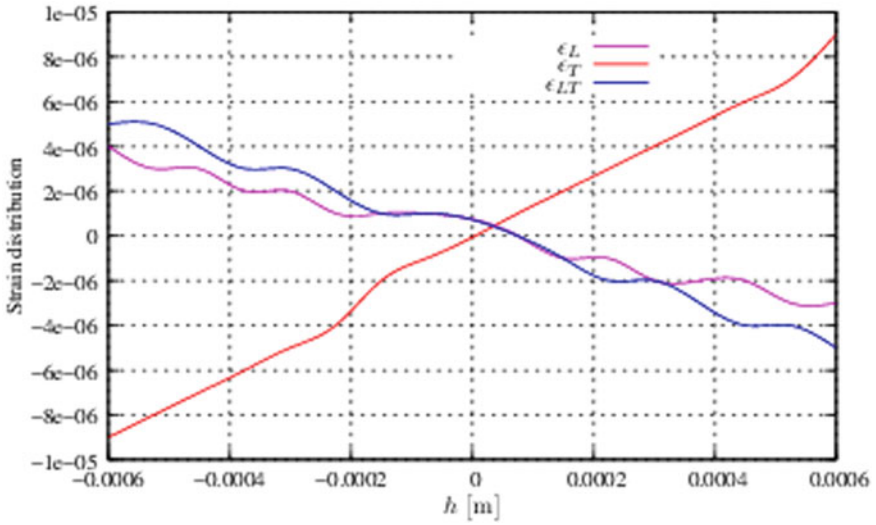

Fig. 54 Strain distribution through-the-laminate-thickness (@D of CD) for max. resultant moment, $M_r = 0.122$ N m @ t = 0.0002 s

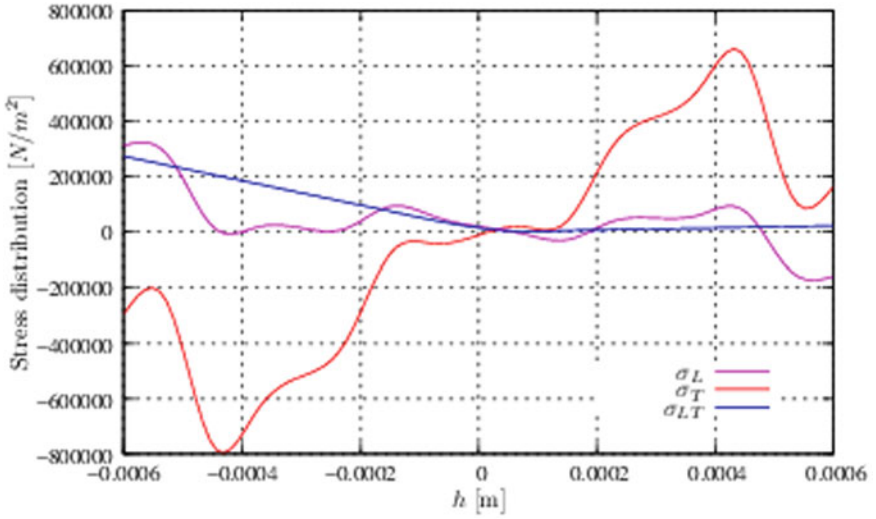

Fig. 55 Stress distribution through-the-laminate-thickness (@D of CD) for max. resultant moment, $M_r = 0.122$ N m @ t = 0.0002 s

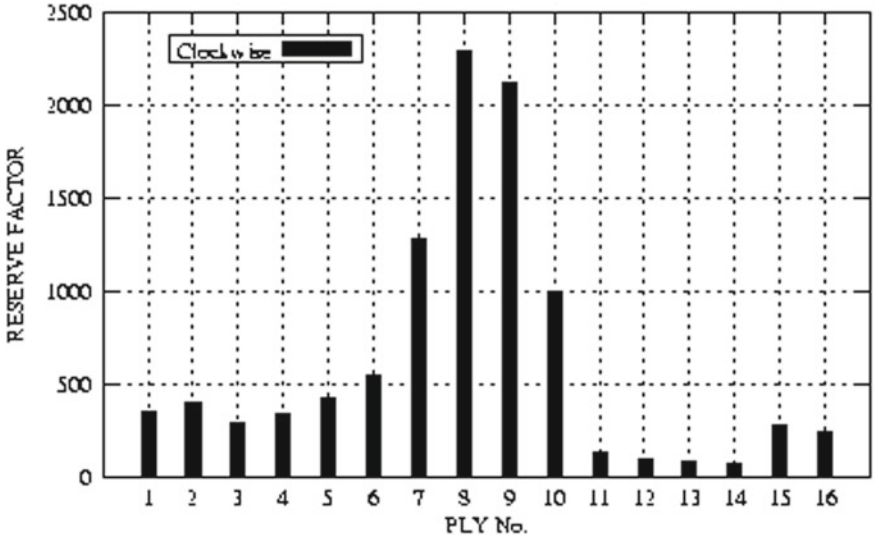

Fig. 56 Reserve factor (R) in each ply ($R_{Laminate} = +63.29$)

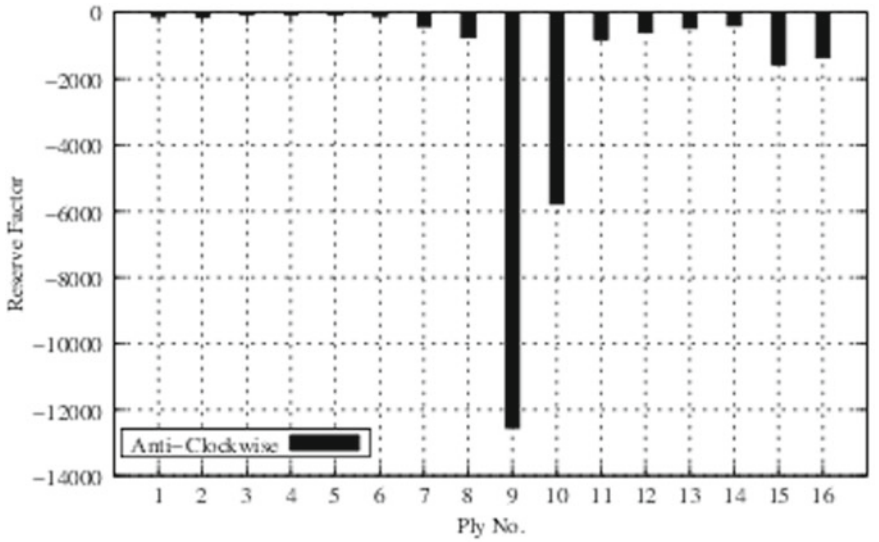

Fig. 57 Reserve factor (R) in each ply ($R_{Laminate} = -51.02$)

5 Conclusions

In this Chapter, the component-laminate load-carrying capacity is evaluated using the Tsai-Wu-Hahn failure criterion for various layups of the three bars in the four-bar mechanism. The reserve factor, R of each ply in the component-laminate is calculated by using the maximum resultant force, $F_r^{\max}$, and the maximum resultant moment, $M_r^{\max}$ occurring at different time steps along the reference curves of all the component-bars and at the joints of the mechanism. The non-linear through-the-thickness stress and strain distributions are reported at different points. This illustrates the failure of each component-laminate and the mechanism as a whole. The Tsai-Wu-Hahn failure criterion is used to predict both the first-ply-failure and the failure of the mechanism as a whole. Also, it is observed that the layer orientation influences the stress distribution in the component-laminates and it is also very important to determine the location of highly stressed regions in the component-laminate amongst all the layers of each component of the system.

References

1. Nobuo, T., Shu, M., Yoji, O.: Smart composite sandwich structures for future aerospace application-damage detection and suppression: a review. J. Solid Mech. Mater. Eng. **1**, 3–17 (2007)
2. Nunes, J.P., Silva, J.F.: Sandwiched composites in aerospace engineering. Adv. Compos. Mater. Aerosp. Eng. (Process. Prop. Appl.) **1**, 129–174 (2016)
3. Harris, C.E., Starnes, J.H., Shuart, M.J.: Design and manufacturing of aerospace composite structures state-of-the-art assessment. J. Aircr. **39**(4), 545–560 (2002)
4. Mrazova, M.: Advanced composite materials of the future in aerospace industry. INCAS Bull. **5**, 139–150 (2013)
5. Tsai, S.W., Wu, E.M.: A general theory of strength for anisotropic materials. J. Compos. Mater. **5**, 58–80 (1971)
6. Tsai, S.W., Hahn, H.T.: Introduction to Composite Materials. Technomic Publishing Company, Lancaster (1980)
7. Hodges, D.H.: Nonlinear Composite Beam Theory, vol. 213 of Progress in Astronautics and Aeronautics, pp. 20191–4344. American Institute of Aeronautics and Astronautics, Inc., 1801 Alexander Bell Drive, Reston, Virginia (2006)
8. Pollayi, H., Harursampath, D.: Geometrically non-linear dynamics of composite four-bar mechanisms. Int. J. Non-Linear Mech. **47**, 837–850 (2012)
9. Harursampath, D.: Non-classical non-linear effects in thin-walled composite beams. Ph.D. thesis, Aerospace Engineering, Georgia Institute of Technology, Georgia, USA (1998)
10. Bauchau, O.A.: Computational schemes for flexible, nonlinear multi-body systems. Multibody Syst. Dyn. **2**, 169–225 (1998)
11. Pollayi, H., Harursampath, D.: Geometrically non-linear dynamics of composite four-bar mechanisms. In: Proceedings of the 49th AIAA/ASME/ASCE/AHS/ASC Structures, Structural Dynamics and Materials Conference, 18–21 Apr, Austin, Texas, USA. Paper: AIAA-2008-2079 (2008)
12. Alizade, R., et al.: Analytical synthesis of function generating spherical four-bar mechanism for the five precision points. Mech. Mach. Theory SCI **40**(7), 863–878 (2005)
13. Sitti, M.: Piezoelectrically actuated four-bar mechanism with two flexible links for micromechanical flying insect thorax. IEEE/ASME Trans. Mechatron. **8**(1) (2003)

14. Armanios, E.A., Makeev, A., Hooke, D.: Finite displacement analysis of laminated composite strips with extension-twist coupling. J. Aerosp. Eng. **9**, 80–91 (1996)
15. Kosmatka, J.B.: Extension-bend-twist coupling behavior of thin-walled advanced composite beams with initial twist. In: Proceedings of the 32nd AIAA/ASME/ASCE/AHS/ASC Structures, Structural Dynamics and Materials Conference, 8-10 Apr, Baltimore, Maryland, USA. Paper: AIAA-91-1023 (1991)
16. Winckler, S.I.: Hygrothermally curvature stable laminates with tension-torsion coupling. J. Am. Helicopter Soc. **31**, 56–58 (1985)